Measurement of the total proton-proton cross section with ATLAS at LHC

Samah Abdel Khalek Abdel Khalek

LAL 13-375
Novembre 2013

THÈSE

Présentée le 28 Novembre 2013

par

Samah ABDEL KHALEK

Discipline : Physique des hautes énergies

pour obtenir le grade de

Docteur ès Sciences
de l'Université Paris Sud, Orsay

Mesure de la section efficace totale proton-proton avec le détecteur ATLAS au LHC

Soutenue devant la commission d'examen composée de :

Mme.	C.	Augier	Rapporteur
M.	P.	Puzo	Directeur de thèse
M.	C.	Royon	Rapporteur
M.	A.	Stocchi	Président
M.	V.	Vorobel	Examinateur

Abstract

It is now nearly fifty years since total proton-proton (pp) cross sections have been found to grow with energy after it was believed for long time that they would become asymptotically constant . The uncertainties of the cosmic ray data, at high energy, do not allow to determine the exact growth with energy of the total cross section . The Large Hadron Collider (LHC) at CERN in Geneva has already delivered collisions with an energy never reached in a particle accelerator. The energy in the center of mass was 7 TeV (2010 2011) or 8 TeV (2012) and will ultimately reached 14 TeV in the near future. Thus, this will provide a good environment for a new precise measurement of the total pp cross section at this energy. The ATLAS detector installed in one of the four LHC interaction points is used to collect the result of the pp collisions. Its sub-detector ALFA located 240 m from the interaction point, is used to track protons resulting from elastic collisions. Therefore, within special beam optics conditions, ALFA is able to measure the total cross section and the nuclear slope. During this PhD the analysis performed on the first data led to $\sigma_{\text{tot}}(pp \to X) = \left(94.88 \pm 0.12_{\text{stat.}} \pm 1.56_{\text{syst.}}\right)$ mbarn and $b = \left(19.45 \pm 0.05_{\text{stat.}} \pm 0.31_{\text{syst.}}\right)$ GeV^{-2} at 7 TeV.

Résumé

Celà fait maintenant presque 50 ans qu'on a découvert que la section efficace totale proton-proton augmentait avec lénergie, alors qu'on pensait précédemment qu'elle deviendrait asymptotiquement constante. Les incertitudes des mesures sur les rayons cosmiques effectuées à haute énergie ne permettent pas de déterminer la forme exacte de l'augmentation de la section efficace avec lénergie. Le LHC au CERN à Genève fournit des collisions avec une énergie jamais atteinte dans un accélérateur de particule. Lénergie dans le centre de masse était 7 TeV en 2010 2011, 8 TeV en 2012 et atteindra 14 TeV dans un futur proche. Le détecteur ATLAS installé sur un des quatre points d'interaction du LHC, est utilisé pour collecter le résultat des collisions proton-proton. Son sous-détecteur ALFA, situé à 240 m du point d'interaction, est utilisé pour détecter les proton résultant des collisions élastiques. ALFA est donc capable, dans certaines conditions particulières de l'optique, de mesurer la section efficace totale et la pente nucléaire. Le travail effectué durant cette thèse a permit de mesurer $\sigma_{\text{tot}}(pp \to X) = \left(94.88 \pm 0.12_{\text{stat.}} \pm 1.56_{\text{syst.}}\right)$ mbarn et $b = \left(19.45 \pm 0.05_{\text{stat.}} \pm 0.31_{\text{syst.}}\right)$ GeV^{-2} à 7 TeV.

Contents

Introduction

The Large Hadron Collider (LHC) at CERN is a 27 km two-rings, superconducting collider. It started its operation in November 2009. LHC set a new world record at the beginning of 2010 by colliding high intensity proton beams with a center-of-mass energy of 7 TeV, then 8 TeV in 2012. It provides new data for different detectors and experiments installed on the LCH collision points.
ATLAS is one of these experiments, and the largest physics detector ever built. It aims to investigate many different types of physics that might become detectable in the LHC energy range. ATLAS covers a wide scientific program, that stretches from precision measurements of the Standard Model to the discovery of new physics.

Any physical process is described by a cross section that measures its probability to occur. For almost all measurements performed at LHC, one crucial ingredient is needed, the precise knowledge of the luminosity. This quantity describes the ability of the collider to produce useful interactions. Therefore, the absolute knowledge of the luminosity allows to measure the absolute cross sections. One way is to calibrate a relative luminosity detector using a dedicated setup called ALFA (Absolute Luminosity For ATLAS).

This thesis describes the ALFA strategy to measure the absolute luminosity, and the total proton-proton cross section. It is based on the measurement of the elastic scattering spectrum, in the limit of the Coulomb Nuclear Interference (CNI) region, by measuring the trajectories of elastically scattered protons at very small angles. To do so, special beam optics conditions are required, and detectors have to move close to the beam in the ATLAS forward region.
Since these ultimate optics conditions request a lot of machine time and development, an intermediate optics option was developed by the end of 2011, and allowed ALFA to measure the nuclear part of the transfer momentum spectrum (t-spectrum). With this optics, a measurement of the total proton-proton cross section was possible, using the luminosity measured by ATLAS, for spectrum normalization.

The work presented in this thesis started by the end of 2010. At the time, detectors were under test beam, for last calibrations before installation in the LHC tunnel. The first data taking took place in Octobre 2011. This will allow to present two different analysis: the first one is related to the test beam and covers detector calibrations and instrumentations, and the second one is related to the data taking and the measurement of the total cross section with the 2011 runs.

Chapter 1 and 2 of this thesis are intended as an introduction to the experiment frame work, including a brief description of LHC accelerator and ATLAS detector system with its subdetectors and their role in the identification of particles. In addition, the second part of chapter 1 presents general accelerators physics concepts and definitions that will be used in this thesis. Thus, the principles of transverse beam dynamics are explained as well as transfer matrix formalism, which allows to predict final particle position, knowing the initial coordinates and the transfer matrix elements.

Chapter 3 introduces methods used in ATLAS for relative luminosity measurements, and its calibration. It also presents ALFA strategy of an independent measurements using the elastic scattering process and the optical theorem.

Chapter 4 describes the experimental requirements to reach the CNI, including LHC beam optics conditions, and ALFA scintillating tracker system. ALFA detectors were designed taking into account LHC constraints and physics requirements. They are constituted of Roman Pots (RPs), a mechanical system allowing the fiber tracker to approach a few millimeters for LHC beam center, and front-end electronics as read out system. Eight detectors are installed in the LHC tunnel, four in each side of ATLAS at 240 m from the interaction point.

The ALFA measurement precision relies on the distance precision between the tracker and the beam. Requested precision is of the order of 10 μm. Two additional trackers (per detector), called Overlap Detector (OD), are used for the distance measurement. Chapter 5 introduces ODs, their role, and a dedicated calibration procedure, performed after the 2010 test beam. This calibration was achieved using a high precision detector as reference.

Chapter 6 describes the distance measurement analysis procedure for the 2011 runs. It shows some detector performance plots, data quality studies, and background contamination during these runs. Multiplicity selection cuts have been used in order to reduce systematic and improve the measurements. A new algorithm was implemented in order to analyze the first data, and a dedicated simulation was needed to estimate the systematic errors. Distance measurements of different stations will be used afterward for detectors alignment, needed for physics analysis.

The last chapter describes the first elastic scattering measurement at the LHC, made by

ALFA. In this chapter we go step by step though the full analysis chain (t-reconstruction, alignment, acceptance, efficiency, ...). Two main methods were used for the reconstruction of the t-spectrum, using the reconstructed position and the transfer matrix. Moreover, an advanced unfolding study will be shown, using different unfolding techniques, to study detectors, and beam resolution impact. Finally, the t-distribution will be fitted to deduce the total cross section and nuclear slope measurement at 7 TeV.

Chapter 1

The Large Hadron Collider and introduction to the beam optics

The essence of the scientific method is to perform experimental measurements that will verify or rebut the theoretical predictions. Therefore, constructing and understanding the necessary tools that will make the measurements possible is an important step in research.
This chapter deals with accelerator physics. It describes the **L**arge **H**adron **C**ollider (**LHC**) [1], a particles accelerator system, and its basic parameters, which provides the particles collisions (proton-proton (pp) collisions are in the interest of this thesis). Second section introduces the beam transversal dynamic concepts, which are needed in following chapters.

1.1 The Large Hadron Collider

The LHC is a two-ring-superconducting-hadron accelerator and collider installed in the existing 26.7 km tunnel that was constructed for the CERN LEP machine.
The aim of the LHC is to reveal the physics beyond the Standard Model by colliding two proton beams[1], with center of mass collision energies up to 14 TeV. Before they are brought into collision, the LHC beams pass through several accelerators where they are accelerated in stages to reach their final energy in the LHC.
An aerial photo of the French-Swiss border near Geneva city is shown in figure 1.1. Figure 1.2 was taken inside the tunnel, where some machine elements figure out.

[1] Beam 1 circulates clockwise in ring 1 and Beam 2 circulates counter clockwise in ring 2

Figure 1.1: Aerial picture of the French-Swiss border near Geneva city. The yellow circle represents the LHC accelerator and collider, installed in the a 26.7 km underground tunnel, 100 m beneath the surface. It is operating since Autumn 2009.

Figure 1.2: The view inside the tunnel. The machine accelerates either protons or lead ions (82 Pb) with two beams traveling in opposite directions. The two beams have to be deflected by opposite magnet dipole fields.

1.1.1 Injection chain

Besides having had the LEP[2] tunnel available to install the LHC, CERN[3] also has an extensive accelerator complex which has been used for past experiments and parts of which were adapted to provide the early boosting stages for the LHC (figure 1.3). The ion source is a duoplasmatron, which makes protons from hydrogen atoms by bombarding them with free electrons to strip off the valence electrons. The protons are first accelerated by the Linac2, a linear accelerator, up to energies of 50 MeV. They are fed into the Proton Synchrotron Booster (PSB) which accelerates them to energies of 1.4 GeV for the next stage, the Proton

[2]The **L**arge **E**lectron **P**ositron (**LEP**) collider was operating from 1989 to 2000.
[3]The European Organization for Nuclear Research.

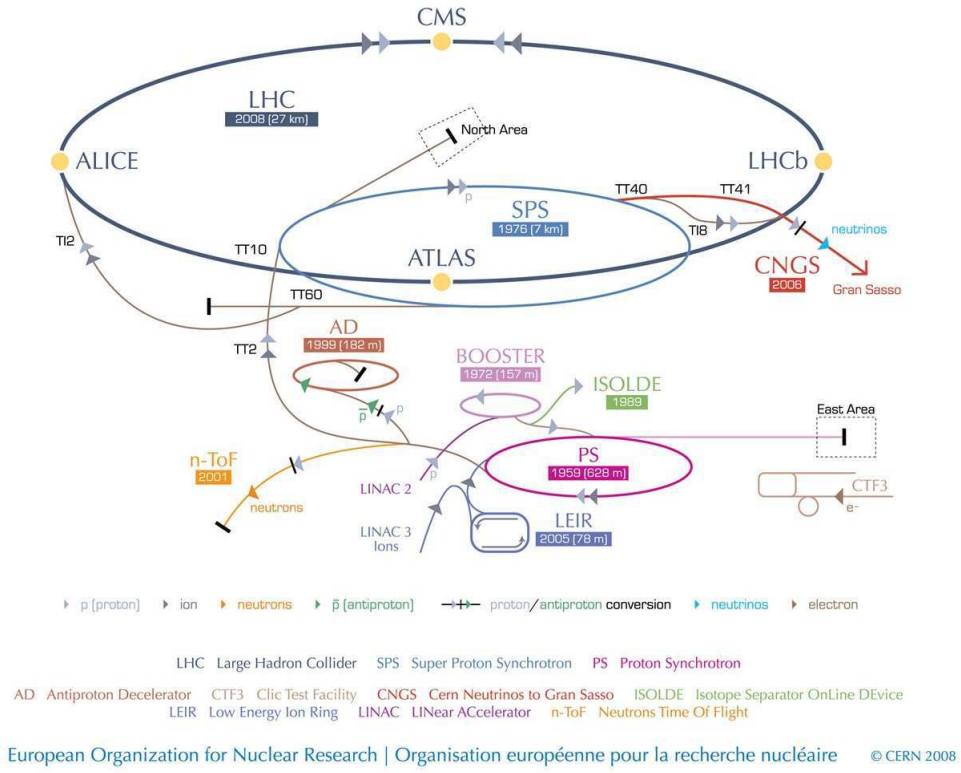

Figure 1.3: The LHC's injection chain.

Synchrotron (PS). The PS came online in 1959 and has received many upgrades over time. It's primary purpose now is to supply protons or ions for the various experiments at CERN, including the LHC. It accelerates protons to 25 GeV and injects bunches[4] of particles (up to 1.6×10^{11} particles) into the next stage, the Super Proton Synchrotron (SPS). The last stage prior to injection in the LHC, the SPS now serves as a booster for the LHC but in the past was operated as the Sp$\bar{p}$S, a p$\bar{p}$ collider. There the protons are accelerated to 450 GeV and injected into the LHC. The energy ramp in the LHC from 450 GeV to the current operating energy of 8 TeV takes about 20 minutes.

As the machine was gradually commissioned, the proton bunches evolved from an initial of 368 bunches per beam at the end of 2010, up to a total of 1380 bunches during the 2012 data taking. The evolution of the number of bunches and other beam parameters are summarized at the end of this section in the table 1.1.

[4]Collection of particles captured within one RF bucket. The RF system provides longitudinal focusing which constrains the particle motion in the longitudinal phase space to a confined region called the RF bucket.

1.1.2 Characteristics of the LHC

The LHC is located in an underground tunnel, 100 m beneath the surface, near the border region between France and Switzerland and close to the city of Geneva. It is operating since Autumn 2009. The machine accelerates either protons or lead ions (82 Pb) with two beams traveling in opposite directions. The two beams have to be deflected by opposite magnet dipole fields.

The LHC was designed as two eight fold symmetry rings with separate magnet fields and beam chambers and with common sections in the experimental regions where the beams collide. As there is not enough space to have two separate rings in the LEP tunnel, the LHC uses twin magnets which consist of two sets of coils and beam channels within the same mechanical structure and cryostat, illustrated in figure 1.4. This design also reduced the overall cost of the machine. The LHC consists of a total of 9593 superconducting magnets of which 1232 are main dipoles[5] of about 15 m long and 392 are main quadrupoles[6].

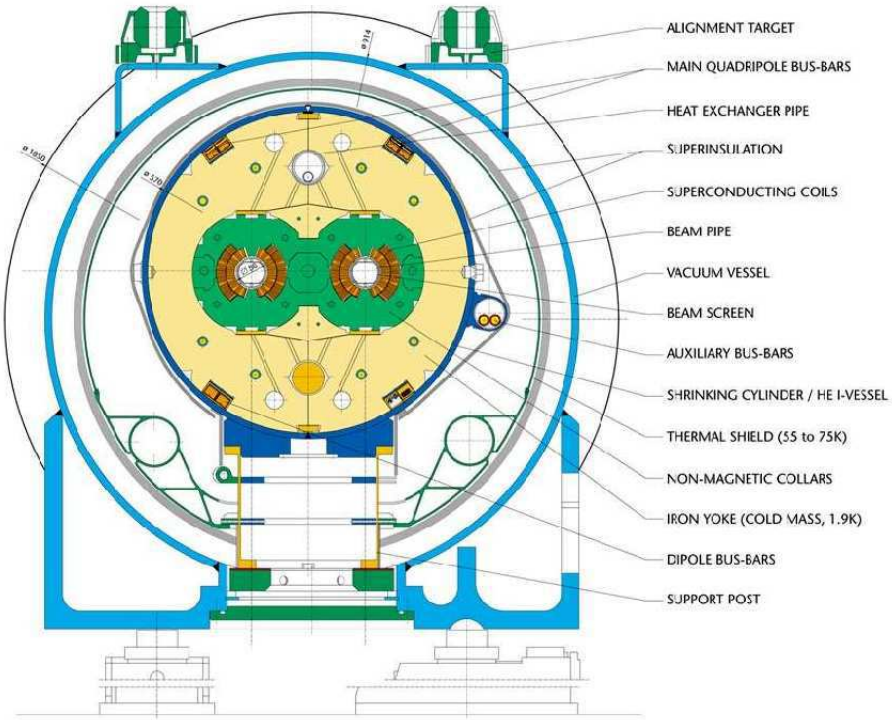

Figure 1.4: Cross section of an LHC dipole magnet showing the two separate vacuum chambers [1].

The LHC beams collide in four Interaction Points (IPs), where the proton-proton collisions are observed by four large experiments, ATLAS (IP1), ALICE [2] (IP2), CMS [3] (IP5) and LHCb [4] (IP8), and two smaller experiments, LHCf [5] (IP1) and TOTEM [6] (IP5). ATLAS

[5]Dipole magnets are used to realize bends in the design trajectory (or orbit) of the particles.
[6]Quadrupole magnets are used for beam focusing.

and CMS are general purpose detectors. One goal of these large detectors is the search for the Higgs boson, while LHCb is specialized in the physics of the B-meson and ALICE was mostly designed for heavy ions collisions and will study the quark-gluon plasma. TOTEM is a forward detector aiming at measuring the proton-proton cross section and studying diffractive processes and LHCf uses the LHC as a source to study processes relevant for cosmic rays in laboratory conditions.

Luminosity at LHC

Another important propriety of the LHC is the machine luminosity, which gives a direct estimation of the number of events per second generated in collisions of any physical process. Assuming a process $pp \to X$, the luminosity $\mathscr{L}$ is the process-independent proportionality factor between the rate $R_{pp\to X}$ and its production cross section $\sigma_{pp\to X}$:

$$R_{pp\to X} = \mathscr{L} \times \sigma_{pp\to X} \tag{1.1}$$

$\mathscr{L}$ represents the **instantaneous luminosity** and is usually expressed in units $\mathrm{cm}^{-2}\mathrm{s}^{-1}$. As running conditions vary with time, the luminosity of a collider also has a time dependence. The integral over time is called **integrated** (or **delivered**) **luminosity** it is commonly denoted with L, and measured in units b^{-1}.
Luminosity precise knowledge is important since for many cross sections measurements the uncertainty on the luminosity dominates the final result. In particular in view of the possibility to constrain the parton distribution functions (PDFs) which will have a direct impact on the systematics of several important measurements, a precision at the level of a few percent is aimed at the LHC [7].

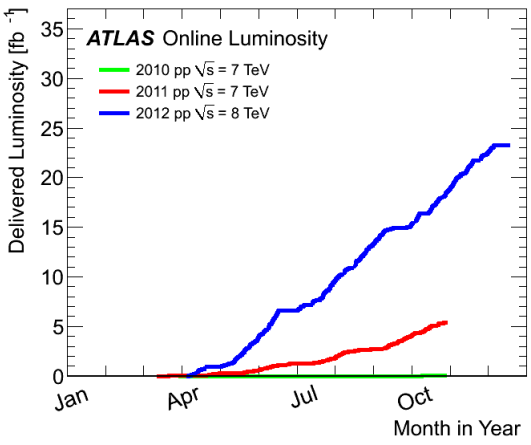

Figure 1.5: The cumulative luminosity versus day delivered to ATLAS during stable beams is shown for 2010 (green), 2011 (red) and 2012 (blue) running.

The LHC was designed to provide a peak luminosity of $10^{34}\text{cm}^{-2}\text{s}^{-1}$ for CMS and ATLAS. The corresponding design parameters and machine real instantaneous luminosity for different years, are listed in table 1.1. The table shows also the evolution of the beam energy, number of protons per bunch (N), number of bunches (k) and bunch spacing in (ns). The beam normalized emittance (ε_N) and the betatron function (β^*) will be introduced in the following section. Figure 1.5 shows the evolution of cumulative luminosity versus day delivered to ATLAS during stable beams between 2010 and 2012.

Table 1.1: Evolution of LHC parameters for high luminosity runs: 2010 to 2012

Parameters	**2010**	**2011**	**2012**	**Nominal**
Energy (TeV)	3.5	3.5	4.0	7.0
N (10^{11} p/bunch)	1.2	1.45	1.58	1.15
k (no. bunches)	368	1380	1374/1380	2808
Bunch spacing (ns)	150	75/50	50	25
Stored energy (MJ)	25	112	140	362
ε_N (μm rad)	2.4-4.0	1.9-2.4	2.2-2.5	3.75
β^* (m)	3.5	1.5-1.0	0.6	0.55
$\mathscr{L}(\text{cm}^{-2}\text{s}^{-1})$	2×10^{32}	3.5×10^{33}	7.6×10^{33}	10^{34}

1.2 Beam optics

The accelerator magnetic elements are designed to guide and focus the beam along the reference circular orbit. Oscillations around this reference are called **Betatron Oscillations**. They describe the transverse motion of the particles and depend on the magnetic fields applied in the ring. This section aims at introducing some general concepts of beam dynamic and defining common parameters and formalism that will be used in this thesis [8, 9].

1.2.1 The matrix formalism

The matrix formalism allows us calculating individual particle trajectories through an arbitrary structure of magnets and also taking into account variations in particle momentum. Particle transverse motion is describe by Hill differential equation of motion:

$$\frac{d^2u(s)}{ds^2} + K(s)\,u(s) = 0 \tag{1.2}$$

The trajectory function $u(s)$ describes a betatron oscillation and can be replaced by $x(s)$ for horizontal plane and $y(s)$ for the vertical one. Amplitude and phase depend on the position (s) along the orbit. The focusing functions $K_{x,y}(s)$ are periodic and because accelerator components usually have uniform or nearly uniform magnetic fields, we can assume they are also piecewise constant. Let K represent either the vertical or the horizontal component with the periodic condition $K(s+L) = K(s)$. The solutions to Hills equation with constant K are:

$$u(s) = \begin{cases} a\cos(\sqrt{K}s + b) & \text{if } K > 0 \text{ focusing quadrupoles} \\ as + b & \text{if } K = 0 \text{ drift space} \\ a\cosh(\sqrt{-K}s + b) & \text{if } K < 0 \text{ defocussing quadrupoles} \end{cases} \tag{1.3}$$

where a and b are integration constants to be determined by the initial values u_0 and u_0' . In the other hand, the evolution of $u(s)$ and $u'(s)$ from the initial position $u(s_0)$ and angle $u'(s_0)$, can be written in the matrix formalism as:

$$\begin{pmatrix} u(s) \\ u'(s) \end{pmatrix} = \mathbf{M} \begin{pmatrix} u(s_0) \\ u'(s_0) \end{pmatrix} = \begin{pmatrix} M_{11} & M_{12} \\ M_{21} & M_{22} \end{pmatrix} \begin{pmatrix} u(s_0) \\ u'(s_0) \end{pmatrix} \tag{1.4}$$

M is called the transfer matrix. Based on the solutions (1.3) and its differentiation, **M** can

be written as:

$$\mathbf{M} = \begin{cases} \begin{pmatrix} \cos(\sqrt{K}l) & \frac{1}{\sqrt{K}}\sin(\sqrt{K}l) \\ -\sqrt{K}\sin(\sqrt{K}l) & \cos(\sqrt{K}l) \end{pmatrix} & \text{if } K > 0, \\ \begin{pmatrix} 1 & l \\ 0 & 1 \end{pmatrix} & \text{if } K = 0, \\ \begin{pmatrix} \cosh(\sqrt{|K|}l) & \frac{1}{\sqrt{|K|}}\sinh(\sqrt{|K|}l) \\ \sqrt{|K|}\sinh(\sqrt{|K|}l) & \cosh(\sqrt{|K|}l) \end{pmatrix} & \text{if } K < 0, \end{cases} \tag{1.5}$$

where $l = s - s_0$.

The transfer matrix for any intervals made up of subintervals is the product of the transfer matrices of the subintervals. Considering the interval of length $l = s_2 - s_0 = (s_2 - s_1) + (s_1 - s_0)$ we get:

$$\mathbf{M}(\mathbf{s_2}|\mathbf{s_0}) = \mathbf{M}(\mathbf{s_2}|\mathbf{s_1})\mathbf{M}(\mathbf{s_1}|\mathbf{s_0}) \tag{1.6}$$

1.2.2 Twiss functions

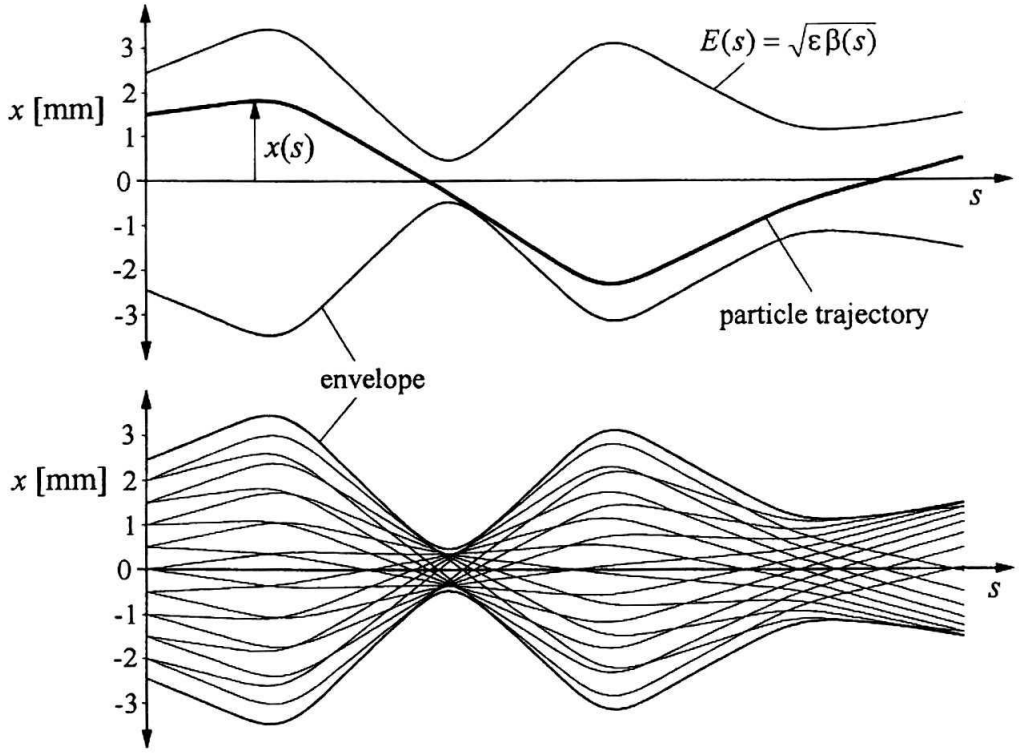

Figure 1.6: Particle trajectories $x(s)$ within the envelope $E(s) = \sqrt{\varepsilon\beta(s)}$ of the beam. Upper figure shows a single trajectory, while the lower figure shows many trajectories together. The beam is made up of a combination of all the individual trajectories [8].

Looking back at the solutions of Hills equations for $K > 0$ (1.2), they can be interpreted as an harmonic oscillator for which the solution is expressed as:

$$u(s) = A\cos(\psi(s) - \phi) \tag{1.7}$$

where $\psi(s) = \sqrt{K}s$, A and ϕ are the constants of integration. For circular accelerators, the function $K(s)$ is periodic, $K(s+L) = K(s)$ where the period L can coincide with the accelerator circumference but normally corresponds to the distance between two FODO cells[7]. The general solution to the eq.(1.2) is:

$$u(s) = A\,w(s)\cos(\psi(s) - \phi) \tag{1.8}$$

Inserting the solution (1.8) and its second derivative into (1.2) and writing $w = w(s)$ and $\psi = \psi(s)$ give:

$$A(w'' - w\psi'^2 - K(s)\,w)\cos(\psi + \phi) - A(2w'\psi' + w\,\psi'')\sin(\psi + \phi) = 0 \tag{1.9}$$

Since the phase $\psi(s)$ has a different value around the orbit and $A \neq 0$, eq.(1.9) can only be satisfied if: $w'' - w\,\psi'^2 - K(s)\,w = 2\,w'\,\psi' + w\,\psi'' = 0$. The last term can be written as

$$\frac{w'}{w} + \frac{\psi''}{\psi'} = 0 \tag{1.10}$$

which can be integrated directly

$$\psi(s) = \int_0^s \frac{d\tau}{w^2(\tau)} = \int_0^s \frac{d\tau}{\beta(\tau)} \tag{1.11}$$

where **beta function** $\beta(s)$ is introduced. It is also known as the **amplitude function**. It depends on the beam focusing, which varies with the position *s*, and is a measure of the beam cross section at that point.
Eq.(1.8) can be finally written as:

$$u(s) = \sqrt{\varepsilon\beta(s)}\cos(\psi(s) + \phi) \tag{1.12}$$

Where A was replaced by $\sqrt{\varepsilon}$ which is termed the **emittance**, and will be explained in the following section. $\sqrt{\varepsilon\beta(s)}$ is the **beam envelope**, in other terms, particles transverse motion along the beam, is within a range marked by the envelope (shown figure 1.6). Since all particles trajectories lie inside this envelope, it defines the transverse size of the beam.
Particle angle can be deduced from the position $u(s)$ by differentiation of (1.12):

$$u'(s) = -\sqrt{\frac{\varepsilon}{\beta(s)}}[\alpha(s)\cos(\psi(s) + \phi) + \sin(\psi(s) + \phi)] \tag{1.13}$$

with

$$\alpha(s) = -\frac{1}{2}\frac{d\beta(s)}{ds} \tag{1.14}$$

Let's also introduce γ, which will be used later:

$$\gamma(s) = \frac{1 + \alpha^2(s)}{\beta(s)} \tag{1.15}$$

α, β and γ are called **Twiss functions**:

[7] A typical structure used in accelerators. F stands for focusing, O for a drift space and D for defocusing.

1.2.3 Beam cross section and emittance

In order to arrive at an expression describing the particle motion in the (u, u') phase space plane, one must substitute the phase (ψ) terms in 1.12 and 1.13, to eliminate it. All positions occupied by a particle in the space of the phase (u, u') describes an ellipse with the equation given by the following formula:

$$\gamma(s)\,u^2(s) + 2\alpha(s)\,u(s)\,u'(s) + \beta(s)\,u'^2(s) = \varepsilon \tag{1.16}$$

The emittance (ε) introduced before as a constant, is now, to within a factor (π), the **area of the phase ellipse**. It's equal to ($\pi\varepsilon$). According to **Louville's theorem**, the area of the ellipse and hence the beam emittance are invariants of the particle motion. As the particle moves along the orbit the shape and position of the ellipse change according to the amplitude function ($\beta(s)$), but the area remains constant. However, it is not the emittance of a single particle in use, but of all particles flowing through the accelerator. By convention, the value is set to the area of the ellipse containing 68% of the particles. The projection of this ellipse on the horizontal axis represents the beam profile (see Figure 1.7). The emittance of the beam is defined in function of **beam width** (σ_u), as the standard deviation of the beam profile Gaussian distribution:

$$\varepsilon = \frac{\sigma_u^2(s)}{\beta(s)} \tag{1.17}$$

The beam emittance decreases with increasing beam energy during acceleration, and a convenient quantity for the operation of a hadron storage rings (and linear accelerators) is the **normalized emittance** defined as:

$$\varepsilon_N = \varepsilon\gamma_r\beta_r \tag{1.18}$$

where $\beta_r = v/c$ and $\gamma_r = 1/\sqrt{1-\beta_r^2}$ are the relativistic gamma and beta factors (v is the particle velocity and c the speed of light in vacuum).
The beam width for a given longitudinal s point along the beam axis is deduced from (1.17):

$$\sigma_u(s) = \sqrt{\varepsilon\beta(s)} \tag{1.19}$$

Differentiation of σ_u gives the beam **angular divergence** (σ_u'):

$$\sigma_u'(s) = \sqrt{\varepsilon\gamma(s)} = \sqrt{\varepsilon\frac{1+\alpha^2(s)}{\beta(s)}} \tag{1.20}$$

1.2.4 Transfer matrix using Twiss functions

If the values of $\beta(s)$, $\alpha(s)$ and $\psi(s)$ at the beginning and the end of a magnetic structure are known, then the transfer matrix is uniquely defined. The elements of this matrix must therefore

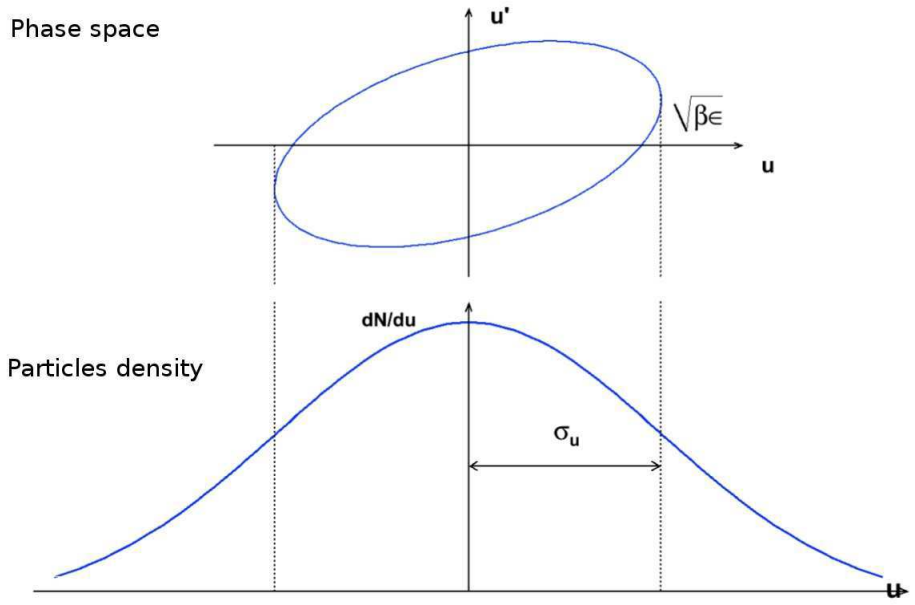

Figure 1.7: Projections of the phase space ellipse on the horizontal-axis, gives the transverse beam width and its angular divergence.

be expressible in terms of the values of the optical functions, without a detailed knowledge of the magnet structure. From the equations 1.12 and 1.13, considering the initial conditions $u(0) = u_0$, $u'(0) = u'_0$, $\beta(0) = \beta_0$, $\alpha(0) = \alpha_0$ and $\psi(0) = \psi_0$, and substituting the ϕ term, one can obtain:

$$u(s) = \sqrt{\frac{\beta(s)}{\beta_0}}[\cos(\Delta\psi) + \alpha_0 \sin(\Delta\psi)]u_0 + \sqrt{\beta(s)\beta_0}\sin(\Delta\psi)u'_0 \tag{1.21}$$

and,

$$u'(s) = \frac{1}{\sqrt{\beta(s)\beta_0}}[(\alpha_0 - \alpha(s))\cos(\Delta\psi) - (1 + \alpha(s)\alpha_0)\sin(\Delta\psi)]u_0 + \sqrt{\frac{\beta(s)}{\beta_0}}[\cos(\Delta\psi) - \alpha_0 \sin(\Delta\psi)]u'_0 \tag{1.22}$$

with $\Delta\psi = \psi(s) - \psi(s_0)$, the phase difference between s_0 and s.
Eq.(1.21) and (1.22) may again be expressed by a transfer matrix 1.4. using the shorthand $\beta = \beta(s)$ and $\alpha = \alpha(s)$, the transfer matrix between an initial longitudinal position s_0, and an arbitrary position s will be written as:

$$\mathbf{M}(s_0|s) = \begin{pmatrix} \sqrt{\frac{\beta}{\beta_0}}[\cos(\Delta\psi) + \alpha_0 \sin(\Delta\psi)] & \sqrt{\beta\beta_0}\sin(\Delta\psi) \\ \frac{1}{\sqrt{\beta\beta_0}}[(\alpha_0 - \alpha)\cos(\Delta\psi) - (1 + \alpha\alpha_0)\sin(\Delta\psi)] & \sqrt{\frac{\beta}{\beta_0}}[\cos(\Delta\psi) - \alpha_0 \sin(\Delta\psi)] \end{pmatrix}$$

Chapter 2

A Toroidal LHC ApparatuS - ATLAS

The LHC provides a rich physics potential, ranging from precise measurements of Standard Model parameters to the search for new physics phenomena. The high luminosity and the large center-of-mass energy of the proton-proton collisions enable high precision tests on the Standard Model, such as the studies on the electroweak bosons W and Z and their properties, and the precise measurements on the top quark mass and its couplings. Furthermore, the search for the Standard Model Higgs boson has been used as a benchmark to establish the performance of important sub-systems of ATLAS[1] [10]. As well, ATLAS is intended to investigate new physical theories.

The experiment was proposed in its current form in 1994, and officially funded by the CERN member states in 1995. In 2008 the construction was completed and ATLAS detected its first single beam events on the 10^{th} of September of that year. Since 2009 (data taken started), over 25 fb^{-1} of pp data have been collected at both $\sqrt{s} = 7$ TeV and $\sqrt{s} = 8$ TeV.

The ATLAS detector is 44 m in length and 25 m in height and it weights 7000 tons. It is divided in a barrel region and two end-cap regions. An overview of the detector is provided in figure 2.1. This section describe the different ATLAS subdetector systems and their role in the identification of particles. But before that, a description of the coordinate system is an important starting point.

[1] The 4^{th} of July, 2012, ATLAS and CMS reported evidence for the existence of a particle consistent with the Higgs boson at the level of five sigma with a mass around 125 GeV.

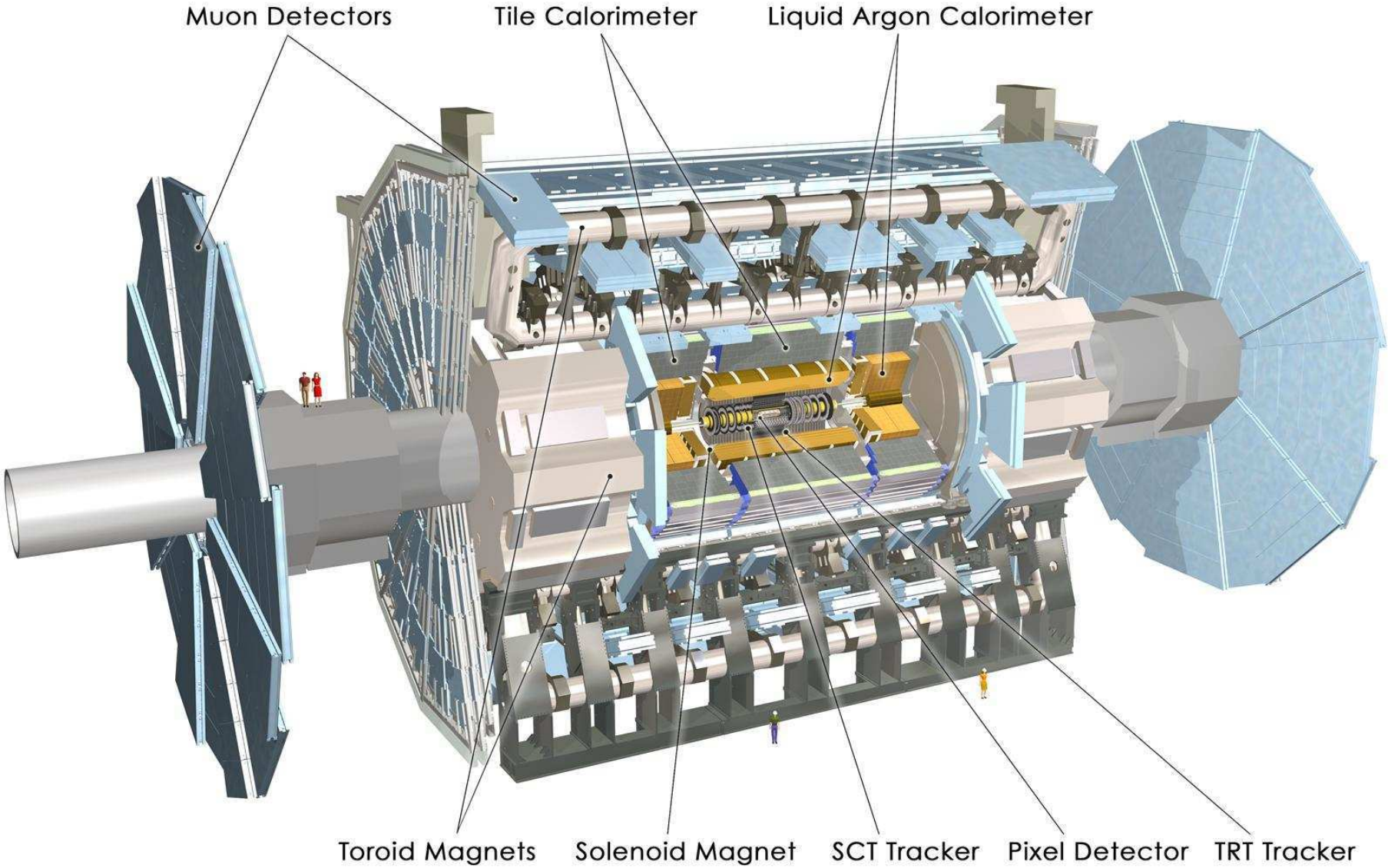

Figure 2.1: Computer generated image of the ATLAS detector. It is 25 m in diameter and 44 m in length, and weighs approximately 7000 tonnes.

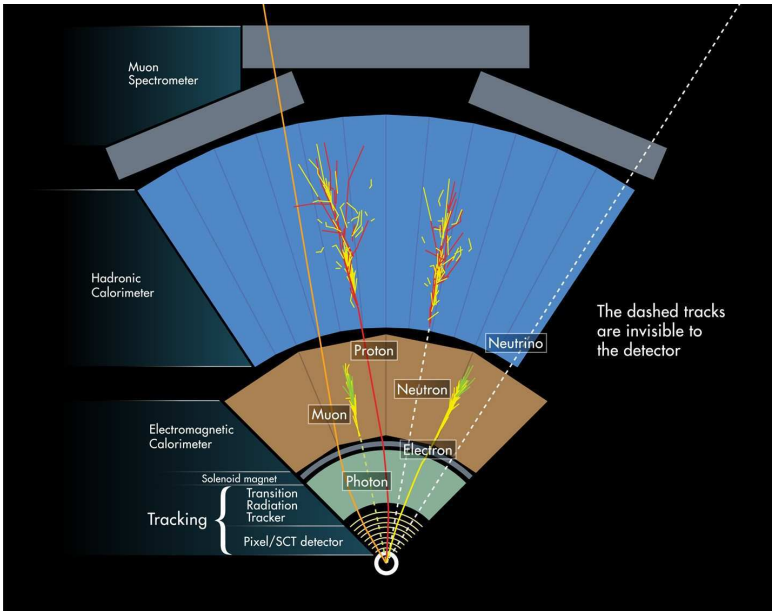

Figure 2.2: Tracks signatures in different subsystems of the ATLAS detector.

2.1 Coordinate system

ATLAS coordinate system and nomenclature used to describe the ATLAS detector is briefly summarized here:

- Nominal interaction point is defined as the origin of the coordinate system.
- Beam direction defines the *z*-axis and the *x*-*y* plane is transverse to the beam direction.
- Positive *x*-axis is defined as pointing from the interaction point to the centre of the LHC ring and the positive *y*-axis is defined as pointing upwards.
- Side-A of the detector is defined as that with positive *z* and side-C is that with negative *z*.
- Azimuthal angle ϕ is measured around the beam axis, and the polar angle θ is the angle from the beam axis.
- Pseudorapidity is defined as $\eta = -\ln\tan(\theta/2)$.
- Distance ΔR in the pseudorapidity-azimuthal angle space is defined as: $\Delta R = \sqrt{\Delta\eta^2 + \Delta\phi^2}$.

2.2 Central detectors

This section introduce different ATLAS subdetector systems and their main role in particles detection. Figure 2.2 summarizes tracks signatures in different subdetectors.

2.2.1 Inner detector

The ATLAS Inner Detector (ID) is designed to provide hermetic and robust pattern recognition, excellent momentum resolution and both primary and secondary vertex measurements for charged tracks above a given p_T threshold of 0.1 GeV. The ID is contained within a cylindrical envelope of 7024 mm length and 1150 mm radius, submerged in a solenoidal magnetic field of 2 T. It covers the pseudorapidity range $|\eta| < 2.5$ and provides electron identification over $|\eta| < 2.0$ and a wide range of energies (between 0.5 GeV and 150 GeV).

The Inner Detector consists of three independent but complementary subdetectors providing different granularity, shown in the figure 2.3: the Pixel detector, the Semi-Conductor Tracker (SCT) and the Transition Radiation Tracker (TRT).

The precision tracking detectors (pixel and SCT)

Pixel and SCT detectors are the closest to the interaction point and cover the region $|\eta| < 2.5$, in order to measure charged particle trajectories at high precision. They both rely on the semiconductor properties of silicon, which ensures that electron-hole pairs are created proportionally to the deposited energy. By applying an electric field, the electrons and holes drift to the electrodes and are detected. This provides both the information that a strip/pixel has been hit and deposited energy.
Figure 2.4(a) is a picture taken during the sub-assembly of the Pixel barrel in November 2006 and figure 2.4(b) shows the work on the SCT barrel.
The pixel detector provides the highest granularity, using silicon pixels with a minimum size of $(R-\phi) \times z = 50 \times 400\ \mu\text{m}^2$, and has approximately 8.10^7 readout channels. It is made of as three concentric cylinders (barrels) around the beam axis, with disks (endcaps) on the side to ensure optimal (ϕ, η) coverage[2]. For the SCT eight strip layers (four space points) are crossed by each track. The layers are double sided with a stereo angle of 40 mrad between the sides in order to gain the ability to observe in three spatial dimensions.

Transition Radiation Tracker (TRT)

TRT (figure 2.4(c)) consists of 0.4×144 cm^2 tubes filled with a Xe-based gas mixture, and measures the ionization of particles traversing the detector. It covers a region up to $|\eta| = 2.0$. The TRT-type detector is much cheaper than the Si types, but also worse off in terms of spatial resolution, as seen from table 2.1. However, since the number of hits is so large (36

[2] $(R-\phi)$ reefer to the lateral plane and (z and R) to the longitudinal one (barrel and endcap respectively)

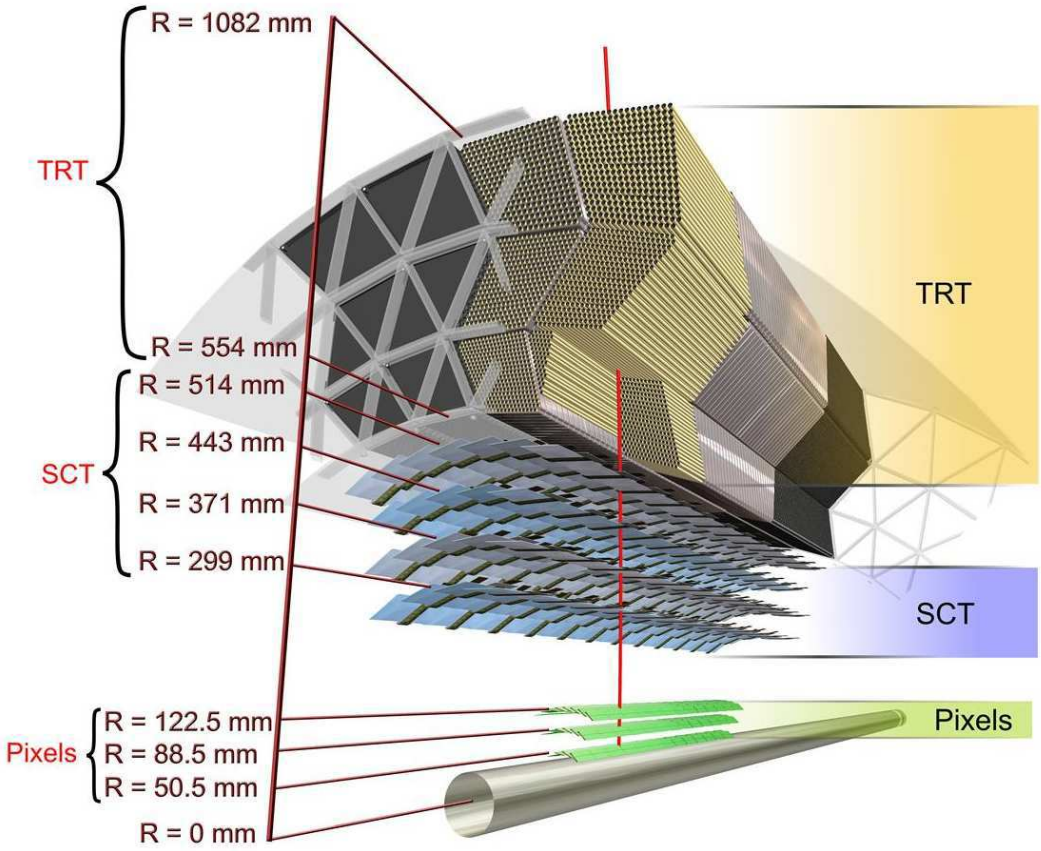

(a) Scheme of the ATLAS inner detector barrel being crossed by one high-energy particle

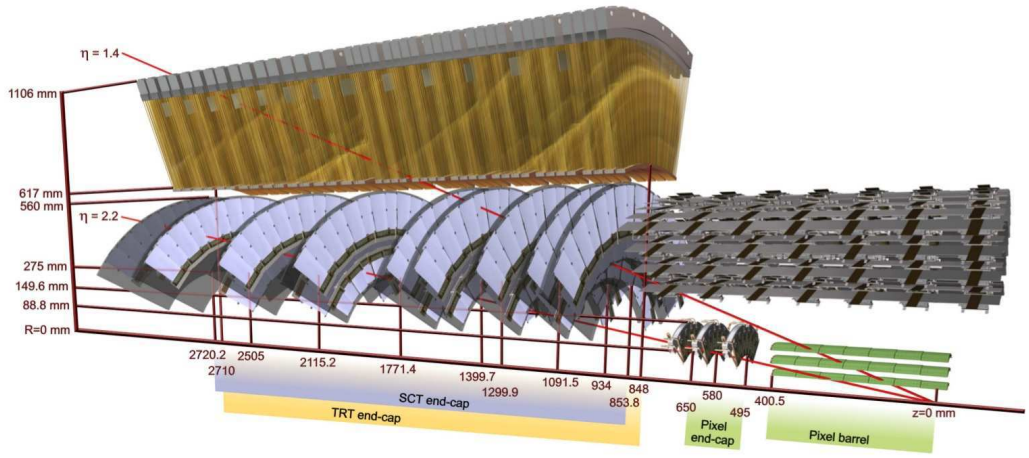

(b) Drawing showing the sensors and structural elements traversed by two charged tracks in the end-cap inner detector ($\eta = 1.4$ and 2.2).

Figure 2.3: Overview of the ATLAS inner detector

per track), the lack of resolution is compensated. The TRT provides both particle trajectory measurements for ordinary particles (low threshold), and adds additional coverage for ultra relativistic particles by measuring transition radiation (high threshold).
Table 2.1 summarize the intrinsic accuracy, and the number of readout channel of each ID subdetector.

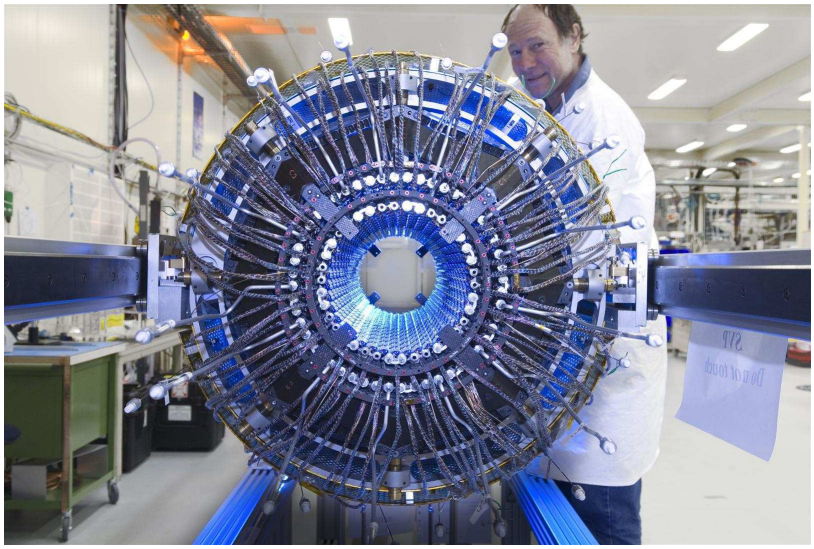

(a) Pixel barrel sub-assembly of ATLAS detector (November 2006).

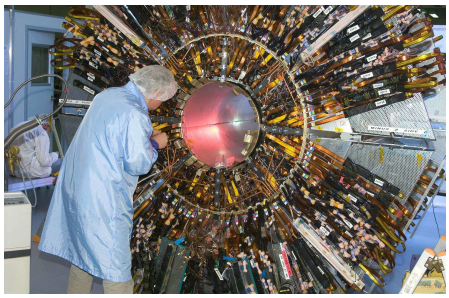

(b) Work on the ATLAS SCT barrel.

(c) TRT prototype for ATLAS experiment (August 1998).

Figure 2.4: Different inner subdetector systems of ATLAS.

Table 2.1: Intrinsic measurement accuracies and amount of readout of the Inner Detector subsystems [10].

Detector	**Intrinsic accuracy [μm]**	**Readout Channels [10^6]**
Pixel	10 $(R-\phi)$ 115 (z and R)	80.4
Strip	17 $(R-\phi)$ 580 (z and R)	6.3
TRT	130 $(R-\phi)$	0.351

2.2.2 Calorimeters

A calorimeter is designed to measure the energy deposition and direction for a contained electromagnetic or hadronic shower. The detector can measure, through complete absorption, both charged and neutral particles from a few GeV up to the TeV scale with high resolution for energy and position measurements, and good signal linearity. The construction follows a sampling principle where layers of absorber material are separated by layers of active material.

Particles entering the absorber develop into a shower and the energy of the shower is then measured by the active material. Weakly interacting particles such as muons or neutrinos do not get stopped by the detector.

ATLAS calorimetric system is symmetric around the beam axis and has full coverage in the ϕ direction and pseudorapidity coverage up to $|\eta| < 4.9$. The figure 2.1 shown the two calorimetric systems which will be briefly detailed in this section.

Electromagnetic (EM) calorimeter

EM calorimeter is a lead (Pb)-liquid argon (LAr) calorimeter of the sampling type (figure 2.5). It makes use of the interaction of $e^{\pm}$ and photons with matter to provide excellent performance in terms of energy and position resolution. The most important energy loss mechanism for $e^{\pm}$ at high energies is the bremsstrahlung effect which results to the emission of a photon, while high-energy photons produce electron pairs via pair production. The shower is developed in Pb plates and sampled through ionization in the LAr. The electromagnetic shower detected by the lead-liquid argon detectors with accordion[3] shaped absorbers and electrodes. The geometry of the Pb-LAr layer structure is shown in figure 2.5(c).

This calorimeter consists of three layers in the barrel and two in the endcaps (EMEC) up to $\eta = 3.2$. In addition, the central region ($|\eta| < 1.8$) is also equipped with a presampler, which corrects for energy lost upstream to the calorimeter. The total thickness is more than 22 X_0[4] and 26 X_0 in the barrel and the endcaps, respectively. The relative energy resolution of the LAr calorimeter is usually parametrized by:

$$\frac{\sigma(E)}{E} = \frac{a}{\sqrt{E}} \oplus \frac{b}{E} \oplus c \tag{2.1}$$

where a is the stochastic term, b the noise term and c the constant term. The target values for these terms are respectively $a \simeq 10\%$, $b \simeq 170$ MeV (without pile-up) and $c = 0.7\%$ [12]. With the current EM performances, the Higgs mass resolutions in $H \to \gamma\gamma$ and $H \to 4e$ channels are respectively 1.4% [13] and 1.9% [14].

The EM calorimeter barrel is housed in the same cryostat as the solenoid magnet, to be described in § 2.2.4, while the two endcap calorimeters are housed in their own cryostat. The first module of the Forward calorimeter is an electromagnetic one, starting from $\eta = 3.1$. It is made of copper plates with embedded copper rods and tubes through them with LAr between the rods and the tubes with a total thickness of more about 27 X_0.

[3]The accordion geometry provides complete ϕ symmetry without azimuthal cracks

[4]The unit of distance traversed by a shower is typically measured in radiation lengths, given approximately by $X_0 = 180A/Z^2$ (A: Mass number, Z: Atomic number.) [11]

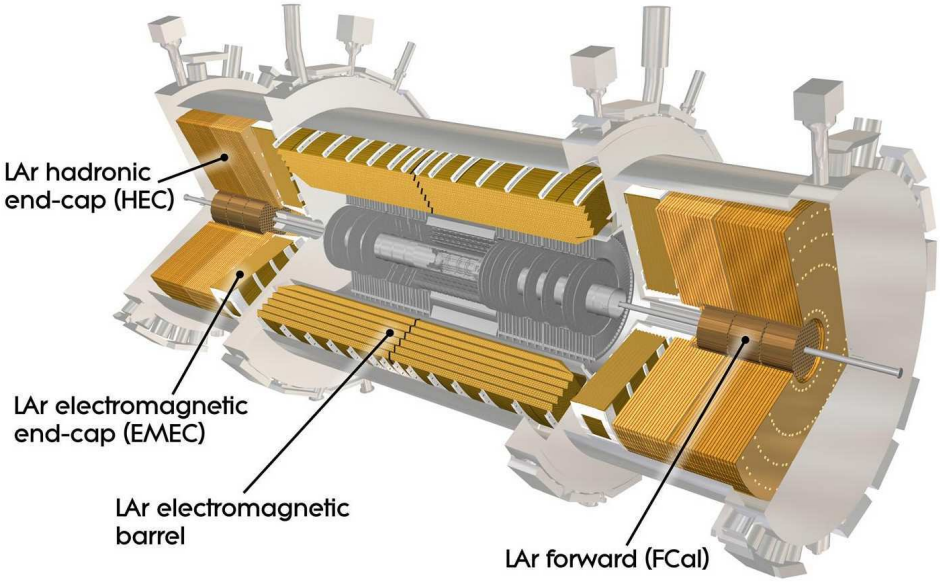

(a) Schematic picture of the LAr calorimeter system

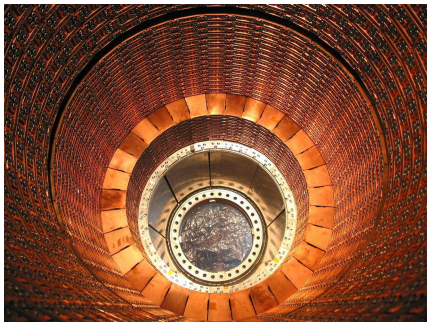

(b) A view inside the LAr calorimeter endcap. The circular inner bore of the EMEC, front and rear HEC wheels.

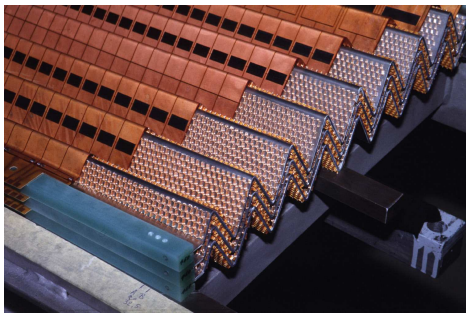

(c) Accordion geometry of the LAr barrel

Figure 2.5: ATLAS electromagnetic LAr calorimeter

Table 2.2 summarizes the EM calorimeter thickness, coverage and readout channels in the barrel and endcap region.

Table 2.2: Electromagnetic Calorimeter: thickness, coverage and readout channels (without presampler) [10].

Detector	Thickness [X_0]	Coverage	Readout Channels
EM calorimeter	-	$\|\eta\| < 3.2$	163968
Barrel	> 22	$\|\eta\| < 1.475$	101760
Endcaps	> 24	$1.375 < \|\eta\| < 3.2$	62208

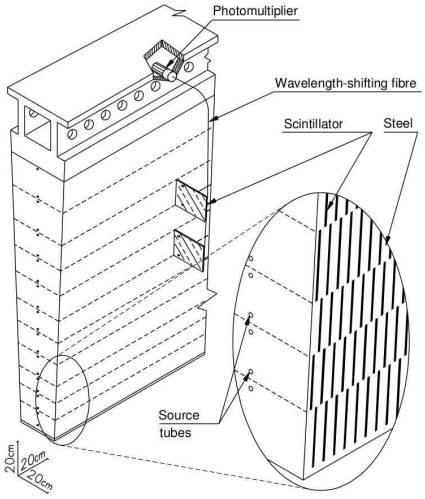

(a) Schematic showing how the mechanical assembly and the optical readout of the tile calorimeter are integrated together.

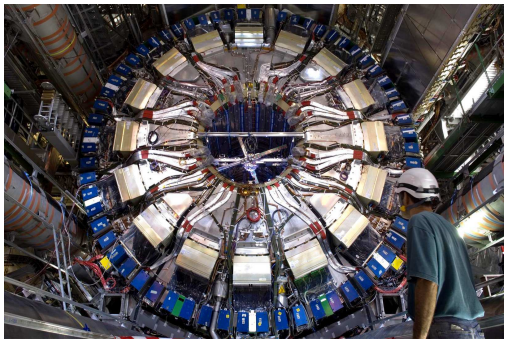

(b) Calorimeter insertion between toroids in the ATLAS experiment detector, July 2006

Figure 2.6: Tile calorimeter and combined electromagnetic-hadronic calorimeter of the ATLAS experiment

Hadronic calorimeter

Hadronic calorimeters (figure 2.6(b)) identify, reconstruct and measure the energy of particle jets and also measure the missing transverse energy of an event.
The approximate 9.7 interaction lengths (λ)[5] of active calorimeter in the barrel (10 λ in the end-caps) are adequate to provide good resolution for high-energy jets [10]. The hadronic calorimetry system consists of:

- **Hadronic barrel** or Tile calorimeter (figure 2.6(a) is a sampling calorimeter with alternate layers of steel (absorber) and plastic scintillator tiles (active material). It covers the $|\eta| < 1.7$ range. It is divided into three layers, with a more coarse granularity in the third layer.
- **Hadronic end cap (HEC)** uses copper (Cu) plates as the absorber and liquid argon (Ar) as the active material. It covers the $1.7 < \eta < 3.2$ region.
- **Forward calorimeter (FCAL)** makes both hadronic and electromagnetic calorimetry with respectively a copper and a tungsten module, in the very forward region $3.1 < \eta < 4.9$.

The endcap hadronic calorimeter parts are housed with the EMEC in the same cryostat.

[5]The longitudinal development of hadronic showers scales with the nuclear interaction (or absorption) length λ.

2.2.3 Muon spectrometer

The muon system is designed for providing muon momentum at a good resolution, using tracking chamber techniques. The muon spectrometer is the outermost part of the ATLAS detector, and is pictured in a cut away view in figure 2.7.

A large toroid magnet system is used to bend the trajectory of the muons as they pass though three stations of tracking chambers. The MS consists of two subdetectors for precision measurements:

- **Monitored drift tubes** which consists of a gas tube with a wire in the center. The gas is ionized by a passing muon. The ionization drifts to an electrode where it is collected, amplified and measured.
- **Cathode strip chambers** where a passing charge is detected by an anode wire, creating an induced charge on a cathode.

and two triggering technologies to provide bunch-crossing identification, well-defined p_T thresholds, and to complete the measurement of the precision-tracking chambers:

- **Resistive plate chambers** where two resistive electrode plates encapsulate a gas gap. Traversing particles causes the gas to ionize, and deformations of an applied electric field is translated to muon position.
- **Thin gap chambers** where closely separated wired are situated in a thin gap between grounded resistive cathode planes. Traversing particles draws a spark between the wires, and a signal is read out.

The main parameters of the four types of chambers in the ATLAS muon spectrometer, is summed up in table 2.3.

Table 2.3: Main parameters of the muon spectrometer: coverage, number of chambers and readout channels [10].

Muon Spectrometer	Coverage	No. of chambers	Readout Channels [10^3]
Monitored drift tubes	$\|\eta\| < 2.70$	1088	339
Cathode strip chambers	$2.00 < \|\eta\| < 2.70$	32	31
Resistive plate chambers	$\|\eta\| < 1.05$	544	359
Thin gap chambers	$1.05 < \|\eta\| < 2.70$	3588	318

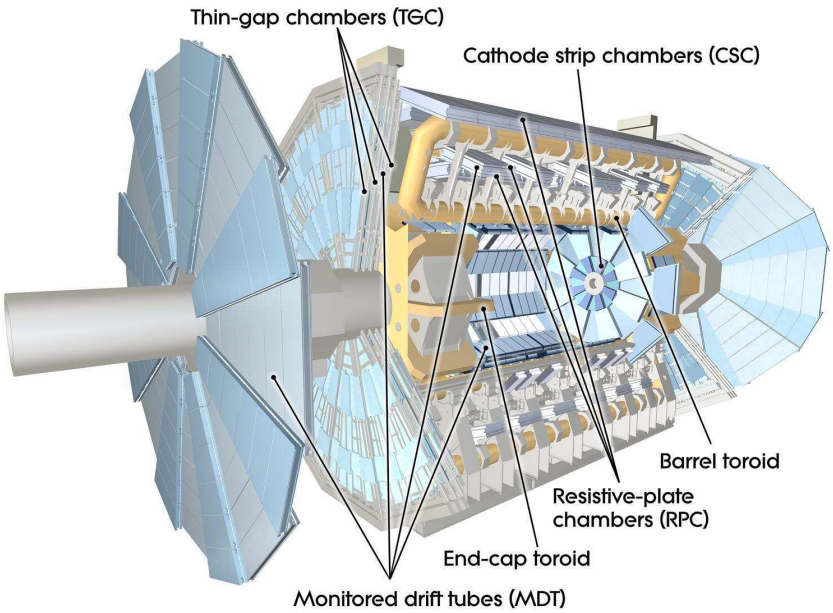

Figure 2.7: Cut away view of the muon spectrometer with it different components

(a) Bare central solenoid in the factory after completion of the coil winding.

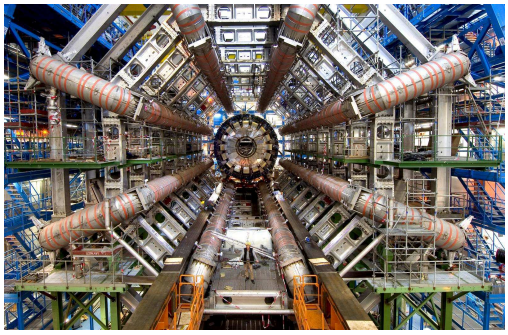

(b) The eight torodial magnets can be seen on the ATLAS detector with the calorimeter before it is moved into the middle of the detector.

Figure 2.8: ATLAS superconducting solenoid (a) and toroid magnet (b) systems.

2.2.4 Magnet system

The ATLAS detector contains two types of superconducting magnet systems in order to provide the bending power needed for the momentum measurement of the charged particles: the solenoid magnet surrounding the Inner Detector and the toroid magnet system embedded in the Muon Spectrometer. This magnetic system is 22 m in diameter and 26 m in length, with a stored energy of 1.6 GJ.

- **The central superconducting solenoid**, presented in figure 2.8(a), is aligned on the beam axis and is designed to provide a 2 T axial magnetic field for the momentum

measurements of the Inner Detector, minimizing the radiative thickness in front of the barrel EM calorimeter.

- **The toroid magnet** system (2.8(b)) provides the magnetic field for momentum measurement in the Muon Spectrometer and has an average field strength of 0.5 T and 1 T in the central and end-cap regions, respectively. The magnetic field which is toroidal and perpendicular to the one of the solenoid, is created by eight superconducting coils in the barrel, and two toroids with eight coils each in the end-cap regions.

2.3 Forward detectors

Three additional detectors cover the forward region of ATLAS. Their location with respect to ATLAS is shown in figure 2.9. The η coverage of ATLAS central and forward subdetectors is shown in figure 2.10.

- **LUCID** (**LU**minosity measurement using **C**erenkov **I**ntegrating **D**etector, [15]) is located at $\pm$17 m of the interaction point (IP) and measures proton-proton inelastic scattering. It is one of the main handles on relative luminosity monitoring.
- **ZDC** (**Z**ero **D**egree **C**alorimeter, [16]) is located $\pm$140 m from the IP. Its main goal is to detect forward neutrons for heavy-ions centrality measurements up to $|\eta| = 8.3$.
- **ALFA** (**A**bsolute **L**uminosity **F**or **A**TLAS, [17]) consists of scintillating fibre trackers located in eight roman pot stations $\pm$240 m from the IP.

LUCID and ZDC will be briefly described in this section. ALFA will be detailed in chapter 4.

2.3.1 LUCID

The LUCID [15] detector surrounds the LHC beam pipe on both ATLAS interaction point sides, at a distance of 17 m. Its layout and position are illustrated in figure 2.11.
One vessel contains 20 aluminum tubes pointing towards the interaction point approximately 10 cm from the beam axis. Each vessel is filled with C_4F_{10} at 1.3 bar for Cerenkov light measurement. Sixteen of the 20 tubes are read out through 15 mm photomultipliers (PMT) and 4 tubes have their collected light transmitted through quartz fibers outside of the forward shielding to be read out by multi-anode photomultiplier tubes. The 16 photomultipliers signals are individually sent to the front-end electronics.
LUCID main purpose is the luminosity measurement for ATLAS, as described in the following chapter.

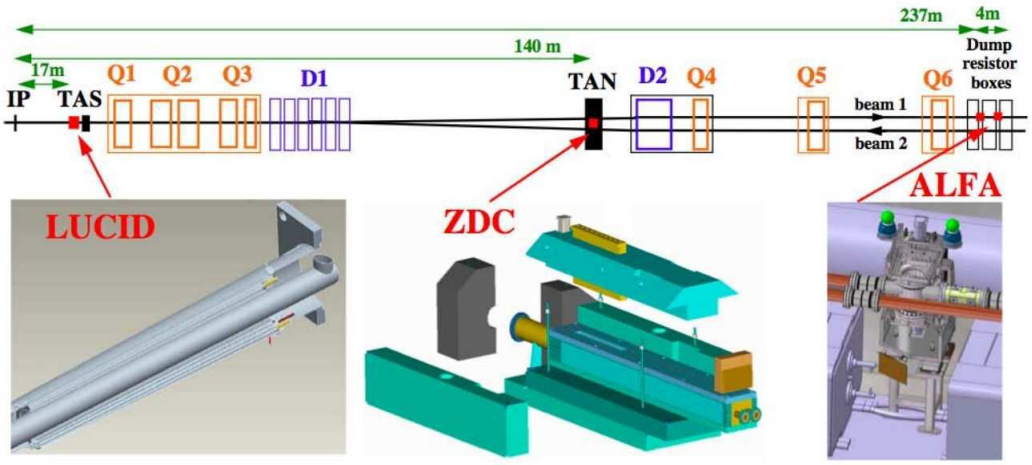

Figure 2.9: Location of the LUCID, ZDC, and ALFA forward detectors along the beam line on one side of the ATLAS detector. The same set of detectors are place symmetrically with respect to the interaction point.

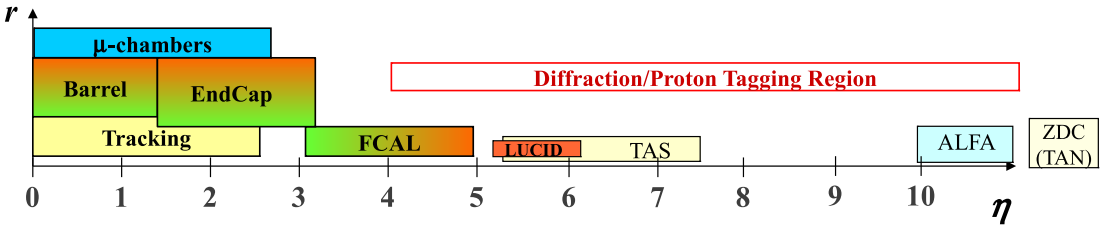

Figure 2.10: η coverage of different ATLAS subdetectors.

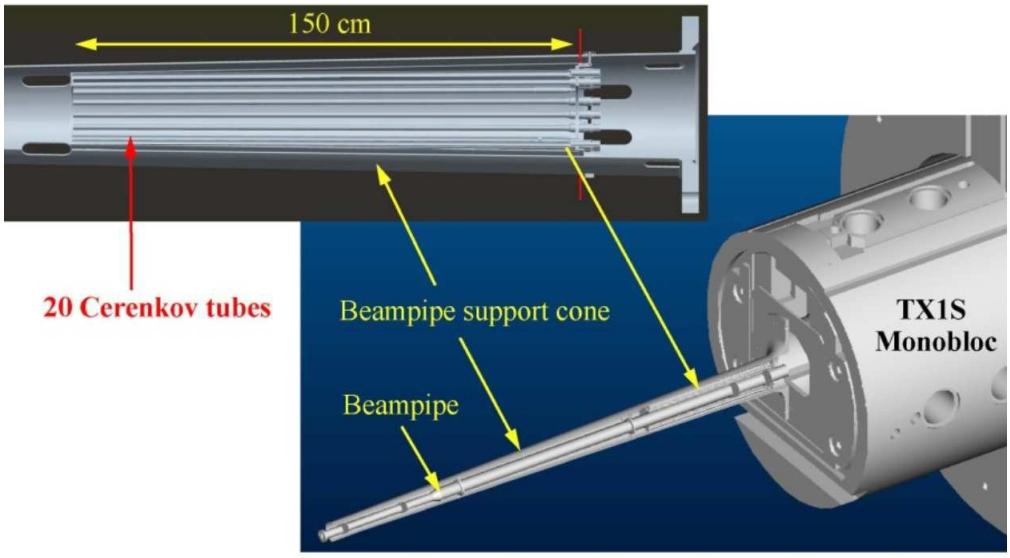

Figure 2.11: Computer-generated view of the LUCID Cerenkov tubes and their arrangement around the beam pipe.

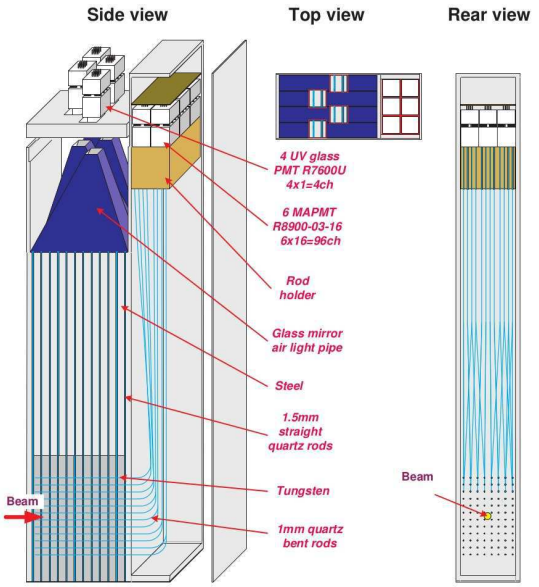

(a) Electromagnetic ZDC module. Beam impinges on tungsten plates at bottom of module, and showers. Quartz rods pick up Cerenkov light from the shower and pipe it to multi-anode phototube at top of module. Phototubes measure light from strips through four air light pipe.

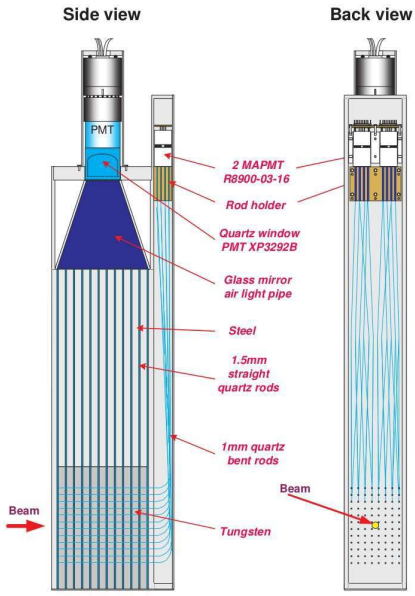

(b) Hadronic ZDC module. It has only one PMT viewing the strips, and two MAPMTs viewing the rods.

Figure 2.12: Electromagnetic and hadronic ZDC modules

2.3.2 ZDC

Zero **D**egree **C**alorimeters are compact calorimeters located at approximately zero degrees to the incident beams on either side of ATLAS, 140 m downstream from the IP. They thus observe forward going neutral particles that are produced in collisions. ZDC [16] is comprised of four modules, one electromagnetic (see figure 2.12(a)) and three hadronic (see figure 2.12(b)). The EM module, consists of eleven 10 mm thick tungsten plates, extended by steel plates, traversed by 96 quartz rods forming an 8×12 matrix perpendicular to the beam axis. On the front face of the module the rods are bent upwards and read out at the top by multi-anode photomultiplier tubes. Therefore, the Cerenkov light induced by particle showers traversing the module provides both position and energy measurements. In order to get an improved measurement of the incident particle energy over that of the position measuring rods, quartz strips are installed between the plates and read out from the top by photomultiplier tubes.

Chapter 3

Luminosity and total cross section measurement methods

After the description in the previous chapters of the LHC machine, the ATLAS setups, and an introduction to the beam dynamics basics, this chapter describes methods used for luminosity and total cross section (σ_{tot}) measurements.
The instantaneous luminosity of the LHC is planned to be 10^{34} cm^{-2}s^{-1} as mention in § 1.1.2. For many of the anticipated physics analyses, in particular for measurements of absolute cross sections, precise luminosity measurement is essential. The information about relative changes in luminosity are also important for monitoring beam stability and beam degradation, in order to efficiently operate the ATLAS trigger and data acquisition system.
In this chapter we describe different methods and detectors used by ATLAS for luminosity measurement, afterwards we will introduce the ALFA independent method for luminosity and total cross section measurements.

3.1 Total cross section

It is now nearly fifty years since total cross sections have been found to grow with energy after it was believed for long time that they would become asymptotically constant [18]. The rise of the cross section with the energy was first observed at the ISR experiment [19]. The growth of $\sigma_{tot}(p\bar{p})$ with s became macroscopically visible with the SPS data at $\sqrt{s} = 0.546$ TeV (UA4 [20]) and $\sqrt{s} = 0.90$ TeV (UA5 [21]), and with the Tevatron data at $\sqrt{s} = 1.8$ TeV (E710 [22], CDF [23]). This growth is the evidence that the proton becomes larger as seen by an incoming hadron of increasing energy.
The pp and $p\bar{p}$ total cross section are shown in figure 3.1. From a phenomenological point

of view, the uncertainties of the data do not allow to rule out the exact growth with energy of the total cross section. There is a discrepancy between the two Tevatron determination at $\sqrt{s} = 1.8$ TeV. The E710 results [24] tends to favor a $\ln(s)$ increase, while the CDF result [25] favor the $(\ln s)^2$ dependence. Cosmic ray data [26, 27] for $\sqrt{s} > 7$ TeV are badly constrained to be really conclusive. Recently, TOTEM measurement at the LHC with $\sqrt{s} = 7$ TeV is in a good agreement with $(\ln s)^2$ dependency [28].

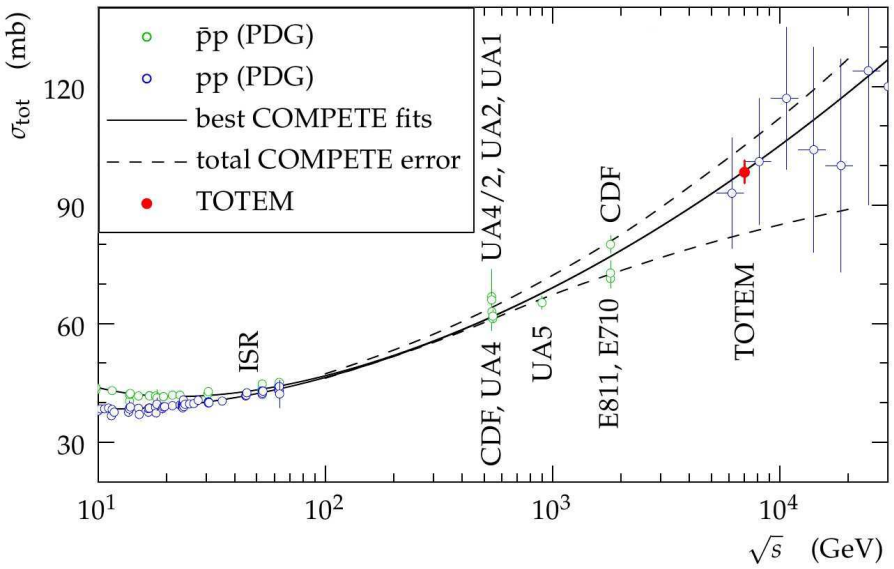

Figure 3.1: The total cross section as a function of the centre-of-mass energy [29]. The green ($\bar{p}p$) and blue (pp) hollow dots represent the data from PDG [30]. For some of the points we have marked the source experiments (the vertical order of the labels respects the vertical order of the points). The red dot is a recent result from TOTEM [31]. TOTEM measurement is not included in the COMPETE fits. The solid black line represents their best fit, the dashed lines show the total error band from all models considered.

3.2 Relative Luminosity measurements

The luminosity $\mathscr{L}$ of a pp collider can be expressed as $\mathscr{L} = R_{inel}/\sigma_{inel}$, where R_{inel} is the rate of inelastic collisions and σ_{inel} is the pp inelastic cross section. For a storage ring, operating at a revolution frequency f_r and with n_b bunch pairs colliding per revolution, this expression can be rewritten as

$$\mathscr{L} = \frac{\mu n_b f_r}{\sigma_{inel}} \tag{3.1}$$

where μ is the average number of inelastic interactions per bunch crossing (BC).
The observed interaction rate per crossing, measured by ATLAS is μ_{vis}. It depends on the subdetector and algorithm in use. The luminosity can then be written as

$$\mathscr{L} = \frac{\mu_{vis} n_b f_r}{\sigma_{vis}} \tag{3.2}$$

where $\sigma_{vis} = \varepsilon \sigma_{inel}$ is the total inelastic cross section multiplied by the efficiency ε of a particular detector and algorithm, and similarly $\mu_{vis} = \varepsilon \mu$. Since μ_{vis} is an experimentally observable quantity, the calibration of the luminosity scale for a particular detector and algorithm is equivalent to determining the visible cross section σ_{vis} [32].

The majority of the algorithms used in the ATLAS luminosity determination are **event counting** algorithms, where each particular bunch crossing is categorized as either passing or not passing a given set of criteria designed to detect the presence of at least one inelastic pp collision. In other words, they calculate μ_{vis}.

The information needed for most physics analyses is an integrated luminosity for some well-defined data sample. The basic time unit for storing luminosity information for physics use is the **L**uminosity **B**lock (**LB**). The boundaries of each LB are defined by the ATLAS **C**entral **T**rigger **P**rocessor (**CTP**), and in general the duration of each LB is one minute.

3.2.1 Luminosity detectors

In order to provide an accurate and reliable luminosity determination, ATLAS uses a variety of different subdetectors and algorithms that measure the luminosity simultaneously.
In the following, detector descriptions are arranged in order of increasing magnitude of pseudorapidity.

Primary Vertex Counting in the ID

The inner detector is used to measure the momentum of charged particles over a pseudorapidity interval of $|\eta| < 2.5$. It is also possible to give a luminosity estimate by counting the number of primary vertices produced in inelastic pp collisions. However vertex counting suffers from nonlinear behavior with an increasing number of interactions per bunch-crossing, which makes a precision luminosity determination using this technique difficult [32].

The Minimum Bias Trigger Scintillators - MBTS

The MBTS consist of two sets of sixteen scintillation counters which are installed on the inner side of the end-cap calorimeter cryostats. They cover a large area in pseudorapidity and the full azimuthal angle. Light emitted by each scintillator segment is collected by wavelength-shifting optical fibers and guided to a PMT. The main purpose of the MBTS was to provide a trigger on minimum collision activity. It has been extremely valuable in early data taking at luminosities below 10^{33} cm$^{-2}s^{-1}$ due to its high acceptance and efficiency. However, this in turn lead to early saturation, and the detector is therefore not suited as a luminosity detector anymore.

Beam Condition Monitor - BCM

The BCM were designed to protect the ATLAS detector from potentially dangerous beam losses. Due to their fast readout and very clean signals this diamond detector is providing in addition, since May 2011, the official ATLAS luminosity. The horizontal and vertical pairs of BCM detectors are read out separately, leading to two luminosity measurements labelled **BCMH** and **BCMV** respectively. Because the acceptances, thresholds, and data paths may all have small differences between BCMH and BCMV. These two measurements are treated as being made by independent devices for calibration and monitoring purposes, although the overall response of the two devices is expected to be very similar. In the 2010 data, only the BCMH readout is available for luminosity measurements, while both BCMH and BCMV are available in 2011 [33].

Calorimetry system

Signal generated by the so called **pile-up** or **minimum-bias** events in the calorimetry system, is one of the relative measurements tools. Their main advantage is the high cross section. However, since no precise absolute cross section can be calculated from theory, only a relative measurement of the luminosity is possible.

The Tile Calorimeter (TileCal) is the central hadronic calorimeter of ATLAS. It is a sampling calorimeter constructed from iron plates (absorber) and plastic tile scintillators (active material), as seen in § 2.2.2. Its cells are defined in each layer according to a projective geometry, and each cell is connected by optical fibers to two photomultiplier tubes (PMT). The current drawn by each PMT is monitored by an integrator system which is sensitive to currents from 0.1 nA to 1.2 mA with a time constant of 10 ms. The current drawn is proportional to the total number of particles interacting in a given TileCal cell, and provides a signal proportional

to the total luminosity summed over all the colliding bunches present at a given time [32].

The detection technique considered is liquid Argon calorimetry (electromagnetic sections of the end-cap regions), where the low p_T particles of minimum bias events deposit most of their energy there (for more details about EM calorimeter, see § 2.2.2). The elementary cells of these detectors behave as ionisation chambers. They are connected together to form readout cells and, with a different granularity, high voltage channels. Figure 3.2 taken form the [34] reference, explains the measurement principle. A charged particle crossing a detector cell, represented by a capacitor of value (C_d), ionises the liquid Argon. The ionisation electrons and ions drift in the field $E = V/d$, with (V) being the potential difference between anode and cathode and (d) their distance, and induce a current on the anode, which is measured with a meter located in the power supply box. This current being proportional to the number of incoming particles, is therefore proportional to luminosity. The resistance (R) represents the total resistance on the high voltage distribution line (resistance of low-pass filters and of calorimeter electrodes). Signal readout is decoupled from the high voltage line by a blocking capacitor (C_b).

The high voltage current is indeed the only way to measure the energy deposited by minimum-bias events in the calorimeters. The feasibility of the this measurement technique is presented in the reference [34]. This approach has two advantages. The response is linear with the luminosity [35] and it is independent from the ATLAS trigger and data acquisition (DAQ) system. In the other hand it is not capable of rejecting beam background, e.g. by performing A/C coincidences [36].

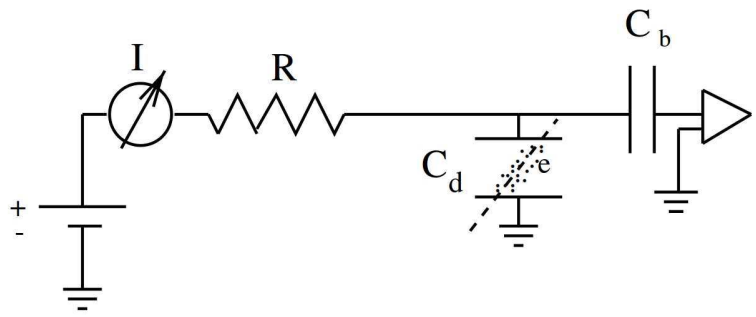

Figure 3.2: Measurement principle of the high voltage current in one high voltage channel. C_d is the detector cell capacitance. The triangle represents the signal readout chain [34].

LUCID

LUCID introduced in § 2.3.1 has been designed to provide the luminosity delivered to the experiment integrated and by bunch.
The LUCID hit pattern is processed by a custom-built electronics card which contains Field Programmable Gate Arrays (FPGAs). This card can be programmed with different luminosity algorithms, and provides separate luminosity measurements for each LHC bunch crossing.

In addition to providing trigger capabilities, the signals from both sides are sent to LUMAT (LUMinosity And Trigger) cards[1] programmed with luminosity algorithms and calibration constants, which allows for an online luminosity determination for each LHC bunch crossing. The algorithms are predefined as coincidence (AND), exclusive, and inclusive OR between the two LUCID detectors.

ZDC

For pp running the ZDC is mainly used for forward particle studies. Their role as a luminosity monitor is only relevant within the ATLAS Heavy Ion (HI) program, where they additionally provide triggers and measure the centrality of the collisions.

For pp collisions, the ZDC single-side signals and coincidence rates provides trigger capabilities as well as, similarly to LUCID, the possibility to monitor relative luminosity. Since 2011, LUMAT cards have been installed on the ZDC readout chain in order to provide an online, bunch-by-bunch luminosity measurement.

3.2.2 Luminosity algorithms

ATLAS primarily uses event counting algorithms to measure luminosity, where a bunch crossing is said to contain an event if the criteria for a given algorithm to observe one or more interactions are satisfied. The two main algorithm types being used are **EventOR** (inclusive counting) and **EventAND** (coincidence counting). Additional algorithms have been developed using hit counting and average particle rate counting, which provide a cross-check of the linearity of the event counting techniques.
Most of the algorithms used do not measure μ_{vis} directly, but rather measure some other rate which can be used to determine μ_{vis}.

[1] Powerful event processor performing the luminosity algorithms and the function of ROD

The LUCID and BCM readouts are configured with online algorithms that provide the Online Luminosity Calculator (OLC) with raw counts based on logical operations (such as a coincidence on the two sides of the detector) of registered events, an event being defined as a signal passing a preset detector threshold. From there the OLC applies the relevant calibrations to the raw counts, provides luminosities to online displays, and allows for their archiving in the COOL conditions database for offline analysis.

The ATLAS strategy to understand and control the systematic uncertainties affecting the luminosity determination is to compare the measurements of several luminosity detectors. The calibrations can be derived from van der Meer scans [37, 38], or ultimately using the ALFA detectors. Figure 3.3 shows the ratio of the integrated luminosity from different measurements with respect to the BCMH_EventOR luminosity, obtained using different luminosity detectors and as a function of time. The absolute scales of the TILE and FCal luminosity measurements were each pegged to that of BCMH_EventOR in May 2011 (run 182161, fill 1787). The absolute luminosity calibrations of the LUCID and BCM algorithms are those derived from the May 2011 van der Meer scans.
Figure 3.4 is a comparison of ATLAS instantaneous luminosity between LAr, MBTS and LUCID (ATLAS run 152409). The LAr instantaneous luminosity is corrected for the dead time in the data acquisition system, and therefore is an estimate of the LHC delivered luminosity at the ATLAS interaction point. Both the MBTS and the LUCID methods are not affected by data acquisition dead time. The uncorrelated method-dependent systematic uncertainties are of order 5% for LAr, LUCID, and MBTS. The curves show only the statistical error as the systematic uncertainty is time independent.

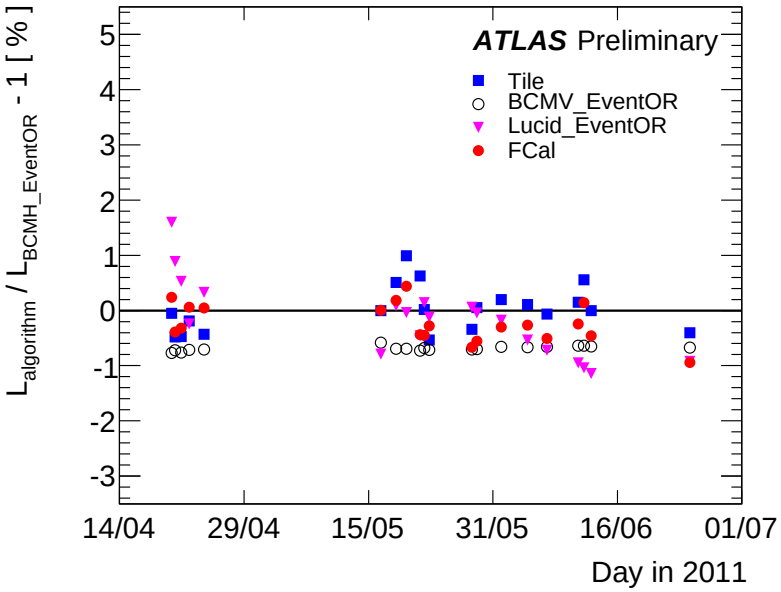

Figure 3.3: The ratio of the integrated luminosity from different measurements with respect to the BCMH_EventOR luminosity, obtained using different luminosity detectors and as a function of time.

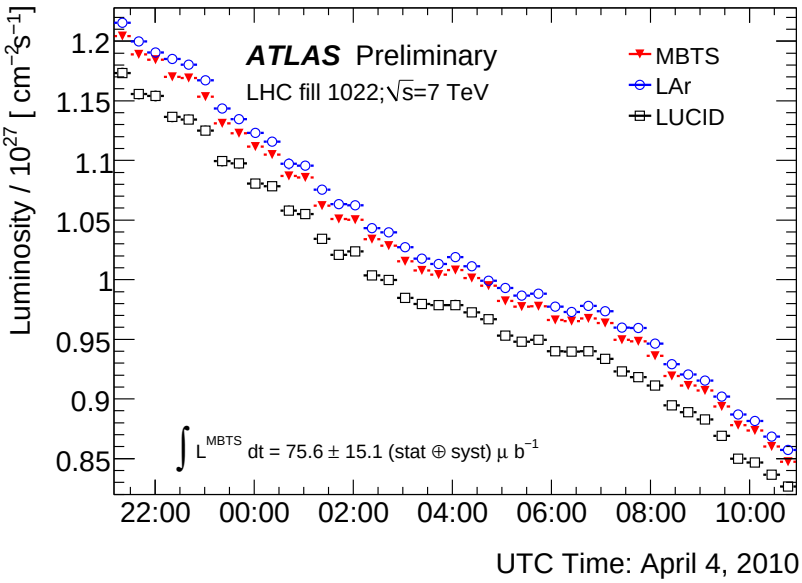

Figure 3.4: ATLAS instantaneous luminosity comparing LAr, MBTS and LUCID (ATLAS run 152409).

3.3 Absolute luminosity measurement

3.3.1 Using Standard Model processes

Using Equation 1.1 with a process that has a known cross section one can determine the absolute luminosity by measuring the corresponding rate. However, the final accuracy on the luminosity is usually limited by the theoretical uncertainty on the calculated cross section.
The leptonic decay of $W^{\pm}$ and Z^0 bosons are often referred to as standard candle processes, because they have clean signals and are theoretically well understood. They have large cross section combined with experimentally well defined final states that are almost background free. Using different sets of PDFs (Parton Density Function), their theoretical cross sections are at the level of 5% and the experimental accuracy is at the level of 1% or below [39]. Recent measurements of $W^{\pm}$ and Z^0 boson production cross sections at the LHC are in agreement with the theoretical values, therefore they are suited to use them in addition for absolute luminosity measurements. Other processes such as muon-pair production via two photon exchange $pp \rightarrow pp\mu^+\mu^-$ could in principle be used as well [40]. Their cross section can be calculated to a level of 1%, but their rate is extremely low and the experimental acceptance and efficiency are difficult to calculate.

3.3.2 Using vdM scan

The calibration of σ_{vis} is performed using dedicated beam separation scans, also known as **v**an **d**er **M**eer (**vdM**) scans [38], where the absolute luminosity can be inferred from direct measurements of the beam parameters. The delivered luminosity can be written in terms of the accelerator parameters and transverse beam profile Σ_x and Σ_y as:

$$\mathscr{L} = \frac{n_b n_1 n_2 f_r}{2\pi\Sigma_x\Sigma_y} \tag{3.3}$$

where n_b is the number of colliding bunch pairs, f_r is the machine revolution frequency (11245.5 Hz for the LHC), $n_1 n_2$ is the bunch population product. During the van der Meer scan, one beam is moved step-wise with respect to the other by a known distance given by the magnet settings, called nominal beam separation, thus allowing for the measurement of Σ_x and Σ_y by fitting the rates, as shown for example on figure 3.5(a) during a scan taken in May 2011. The peak rate μ_{vis}^{MAX} can then be compared to the measured luminosity and the visible cross section extracted as follows [36]:

$$\mu_{vis}^{MAX} = \frac{\mathscr{L}\sigma_{vis}}{n_b f_r} = \frac{n_1 n_2 \sigma_{vis}}{2\pi\Sigma_x\Sigma_y} \quad\Longrightarrow\quad \sigma_{vis} = \mu_{vis}^{MAX}\frac{2\pi\Sigma_x\Sigma_y}{n_1 n_2} \tag{3.4}$$

In parallel, the numbers of protons per bunch ($n_1 n_2$) are measured by LHC instruments. The uncertainty on these bunch currents measurements dominates the total systematic uncertainty on the determination of the visible cross section.

Measurements of the LHC luminosity have been performed by ATLAS in pp collisions at $\sqrt{s} = 7$ TeV using multiple detectors for relative measurements and vdM scan for absolute calibration. A relative luminosity uncertainty of $\delta\mathscr{L}/\mathscr{L} = \pm 3.7\%$ is obtained in 2011 [41]. In the following we will introduce different strategies and methods for absolute luminosity measurements. They are based on the elastic scattering events, and will provide an independent measurement.

3.4 Absolute luminosity and σ_{tot} determination using elastic scattering at small angle

Elastic scattering is the process where both initial state protons remain intact (apart from changes in momenta). This is one of the most common processes and the most fundamental process, where the momentum transfer from one proton to the other is usually small. The Mandelstam variable (t) is defined as the square of the four momentum transfer and will be used extensively in this thesis.

$$t = (p_1 - p_3)^2 = (p_2 - p_4)^2 \tag{3.5}$$

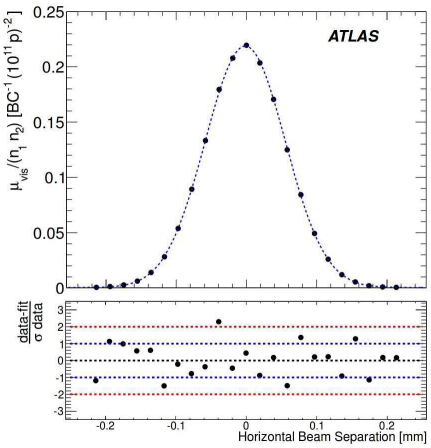

(a) Specific visible interaction rate versus nominal beam separation for the BCMH_EventOR algorithm during scan VII in the horizontal plane for BCID 817. The residual deviation of the data from the Gaussian plus constant term fit, normalized at each point to the statistical uncertainty (σ data), is shown in the bottom panel.

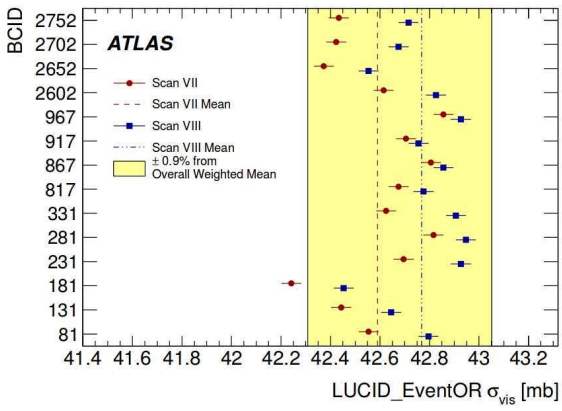

(b) Measured σ_{vis} values for LUCID_EventOR by BCID for scans VII and VIII. The error bars represent statistical errors only. The vertical lines indicate the weighted average over BCIDs for scans VII and VIII separately. The shaded band indicates a 0.9% variation from the average, which is the systematic uncertainty evaluated from the per-BCID and per-scan σ_{vis} consistency.

Figure 3.5: van der Meer μ_{vis} profile and σ_{vis} values during a scan taken in May 2011 [32].

where p_1 and p_2 are the four-momenta of the incoming protons and p_3 and p_4 their four-momenta in the final state (in the case of elastic scattering). Protons initial trajectories is then

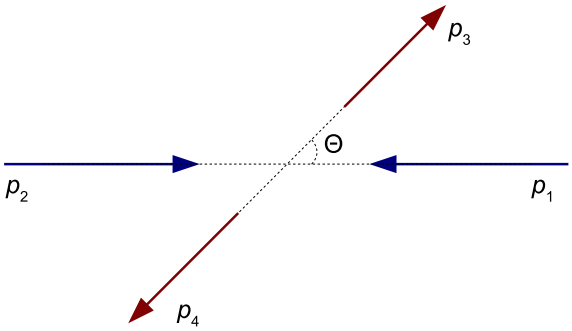

Figure 3.6: Drawing of the elastic scattering. The four-momenta p_1 and p_2 are for incoming protons, p_3 and p_4 their four-momenta in the final state, and θ for the scattering angle.

deviated by an angle θ, called **scattering angle** (figure 3.6). t can be written then,

$$t = -2\,p^2(1-\cos\theta) \approx -(p\theta)^2 \tag{3.6}$$

The last step is valid in the **low scattering angle** limit $\theta \to 0$.

3.4.1 Elastic differential cross section

Elastic scattering has been used for many years as an aid in understanding the effective size or any internal structure of particles [42]. The measured elastic cross section is actually the sum of nuclear scattering events, electromagnetic Coulomb scattering, and scattering due to the interference of the electromagnetic and nuclear amplitudes.

Nuclear amplitude

The rate of elastic scattering is linked to the total interaction rate through the optical theorem [43], which states that the total cross section is directly proportional to the imaginary part of the forward nuclear scattering amplitude $F_n(t)$, extrapolated to zero momentum transfer ($t \to 0$):

$$\sigma_{tot}(s) = 4\pi\Im[F_n(s,t\to 0)] \tag{3.7}$$

where $\Im$ stands for the imaginary part. For $t \to 0$, differential elastic cross section can be parametrized as [44]:

$$\frac{d\sigma}{dt}(s) = \frac{d\sigma}{dt}(s)\bigg|_{t\to 0} \exp(-b|t|) \tag{3.8}$$

where b is the nuclear slope of strong interaction. $\frac{d\sigma}{dt} \propto |F_n(s,t)|^2$ then,

$$F_n(s,t) = F_n(s,t\to 0)\exp(-b|t|/2) \tag{3.9}$$

Expanding $F_n(s,t\to 0)$, one can write:

$$F_n(s,t\to 0) = \Re[F_n(s,t\to 0)] + i\Im[F_n(s,t\to 0)] = \Im[F_n(s,t\to 0)](\rho + i) \tag{3.10}$$

with ρ the ratio of real nuclear amplitude part ($\Re$) over the imaginer one,

$$\rho(s) = \frac{\Re[F_n(s,t\to 0)]}{\Im[F_n(s,t\to 0)]}.$$

Supposing that $\rho(s)$ have a neglect variation in the LHC energy scale range, $F_n(t\to 0)$ is then written as:

$$F_n(t\to 0) = \frac{\sigma_{tot}}{4\pi}(\rho + i)\exp(-b|t|/2) \tag{3.11}$$

Considering that the dispersion energy is negligible ($\Delta E/E \approx 10^{-4}$), and the center of mass energy (s) is set by the dipole magnetic field, we drop out the s dependence of the equations [45].

Coulomb amplitude

The Coulomb scattering cross section is the square of the amplitude, which can be written as [44]:

$$F_c(t) = \frac{-2\alpha\hbar c}{|t|} G^2(t) \exp(-i\alpha\phi) \tag{3.12}$$

with $\alpha \simeq 1/137$ the fine structure constant, $G(t)$ the proton electromagnetic form factor and ϕ the relative phase between Coulomb and nuclear amplitudes.
The dipolar form factor $G(t)$ is the Fourier transform of the proton spatial charge distribution, and can be written as:

$$G(t) = \frac{\lambda^2}{(\lambda + |t|)^2} \tag{3.13}$$

with $\lambda = 0.71$ GeV^2 and slightly changes with the energy [45].
The phase (ϕ) in (3.12) can be written as function of the nuclear slope (b):

$$\phi(t) = \ln\left(\frac{2}{b|t|}\right) - \gamma_E \tag{3.14}$$

with $\gamma_E = 0.577$ is the Euler constant [45].

3.4.2 Luminosity determination from Coulomb scattering

Coulomb term is well understood theoretically and can easily be calculated. An approach, based on that fact, is to measure elastic scattering down to such small t-values that the cross section becomes sensitive to the electromagnetic amplitude. Using this additional constraint from the Coulomb term, allows determination of both luminosity and the total cross section without a measurement of the inelastic rate. This method was used previously by the UA4 collaboration at the CERN SPS where a precision of 3% on the absolute luminosity measurement was achieved [46].

The rate of elastic scattering at small t-values can be written as

$$\frac{\mathrm{d}N_{el}}{\mathrm{d}t} = \mathscr{L}\pi|F_c + F_n|^2, \tag{3.15}$$

using (3.12) and (3.11), it will be written as:

$$\frac{\mathrm{d}N_{el}}{\mathrm{d}t} = \mathscr{L}\left(\frac{4\pi\alpha^2 G^4(t)}{|t|^2} - \frac{\sigma_{tot}\alpha(\rho - \alpha\phi)G^2(t)}{|t|} e^{(-b|t|/2)} + \frac{(1+\rho^2)\sigma_{tot}^2}{16\pi(\hbar c)^2} e^{(-b|t|)}\right) \tag{3.16}$$

where the first term is Coulomb contribution, second one corresponds to **C**oulomb-**N**uclear **I**nterference (**CNI**), and third one to the nuclear interaction.
Using eq. (3.16) to fit the experimental t spectrum, leads to the measurement of 4 parameters:

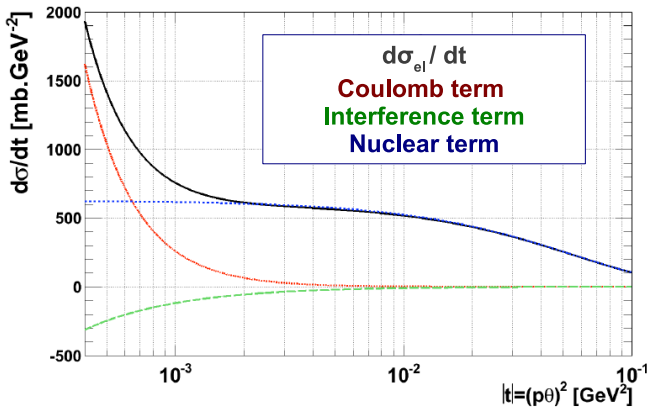

Figure 3.7: The elastic cross section as a function of $|t|$ with $\sigma_{tot} = 100$ mb, $\rho = 0.13$ and $b = 18$ GeV^{-2}. Contribution of different term is illustrated with different colors, red for Coulombian, green for Interference, and blue for Nuclear term. For $|t| < 10^{-3}$ GeV^2 Coulomb term is the dominant one.

luminosity ($\mathscr{L}$), total cross section (σ_{tot}), nuclear slope (b) and phase of the nuclear amplitude (ρ).

Figure 3.7 illustrates the contribution of different amplitudes in the elastic cross section (as given by (3.16)). In the very forward direction ($|t| < 10^{-3}$ GeV^2) the elastic differential cross section is dominated by the almost real Coulomb amplitude. For $|t|$ between 10^{-4} and 10^{-3} GeV^2, the Coulomb and nuclear amplitude are of the same order of magnitude, which make this measurement possible.

3.5 Alternative methods for absolute luminosity and total cross section determination

3.5.1 Using the optical theorem

One can write:

$$\left.\frac{d\sigma_{el}}{dt}\right|_{t\to 0} = \pi\left(|\Re(F_n)|^2 + |\Im(F_n)|^2\right) = |\Im(F_n)|^2(\rho^2+1)) \tag{3.17}$$

By measuring the total interaction rate N_{tot} and the elastic rate $dN_{el}dt|_{t\to 0}$ in the forward direction simultaneously, both the luminosity and the total cross section can be determined. One can use (3.17), and the definition of luminosity $\mathscr{L} = N\sigma$, to derive:

$$\begin{cases} \mathscr{L} &= \dfrac{N_{tot}^2\,(1+\rho^2)}{16\,\pi\,[dN_{el}/dt]_{t\to 0}} \\ \\ \sigma_{tot} &= \dfrac{16\,\pi\,[dN_{el}/dt]_{t\to 0}}{N_{tot}\,(1+\rho^2)} \end{cases} \tag{3.18}$$

Using (3.18) above is the standard way of determining the luminosity from elastic scattering. This method requires a precise measurement of the inelastic rate with good coverage in rapidity η. It will be the method used by TOTEM experiment [47] to measure absolute luminosity recorded at CMS experiment and the total pp cross section.

3.5.2 Using Elastic rate extrapolated to $t = 0$

While the determination of absolute luminosity by Coulomb normalization is our primary goal, an intermediate physics plan can be achieved even if the CNI region is not reached.
The total cross section is one of the basic parameters of hadron scattering processes. It can be determined by measuring simultaneously two of the three following quantities: total interaction rate, forward elastic rate and machine luminosity.
The most direct method determines σ_{tot} by the ratio between the total interaction rate, measured in a detector with full solid-angle coverage, and the luminosity, as shown previously in § 3.5.1.
A second method exploits the optical theorem, extrapolating the measured rate of elastic scattering ($\mathrm{d}N_{el}/\mathrm{d}t$) to $t = 0$. In fact, replacing N_{tot} in 3.18 above with $\mathscr{L}\sigma_{tot}$ gives:

$$\frac{1}{\mathscr{L}} = \frac{\sigma_{tot}^2(1+\rho^2)}{16\pi\,[\mathrm{d}N_{el}/\mathrm{d}t]_{t\to 0}} \tag{3.19}$$

An absolute calibration of the machine luminosity is then required [48] in order to constraint σ_{tot}. A lot of progress have been done at this stage in the ATLAS side. A precision of few percent on the absolute luminosity measurements (for high luminosity runs) have been reached in 2011, using different algorithms and detectors. Hence a determination of the total cross section with an uncertainty half that of the LHC derived luminosity can be achieved. In this way, the precision in the ratio of a given cross section over the total cross section will always be a factor two better than the precision of the absolute luminosity obtained from the machine parameters.
This method have been applied the last 2 years by ALFA, to measure the pp total cross section, using a the luminosity provided by the ATLAS Luminosity group. More details about machine optics parameters, run conditions and measurements results, comes later in the data analysis chapter 7.

Chapter 4

ALFA experimental setups

ALFA experiment aims to provide an **independent measurement** of the absolute luminosity and total pp cross section, based on the Coulomb scattering strategy, introduced in § 3.4.2. To do so, ALFA have to reach the Coulomb Nuclear Interference region (CNI), which requests the measurement of very small scattering angles in the order of a few micro radians. This in turn requires special LHC beam optics configuration called **parallel-to-point focusing optics**. It can be used in combination with rather few bunches of low intensity compared to nominal LHC, with instantaneous luminosities in the range of 10^{27} cm^{-2}s^{-1} to 10^{28} cm^{-2}s^{-1} [17]. This chapter summarizes the ALFA experimental setups. It begins by a description of the beam optics needed for the measurement. Detectors in use are also described, starting by the roman pot concept, which houses the ALFA tracker and allows movement close to the beam during data taking. The tracker is fibre based system using a front-end electronic technology.

4.1 Required beam optics

Figure 4.1 shows the spacial position of elastic scattered protons at 23 m from the IP (just before the LHC focusing triplet[1]). Most of scattered protons are quite close to the beam core, within a contour of 3 σ_u (σ_u is the beam width introduced in § 1.2.3). In other words, detectors have to be placed close to the beam, in the order of 3 σ_u, to track these elastic protons. Detectors lower limit movements are related to the machine collimators position, they are not allowed to move further than collimators, for safety reasons. A conservative distance limit to

[1] Assembly of three quadrupole magnets used for a reduction of the optical β-functions at the IPs. The LHC triplet assembly consists in fact of four quadrupole magnets but the central two quadrupole magnets form one functional entity.

the beam was set in early studies[2] at 12 σ_u.
Consequently, detectors should be placed beyond the focusing triplets, where intercepted scattered protons are well separated from the beam. At this position, scattered protons will go through the LHC optics elements, therefore a good knowledge of the optics and beam dynamics is crucial for the measurement.

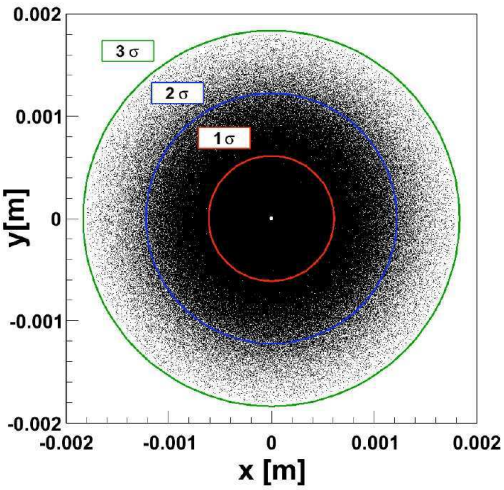

Figure 4.1: Elastic scattered protons (7 TeV) distribution at 23 m from the IP (just before the focusing triplet). Scattered protons are quite close to the beam core (shown in term of $\sigma \equiv \sigma_u$) and can be hardly detected [45].

Reaching the CNI region at the LHC is a very challenging task. At the nominal LHC energy (7 TeV), the strong amplitude is expected to equalize the electromagnetic amplitude for $|t| \approx 6.5 \cdot 10^{-4}$ GeV^2 [45]. This corresponds to a scattering angle[3] (θ^*) of ≈ 3.5 μrad.
Thus, beam divergence at IP ($\sigma_u'^*$) should be negligible compared to θ^*. Referring to the LHC nominal optics in table 1.1 ($\varepsilon = 3.75$ μm rad and $\beta^* = 0.55$ m), beam divergence is expected around 30 μrad, therefore the LHC nominal optics do not fulfill experimental requests.
The needs to reach such small scattering angles imposes very stringent requirements on the beam optics and the beam conditions, as well as on ALFA detectors.

[2]Later during 2012 runs, detectors reach the distance of 5 σ_u.

[3]To indicate the scale of the difficulty: at the SPS collider the Coulomb region was reached at scattering angles of ≈ 120 μrad. This large difference is mainly due to the energy difference but also because the total cross section increases with energy.

4.1.1 Parallel-to-point focusing optics

The most suitable method concerning the optics employs a so-called **parallel-to-point optics** from the IP to the detector. In this type of optics the betatron oscillation between elastic collisions and the detector position has a 90° phase difference in the vertical plane ($\Delta\psi_y = 90°$). Thus, all particles scattered at the same angle are focused on the same locus at the detector, independent of their interaction vertex position (see figure 4.2). Therefore, a transverse position measurement[4] at the detector (u), represents an angular measurement at the IP ($u'^* \equiv \theta_u^*$). In this kind of optics the beam is quasi-parallel at the IP ($\alpha^* = 0$) and must have an intrinsic beam divergence significantly smaller than the smallest scattering angles to be observed [17].

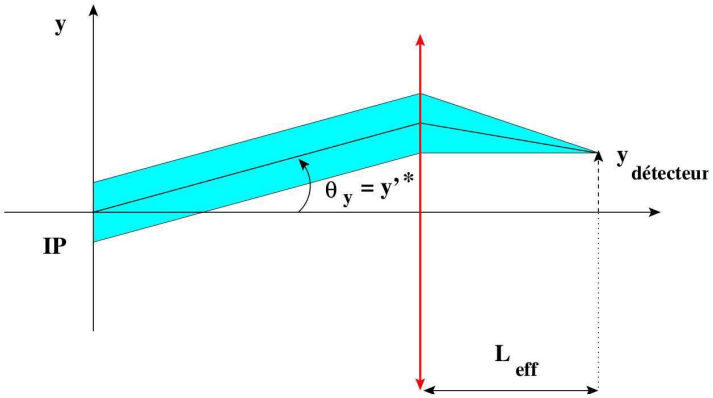

Figure 4.2: Parallel to point focusing optic: all particles scattered at the same angle are focused on the same locus at the detector, independent of their interaction vertex position.

High β^* needs

Referring to the beam dynamic notions, introduced in § 1.2, the observed position (u) and angle (u') of the nominal orbit on the detector plane, is related to the particle vertex (u^*) and trajectory slope (u'^*) at the IP, by the transfer matrix (1.2.4). One can rewrite (1.21) using the (*) notation, and replacing u' by θ_u:

$$u = \sqrt{\frac{\beta}{\beta^*}}[\cos(\Delta\psi) + \alpha^* \sin(\Delta\psi)]u^* + \sqrt{\beta\beta^*}\sin(\Delta\psi)\theta^* \tag{4.1}$$

Considering 2 elastic scattered protons, to the Left (L) and Right (R) side of the IP as shown in figure 3.6. This is so called back-to-back event, where scattering angles are equal

[4] $u(s)$ can be replaced by $x(s)$ for horizontal position and $y(s)$ for vertical one. At the detector longitudinal position, the (s) notation will be dropped down for all quantities, and $u(s)$ will be simplified to u

with opposite sign ($\theta^*_{uL} = -\theta^*_{uR} = \theta^*_u$), and both protons came from the same vertex (u^*). Hence, taking the difference of the left (L) and right (R) arm measurements the vertex contribution cancels. Using (4.1) one can write:

$$u_L - u_R = 2\sqrt{\beta\beta^*}\sin(\Delta\psi)\,\theta^*_u \;\;\rightarrow\;\; \theta^*_u = \frac{u_L - u_R}{2L_{eff,u}} \tag{4.2}$$

with the effective level arm $L_{eff,u} = \sqrt{\beta_u\beta^*}\sin(\Delta\psi_u)$ and supposing that $L_{eff,u_L} = L_{eff,u_R}$, which means an equal level arm on both sides of the IP. The $L_{eff,u}$ ($\equiv M_{12}$ using the matrix formalism introduced in § 1.4) determines the precision of the scattering angle measurement (see figure 4.2). Eq.(3.6) can be written as:

$$-t = p^2(\theta^{*2}_x + \theta^{*2}_y) \tag{4.3}$$

Using the position on the left and right IP sides, one can use (4.2) to compute θ^*_u. Thus, (4.3) gives the t- value.
This t-reconstruction method is called **subtraction** method.

Parallel to point focusing optics requires $\Delta\psi_y = 90°$ and $\alpha^* \approx 0$. Eq.(4.1) will be reduced to $y = \sqrt{\beta\beta^*}\theta^*_y$. The minimum t-value reachable (t_{min}) is given by particles scattering only in vertical plane:

$$-t_{min} = p^2\theta^2_{min} = \frac{p^2 y^2_{min}}{\beta\beta^*} \tag{4.4}$$

where y_{min} is the smallest distance possible between the center of the beam and the edge of the detector. It can be written as a multiple (n) beam width (σ_y) at detector position:

$$y_{min} = n\sigma_y = n\sqrt{\varepsilon_N\beta} \tag{4.5}$$

Using eq.(4.4) and (4.5), t_{min} can be written as:

$$-t_{min} = p^2 n^2 \varepsilon_N/\beta^* \tag{4.6}$$

Thus t_{min} depends on the distance of the detectors to the beam (n), the emittance (ε_N), and on beam envelope at IP (β^*).

Early studies in [17] have shown that, using a normalized emittance ε_N of 1 μm rad, and a minimum distance to the detector corresponding to $n = 15$, $t_{min} \approx 6\cdot 10^{-4}$ Gev^2 can be reached for a β^* of 2600 meters or larger. Taking the detector geometry acceptance into account, therefore detector has to be placed at a closer distance of about $n = 12$.

In this study, possible beam instability was taken into account, which imposes limits on the minimum distance of approach (y_{min}). Eq.(4.4) shows that t_{min} is proportional to $1/\beta\beta^*$. For $\beta^* = 2600$ m, and supposing that y_{min} is limited to 1.5 mm, consequently, this imposes additional requirement on the optics that β (at the detector longitudinal position) should be larger than 70 m.
Nominal optics requirements are then summarized by:

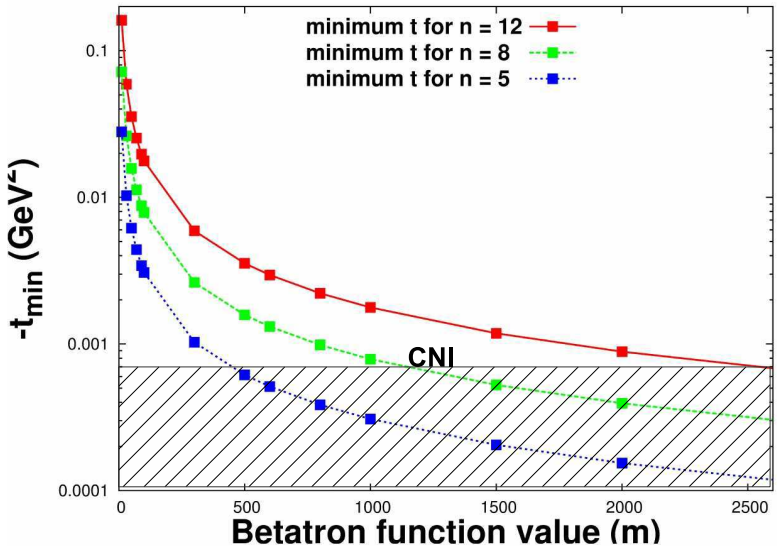

Figure 4.3: Evolution of t_{min} values as function of β^*, for three different detector positions (n = 5, 8 and 12), with 3.5 TeV energy and with a normalized emittance equals to 3.75 μm rad [49].

- $\beta^* > 2600$ m at IP and $\beta > 70$ m at ALFA stations,
- $\Delta\psi_y = 90°$, $\alpha^* \approx 0$ and negligible dispersion,
- $\varepsilon_N \leq 1\,\mu$m rad.

Table 4.1 shows full high β^* optics parameters.
Under these conditions the beam will be stretched in the vertical plane, at detector longitudinal position. Therefore parallel-to-point focusing optics requires detectors only in the vertical plan.

Table 4.1: High beta optics (β^* = 2625 m) parameters for beam 1, at $\sqrt{s} = 7$ TeV beam energy and for an emittance of $\varepsilon_N = 1\,\mu$mrad. The ”–“ is used to separate parameters of the inner and outer stations at the same side [49].

IP		**RPs**	
ε_n (μm.rad)	1.0	β_x (m)	95.2 – 97.9
β_x^* (m)	2625	β_y (m)	123.9 – 117.1
β_y^* (m)	2625	σ_x (μm)	113 – 114
α^*	0.0	σ_y (μm)	129 – 125
D_y^* (m)	0.0	σ_x' (μrad)	1.19 – 1.17
$D_y^{*\prime}$	0.0	σ_y' (μrad)	1.04 – 1.07
σ^* (mm)	0.593	$\Delta\psi_x$ (2π)	0.534 – 0.541
$\sigma^{*'}$ (μrad)	0.226	$\Delta\psi_y$ (2π)	0.247 – 0.252

Recent studies in [49] summarized in figure 4.3, have shown that the CNI region can be

reached in three different scenarios, which depend on the distance that detector can reach (n). This figure shows the variation of t_{min} as function of β^*, for different cases:

1. $n = 12$, CNI can be reached for $\beta^* \approx 2600$ m;
2. $n = 8$, CNI can be reached for $\beta^* \approx 1100$ m;
3. $n = 5$, CNI can be reached for $\beta^* \approx 500$ m;

with energy of 3.5 TeV and a normalized emittance of 3.75 μm rad.
Moreover, these scenarios reveal the importance of having a movable detectors, which can be adapted to the beam conditions and measurement needs.

4.2 Roman Pot structures

The **R**oman **P**ot (**RP**) technique has been successfully used in the past for measurements very close to the circulating beams in a number of experiments at different accelerators, such as UA4 at CERN [20], CDF and DØ at Tevatron [23, 50].
The ATLAS RP design has been derived from the TOTEM design and adapted to the ATLAS constraints. They have been designed to approach the tracking detectors (scintillating fibre-based) at about 1 mm (with the high β^* designed optics) from the circulating beams. A sketch of the RP concept is shown in figure 4.4, in retracted position and working position. The working position will bring the bottom surface of a pot to a minimal distance from the beam. The positioning of the pot will have to be agreed with the LHC and can only happen when the pots are in the shadow of an upstream collimator. The RPs are located at about 240 m from

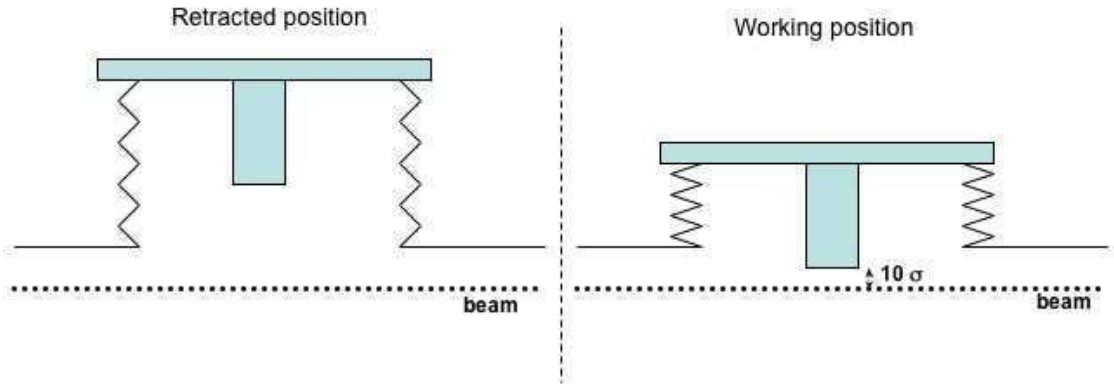

Figure 4.4: Roman pot concept: on the left the retracted position is shown where the Pot is placed out from the beam; on the right in working position, the Pot is approached up to 1 mm (10 σ_y) from the coasting beam.

the ATLAS interaction point on both sides. The chosen position between the sixth and seventh

quadrupole is shown in the schematic layout given in figure 4.5, and was decided taking into account optics studies and LHC setups constraints.

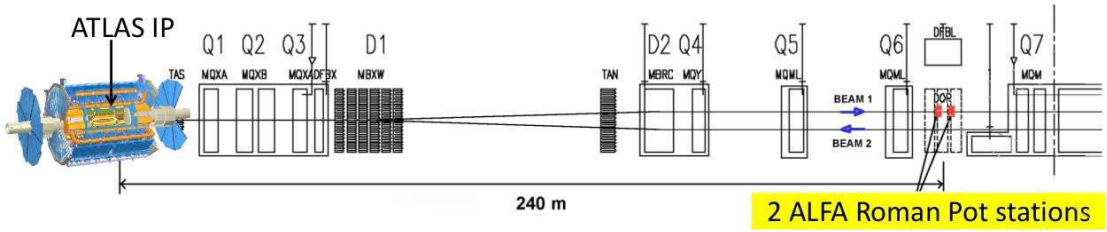

Figure 4.5: Schematic layout of the LSS1 near ATLAS with the proposed location of the RP station (one side).

Two RP stations separated by a distance of ≈ 4 m, are installed at each side of the IP (figure 4.6). The complete system comprises in total 8 pots units. The space for the these units are limited by dump resistor boxes (DQRs) that are necessary for dumping the current of the main magnets in case of quenches.

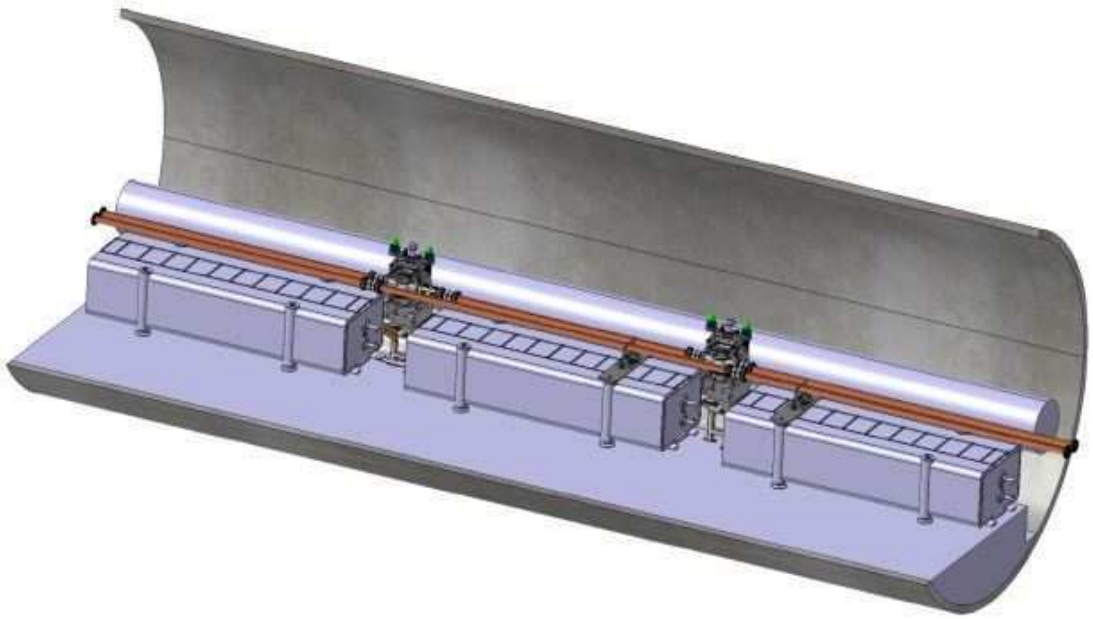

Figure 4.6: 3D view of the roman pot station on one side of IP.

4.2.1 Roman pot mechanics

The RPs have been designed to satisfy the strict requirements of detector positioning precision, and also the constraints of the LHC accelerator. The detectors and the read-out electronics are physically separated from the LHC primary vacuum. This allows the independent moving of the top and bottom pot to nominal position, via a high precision roller screw, moved by a step motor. The screws, the motors and the positioning sensors are developed by the LHC Collimators group. Each unit is composed of a main body ensuring the needed stiffness of the system, and two sets of movable arms, each able to ensure the precise vertical movement of the two pots. A 3D view of a RP unit is shown in figure 4.7(a).
The precision of the coarse positioning will be determined by the reading of the Linear Variable Displacement Transducers (LVDTs) position sensors mounted on each Unit. More details about LVDT measurement can be found in [17] (§ 4.4). The ultimate relative position of the two pots, will be determined with high precision by overlap detectors.

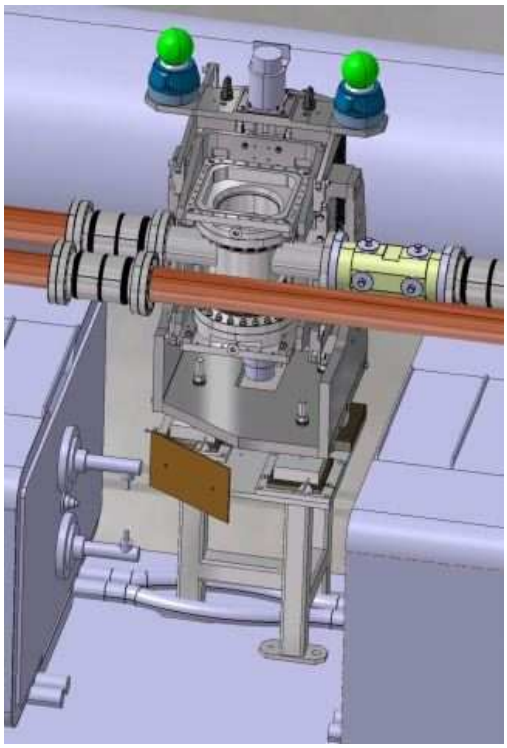

(a) A RP Unit (3D view). It is possible to see the support and the specific shape of the base plate to have enough clearance from the DQR connectors and cables. On the right the position of a BPM is shown.

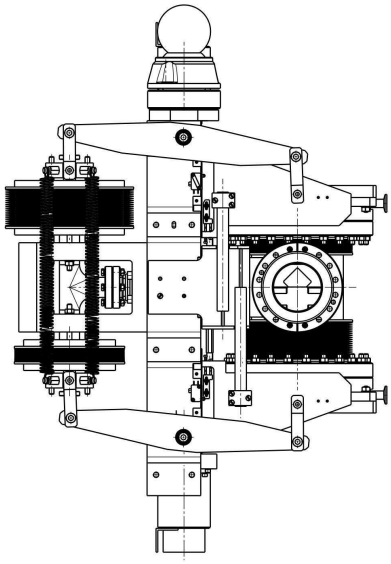

(b) Roman pot Unit design. On the right the top Pot is completely in the vacuum chamber, while the bottom is in retracted position. On the left one can see the Compensation System.

Figure 4.7: Schematic view and design of the roman pot station [17].

4.2.2 The Pot

A secondary vacuum minimizes also the deformation induced by the LHC primary vacuum on the bottom window of each Pot (figure 4.8). The Pot will house the detector and therefore its design had to take into account the constraints imposed by the tracking detector as well as the compatibility with the movement system and the rest of the RP Unit. The thickness of the Pot walls is of 2 mm, while the thin window is only 150 μm thick. That allows minimizing the distance between the beam and the detector. The thin window allows placing the detectors at a distance of about 1 mm from the beam and minimizes the amount of material in front of the detector [17].

Due to the LHC primary vacuum the two pots of each unit will be pulled into the main vacuum chamber with a force of about 2.7 kN. In addition, the gravity force due to the movable parts weight and the detector and read-out weights, have to be taken into accounts. The compensation system, illustrated in figure 4.7(b), consists of an interconnected vacuum chamber with two bellows of a diameter larger than the main vacuum chamber ones. They allow having an over compensating force of about 3.6 kN [17].

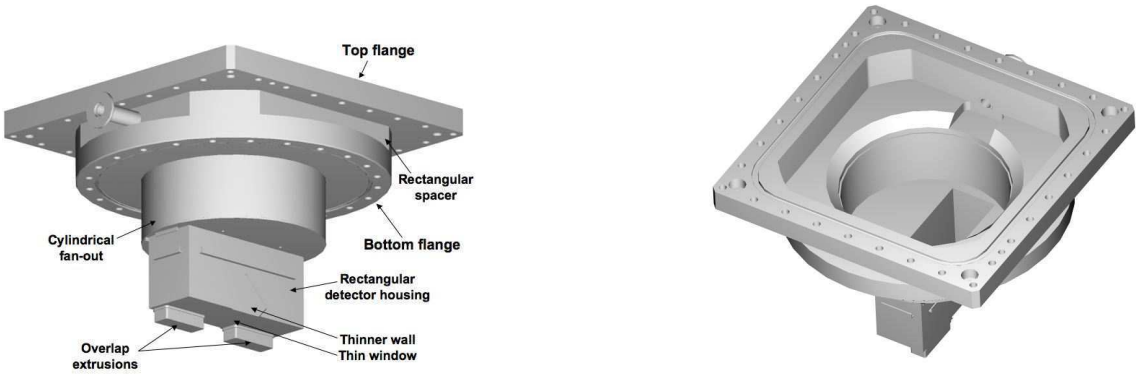

(a) (b)

Figure 4.8: 3D view of the outside (a) and the inside (b) of ALFA pot [17].

4.3 Scintillating fibres detector

The detector consists of two active parts dedicated for high energy protons detection. The first, the **M**ain **D**etector (**MD**), allows the reconstruction of elastic scattered proton paths from interaction point. The second **O**verlap **D**etectors (**OD**), detects particles beam halo, to measure the distance between the top and bottom detectors (MD).

4.3.1 Requirements

This § summarizes tracker detector requirements, taking into account LHC challenging conditions, and physics needs.

Good radiation hardness

Designed detector will be exposed for two main sources of radiation: interaction point, and beam halo. A study in [51] indicates that accumulated dose levels reach 10^5-10^6 Gy/yr close to the beam (215 m away form the IP and at a distance of 15 σ_y) at a luminosity of 10^{34} cm^{-2}s^{-1} and β^*= 0.5 m. Scaling down to a luminosity of 10^{27} cm^{-2}s^{-1} gives accumulated doses of 0.01-0.1 Gy/yr [17]. Notice that a realistic running scenario for elastic scattering is of order one week.
A rough estimate to the radiation contribution from beam halo in [17], gives a dose of 10-100 Gy/yr. Thus, the halo contribution dominates completely and a total radiation hardness up to 100 Gy/yr is sufficient.

Dead space at the detector edge

The amount of dead space at the edge of detector, i.e. the size of the insensitive region, is a critical parameter. It is important to minimize this space to approach the beam as close as possible, and in this way maximize the acceptance for small ($-t$) values.

Spatial resolution

The spatial resolution of the detector has to be significantly smaller than the spot size of the beam at the detector σ_y in order not to be limited by the detector resolution. With a spot size of 130 μm (table 4.1), a spatial resolution of about 30 μm is considered adequate.
It is also necessary to measure the direction of the protons at the detector in order to be able to remove background. With a lever arm of 4.14 m between adjacent RPs, a detector resolution of about 30 μm is again adequate for this purpose [17].

Electromagnetic shielding

For detectors and electronics operating close to the beam the electromagnetic radiation from the circulating bunches induces pick-up noise. Thus it is important to have detectors with low sensitivity to the electromagnetic pick-up or to install adequate electromagnetic shielding. In turn, such shielding contributes to the dead space between the beam vacuum and the sensitive part of the detector, and will limit t_{min}.

4.3.2 Scintillating fibre detector

A tracking detector based on scintillating fibres was able to fulfill all of the above requirements in a simple and cost effective way. Scintillating plastic fibers are intrinsically edgeless particle sensors. They are immune to signal pick-up from the circulating LHC beams and do not require cooling, which facilitates operation under vacuum and integration in the RP.
These detectors have proven their excellent performance already in many HEP experiments, e.g. in the UA4/2 experiment at the pp collider at CERN [20, 52], or the fibre tracker of the D0 experiment [50] at Fermilab.
Fiber trackers are simple in construction and operation. They do not need any internal calibration and can work at very high flux. Their sensitivity up to the edge is just limited by the inactive cladding ($\approx$10 μm).
Based on that, ALFA designed 2 different tracker systems (main detector and overlap detector) for different purposes, and they were mounted in the RP structure.

Main Detector (MD)

The main tracker consists of 20 layers of 64 fibers. As shown in figure 4.9(a), layers are alternately oriented at $\pm$45°, which allows to reconstruct the *x* and *y* positions of the charged particle. This configuration is called UV, where U and V characterize perpendicular orientations of the layers. The fibers are glued on a Ceramic plate 170 microns thick (see figure 4.9(b) and 4.10(a)).

Some fibers (24 fibres) have a 90° cut at the end. The other 40 fibers are cut at 45°. This is done to get the fiber as close as possible to the RP windows and thereby to the beam as suggested by detector requirements § 4.3.1. Fibers are coated with aluminum at the end to make a mirror and to increase the reflectivity index.

Ten layers (10 U and 10 V), staggered by multiples of 0.5 mm $\times\sqrt{2}/10 = 70.7\,\mu$m, are

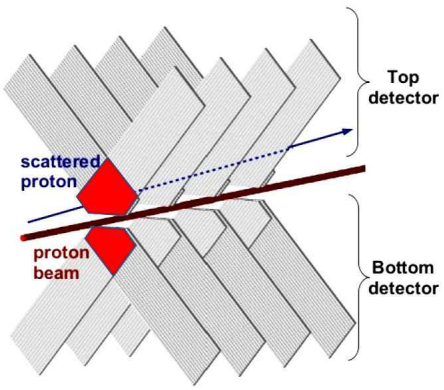

(a) 20 layers of 64 fibers. Layers are alternately oriented at $\pm 45°$, which allows to reconstruct the x and y positions of the charged particle. In red: the detector acceptance.

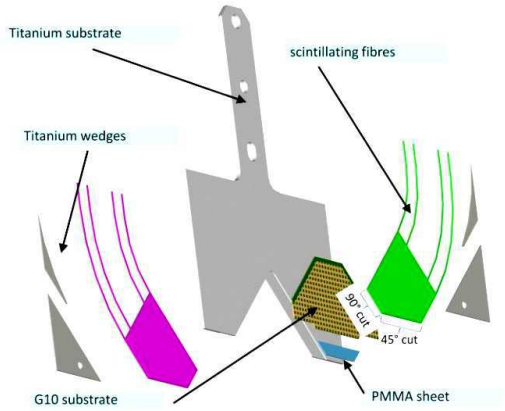

(b) The pieces to make a detector plan. The green fibers make up a V layer. The purple fibers make up a U layer.

Figure 4.9: Main detector fibres arrangement of one layer, and photo of a fibres connector.

assembled through precisely machined hardened steel blades on precision pins to a detector with an effective fiber pitch of 50 μm. Its ultimate spatial resolution, ignoring any geometrical imperfections, is $\sigma_x = \sigma_y = 50\,\mu\text{m}\,/12 = 14.4\,\mu\text{m}$. The z-spacing of the planes is 2.3 mm. The staggering step of 70 μm per plane means that the fibre positions are aligned under an angle of 28 mrad relative to the z-axis. To achieve optimum spatial resolution with this detector concept, the beam divergence σ'_x and σ'_y must be small compared to this angle.

The fibres are routed over about 25 cm to a connector flange (see figure 4.10(b)). Groups of 64 fibers (8×8 fibres with a pitch of 2.3 mm) are glued into O-ring sealed connectors which fit into this flange. The scintillation light is then read by photodetectors with matched read out pitch which are mounted on the opposite side of the connector flange, without an optical contact medium.

Overlap detector

Have a different layers arrangement, and it's dedicated only to measure distance between upper and lower MD edges. The precision of this measurement is the key for the luminosity and total cross section measurement as we will see later in chapter 5 (Overlap detector calibration), where the overlap concept will be introduced, followed by a dedicated calibration study.

(a) Photo of detector plane. The fibers for the V layer are shown. The fibers for the U layer are on the back of the titanium substrate. The 45° fibers are not cut yet [53].

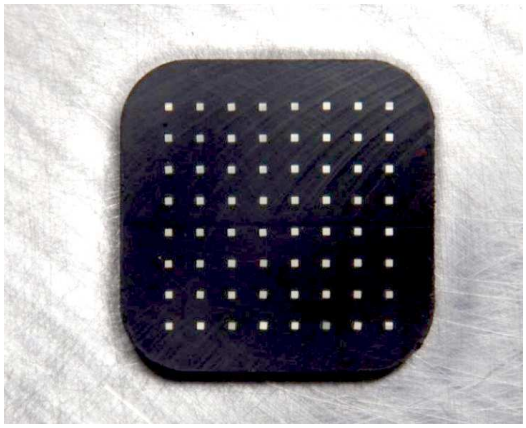

(b) Fiber connectors on an ALFA detector. Groups of 64 fibers (8 $\times$ 8 fibres with a pitch of 2.3 mm) [53].

Figure 4.10: Illustration of the main detector layers.

4.3.3 Trigger scintillators

Both ALFA main detectors and overlap detectors are equipped with dedicated trigger counters which define the active area. As the fibres are also sensitive in the part which is only used as light guide, the trigger counters avoid false hits in this part which can be generated by beam halo particles. A conventional fast plastic scintillator tile of 3 mm thickness, whose shape matches the overlap area of the U and V fibres and which is mounted directly in front of the 10 planes, generates a local trigger signal. Similarly, rectangular scintillator tiles of 15 $\times$ 6 mm^2 are mounted in front of the two active zones of the overlap detectors.
Uniform response is a key requirement to the trigger counters. Any position dependence would lead to distortions in the measured t-distribution or, in case of the overlap detectors, to false position reconstruction. Consequently, efficient light coupling and guiding is required. Tests with compact and flexible wavelength shifter bar readout schemes revealed a marginal number of detected photons (< 10) and consequently the risk of efficiency variations. The scintillation light is collected and guided to small single channel photomultipliers (Hamamatsu R1635, 8 mm) which, for simplicity, are located on the vacuum side of the connector flange. The yield, measured with a Sr-90 source, was of the order 40 detected photons, which promises 100% detection efficiency over the full surface.

Figure 4.11 shows the real arrangement of the fibre layers and triggers. It also shown how the fibres were connected to the Multi-Anode photomultipliers via connectors.

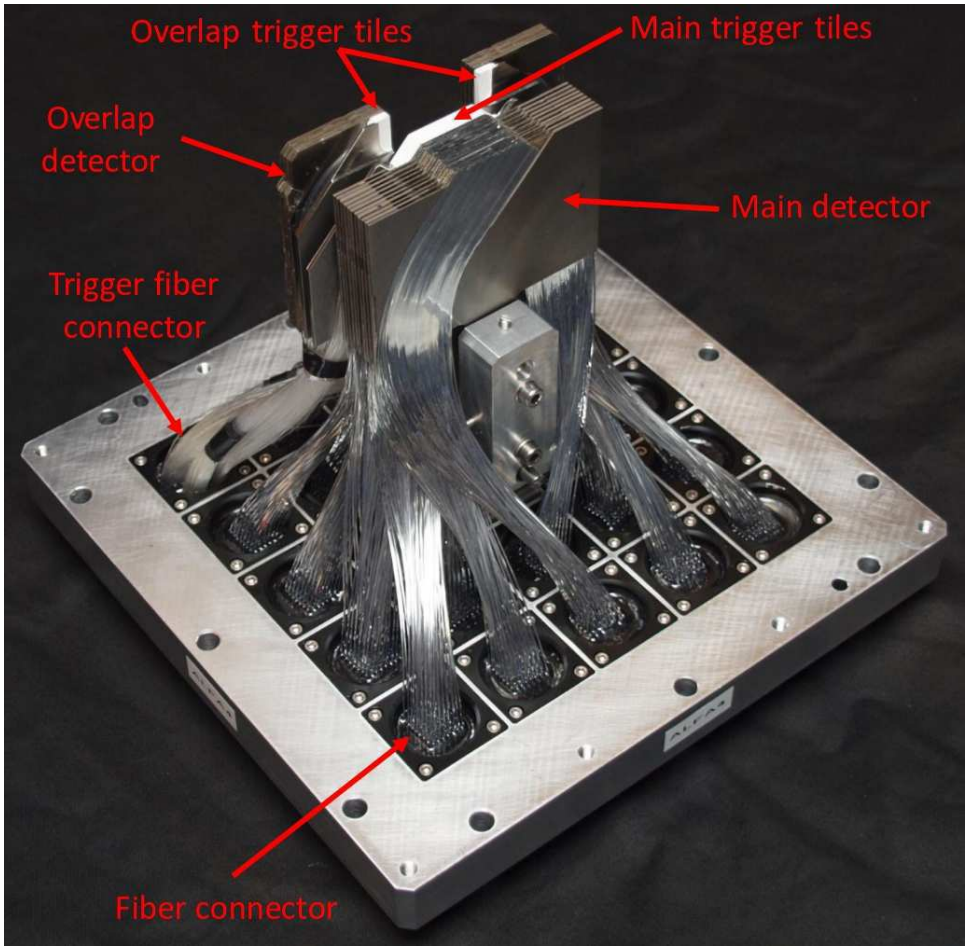

Figure 4.11: Photo of the full detector, before insertion in the RP. It shows position of different components, layers arrangement, and fibres connections [54].

4.3.4 Multi-Anode photomultiplier

The scintillation signals of the tracking detectors are amplified by 64 channel Multi-Anode PhotoMultipliers (MAPMTs) Hamamatsu R7600 (shown in figure 4.12). The light signals of traversing protons are directly guided by the scintillating fibres to the 8×8 pixel grid at the photo-cathode of the MAPMT. The length of the light guides is about 25 cm and a signal of typically 4 photoelectrons is generated by a charged particle passing a fibre.
The signals of the 1280 fibres of each MD are amplified in 20 MAPMTs. Three more MAPMTS are used for the 3×60 fibres of the ODs.
With 10 amplification levels, they reach a gain of 10^6 with a voltage of 900 V. Each channel is 2×2 mm^2 and separated by 0.3 mm. The detector fibers (main layers and overlap layers) are glued into fiber connectors (shown in figure 4.10(b)), which represents the intermediate support between fibres and MAPMT inputs.
This MAPMT choice, fulfill ALFA main requirements [17]:

- high quantum efficiency at the wavelength of maximum scintillation;

- capability to detect single photons;
- fast signal characteristics to allow unambiguous identification of LHC bunches;
- high gain in order to allow the use of simple read-out electronics;
- relatively low cost per read-out channel;
- robustness and reliability;
- moderate radiation hardness;

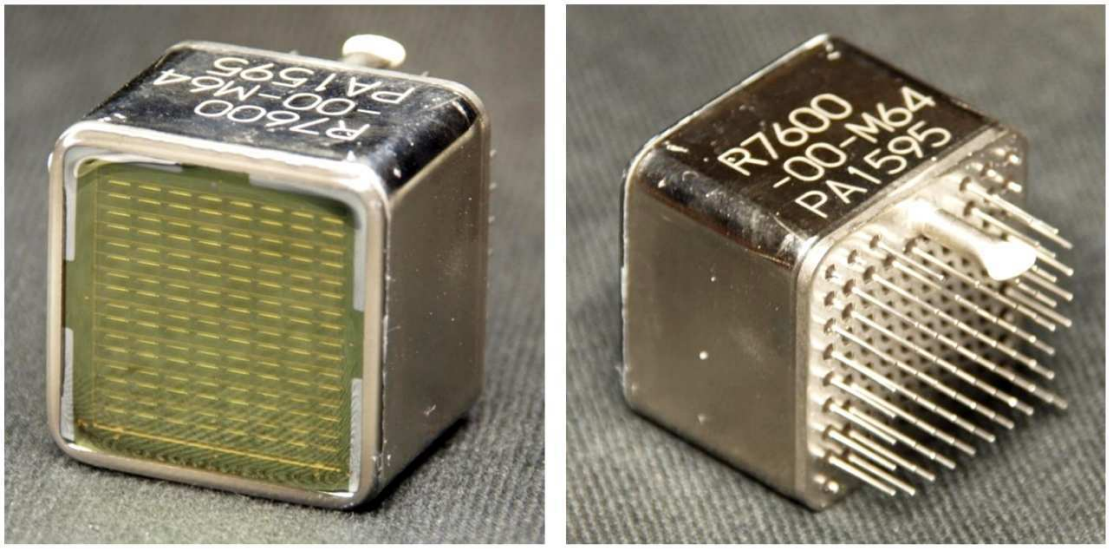

Figure 4.12: Left: the MAPMT from the front. The windows of each channel are shown. Right: The MAPMT from the back. The vacuum pin (white) and the pins are shown. The center 64 pins are for each MAPMT channel. The outer pins are the voltage for each dynode [53].

A sufficiently high light or photoelectric yield is a key requirement for good detection efficiency and finally spatial resolution. The expected photoelectric yield

$$N_{pe} = N_{scint}\,\varepsilon_{acc}\,\varepsilon_{transp}\,\varepsilon_{refl}\,\varepsilon_{gap}\,\varepsilon_{Q_{eff}} \tag{4.7}$$

where different parameters are respectively:

- N_{scint} is number of scintillation photons generated at the Minimum Ionization Particle(MIP). The energy loss in polystyrene is 2 MeV/cm and scintillation yield of 8300 photons/MeV. With fibres of 0,48 mm of active space, $N_{scint} = 2 \times 8300 \times 0.048 = 797$ scintillating photons
- $\varepsilon_{acc} = 0.042$ is the geometrical acceptance factor of a rectangular fibre
- $\varepsilon_{transp} = \exp(-30/70) = 0.65$ represents the transport efficiency due to optical absorption
- $\varepsilon_{refl} = 1.58$ (resp. 1.42) for 90° cut (resp. for 45° cut) is the gain due to reflection from the opposite fibre end
- $\varepsilon_{gap} = 0.9$ is the transmission at the fibre-air-glass interface without any grease
- $\varepsilon_{Q_{eff}} = 0.14$ represents the effective quantum efficiency of the MAPMT. It is the product

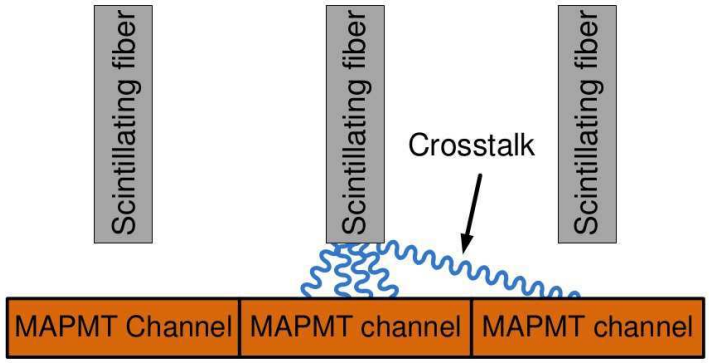

Figure 4.13: Light transition from the scintillating fiber to the MAPMT. A fraction of the light hits a neighbor MAPMT channel. This fraction is label crosstalk [53].

of quantum efficiency at 450 nm (≈ 0.2) and photoelectron collection efficiency (≈ 0.7) which was communicated by M. Metzger, Hamamatsu Photonics, Switzerland, for the R7600-00-M64 MAPMT

Eq. (4.7) leads to $N_{pe} = 4.3$ for fibers with a 90° cut and 3.9 for fibers with a 45° end cut. A photoelectric yield of 4 promises an excellent single fibre detection efficiency. An optimistic estimate can be derived from $\varepsilon_{det} = 1 - \mathrm{P}(0,4)$ where $\mathrm{P}(0,\mu) = \exp(-\mu)$ corresponds to the Poissonian probability to have zero photoelectrons when the average number is μ. From μ = 4 follows a single fiber efficiency $\varepsilon_{det} = 98.2\%$. This simple estimate ignores geometrical inefficiencies (cladding, glue between fibres) and assumes that a single photoelectron can be detected by the data acquisition system with 100% efficiency.

Cross talk

Channels cross talk can be produced or detected at different stage. The aluminization of the fibres suppresses efficiently propagation of the primary scintillation light between fibres. Apart from coupling effects in the electronics chain, there remain two further sources of cross talk:

- Optical cross talk at the level of the MAPMT input window is the result of photo hitting a neighbor channel by a direct pass as shown in figure 4.13, or with multiple reflections in the MAPMT input window. With an average of four photoelectrons per fiber hit, the amplitude of the crosstalk signal is at the peak of the single photoelectron (figure 4.14). The rate is 1.3% (resp. 0.4%) for the direct neighbors (resp. diagonal) in MAPMT.
- *Delta ray*[5] phenomena can also produce cross talk in layer adjacent fibres. In this case the signal amplitude is expected to be of the same size as the actual signal and a discrim-

[5]used to describe any recoil particle caused by secondary ionization.

ination is not possible. The rate of crosstalk due to these events is respectively 3.7%, 1.3% and 0.9% over the three nearest neighbors of the central fiber.

We notice that contribution of electronic cross talk is negligible since measurements have shown that it may appear only with more 10 detected photoelectrons (detailed in [45], § 5.2).

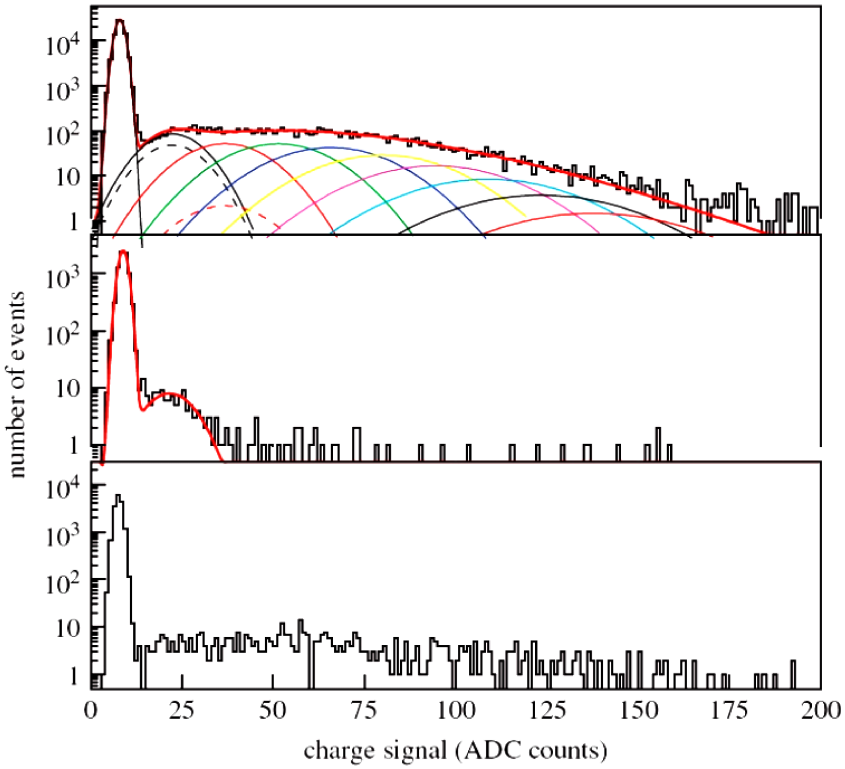

Figure 4.14: Comparison between charge signal spectrum of typical fibre hit event (top), optical cross talk (middle), and physics cross talk [55].

4.4 Readout electronics

The knowledge of the fibre hit is sufficient for tracks reconstruction in the fibre detector, as long as the fraction of cross talk and the induced noise are maintained small. The results from the test beams shows that those conditions are fulfilled. Therefore, a binary readout system were chosen instead of analogue readout.
Before the description of the ALFA readout system, let's check first the main requirements (as described in [17]), which take into account the limited space and difficult access conditions:

- Channel-by-channel adjustable amplifier gain to compensate for the MAPMT gain spread
- High speed: it must be possible to associate signals unambiguously with a LHC bunch crossing

- Adjustable threshold with a minimum setting of (< 0.5 *pe*) in order to guarantee high detection efficiency. A common threshold for 64 channels is acceptable if the gains can be adjusted
- Negligible cross talk between channels (less than 3%)
- Compliance with standard ATLAS read-out scheme
- Integration and Compactness: the restricted space in the RP environment requires to design a front-end electronics which is highly integrated, i.e. which deals with the 64 channels of one MAPMT, and which can be mounted directly on the back of the MAPMT, respecting the 40 mm grid of the MAPMT arrangement on the pot
- Reliability and robustness: the RP detectors are located in the LHC tunnel, about 240 m from the ATLAS cavern, making interventions extremely difficult. The electronics moves together with the RPs between beam and garage position
- Radiation tolerance: the radiation environment during the specific luminosity runs is not expected to pose serious problems for the electronics. In normal physics runs, once the LHC machine is operated at close to nominal luminosity, the scintillating fibres would soon suffer from radiation damage, and, at a lower degree, the electronics could be degraded as well. It is therefore foreseen to dismantle and remove the detectors and the electronics parts from the pots. The connectivity of the system must allow for a rapid removal/installation of the system

4.4.1 PMF: PhotoMultiplier Front-end electronic

The first part of the electronics readout is located on a stack of Printed Circuit Boards (PCB) located atop of each PMT tube. The assembly of the PMT with the PCB, connectors and all components is named PMF (PMF electronics figure 4.15). It is made of a MAPMT and three boards (3 cm $\times$ 3 cm) in its shadow:

- the HV board which brings the high voltage to the MAPMT
- the passive (or intermediate) board which routes the signals to connectors located on the edge
- the active board which has the read out chip MAROC (Multi Anode ReadOut Chip) directly wire-bonded on the PCB on one side and a FPGA (Lattice) on the other side

Inside a PMF, each PMT anode is connected to the input of one channel of the 64 channel readout chip MAROC. MAROC (Multi Anode ReadOut Chip) is a 64 inputs ASIC which allows correcting for the gain spread of MAPMT channels thanks to a 6 bits variable gain preamplifier. For each channel the signal is shaped (fast shaper, 15 ns) and discriminated to produce a trigger output [56].
A multiplexed charge output is also produced both in analog and digital thanks to a Wilkinson

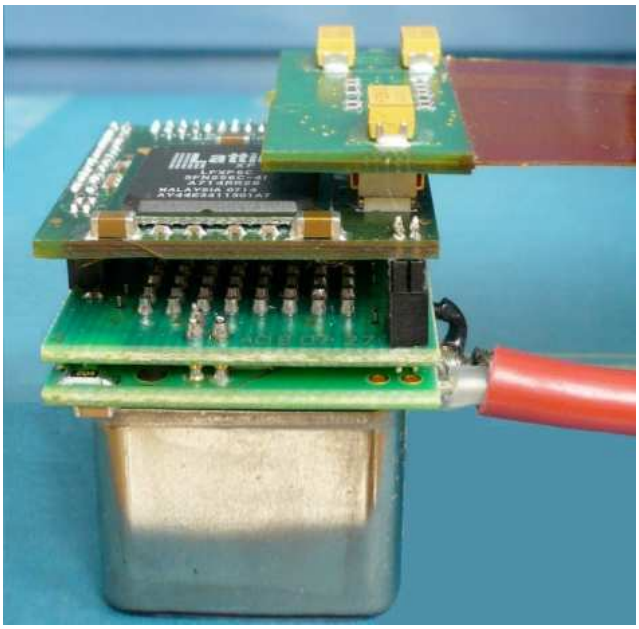

Figure 4.15: MAPMT with full PMF mounted: MAPMT + isolator + spacer + voltage divider + spacer + isolator + passive board + active board.

ADC. The block diagram represented on figure 4.16 summarizes the different features of this chip [56].
The option of reading out the analogue amplitude (slow shaper path) of signals through this multiplexer is maintained for the commissioning of the detector. This feature is not used during normal operation.
The MAROC chip is required to have a detector efficiency of 100% for signals larger than 1/3 photoelectron. The crosstalk between neighboring channels is better than 1%. Additionally the charge measurement should be feasible up to a signal of 30 photoelectrons with a linearity of 2%.

The PMFs will be arranged in a 5 by 5 matrix for each RP. Each line of up to 5 PMFs will be linked to the motherboard through a kapton cable. In total 23 PMFs per RP will be installed, 20 for the standard scintillating fibers layers and 3 for overlap detectors.

4.4.2 Triggers system

The trigger system is based on scintillators presented in § 4.3.3. The motherboard (located on each Roman pot) combines the signals of various scintillators as shown in figure 4.17: M1 and M2 triggers scintillator for MD, OL and OR for overlap right and left side. The motherboard must also manage the trigger system used in case of calibration of the electronic chain with

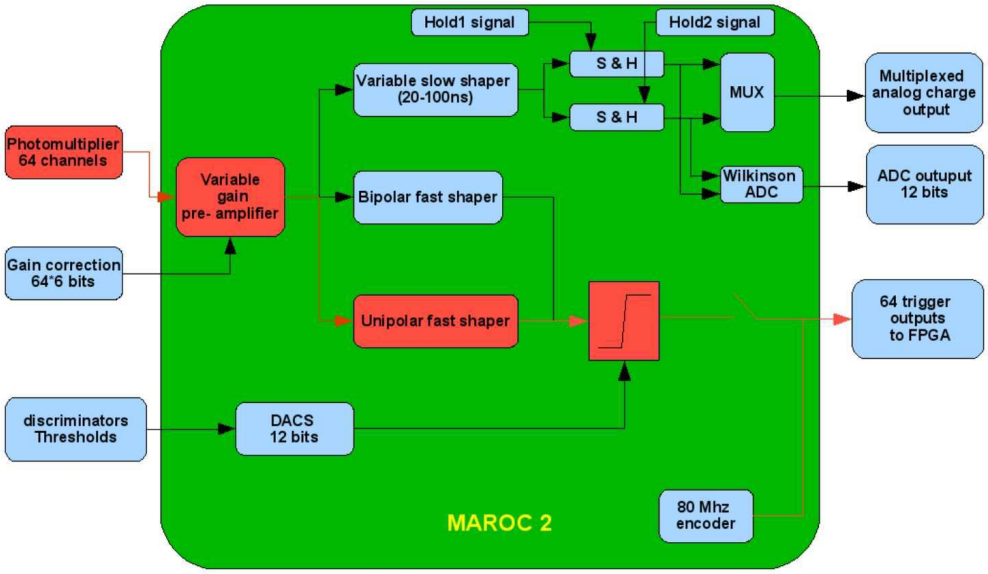

Figure 4.16: Simplified diagram of a MAROC channel chip (in its second version). Three different possible signal paths can be distinguished: the slow shaper for analog output and unipolar and bipolar shapers for digital output. Passage using the fast unipolar shaper was highlighted in red and will be used for the measurement [45].

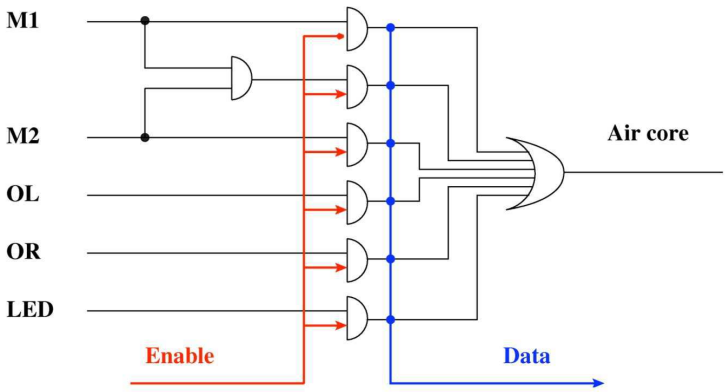

Figure 4.17: Triggers logic motherboard scheme [45].

LED[6].

According to the chosen configuration, a trigger signal will be sent, via air-core cable (figure 4.18), to the CTP (Central Trigger Processing) in USA15, which will receives eight different signals from eight detectors in the LHC tunnel. These air-core cables are fast cable, with a transit time less than 2 μs, which allows a temporary storage of the events in the pipeline. The main feature of these cables is their velocity (0.93 c) and wide dynamic range up to 4.9 GHz.

[6]LED is used to create a test signal, injected at the scintillating fibers side of the detector. This will be used for the commissioning of the electronic system, and can not be used to check the calibration of the photomultipliers.

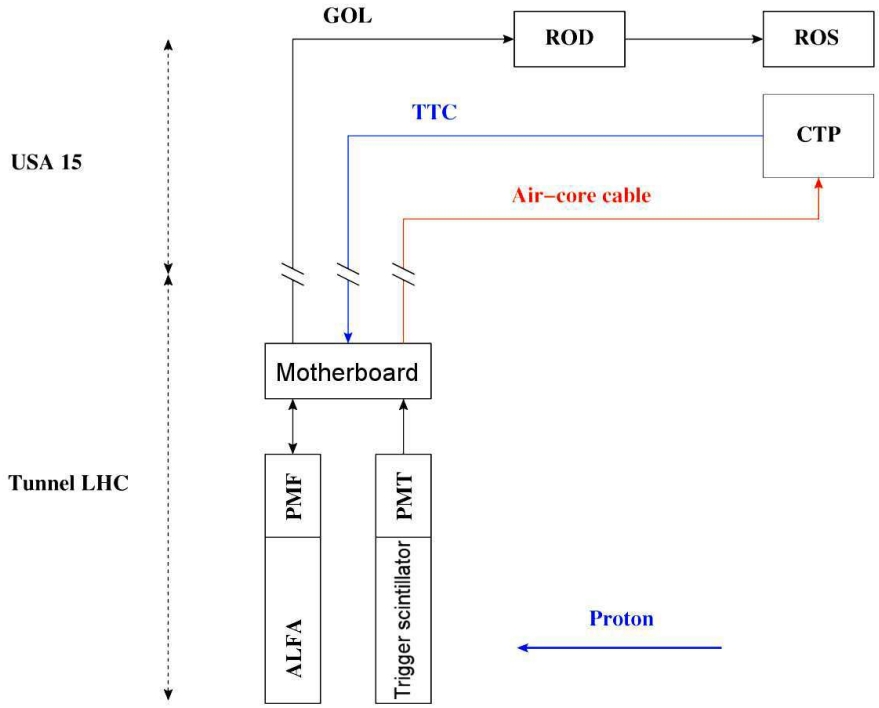

Figure 4.18: Global scheme of the ALFA trigger logic system. A scintillator locally detects a charged particle. The decision of storing the event is made at the ATLAS CTP. GOL (Gigabit Optical Link) transmits data from the motherboard to the ATLAS acquisition system. The data reaches first in the ROD (Read Out Decoder) are then sent to the ROS (Read Out System) where all the data acquired by the ATLAS sub-detectors is processed [45].

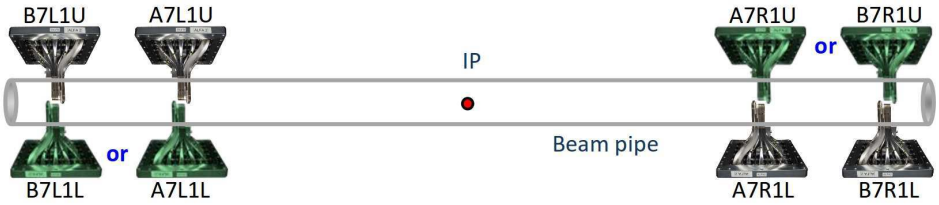

Figure 4.19: Triggering an elastic event, where green stations represent a fired trigger [54].

The coincidence between the various detectors is performed at the CTP, which look for some predefined triggers coincidence configurations between different detector online. The primary elastic recording signature (shown in figure 4.19), is 4 fired triggers, two for top detectors on one IP side, and other two for bottom detectors on the other IP side (and vice versa). A list of triggers needed for the analysis is reported in [54], with the 2 primary triggers configurations for elastics, and other configurations for background studies, diffractive events, overlap detector analysis, ...

Once decision is made at the ATLAS CTP, it will be sent back to the Motherboard. Motherboard storage pipeline should be synchronized with the CTP, as we have a delay of few μs. If the CTP decision is to record event, then GOL (Gigabit Optical Link) transmits data from the motherboard pipeline to the ATLAS acquisition system. The data reaches first in the ROD

(Read Out Decoder) are then sent to the ROS (Read Out System) where all the data acquired by the ATLAS sub-detectors is processed.

4.4.3 Motherboard

As mentioned before, the complete data acquisition is performed at the Roman pots. For each detector, 3 main objectives have to be achieved:

- collect the data from the 23 PMFs
- ensure the long distance connection to the ATLAS acquisition system
- control the motherboard operation using the ELMB system (Embedded Local Monitor Board) developed at CERN

The layout of the motherboard is shown in figure 4.20. Trigger features are integrated in a printed circuit board called mezzanine. Figure 4.21 presents its features. The functionality separation between the main part of the motherboard and the mezzanine is purely technical: it helped to lunch the motherboard production, while the trigger features were still under discussion.

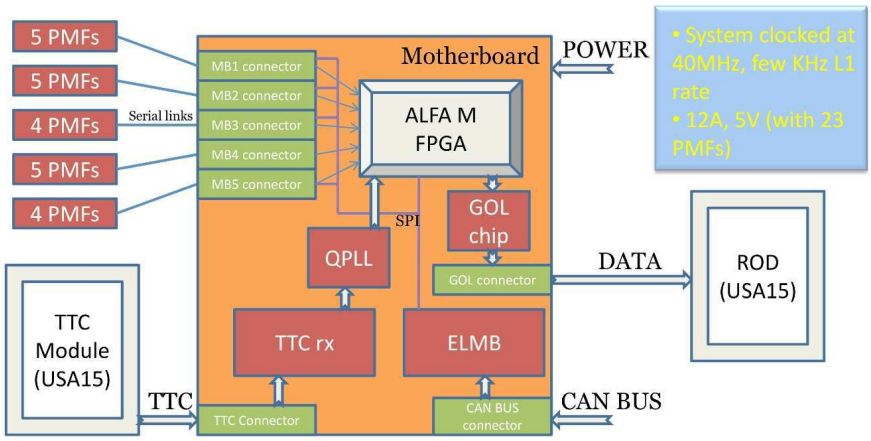

Figure 4.20: The motherboard diagram. Raw data from the PMFs are transmitted to FPGA ALFA-M. The ALFA-M collects and arranges data, which corresponds to the same event and transmits them via the GOL in the ROD USA15 located in the ATLAS cavern [45].

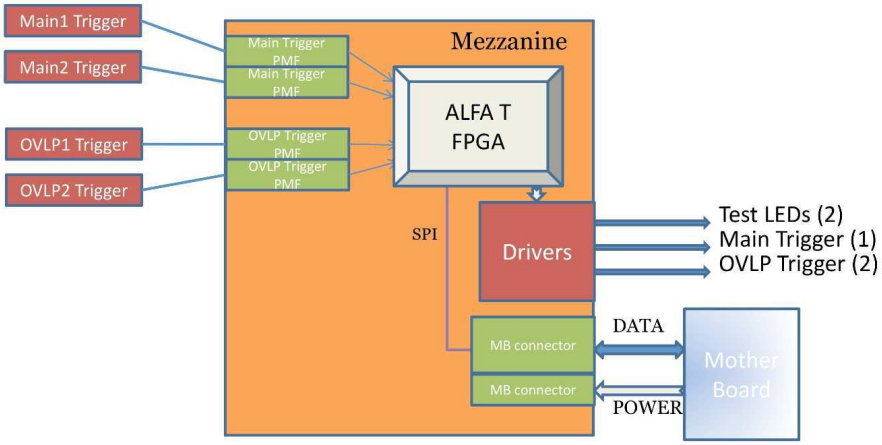

Figure 4.21: Diagram of the mezzanine. Four specific PMFs provide trigger signal and timing . The triggers outputs are used to combine the inputs from the two scintillators trigger (main and overlap detectors) [45].

Chapter 5

Overlap detector calibration

This chapter deals with the **O**verlap **D**etector (**OD**), aiming to measure vertical distance between upper and lower detectors of an ALFA station. First section is an introduction to the OD design, measurement needs, precision challenge, and tracks reconstruction algorithm. Second section is focused on the technical details of OD calibration during CERN test beam, in October 2010, few months before the installation of ALFA stations in the LHC tunnel. It was the first check of the overlap detector performance and precision, using high precision telescope.

5.1 Detector needs and precision challenge

As shown in previous chapters, the luminosity determination in ATLAS requires an absolute knowledge of the transverse momentum for elastic events, which will be determined from the scattered proton angle (θ^*). Consequently, it is derived from the transverse coordinate *x-y* measured with ALFA. Therefore, the absolute measurement of the detector position with respect to the LHC beam spot is a crucial point, and the precision with which the distance between the two detectors is known has a direct consequence on the uncertainty of the luminosity. Earlier simulations have shown that, for the high β^* optics, if upper and lower detectors approach the beam to 1.5 mm, a systematic shift of $\Delta y = 15$ μm represents a positioning error $\Delta y/y$ of 1%, and consequently an angular error $\Delta\theta/\theta$ of 1%. This implies a 2% error in the luminosity. So to reach 1-2% on $\mathscr{L}$ determination, distance between the two half detectors has to be known with a precision of about 10 μm [57].

The vertical distance between the two detectors can be determined by dedicated detectors, called the Overlap Detector (OD), designed only for this purpose. They are used to measure only the vertical coordinate. Two ODs are mounted below (and above) the actual detector

planes. They move with the detector planes and their relative position to those is fixed and well known (TB calibration). The ODs detect particles in the beam halo region. The active areas of the ODs begin to overlap when the detector halves approach each other. This technique is challenging as one does not have a proper simulation of the beam halo, and there was no idea if it would work with good efficiency.

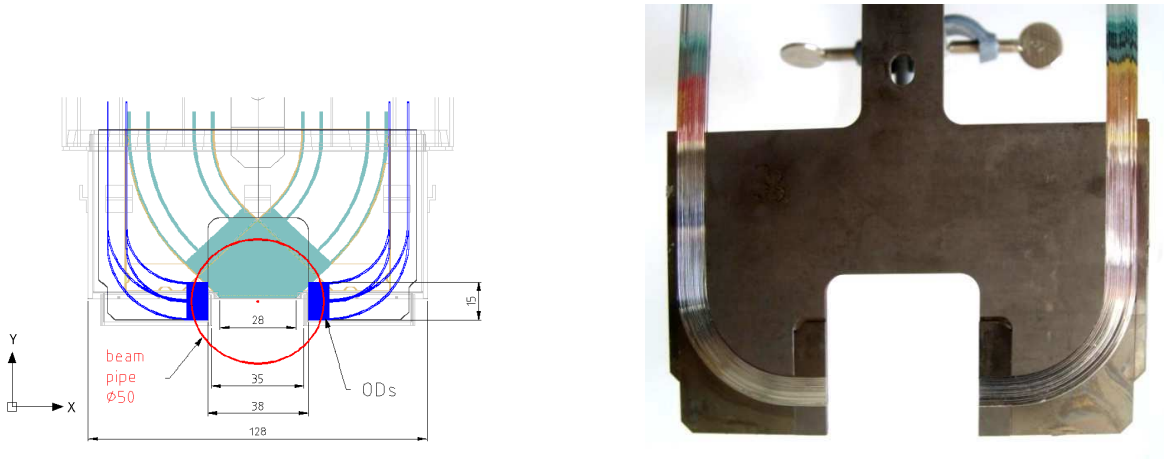

(a) Frontal view of the full detector assembly with the overlap detectors (blue). The red spot and the circle in the center represent the beam axis and the beam tube (diameter 50 mm).

(b) Photo of an overlap plan. One layer of fibers is shown. The other layer is on the back of the titanium substrate and has fibers next to the titanium edge.

Figure 5.1: (a) illustration and (b) photo from a frontal view of the Ovelap detector.

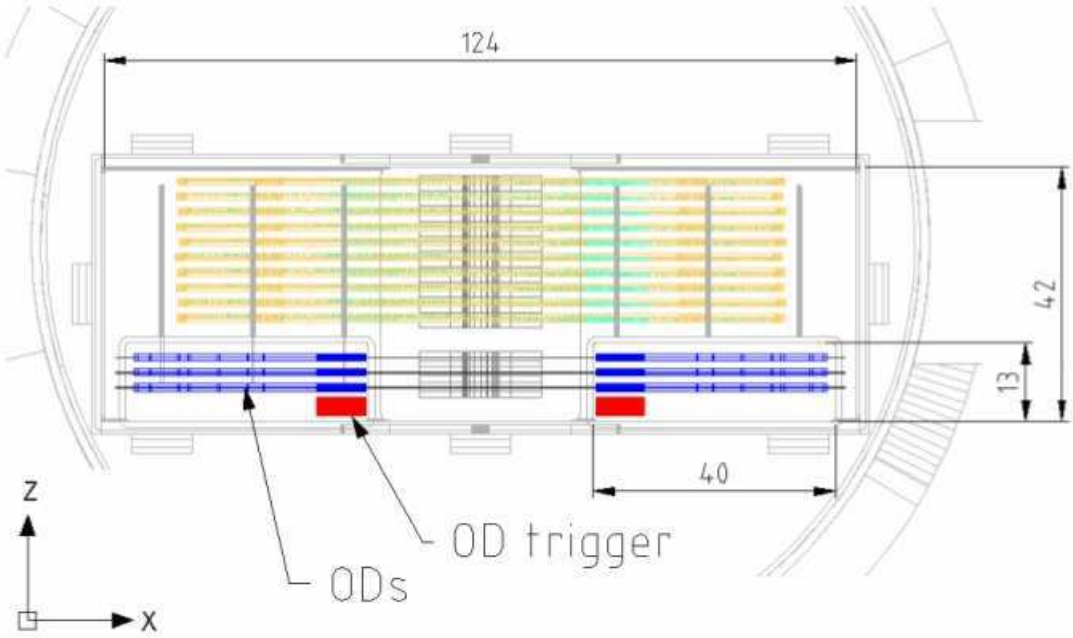

Figure 5.2: Top view of the detector assembly. The first three planes (blue) belong to the overlap detectors. The overlap triggers are also shown (red). Units in mm.

5.1.1 Detector design

The overlap detectors consist of horizontally mounted scintillating fibres of the same type and size as the main detector ones. An OD comprises 3 planes of 30 fibres. Two planes are vertically staggered by 166 and 333 μm, respectively, from the first one. They cover an active area of 6×15 mm^2. The horizontal fibres are bent by 90° and routed upwards to the MAPMTs. They are connected to the front end electronics in the same way as MD fibres. In order to maximize the bending radius of the fibres, the 30 fibres are split into two layers of 15 fibres each which are mounted on the front and the back side, respectively, of a titanium substrate support plate. Two 3 mm thick plastic scintillators cover the OD active area, and act as trigger counters. Front and top view of the overlap detectors integrated with the main detectors are shown in figure 5.1 and 5.2. The detectors need to be located in special extrusions of the Roman Pot. The design of the ODs is a compromise between manifold physics and technical constraints. In the horizontal plane the distance between OD edge and the beam axis is 19 mm which means that about 2/3 of the active surface is inside the beam tube radius of 25 mm. The longitudinal distance between the two OD sets is 46 mm. The ODs start to overlap when the two pots are at 8.5 mm from the beam axis. The maximum vertical overlap is 15 mm. The overlap detectors provide the coordinate information in discrete steps of $500/3 = 166.6$ μm. The difference of the hits in the two detectors can also be measured only in discrete steps of 166.6 μm. Differences smaller than 166.6 μm are derived by averaging the measured differences over a sample of events with sufficiently large statistics. The achievable precision of such a measurement is discussed below. The design has the unwanted feature that the second overlap detector is located vertically on the same level as the bottom face of the first Roman Pot (figure 5.5(a)). This means that a fraction of the protons which go through the second overlap detector had a chance to interact with ≈ 20 mm of stainless steel [57].

Ideally the overlap measurements are made with TeV protons which are transported parallel to the primary beam. Therefore, the overlap detectors should be included inside the aperture of the beam tube with a diameter of 50 mm, moreover it should be within the aperture of the beam screen[1] which at this position has a horizontal diameter of 44 mm. Outside of this limit the composition of the beam halo may be dominated by shower particles originating from hadronic interactions of the beam with collimators and structural components.

5.1.2 Reconstruction algorithm

Reconstruction algorithm transforms signals on fibres, so called **hits**, to a spacial position using fibres metrology files. All fibres (MD or OD) are defined by a slope, intercept and depth

[1] Perforated tube inserted into the cold bore of the superconducting magnets in order to protect the cold bore from synchrotron radiation and ion bombardment.

(or layer number), in the detector reference system.
The MD track reconstruction and selection are developed in the reference [45]. This section concerns the track reconstruction in the overlap detector.
The reconstruction algorithm scans all fibres and selects hits. It then locates them using metrology files, and finally, combines fibres information to reconstructs tracks. As the OD is made of only 3 layers, fibres hits are considered a track, only if 3 fibres from different layers overlapped, by projecting them on the *y*-axis. Projection method will be detailed in the following.

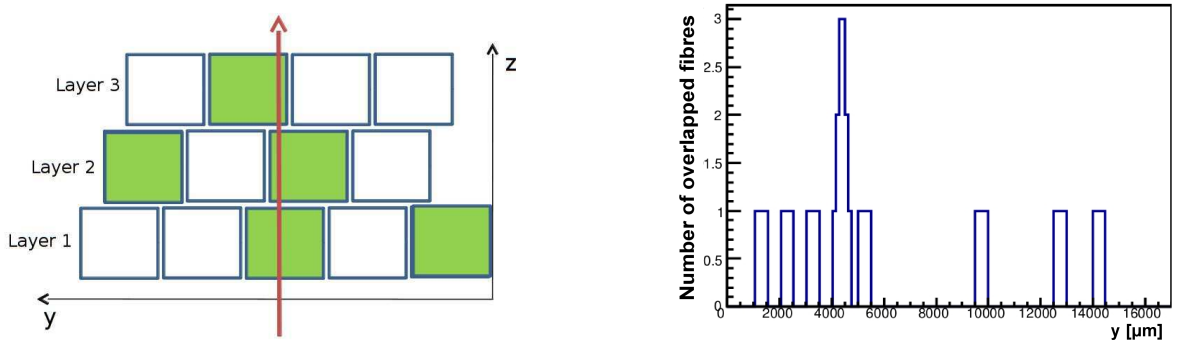

(a) Drawing shows a part of overlap detector, where a track (red) hits 3 fibres (green). Some random fibres show signal too, due to a cross talk or electronic noise. Fibres position and width is known using the metrology file.

(b) Overlap detector event viewer. *y*-axis here refer to the OD reference system. Active fibres are projected over the *y*-axis using there real position and width. In this example one can distinguish a track around 4 mm with some noisy fibres.

Figure 5.3: Illustration of an OD event with a real hit.

5.1.2.1 Single track algorithm

Figure 5.3(a) illustrates the case of a single track passing through the overlap detector. Green fibres are the hits. Track position is then given using metrology information of at least 3 overlapped fibres in the 3 layers. Figure 5.3(b) shows the projection of fibres activities with respect to their positions and widths. Result of this projection is a **peak** of height 3 (refers to the number of overlapped fibres) around reconstructed track position. Precision of reconstructed position is the peak **width**. Other bumps around the peak may come from cross talk between fibres or any other noise. Ideal detector, with designed staggered plan, gives a reconstruction width of 166 μm, for any position. In realty this is not the case. It depends on the detector metrology, and differs from one detector to another.
The single track algorithm requires 3 main conditions for reconstruction:

- minimum of one fibre hit per layer

- projection of fibres activities on *y*-axis gives only one peak of 3 overlapped fibres
- peak width (or track precision) is less than 0.5 mm, to avoid cross talk

Glue separating fibres, and fibre inefficient longitudinal edges form a kind of non-active material gaps. Particles passing through these gaps won't be detected. However, the way that the 3 layers are staggered makes impossible for a particle to go in 3 continuous gaps. The average gap width is estimated to $\approx 30\ \mu$m ($\approx 10\ \mu$m for fibre edges and $\approx 10\ \mu$m or less for glue). About 12% of the total tracks crossing the OD pass through different layer gaps. This will affect the reconstruction algorithm as it requests for at least 3 fibres hits from different layers. In order to increase the reconstruction efficiency by reducing the gaps effect, an additional loose option was added to the algorithm. This option allow the reconstruction of tracks using only two overlapped fibres instead of three. Therefore, it may not be useful in some cases, especially in high background data taking conditions.

5.1.2.2 Multi tracks algorithm

The needs to develop this algorithm appear after the first data taking. It was due to the high activity detected in the LHC tunnel, as explained in § 6.6. The aim was to improve statistics by increasing the number of reconstructed tracks per OD.
It follows the same procedures as single track algorithm for tracks identifications. Two more conditions are required in addition to the previous algorithm, concerning total tracks number, and separation distance between them.
Multi tracks algorithm conditions are:

- minimum of one fibre hit per layer
- projection of fibres activities on *y*-axis gives at least one peak of 3 overlapped fibres
- peaks width (or tracks precision) are less than 0.5 mm, to avoid cross talk
- separation distance between two peaks (which pass conditions above) is more than 1 mm
- maximum number of reconstructed tracks is fixed up to 6 per OD

Figure 5.4 shows some of the various multi tracks cases, where the red color represents the algorithm rejection and green one represents the accepted tracks. In the (a) case the algorithm succeeds to reconstruct two separated tracks (green), but this even is rejected do to the separation limits between two tracks (red), where one of them exceeds also the track (peak) width limit. Case (b) is also rejected due to the track separation limits. It's a signature of a shower detected in one side of the OD.
Cases (c) and (d) show some accepted cases, where tracks are well separated, peak width less than 0.5 mm, and all other conditions are fulfilled.

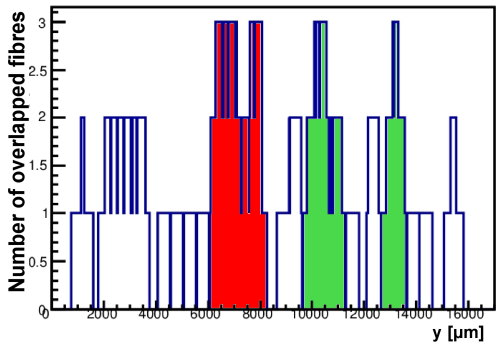

(a) Rejected event due to the distance separating tracks and track width.

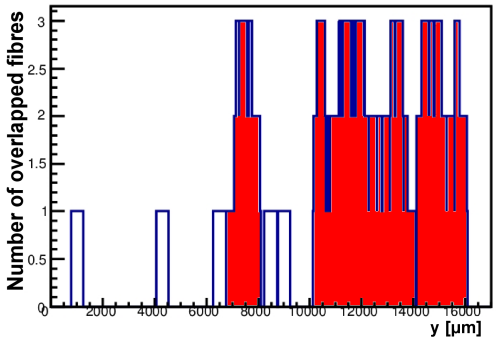

(b) Rejected event due to the distance separating tracks.

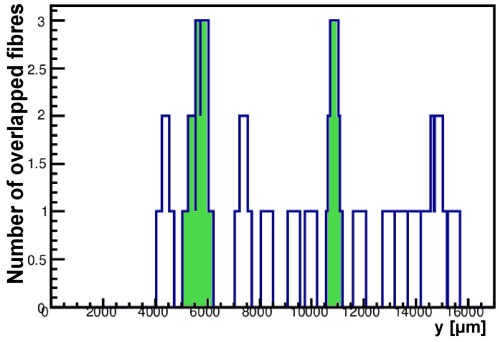

(c) Two tracks reconstruction.

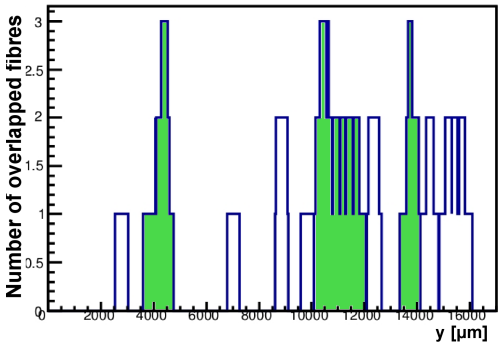

(d) Three tracks reconstruction.

Figure 5.4: Four different examples of multi track algorithm used in the overlap detector event viewer. Horizontal axis refers to the OD reference system. Active fibres are projected over the horizontal axis using their real position and width.

5.1.3 Distance measurement

Overview

The distance of the detector halves can be calculated from the measurement of particles which traverse both ODs:

$$d = \frac{1}{N}\sum_i (y_{u,i} - y_{l,i}) \tag{5.1}$$

with N total number of recorded events, y_u vertical position in the upper detector (corresponds to $D_{up} - d_{up}$ on figure 5.5(b)) and y_l for the lower detector (corresponds to $D_{low} - d_{low}$ on figure 5.5(b)).

Distance measurement requires at least one reconstructed track per OD. Single track algorithm considers both reconstructed tracks refer to the same original particle path. Equation 5.1 is then applied using tracks positions.
In case of multi tracks in the ODs, a good matching between upper and lower tracks is needed.

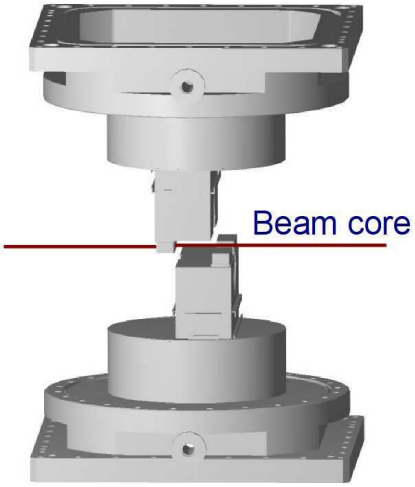

(a) 3D view of the upper and lower detectors, illustrates the concept of the overlap detectors. The red line represents the beam core, which is not intercepted by the ODs. They surround the beam, and intercept beam halo particles.

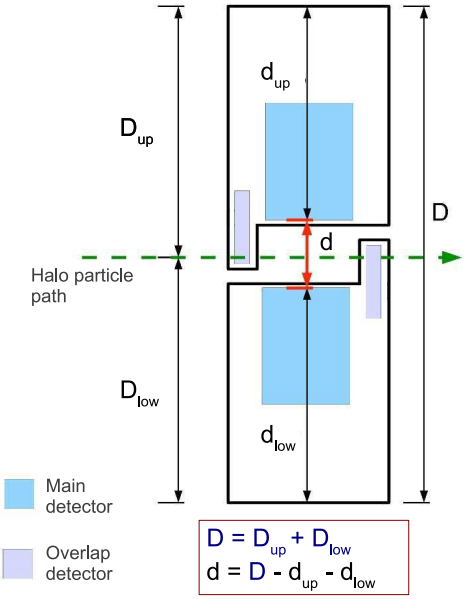

(b) Distance **d** separating upper and lower MD edges, is calculated using the horizontal beam halo path, reconstructed by ODs.

Figure 5.5: Overlap detectors distance measurement strategy (both illustrations from side view).

Let's consider, as example, 2 tracks (A and B) in upper OD, and (A' and B') in the lower one. They can be combined in 2 different ways (AA' and BB' or, AB' and BA'). Only one good arrangement returns the correct matching with the original 2 particles paths.
Finding a good matching tool, is one of the tasks which needs more studies and improvements, and is the next main topic to develop in the OD analysis. One simple way to do such combination, will be to get a preliminary distance measurement using the single track algorithm, then use this distance information in order to avoid bad tracks combinations. Method details will be described later in § 6.6 with distance measurements using multi tracks.

The required measurement precision is obtained by recording a sufficiently large number of tracks and calculating their average in the two ODs. The achievable precision depends on three factors as cited in [57]:

- The intrinsic spatial resolution of the OD
- The statistics of particles detected with the OD
- The alignment uncertainty between the ODs and the detector halves

It turns out that additional factors are missing in this preliminary list such as metrology imperfections and background contribution, which will be developed bellow.

5.1.3.1 Metrology imperfections bias

Metrology suffers from different types of imperfections which induce additional bias to the measurement. Plans are not perfectly staggered by 500/3 μm thus influencing the resolution of the detector, as we will see later. Moreover, fibres gaps and active width differ from fibre to fibre on the same layer, and a slight slope of fibres in the transverse plan was identified and measured. Since the high precision is the main challenge of the OD analysis, all these suspicious points should be considered.
Simulation was called for a precise estimation of the possible bias due to metrology imperfections. Simulation considered different OD metrology, including fibers width, slope and intercept.
In order to constraints only these effects, simulation have to be perfect at all other stages. Fibres are considered 100% efficient, simulated tracks are perfectly longitudinal and follow beam direction, with no shower development or fibre cross talk. Then detectors have to be placed at a certain distance D_{true}, and using the single track algorithm a D_{reco} will be reconstructed.
Perfect detectors metrology gives $D_{true} = D_{reco}$, with an error less than 1 μm (due to rounding errors).
The real metrology was tested to estimate the imperfections bias $B_{imp} = D_{true} - D_{reco}$. Bias B_{imp} differs from station to station, and depends also on the measured distance, as not all fibres imperfections have to be considered, only fibres in use for the distance measurements. For example if upper and lower OD are half overlapped, then bias concerns only the lower half of both ODs, which differs from the full OD overlapped situation.

5.1.3.2 Background

Many background sources have to be considered for OD analysis, and may have the last word on the distance measurement precision. ODs were designed to consider only halo tracks parallel to beam direction. Non-horizontal tracks are considered backgrounds as they return biased distance measurement. Looking back again to figure 5.5(b), deviated tracks make $D \neq D_{up} + D_{low}$, which affect and bias measured distance. This case was not seen during test beam as ODs were directly disposed to the beam, but it was observed during the data taking periods in the LHC tunnel. We will come back on this topic in the next chapter where backgrounds has serious impact on the measurement precision.
Fibres cross talk may also bias the measurement, where fake fibres hit with (or instead of) true ones. As we have only 3 layers compared to 20 layers for the main detector, the OD cross talk have then larger impact. It can happen at fibres level or at the connection between fibres and PMATs.

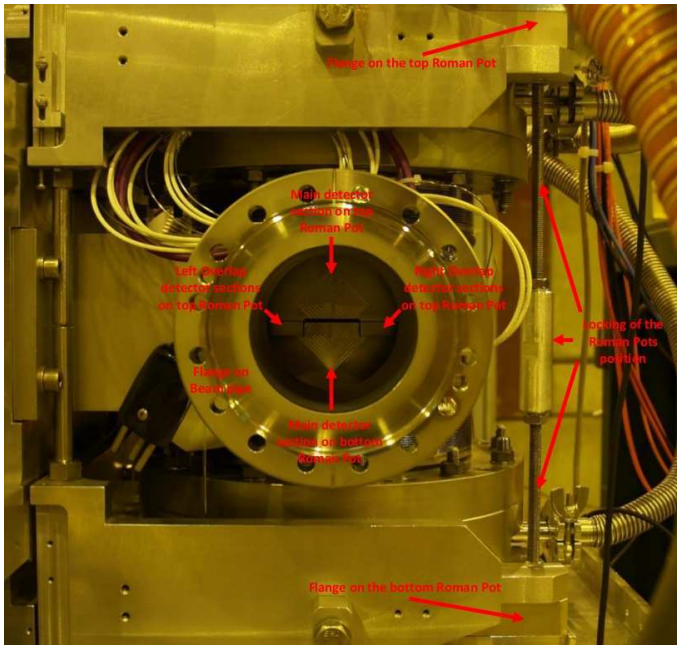

Figure 5.6: ALFA station during test beam. Upper and lower detector went close to 1-2 mm distance.

5.2 Overlap detector calibration during test beam

ALFA team have planned to install all detectors during the LHC shutdown (end of December 2010 and beginning of January 2011). Before, test beam took place at CERN, in September 2010 on H6 beam line. It aimed to prepare, commission and calibrate ALFA stations for the installation. During it, 7 ALFA detectors, forming 3 complete stations[2] were commissioned. Tests cover mechanics, electronics and fibre tracker performance. The tracker detectors was mounted in the Roman Pot structures.

One of the main test beam tasks was the OD performance check. Upper and lower MDs went close to 2 mm. An independent measurement of distance was possible, using OD.

An external high resolution tracking system, or beam telescope called **EUDET** [58], was installed in front of the ALFA station. This independent reference was used, once aligned with the MD, for resolution studies, edges detection, efficiency measurements, dead fibres check, mapping and fibres metrology correction.

As the OD will be used to a precise measurement of the MD position, an absolute check of the OD spacial fibres position with respect to the main detector is then performed. Telescope shows important shift between fibres expected and real positions. This section is about the ALFA-EUDET alignment, fibres metrology correction, result of distance measurement during TB, and OD performance.

[2]One detector was already in the tunnel since since few months, and was therefore not calibrated.

5.2.1 EUDET telescope

EUDET is an initiative that has the aim to provide infrastructure for detector R&D, whose program was closed on 31st December 2010 [58]. Such a device can determine the path of a charged particle for any device under test. The EUDET beam telescope is made of six pixel detectors planes. The telescope trigger is provided by the coincidence of four scintillators that ensure that the particles traveled throughout the whole telescope. The intrinsic resolution of the telescope is $\approx 4.5\,\mu$m for the setup we had.

5.2.2 Alignment and different runs

The alignment of the high precision EUDET telescope with the ALFA MD is a crucial point in the following analysis. As EUDET does not cover the whole ALFA MD and OD space, different runs were performed to scan the overall ALFA active area. Three main runs were considered in this analysis as shown in the figure 5.7, where EUDET covers:

- the central zone of the upper and lower MDs. This run is used to study the MDs edges, dead zone, efficiency of these edges, and also to calculate the distance between the upper and the lower detector. This distance will be compared later with ODs measurements
- the left (resp. right) zone where a part of the MDs is covered and the left (resp. right) upper and lower overlap detectors. The MD covered zone will be used for the alignment between EUDET and ALFA. Using these runs a full fibers metrology correction was performed and summarized in the following subsection

Figure 5.7 shows a schematic representation of the test beam setup EUDET+ALFA where EUDET is represented for simplicity by four layers.
The ALFA station is represented schematically by a blue box (MB0, the upper detector) and a red one (MB1, the lower one). The EUDET reference system is represented by the axis X, Y, Z whereas for MB0 and MB1 by the axis X', Y', Z' and X'', Y'', Z'' respectively. Indexes $A0$, $A1$ and E refer respectively to MB0, MB1 (detectors) and EUDET telescope [59].

Assuming that MB0 is rotated only along the Z-axis in the EUDET reference system by an angle ϕ, and neglecting effect of other rotations, one can write:

$$\begin{pmatrix} X_{A0} \\ Y_{A0} \\ Z_{A0} \end{pmatrix} = \begin{pmatrix} \cos(\phi_{MB0}) & -\sin(\phi_{MB0}) & 0 \\ \sin(\phi_{MB0}) & \cos(\phi_{MB0}) & 0 \\ 0 & 0 & 1 \end{pmatrix} \begin{pmatrix} X'_{A0} - \mathrm{X}_{\mathrm{off0}} \\ Y'_{A0} - \mathrm{Y}_{\mathrm{off0}} \\ Z_E \end{pmatrix}$$

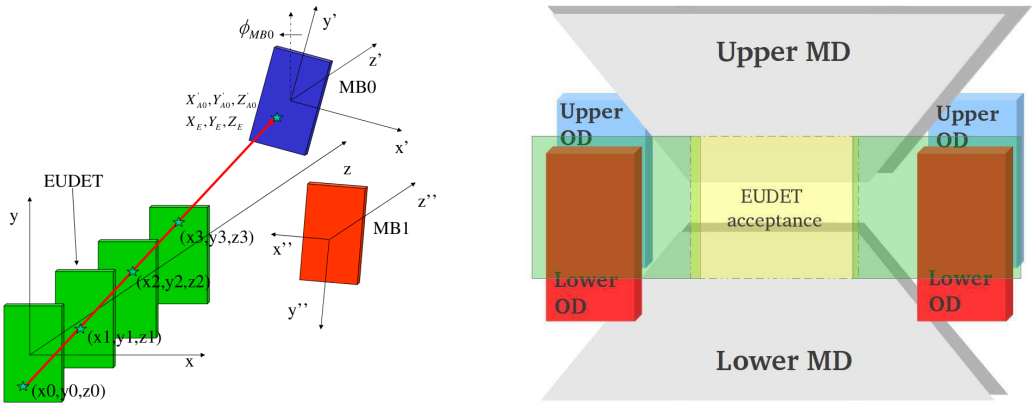

Figure 5.7: Schematic representation of the EUDET/ALFA test beam setup, showing the coordinate system on the left [59] and different EUDET coverages on the right.

Minimizing X_{A0}, Y_{A0}, Z_{A0} to the points measured by EUDET X_E, Y_E, Z_E and using the χ^2 defined in (5.2), it is possible to determine the position offset X_{off0} and Y_{off0}, the rotation angle ϕ_{MB0} and Z_E.

$$\chi^2 = \sum_i \left[\left(\frac{X_{A0} - X_E}{\sigma_x} \right)^2 + \left(\frac{Y_{A0} - Y_E}{\sigma_y} \right)^2 \right] \tag{5.2}$$

One can notice that the errors σ_x and σ_y are expected to be comparable so they can be omitted from the formula above, since they become only normalization factors [45].
Once all parameters are determined, X_{A0}, Y_{A0}, Z_{A0} and X_{A1}, Y_{A1}, Z_{A1}, can be calculated starting from $X'_{A0}, Y'_{A0}, Z'_{A0}$ and $X''_{A1}, Y''_{A1}, Z''_{A1}$.

Some difficulties appear in the determination of ϕ_{MB0} and ϕ_{MB1} for the left and right OD runs, due to limited statistics in the small covered MD part. After many tests and efforts, we decided to use the angle of the central run as reference. Then the procedures of alignment become:

- Start by the central run alignment. Use the χ^2 defined by (5.2) to deduce the alignment parameters (ϕ_{MB0}, X_{off0} and Y_{off0}) for MB0, and repeat the same for MB1;
- Move to the left (resp. right) run, which was taken basically just after the central run, in the same experimental conditions. Fix ϕ_{MB0} and ϕ_{MB1} during the minimization procedure and deduce only the vertical and horizontal offset.

5.2.3 Metrology correction

EUDET telescope is used as a fibres scanner (fibres width is 0.5 mm). The aim is to correct any possible misplacement of the fibres positions (in the *y*-*z* plan) with respect to the ALFA

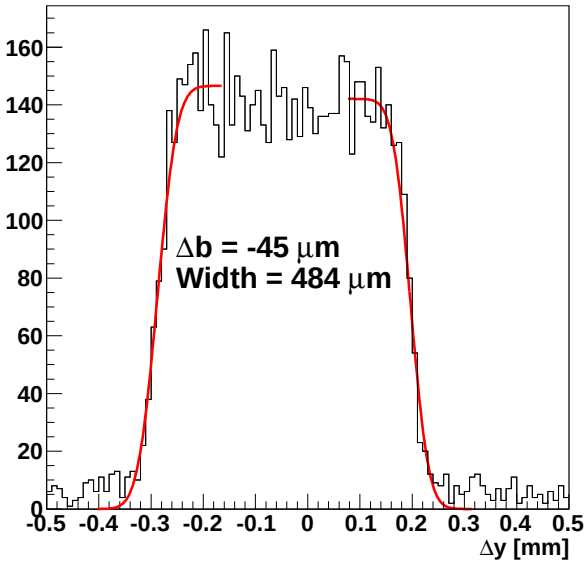

Figure 5.8: Example, given for a typical fibre, of the difference (Δb) between the fibre expected position and the one produced by the EUDET telescope. A large shift of 45 μm have to be compensated. Fibre edges are fitted using $Erf(x)$ function.

coordinate system. Test beam runs provide enough statistics to do this test ($\approx 5 \times 10^5$ events per run).
Since the EUDET alignment is based on the MD system (the MD is the reference system), scanned fibres have shown a large shift between position measured by the telescope and the expected one. An example of one fibre scan is shown in the figure 5.8. Edges are fitted using the **error function** $Erf(x)$. It returns the position of the right and left edges (at the curve midheight between upper and lower limits), afterwards the fibre width and shift are deduced. An example of full layer fit is shown in figure 5.9.

As mentioned in § 5.2.2, EUDET does not fully cover the OD. Twenty fibres out of 30 per layer are covered and calibrated. Uncovered fibres are fixed using the half layer mean value shift. Figure 5.10 shows the correction needed per fibre for a full overlap detector (3 layers). Statistical fit errors are also shown. A small difference between the first and the last 15 fibres of the bottom layer is present. This can be explained by the fact that layers are splitted into two parts as mentioned in § 5.1.1.

5.2.4 Detector resolution and offset

Detector resolution is the main component of the uncertainty on the position measurement. It depends on the metrology and differs from OD to OD. Designed OD with equal shift between layers of 166 μm gives a theoretical resolution of $166\ \mu\text{m}/\sqrt{12} = 48\ \mu$m. Since gaps between

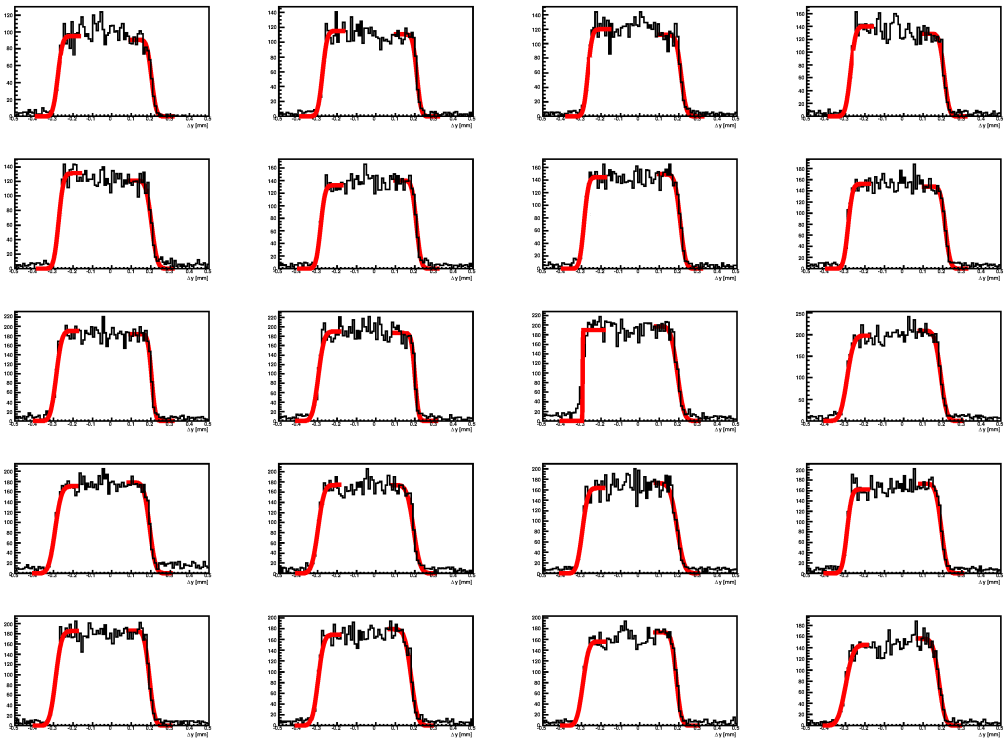

Figure 5.9: Full layer scan. 20 fibres shown in this figure are fully covered by the EUDET telescope. Uncovered fibres are calibrated using the half layer's mean value shift.

fibres exist and the effective width of the fibres is less than 0.5 mm, theoretical resolution is then reduced to 40 μm. This is the best resolution which one can reach with a 3 equally staggered layers detector.
Due to some experimental difficulties, equally staggered layers was unachievable. Resolution varies from 44 to 86 μm. It was estimated by simulation, after the precise calibration of the fibres positions and fibres width measurements. Table 5.1 summarizes resolution for all detectors in both sides. Sides (negative and positive) and tunnel label column refer to the one used in the tunnel after the installation. Resolution was estimated using the standard deviation of the OD reconstructed track from the simulated one:

$$Res = \sqrt{\frac{1}{N}\sum_{i}^{N}(y_{T,i} - y_{A,i})^2} \tag{5.3}$$

y_{sim} corresponds to the vertical position on the EUDET telescope, and y_{rec} is the reconstructed position by the ODs.

Differences between resolution of different detectors can be explained by figures 5.11 and 5.12. Both are illustrations of the real fibres metrology distribution. Colored rectangles show different allowed reconstruction zones, where 3 fibres of 3 layers overlapped. The width of colored rectangles is the result of the layer staggering and is linked to the detector resolution. Large width lead to bad resolution, but as mentioned above, the best resolution can be achieved with equal staggering plans.

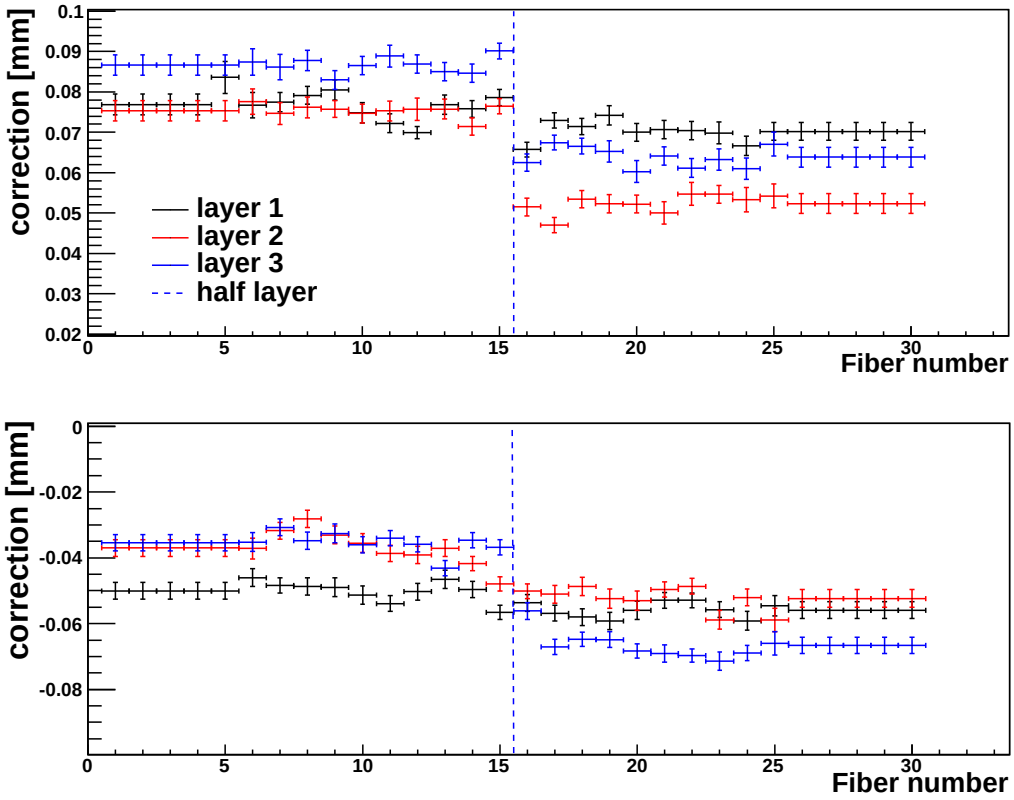

Figure 5.10: Calibration needed for a full ODs (2 different ODs are shown). *x*-axis is the fibre number, *y*-axis is the correction needed, for the three different layers of the OD. One can notice the small calibration difference between first and second layers halves.

Detector layers in figure 5.11, ALFA1 and ALFA3, are better distributed and staggered than ALFA5 and ALFA7 of the figure 5.12 where one can see large differences between rectangles width. Thus, resolution of ALFA1 and ALFA3 is 46 μm, ALFA5 is 71 μm, and ALFA7 is 70 μm.
These resolution values will be used later to estimate statistical errors of the measurements.

Table 5.1: Resolution of the ALFA overlap detectors (in mm) for both sides (negative and positive), estimated from metrology files.

Detector	Positive side	Negative side	Tunnel label
ALFA1	0.046	0.049	B7L1L
ALFA2	0.044	0.047	B7L1U
ALFA3	0.046	0.049	A7L1L
ALFA4	0.073	0.086	B7R1L
ALFA5	0.071	0.081	A7R1U
ALFA6	0.077	0.083	A7R1L
ALFA7	0.070	0.062	B7R1U
ALFA8	0.077	0.073	A7L1U

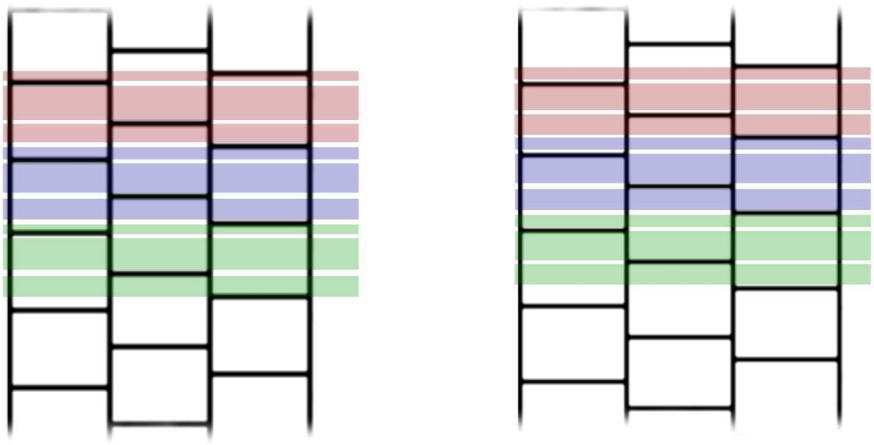

Figure 5.11: Drawing of the real OD metrology for ALFA1 positive OD side (figure on the left) and ALFA3 positive OD side (figure on the right). Colored rectangles indicate different allowed reconstruction zones, where 3 fibres of 3 layers overlapped. Different colors highlight the repetitive OD structure. Vertical rectangles widths give an idea about layer staggering.

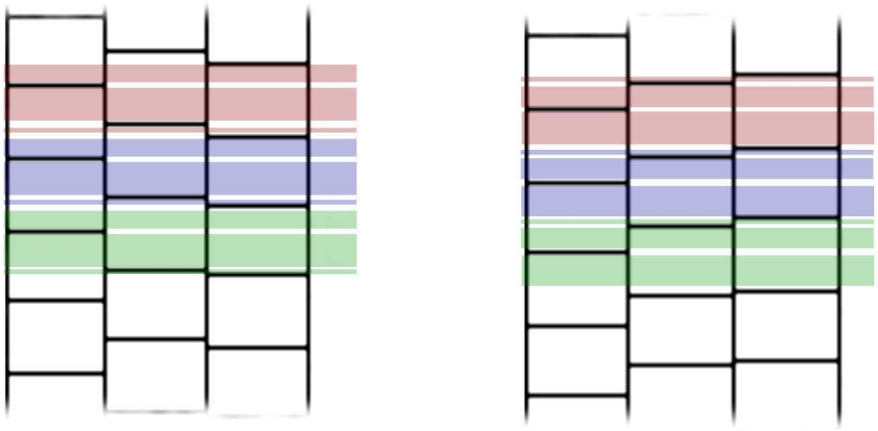

Figure 5.12: Drawing of the real OD metrology for ALFA5 positive OD side (figure on the left) and ALFA7 positive OD side (figure on the right). Colored rectangles indicate different allowed reconstruction zones, where 3 fibres of 3 layers overlapped. Different colors highlight the repetitive OD structure. Vertical rectangles widths give an idea about layer staggering.

5.2.5 Tracks selection cuts

In addition of the single track reconstruction constraints, a layer multiplicity cut was added to reduce any possible contamination by showers or cross talk. It puts some limits on the number of hits per layers. For example, one can ask for 1 hit per layer, in order to have one clean track. Increase statistical errors can be the result of hard cuts. This factor should be taken into account when choosing the cuts.
During test beam, the selection requested 1 hit per any of the 3 layers. It keeps a good statistics

for the analysis, and cut down undesirable events.

5.2.6 Systematics and the 10 μm challenge

Distance measured during test beam used the single track algorithm for reconstruction. Collected data was enough to neglect the statistical error, and to focus on systematical error. The remaining question was the possibility to reach a precision in the order of 10 μm.

Studies achieved during test beam for calibration and performance can be used to estimate systematic errors of the OD measurements. Since all sources are expected uncorrelated, final error is a quadratic sum of all possible source of uncertainty and systematics, such as fibres position, detector resolution, and alignment with respect to the MD. Noticing that bias due to metrology imperfections will not be added to systematics and will be used to unfold final distance result instead.

The main distance measurement error sources is listed bellow:

- Error on the fibres position is the result of the EUDET-ALFA alignment precision, and fibres metrology correction methods:
  - Alignment error (σ_{Al}) result of the minimization of the χ^2 described in §5.2.2, and is better than 4 μm
  - Error of the fibres metrology correction method (σ_{fib}), depends on the fit of each fibre. It varies between 3 μm for checked fibres and 5 μm for fibres outside EUDET acceptance
- Edges position errors depend on detector (σ_{ed}) and were precisely measured by EUDET [59]. Statistical error on the edge fit are less than 2 μm
- Contribution of the detector resolution in the final error, depend on the statistics of the run:

$$\sigma_{stat}^2 = \frac{\sigma_u^2 + \sigma_l^2}{N} \tag{5.4}$$

  where σ_{stat} is the statistical error, σ_u (resp. σ_l) the upper (resp. lower) detector resolution, and N the total number of collected events. For example, with a resolution of 60 μm per OD, the number of events needed to reduce σ_{stat} to 1 μm is 7200.

Considering that resolution contribution in the final error falls with high statistics collected during test beam. Table 5.2 summarizes different systematic uncertainty sources. Last column in the table shows final systematic errors on distance measurements, combining both sides of the stations. Systematics for all detectors stand bellow 10 μm, as shown in the table.

Table 5.2: Systematic error per station, where σ_{Al} refers to EUDET-ALFA alignment errors, σ_{fib} is the fibres metrology precision, and σ_{ed} is the detector edge precision. The " — " notation is used to separate stations sides.

Station	σ_{Al} [μm]	σ_{fib} [μm]	σ_{ed} [μm]	Systematics [μm]
ALFA74	4 — 4	3 — 5	1 — 1	8
ALFA38	4 — 4	4 — 4	1 — 2	8
ALFA56	4 — 4	5 — 5	1 — 1	9

5.2.7 Test beam distance measurement results

In order to check the consistency of OD calibrations and systematic errors estimations, one can use EUDET direct distance measurement of the upper and lower MD edges. Since the EUDET measurements are totaly independent from any possible bias caused by the detector or the EUDET-ALFA alignment, it can be used to judge OD measurements precision.
EUDET distance measurement was an independent dedicated analysis, described in [59]. In the following we will summarize it and highlight some points of interest for our study.
In addition of the direct distance measurement, EUDET was used to check the position of triggers in front of MD fibres. For this reason, 2 trigger combinations were used:

- EUDET trigger and MD trigger, to a precise determination of the MD triggers edges. Looking to figure 5.13, one can distinguish the upper and lower MD triggers edges. This will be used later in the analysis for some efficiency studies. The small bumps shown between edges represent the position of the RP edges, where particles hit the RP bottom plate and produce a shower that triggers ALFA.
- EUDET trigger and MD trigger and fibre hits (or trigged fibres), this configuration gives a precise measurement of the fibres edges position. The overlap distance studies are then compared to these measurements.

To increase precision and to take into account any possible rotation or misalignment of the detector edges, the MD is divided into 5 slices along the x-axis. Each slice is then projected on the y-axis which gives a distribution similar to figure 5.13.
Results of EUDET direct measurement and OD measurement are summed up in the figure 5.14 for ALFA74 (ALFA7 in the upper side and ALFA4 in the lower, forming a station during test beam), and ALFA38 stations. ALF56 is shown in figure 5.14. The red points located at $\pm$ 22 mm represent the OD distance measurement taking into account all corrections and calibrations. Error bars correspond to the systematics described in table 5.2. The 5 black points and fit correspond to the EUDET measurement where one can extrapolate EUDET fit to $x = \pm 22$ mm, and estimate distance at ODs. The blue dotted area represents the error of the total systematic errors of EUDET measurements [59]. We notice that blue points on the plot refer to the OD measurement before calibration of fibres position. One can see the impact of

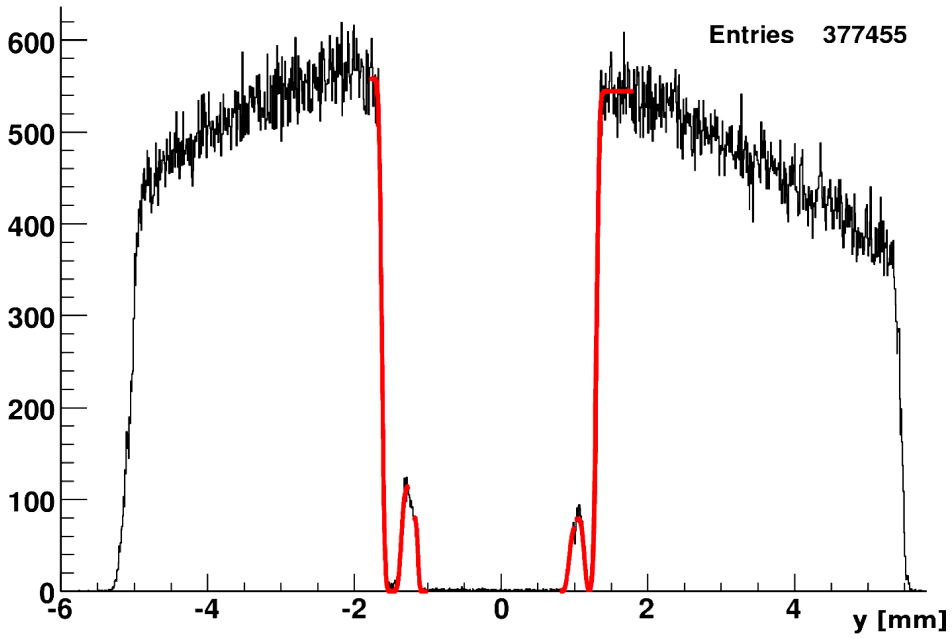

Figure 5.13: Projection of EUDET tracks in the vertical plane (*y*-plan) using the combination of EUDET trigger + ALFA trigger. One can distinguish the upper and lower MD triggers edges. The small bumps between edges represents showers produced on the RP edges. Particles hit the RP bottom plate and produce a shower that triggers ALFA [59].

the calibration, which drive the OD points close to those measured by EUDET.
All plots show a compatibility between OD measurements and the extrapolation of EUDET measurements, with the corresponding error bars. Another systematic errors may appear later in the data taking case due to backgrounds or other effects. For the test beam we focused on detector and calibration systematics.

5.3 Conclusion

At this point, I want to highlight the importance of this test beam phase in the better understanding of the overlap detector performance, and the precision that distance measurement can reach. It was the first experimental test of the ODs. The ultimate precision on the distance measurement has direct impact on the luminosity and total cross section measurement precision. Therefore, figure 5.14 shows the importance of the dedicated calibration achieved. Distance measured before it (in blue) looks totaly biased in comparison with EUDET direct measurements.
Under the beam test condition (no showers, horizontal tracks, high statistics) results have shown that the 10 μm challenge can be achieved with actual detectors performance. What will be the situation in the tunnel? How the background will affect the measurement? What

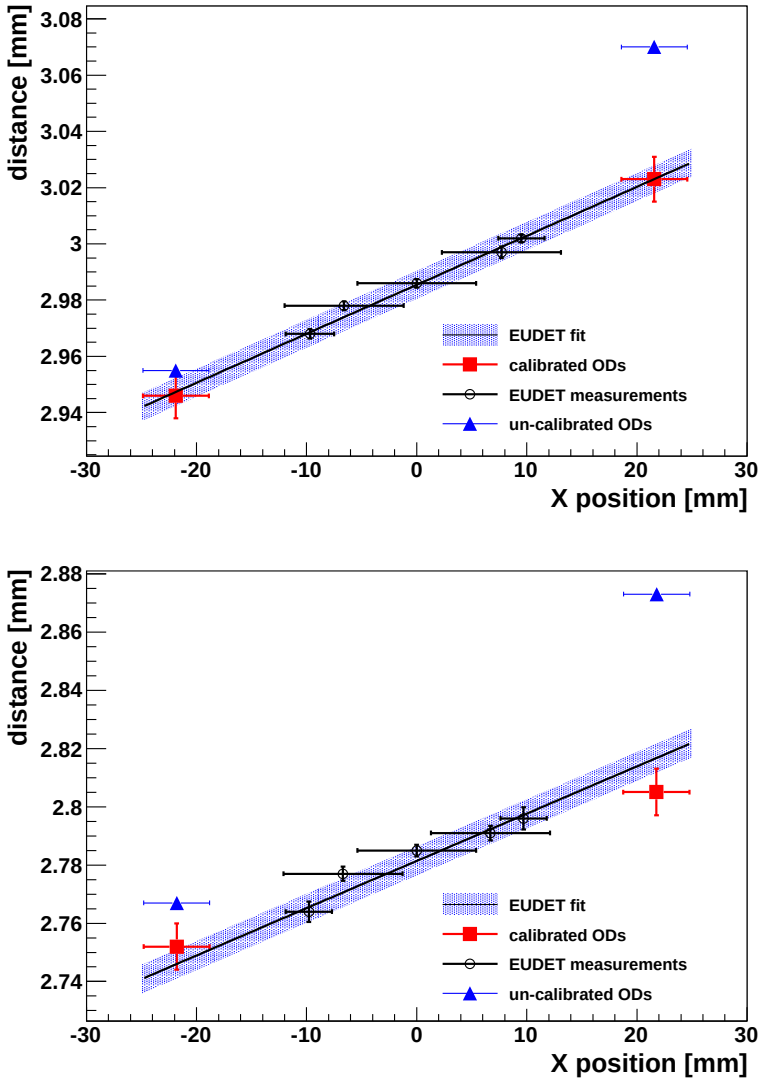

Figure 5.14: Comparison between OD distance measurements (red points) and EUDET (black fit) for the ALFA74 (top) and ALFA38 (bottom) stations.

precision will we achieve? These questions will be the main topic of next chapter...

From the personal side, test beam was happening at my arrival, so I had the chance to see and check different ALFA parts (roman pots, trackers, electronics, ...) and setups. Afterwards, as test beam analysis was ongoing, I become more familiar with the detector, and the ATLAS/ALFA framework. OD calibration (mainly metrology correction) requested a good knowledge of detector performance, EUDET precision and EUDET-ALFA alignment. The direct measurement of the distance between upper and lower MD edges was an important task too, it gave us the ability to compare the result of the calibration, by comparing this direct measurement to the one achieved by the OD after calibration. By this comparison we discovered that alignment procedure has to be modified as mentioned in § 5.2.2 section. The

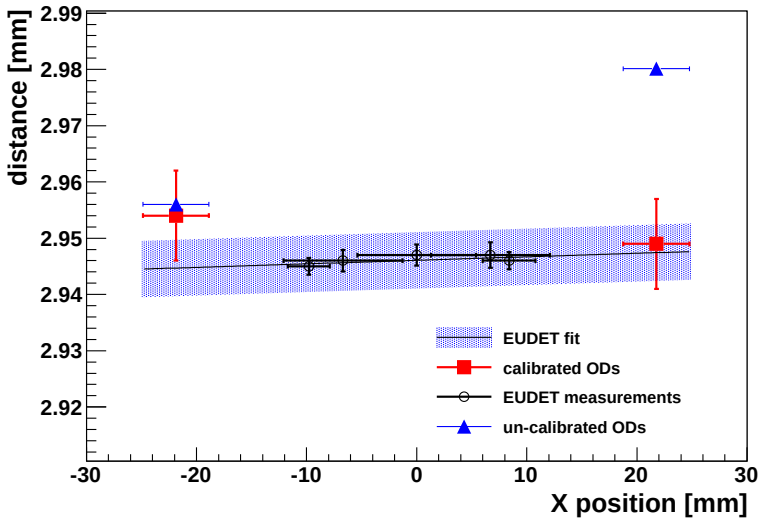

Figure 5.15: Comparison between OD distance measurements (red points) and EUDET (black fit) for the ALFA56 station.

variety of treated topics during test beam gave me a solid experience with the experimental instrumentation.

Chapter 6

Overlap detector data analysis

This chapter is about overlap detector status and distance measurement analysis for the first ATLAS/ALFA data taking (October 2011). Methods and analysis procedures described in this chapter can be developed and used for future runs.
The chapter begins by a description of the run conditions, followed by a summary about detectors performance, and the quality of collected data. This includes study of the multiplicity, fibres efficiencies, and background contamination.
The § 7.2 describes the OD simulation, which was developed and used to understand and investigate distance measurement systematics. It is followed by a distance measurement analysis section, where we show the analysis algorithm, selection cuts, systematics and results.
At the end of this chapter, we come back to the possibility to improve results, using multi tracks algorithm, introduced in § 5.1.2.2.

6.1 Run condition

Special runs were dedicated for OD data taking, using (**OR**) trigger logic. The OR was chosen to collect the maximum amount of data. Upper and lower ODs coincidences will be studied and combined later in analysis. This was possible due to the low background rate of LHC.
Table 6.1 summarizes the amount of collected data for different runs, the corresponding triggers logic, and a preliminary distance measurement as function of beam vertical size[1]. In this table we can distinguish three triggers logic:

- OD(OR): records events if any OD trigger fires
- OD(OR) + MD(OR): stores events if any of OD or MD trigger fire

[1] measured by the beam scraping technique as explained in § 7.3.1

- OD(OR) + MD(VETO): requires in addition of OD trigger hit, a no-fired MD trigger.

Table 6.1: Runs during 90 m data taking. Runs numbers, total number of collected events, trigger logic are reported, with the vertical distance separating ALFA MD with the center of the beam. It was estimated during the scraping test.

Run number	Events ($\times 10^3$)	Triggers	Scraping distance
191323	577	OD(OR) + MD(VETO)	8.0 σ_y
191366	10000	MD(OR) + OD(OR)	6.5 σ_y
191367	1240	OD(OR)	6.5 σ_y
191373	73000	ATLAS COMB	6.5 σ_y
191377	1550	OD(OR)	6.5 σ_y
191382	686	OD(OR)	6.5 σ_y
191383	1800	OD(OR)	6.5 σ_y
191388	7000	MD(OR) + OD(OR)	6.2 σ_y

Large data collection started with run 191366. A stable beam was established by the LHC team with the $\beta^* = 90$ m optics condition. Run 191367 was the first run with only OD(OR) triggers logic. As we decided to collect data at 6.5 σ_y, the run was dedicated for distance measurement analysis using OD. Run 191373, was a combination of ATLAS sub-detectors systems including ALFA, in order to make a physics measurement.
Other runs quoted in table 6.1 were with the same triggers logic. We notice that during run 191382, TOTEM detectors moved to 5.5 σ_y which can probably affect the beam halo. And finally, run 191388 was recorded with a slight change in the ALFA position (6.2 σ_y). Analysis presented in this chapter concerns runs at 6.5 σ_y, since the physics data were taking at this distance.

Parallel to point focusing optics stretch the beam in the vertical direction. Referring to the 90 m table 7.1, σ_x at RP was ≈ 0.374 mm. It means that OD vertical edge was at $\approx 50\ \sigma_x$ from the beam, and ODs are immersed in the beam halo, where it's hard to predict or simulate a clear model for particles distribution and motion. The recording rate was totally unpredictable too. Figure 6.1 illustrates position of the ALFA stations with respect to the LHC sectors or sides around ATLAS IP, ALFA stations names, recorded trigger rates, and trigger combinations rates. A detailed description of this figure can be found in the figure caption. Trigger rates correspond to run 191367, and were normalized to the total rate.
The difference in number of collected events between outer (**B7**) and inner (**A7**) stations was remarkable, and will be studied in the following §. Low rate between upper and lower coincidence for inner detector was observed. About 40 k trigger coincidences were recorded in ≈ 52 minutes with an occupancy of ≈ 13 Hz.

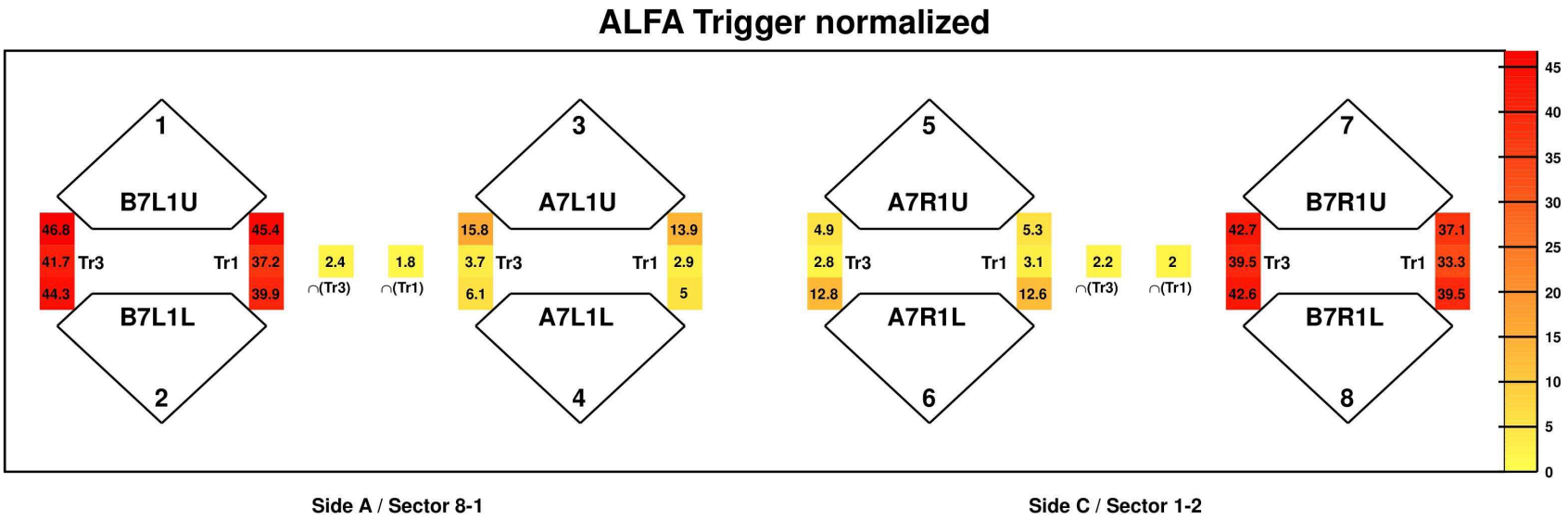

Figure 6.1: Normalized triggers rates for MD and OD, in all stations during the OD run 191367. Diamond geometry is a drawing of the main detector with its corresponding names. **B7** stands for outer or far stations from the IP, **A7** for inner or near stations, **L1** for left side with respect to the IP, **R1** for right side, **U** for upper, and **L** for lower. Each detector has 2 OD trigger (**Tr1** for negative side and **Tr3** for positive one). Numbers shown on the OD trigger is the normalized number of trigger bits with respect of the total number of event given in table 6.1, with a color scale between yellow and red. Numbers in between are the coincidences between upper and lower ODs. ∩(Tr1) and ∩(Tr3) are the coincidence between same side triggers of inner and outer stations. Side A and C distinguish both sides of the IP.

Evolution of the triggers rates with respect to the run time, are shown in figure 6.2 for a typical run. The rates slightly decreased about 10% between the beginning and the end of the run. Rate fluctuations were recorded by all stations in the same time slot. The large difference between B7L1 and A7L1 rate is shown again in this plots.

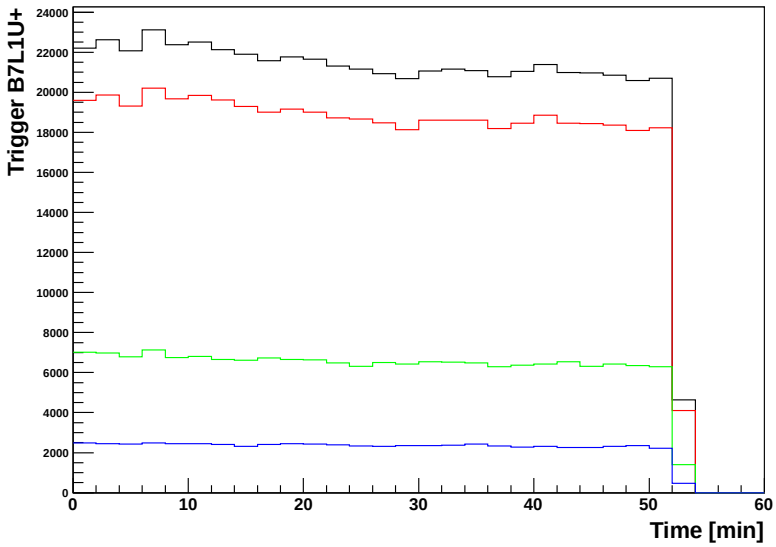

Figure 6.2: Triggers rates with a bins of 2 minutes for different OD triggers. B7L1U+ in black, B7L1L+ in red, A7L1U+ in green and A7L1L+ in blue.

6.2 Detector performance

6.2.1 Triggers

Figure 6.3 shows different efficiency studies in different colors for all overlap detectors during run 191367. Black dashed line represents the detection efficiency, or the number of cases where at least 2 fibres hit with a fired OD trigger, divided by the total number of triggers. Reconstruction efficiency (in red) represents the number of cases where at least one track is reconstructed, divided by total number of trigger. This depends on data quality and reconstruction algorithm, and it is not an indication of tracks quality. Reconstructed tracks in outer stations come mainly from the multi track algorithm.
In green (resp. dashed blue) the number of reconstructed tracks (resp. recorded activity - at least 4 hits) without fired trigger over the total number of tracks. For inner stations, 25 to 30% of tracks were reconstructed without recording fired trigger of the corresponding station (other triggers fire which allow the recording of the event). If we avoid any inefficiency prob-

lem, these cases can be explained by the fact that OD triggers cover only a limited part of the fibers. Back to figure 5.1(a) one can distinguish between the blue rectangle (OD active area covered by trigger), and the fibres connection (blue curved line). This uncovered part of the fibre can be exposed to the beam halo track, and produce a signal without a trigger hit. Reconstructed tracks without a trigger hits are considered (in most of case) as background, ans should be avoided.

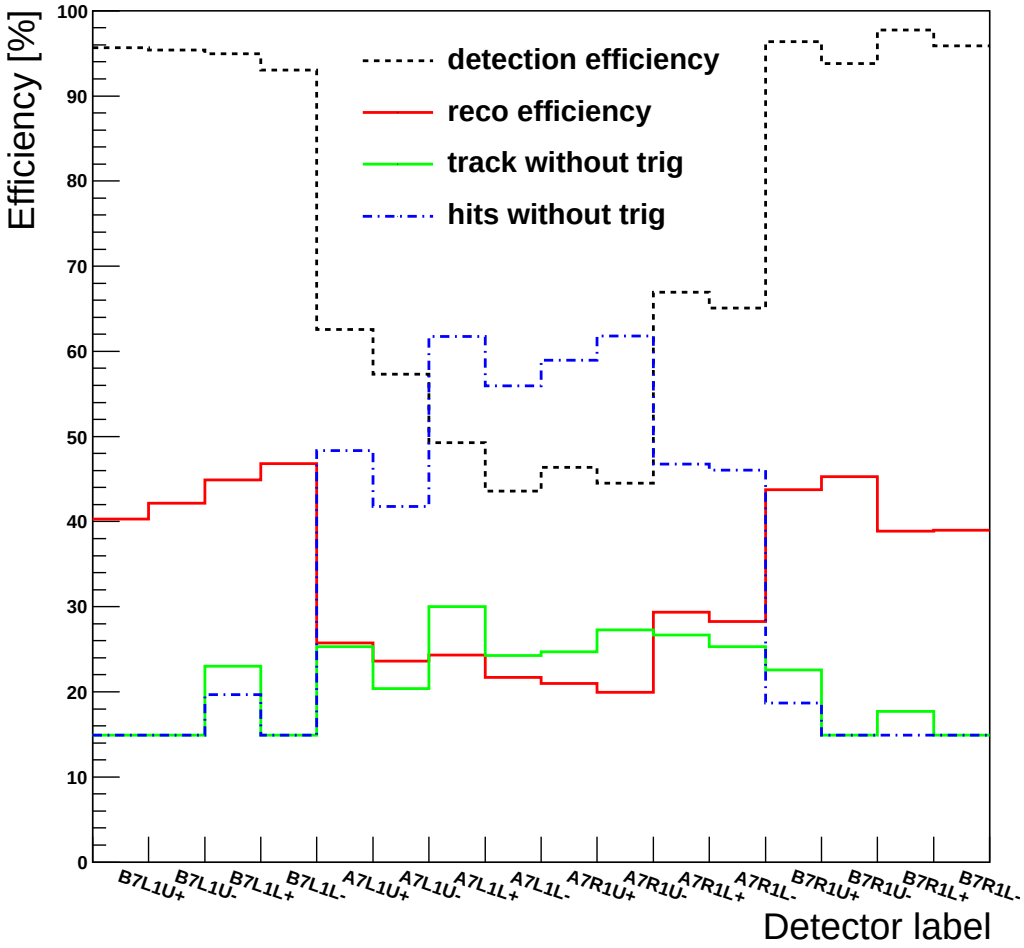

Figure 6.3: Performance of the OD trigger during the run 191367.

6.2.2 Relative efficiency

Fibres efficiencies plots reflect fibres performance during data taking. High or low efficiencies may be the result of electronic high voltage problem, dead channel, or any other reasons. Single fibre activity (or hits) will be compared to the total detector mean activity. Results are shown in figures 6.4 and 6.5 (after normalization with respect to layer activity). Figures 6.4

show the outer station in set of 4 ODs. The 8 ODs of the 2 outer stations B7L1 and B7R1 are

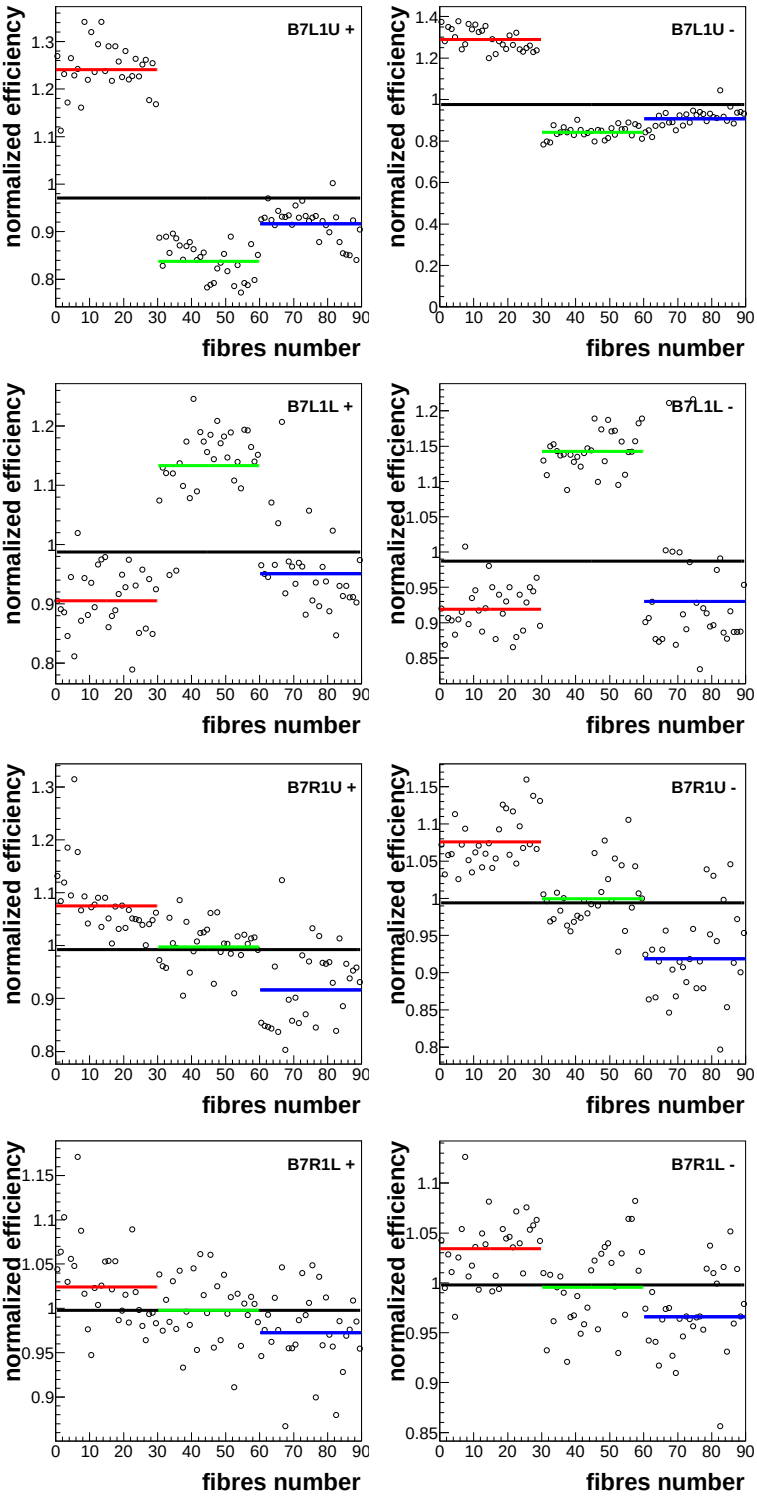

Figure 6.4: Relative efficiency measurements for outer stations. Each plot represents an OD, names are reported in the upper corner. + and - mean the negative and positive OD sides. Fibres numbers from 0 to 30 (resp. 30 to 60 and 60 to 90) correspond to layer 1 (resp. 2 and 3). Colored lines represent the fit of different layers distributions. Black line is an horizontal linear fit of the distribution of all fibres.

shown in 6.4 where one can notice:

- high activity of the layer 1 in both negative and positive side of B7L1U station. About 30% of difference among layer 1 and the 2 others. This is not the result of high layer efficiency, it's probably caused by electronic saturation, where all 30 channels of the layer illuminate. This hypothesis will be confirmed later by multiplicity studies
- idem for layer 2 in the B7L1L OD
- 1 dead channel in the B7L1U negative side.

Apart from few fibres, fluctuations around layers mean values are $\approx 10\%$, which have no serious consequences on the distance measurement. The 8 ODs of the 2 inner stations A7L1 and A7R1 are shown in 6.5:

- a total of 3 low efficient fibres in the A7L1L
- 1 high active fibre in A7L1U+
- A noticeable large spread around layers mean values for inner stations

Fibres efficiency can directly affect distance measurement studies. Estimation of that bias can only be made by simulations. It will be shown later in § 7.2 that this effect is negligible, and estimated to be less than 1 μm on the final distance measurement.

6.3 Data quality

6.3.1 Multiplicity

The multiplicity is defined as the number of hits per layer for a recorded event. Multiplicity distribution gives the first impression about the run quality. Events with multiplicity larger than 15, indicate that the detector was exposed to showers (in particularly seen in outer stations). High multiplicity cases have a direct impact on distance measurement. Track identifications become harder as the reconstruction algorithm falls computing these cases and may induce background to the distance measurements. In the other hand, low multiplicity events (less than 5) result of the detection of single protons, and can be easily reconstructed.
Comparison of multiplicity plot show large difference between stations. Figure 6.6 shows the multiplicity distribution for different inner ODs stations during the run 191367. This is the raw multiplicity distribution where the only requirement to fill these histograms is a fired trigger of corresponding OD. The number of hits per layer varies from 0 (no hits at all) to 30 (all fibers are fired).
For inner stations, low multiplicity (1 to 10) cases dominate other cases. It means that no

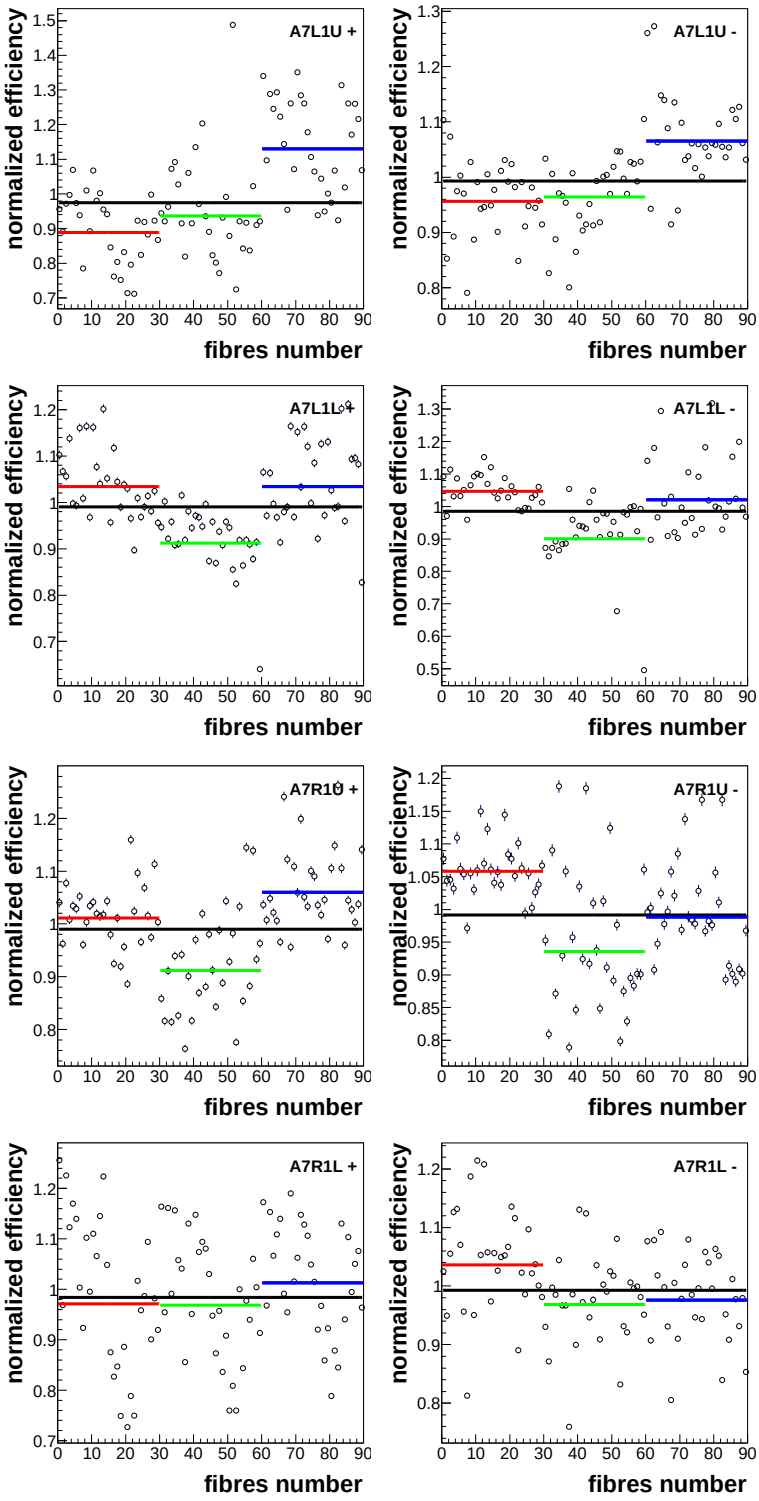

Figure 6.5: Relative efficiency measurements for inner stations. Each plot represents an OD, names are reported in the upper corner. + and - mean the negative and positive OD sides. Fibres numbers from 0 to 30 (resp. 30 to 60 and 60 to 90) correspond to layer 1 (resp. 2 and 3). Colored lines represent the fit of different layers distributions. Black line is an horizontal linear fit of the distribution of all fibres.

large shower events were detected. In addition, comparison between layers multiplicity shows consistency for all inner OD, which indicate a coherent detectors performances.

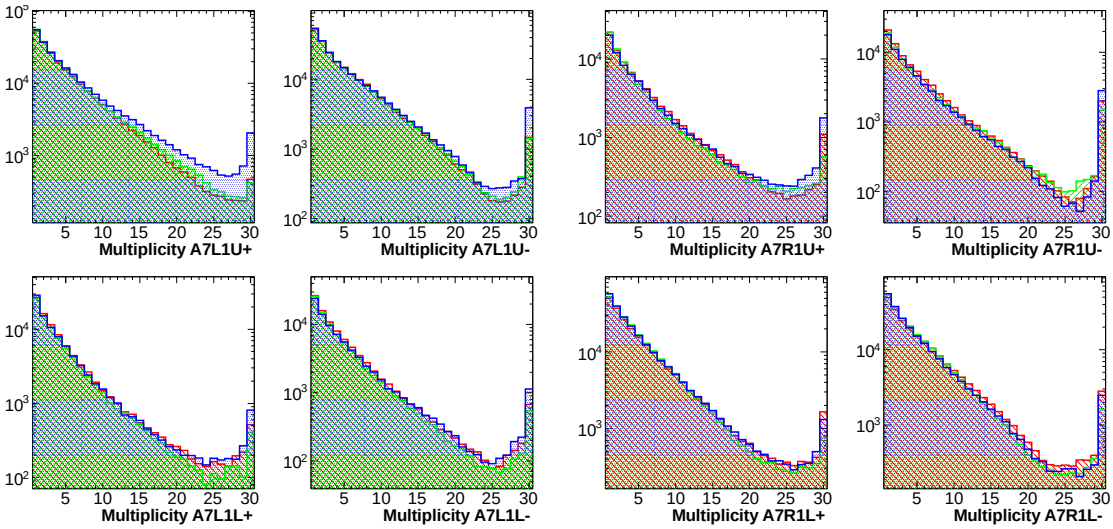

Figure 6.6: Multiplicity distributions for inner stations. Horizontal axis represents the number of hits per layer which vary from 0 (no hits at all) to 30 (all fibers are fired). The 3 colored curves represent the 3 layers of the OD. Red for layer 1, green for layer 2, and blue for layer 3. The vertical axis represent the total number of events during the run, for a given multiplicity. Vertical axis is drawn with logarithmic scale. Stations names label are written on the horizontal axis.

Outer stations show different behavior as shown in figure 6.7, with a large amount of recorded events with medium (10 to 20) and high (20 to 30) multiplicity. It means that outer stations suffer of showers, and electronics saturation.

Some layers show strange behavior, like layer 1 in both sides (positive and negative) of

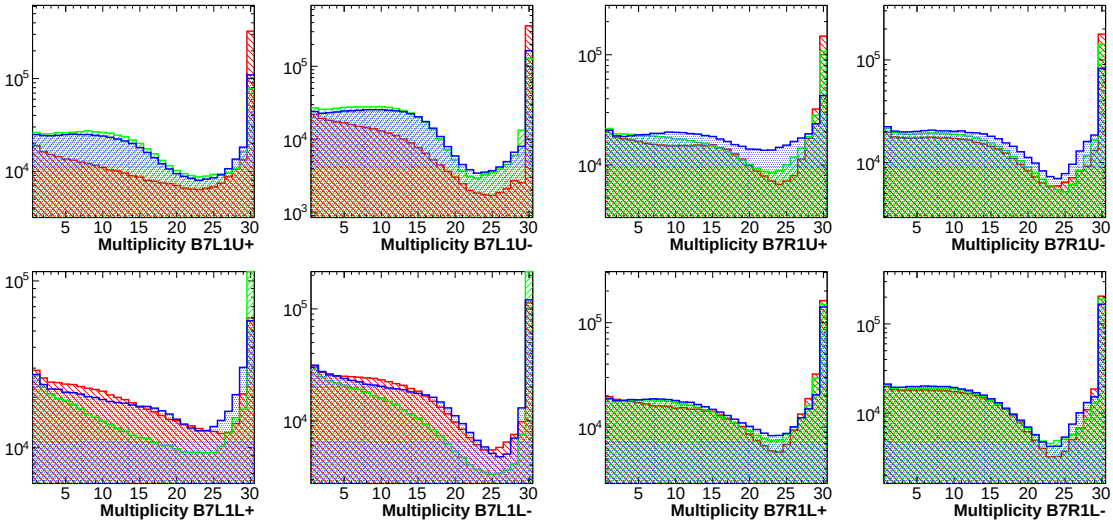

Figure 6.7: Multiplicity distributions for outer stations. Horizontal axis represents the number of hits per layer which vary from 0 (no hits at all) to 30 (all fibers are fired). The 3 colored curves represent the 3 layers of the OD. Stations names label are written on the horizontal axis.

B7L1U, and layer 2 in both sides of B7L1L. They show more electronic saturation (multi-

plicity > 25) and less detection efficiency compared to the other layer along the multiplicity distribution.
Taking into account that inner station are installed 4 m in front of outer one, with respect to the beam direction, one can conclude that large amount of shower events seen in outer stations, may be generated by interaction between beam particles and inner stations. To validate this supposition, inner-outer correlation have to be checked, as shown next.

Figure 6.8 describes the correlation between upper and lower OD mean multiplicity (mean of the 3 layers) of all stations sides. One can see a similar behavior in the distribution spread of the A7L1 and A7R1 plots. In the L1 side, lower OD faces upper one. Halo particles hit the lower OD first, where showers may be developed. These showers seems to be detected in the upper OD. The 2 corresponding plots show that multiplicity correlation is shifted to higher values in the horizontal axis, which correspond to the upper detector (A7L1U both sides + or -). It means that multiplicity seen in the upper detector is slightly higher than lower one, for the same event. In other words, more fibers were touched in upper OD than lower OD, and this is a clear shower signature. In the R1 side we have the opposite situation. Upper OD face lower one. An inverse effect is seen in the 2 corresponding plots (A7R1U versus A7R1L for + or - sides), where the multiplicity is higher in the lower OD.
Eventually, high multiplicity events show no clear correlation in both L1 and R1 sides for inner stations. This can be interpreted by the lack of showers activities, particularly in front of inner stations. Moreover, high multiplicity cases are not correlated, and may be the result of electronic saturation or other biases, of different detectors independently.

Outer stations plot of figure 6.8 are totally dominated by correlated high multiplicity events, in both R1 and L1 sides of IP. It means that halo contains significant particles showers in front of outer station, which hit both upper and lower stations at the same time. No-correlated high multiplicity events exist too, but less pronounced, which leave the door open for the electronic saturation possibility. More investigations were done to understand the shower development state, between inner and outer stations. Other correlation plots are shown in figure 6.9 where inner OD multiplicity is shown as function of outer OD multiplicity, for all stations sides, and IP sides. Distributions show that low multiplicity events seen in inner station are sometimes associated with higher multiplicity in the outer stations, for all cases. This is a signature of showers initiated in inner stations.

Concluding, multiplicity variable is an important ingredient for event selection cut, in order to improve distance measurements. Cuts have to be chosen in a way to reduce the systematic effect of high multiplicity events and keep enough statistics for the measurement. This will be discussed later in the event selection cuts §.

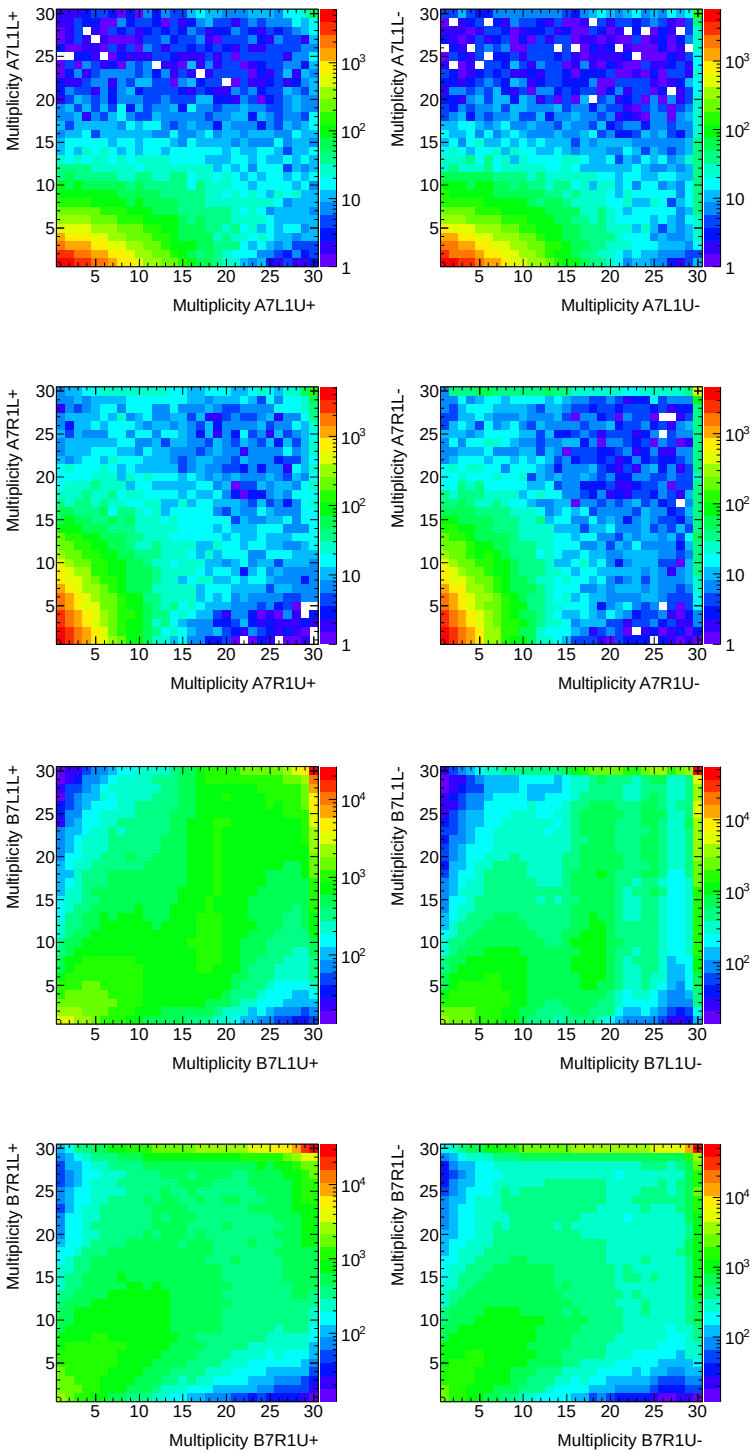

Figure 6.8: Correlation between the lower OD mean multiplicity and upper one, for inner (4 top plots) and outer (4 bottom plots) stations.

6.3.2 Backgrounds contamination

The OD distance measurement is based on the following scenario:
one considers 2 overlap detectors for upper and lower station, in front of each other. A halo

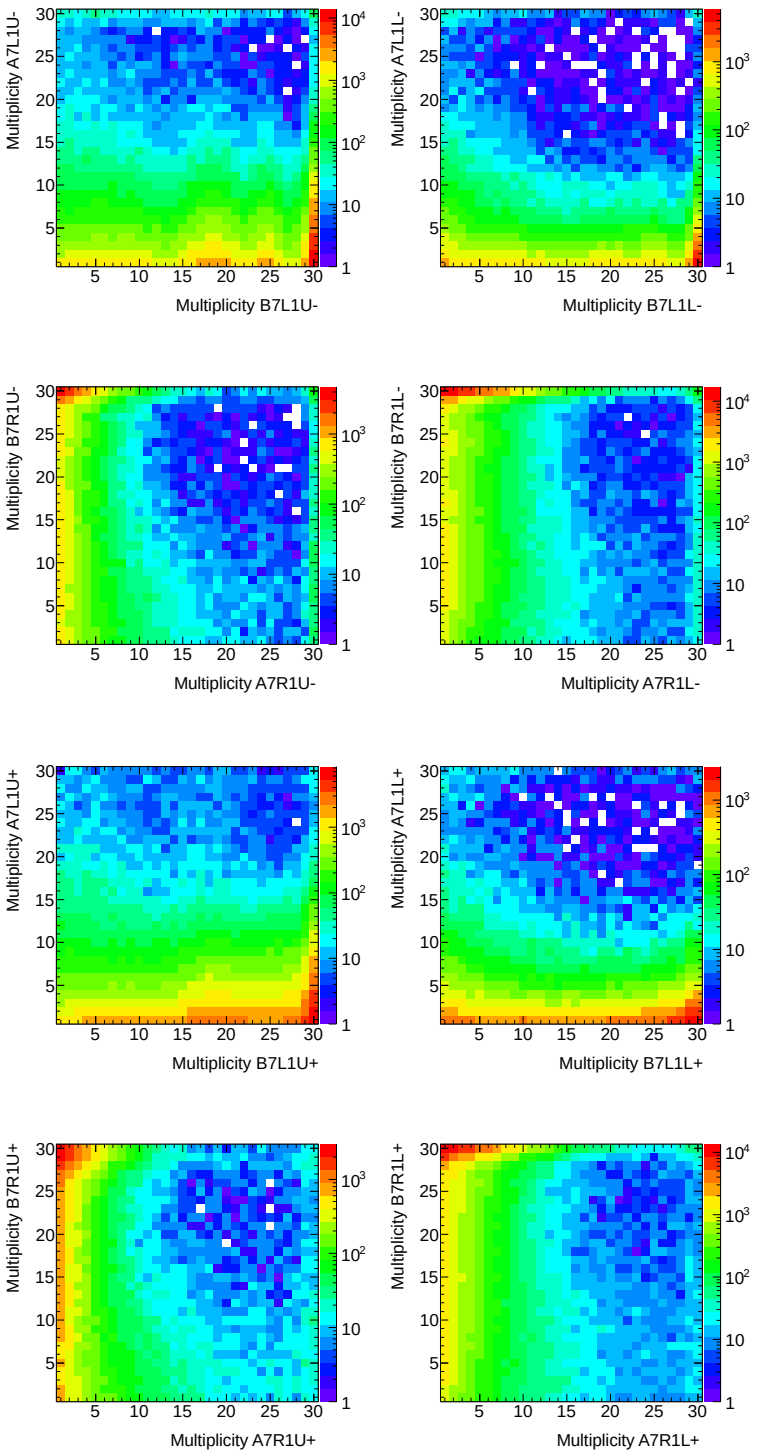

Figure 6.9: Correlation between the OD mean multiplicity of inner and outer stations on the same side. Negative OD side on the left side (4 plots) and positive side on the right (the other 4 plots).

particle traveling in the longitudinal plan, fires the first OD trigger, hits fibers of different layers, goes through second OD, fires trigger and illuminate other fibres. Reconstructed tracks in both detectors are supposed to be the path of the same particle. Consequently, recorded events in 2 different ODs of the same ALFA station and side (i.e. B7L1U+ and B7L1L+), are

supposed to be fully correlated.
Under this circumstances, one can combine both measured vertical positions, using equation 5.1 to calculate distance in an analytic way.
In order to visualize the distance distribution, an histogram was proposed. It will be filled by events measured distance (distance calculation is shown in figure 5.5(b)), with an axis range between 0 and 20 mm.
Distance distribution of run 191367 in figure 6.10 shows peak around a value ($\approx$ 12 mm) with large tail. The peak represents what we call **signal**, or the combination of correlated tracks of the same initial proton path. Large spread around indicate other bad track combinations, which results in a **background** tail seen on the distributions.
Spikes seen in figure 6.10, come from the limited detector resolution and the histogram binning choice. In other words, this is due to the number of layer used for this detector. Increasing the layers number gives a continuous distribution.
Backgrounds are mainly the result of :

- tracks with a non negligible transversal momentum (p_y) introduced in 5.1.3.2. They were not seen during test beam, as ODs were targeted by orthogonal particles. Once submerged in the beam halo, ODs were exposed to random direction particle tracks.
- combination of 2 uncorrelated tracks (events which do not correspond to the same path). They may be generated by showers, cross talk, fibres inefficiencies or simply 2 different particles hitting the un-overlapped part of ODs and will be reconstructed as one event.

Selection cut will be introduced later to reduce background contamination. Also, distance measurement systematics (due to the background) will be studied using simulation.

6.4 Simulation

6.4.0.1 Needs

A simulation was developed taking into account OD metrology, geometry, and the possibility to have non horizontal tracks or uncorrelated events. Comparison between true simulated distance and reconstructed distance (using real detector metrology and geometry) gives the possibility to estimate contribution of different bias sources, such as metrology imperfections, background, and showers. Simulation aims to:

- understand the contribution of different measurement biases
- test the iteration algorithm[2] performance and stability

[2]Iteration algorithm, introduced in § 6.5.1, will be used to study the distance distribution and to estimate

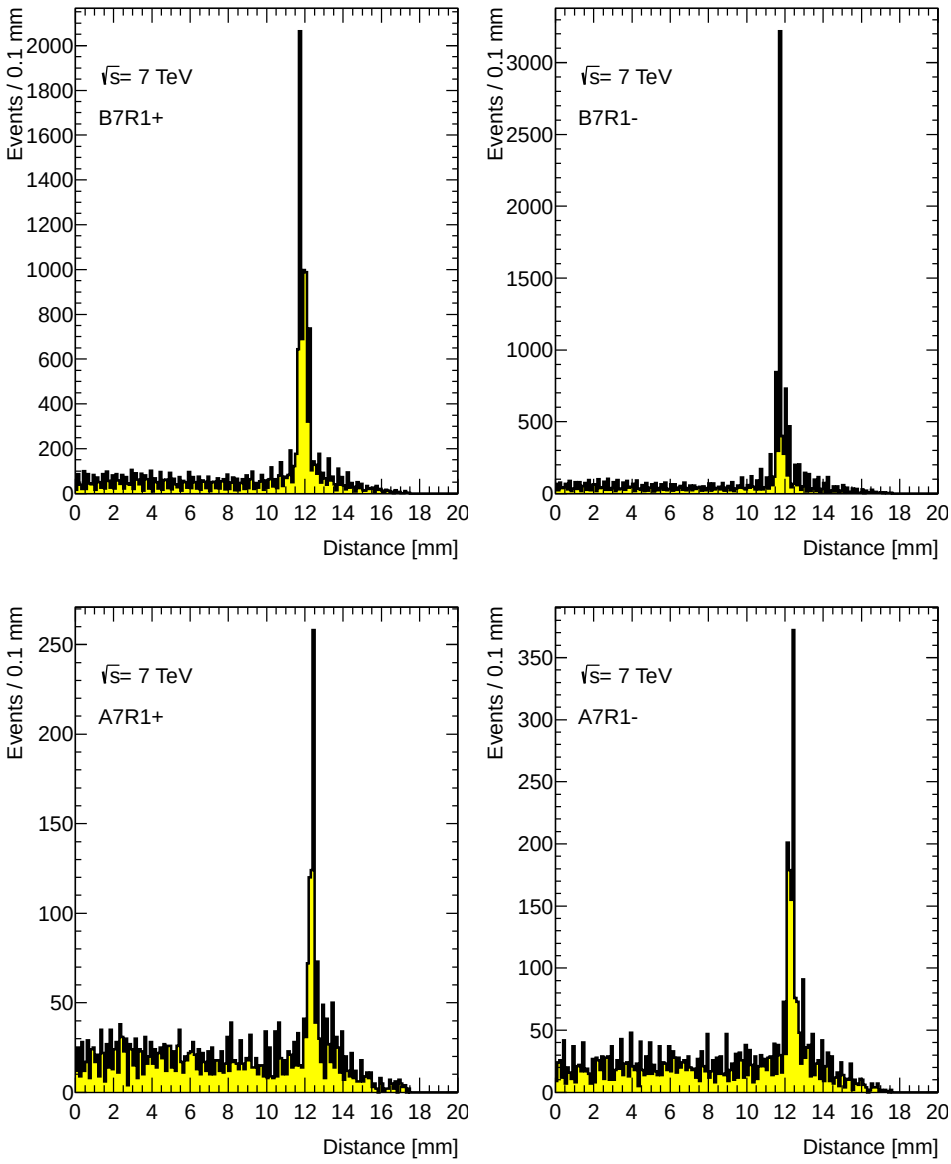

Figure 6.10: Distance distribution for B7R1 (top) and A7R1 (bottom) stations for the 191367 run. Left and right plots represent different sides. One can distinguish a peak near 12 mm, representing the combination of correlated tracks associated to the signal, and the large spread around indicate a background contaminations.

- use it later for more systematic errors studies as shown in § 6.5.4

6.4.0.2 Procedure

Simulation procedure is summarized as follow: detectors are fixed around a virtual beam core (origin of transversal plan) with a given distance D_{true} separating upper and lower MD. Tracks

preliminary background systematics.

are then randomly generated, using flat distribution between $[-15, +15]$ mm for vertical plan, and $\pm[19, 25]$ mm for horizontal one ($\pm$ for different OD sides).
Afterwards, they are extrapolated in the *z* direction, and virtually hit corresponding fibres in different ODs layers. Position and width of the fibres are defined using the OD metrology, in order to reproduce the experimental situation. This allows also studying the impact of the OD metrology imperfections.
OD tracks are then reconstructed using fibres hits, and the distance D_{rec} is calculated by combining upper and lower tracks positions.

6.4.0.3 Background

In order to reproduce distributions similar to data distributions in figure 6.10, different sources of background were included in the simulation. Summarizing them:

- horizontal tracks will reproduce the signal (or the peak on the distance distribution). These tracks are slightly tilted by the divergence, which modified the tracks slopes. The divergence is defined as mix of 3 Gaussian distributions (Gauss(1)+Gauss(2)+Gauss(3)), in order to reproduce the data model as close as possible. The Gaussian sigma and normalization factor are reported in table 6.2 and the central value is 0
- large background tail will be reproduced by simulating uncorrelated random events in the upper and lower OD for the same station. To do so we use two random generator of flat distribution for upper and lower OD, then two different tracks will be reconstructed, and will reproduce the background tail as we will see later. Contributions of these events are shown in the table 6.2
- hitting randomly neighbor fibres to simulate the cross talk effect. Based on § 4.3.4 and MD studies in [45], we assume that in 5% of fiber hit cases, neighbor fibres are fired too

As stated before distance separating upper and lower ODs is 45 mm, and the space between 2 consecutive OD layers is 2 mm (reminding that fibre width is 0.5 mm). It means that longitudinal tracks with a divergence of few mrad, once extrapolated 45 mm to the second OD, will have a serious impact on the D_{rec} in the order of 100 μm.

6.4.0.4 Simulation tunning

Tunning the simulation requests the optimization of four parameters. They are the contribution of three Gaussian and uncorrelated events. To do so, a tool was developed to constrain these four free parameters, by comparing simulation and data distribution. This tool is based on an iterative minimization procedure described in the following:

Table 6.2: Background simulation recipes. Contribution in % of different background sources in simulation. They were tunned using data

Station	**Uncorrelated events**	**Gauss(1)** $\sigma = 0.2$ **[mrad]**	**Gauss(2)** $\sigma = 2$ **[mrad]**	**Gauss(3)** $\sigma = 6$ **[mrad]**
B7L1+	88.5	0.0	10.0	1.3
B7L1-	92.1	0.0	7.7	0.0
A7L1+	96.1	0.6	3.0	0.1
A7L1-	93.7	4.3	1.6	0.2
A7R1+	93.9	1.7	3.0	1.3
A7R1-	96.9	0.1	2.9	0.0
B7R1+	86.0	0.6	9.9	3.3
B7R1-	93.1	0.0	6.7	0.0

Different Gaussian sigmas choice was based on the knowledge that a clean distance peak width (without background and divergence) variates between 0.3 and 0.6 mm (they depend on detector metrology and relative distance). We make sure that additional divergence will reproduce a peak with the same range width.
Simulation fills the same distance histogram (range and binning) as data. Then we defined the χ^2 as:

$$\chi^2_{minim} = \sum \frac{(d_i - s_i)^2}{\sigma^2_{d_i} + \sigma^2_{s_i}} \tag{6.1}$$

with d_i content of data bin i, s_i content of simulation bin i, and σ the corresponding statistical error. For each simulated iteration, we calculate the χ^2 value, and using the root TMinuit package we find the minimum χ^2 value. In other words, we find the best match between data and simulation.
Results are reported in table 6.2 as contribution of different background sources. These numbers represent the recipes of the final tunned simulation

Figure 6.11 shows a comparison between data distance distribution and simulation for 2 stations, B7R1 (outer) and A7L1 (inner). Comparison shows the difficulties to reproduce a perfect simulation model which fits data, in particularly for inner station, with the low data statistics. For this reason the only use of simulated models will be to estimate detector imperfections bias and for more detailed systematic studies.

6.5 Distance measurement procedures

Facing the new data, and the unexpected level of background, new tools were needed to analyze the distance distribution, and separate the real distance (peak) from background. Even if

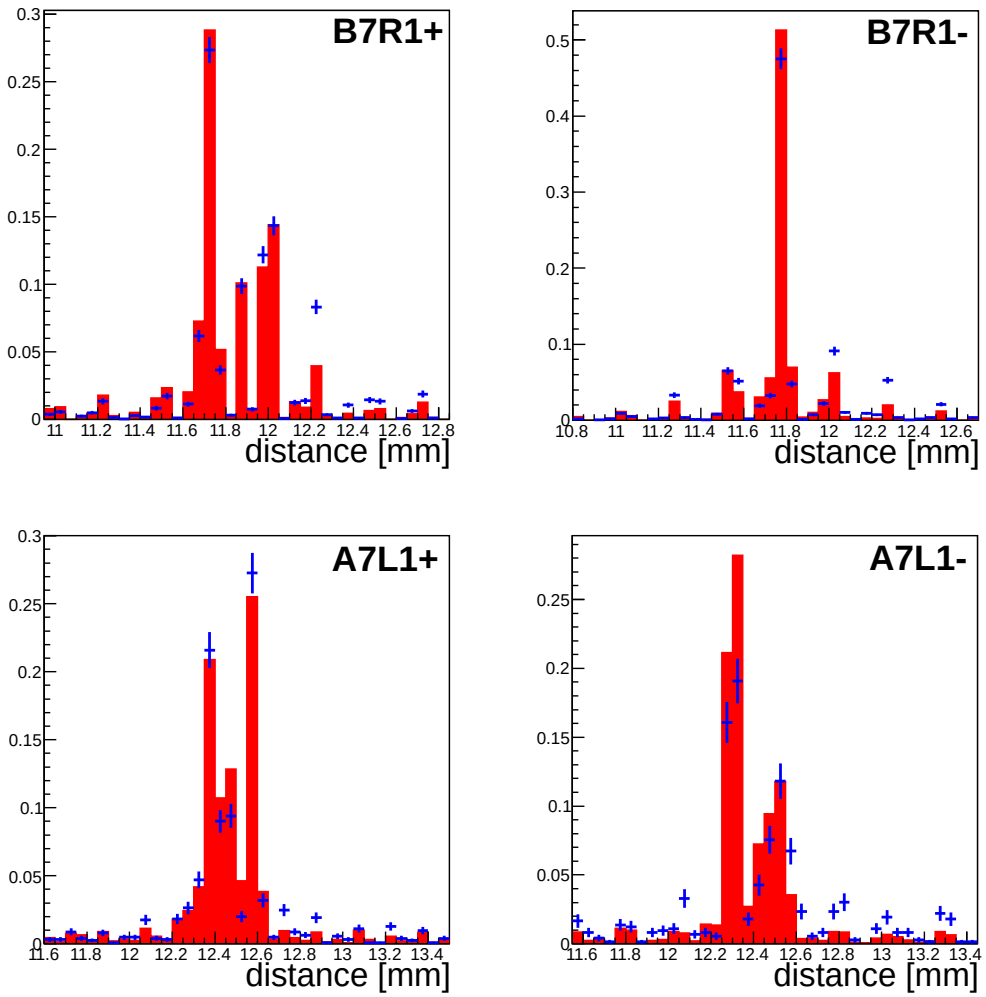

Figure 6.11: Comparison between data (blue crosses) and simulation (red histogram) near the peak region.

the peak position is clear in most of cases, an algorithm is needed to study the impact of the irreducible background in the peak region and its close neighborhood.

In the following, we will describe an algorithm, developed after the data taking phase, in order to get the distance measurement even in high background contamination conditions. In other words, this algorithm is able to distinguish signal and background on the distance distribution plots. Systematic errors of the measurement are related to the level of background around the peak.

We notice that in this § single track algorithm is only considered for tracks reconstruction. Independent study using multi tracks algorithm will come in § 6.5.4.

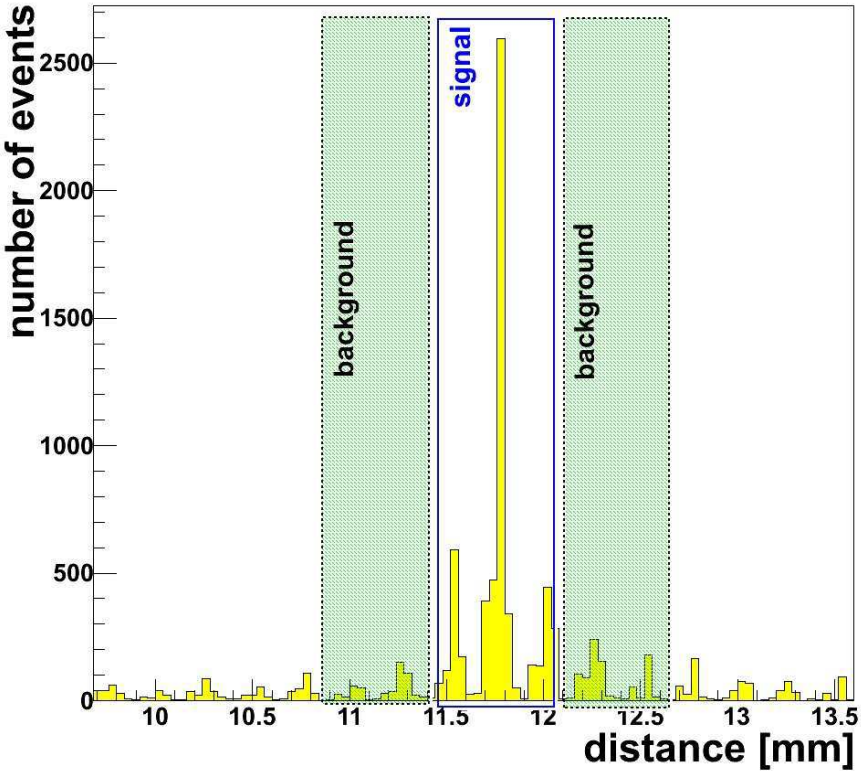

Figure 6.12: Example of iteration algorithm identifying the signal and estimating the background impact. Distance distribution histogram with a binning of 40 μm.

6.5.1 Iteration algorithm

Considering distance distribution of figure 6.12, the algorithm proceeds, with a defined number of iterations ($N_I = 10000$), as follow:

1. scan the distribution by a predefined *window* with random width, between 0.3 and 0.6 mm in order to find the peak (maximum number of events in a given window). Within this window, events are considered as signal, and outside it as background
2. once founded, compute the number of collected events within this window (blue rectangle on figure 6.12). Let's call it S_P (P stands for Peak). In other words, calculate the number of events returning the distance measurements in the window acceptance limit
3. estimate the background level around the signal using the same defined window width. To do so, we fix 2 *background windows* on both sides of the peak window and we compute the number of tracks which probably contribute as background (green area on figure 6.12). B_P stands for background near the peak. It's the total number of events in both windows divided by 2
4. fluctuate the window position using a random Gaussian distribution, centered in the window. This step aims to take into account the effect of neighbor background on the distance measurement

5. Gaussian sigma is inversely proportional to window width. It represents the doubt on the window position and vary from 0.4 mm for small window width, to 0.2 mm for larger width
6. last step (5) changes the window position but keeps the same width. The new number of signal events (S_G) and background (B_G) is computed again. The distance measurement D_i for this iteration is estimated by the tracks within the new window acceptance
7. putting some limits on the Gaussian random generation, we request that $S_G/B_G > 0.4 \times S_P/B_P$. It means, we do not accept that the new window position gives a signal over background ratio 40% smaller than initial one (the 40% will be changed later to check the systematic of the method)
8. define a weight of the current iteration by:

$$W_i = \frac{S_G - B_G}{S_P - B_P} \tag{6.2}$$

   where i is an integer varying from 1 to N_I (maximum number of iterations).

After N_I iterations the final reconstructed distance is estimated as:

$$D_{rec} = \frac{\sum_{i=1}^{N_I} W_i D_i}{\sum_{i=1}^{N_I} W_i} \tag{6.3}$$

The distribution of the D_i around the central mean value D_{rec}, is given by (taking weights into account):

$$\sigma = \sqrt{\frac{V_1 \sum_i^{N_I} \sigma_i}{V_1^2 - V_2}} \tag{6.4}$$

with $V_1 = \sum_i^{N_I} W_i$, $V_2 = \sum_i^{N_I} W_i^2$ and $\sigma_i = W_i (D_i - \sum_i^{N_I} \frac{D_i}{N_I})$.
The σ depends on the amount of background near the peak, and will be considered as preliminary systematic error, caused by the background contributions. Advanced systematic studies will be shown later, in § 6.5.4.

6.5.2 Events selection cut

Some of background sources can be explained by the layer multiplicity observable, such as cross talks, showers, and electronic biases. Limiting the number of allowed hits per layer, or multiplicity, may have impact on the level of background around the peak.

Two type of cuts were studied:

- **Static cuts**, which require the same multiplicity for all layers with OR between upper and lower OD, i.e. multiplicity cut 3 gives following condition 3-3-3 (upper OD layers) OR 3-3-3 (lower OD layers). Indeed, if one OD has an equal or smaller multiplicity

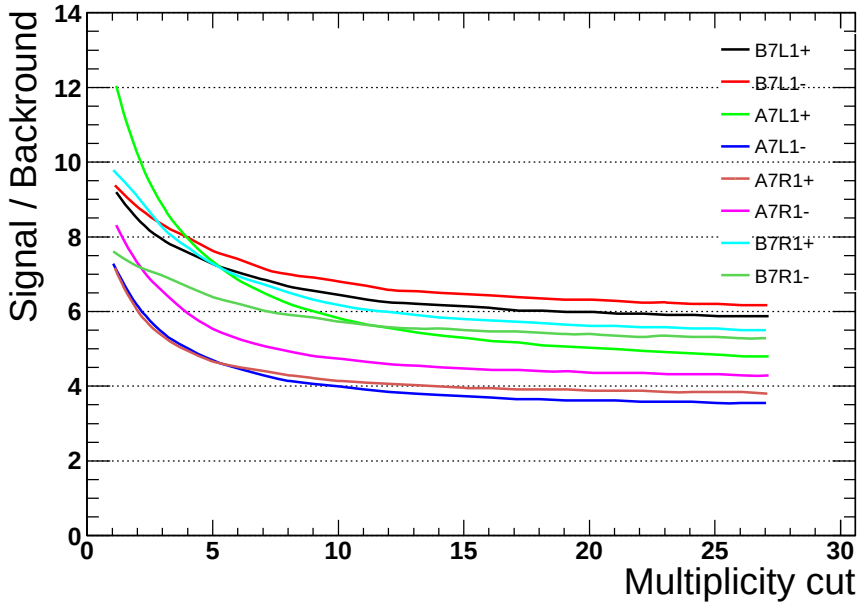

Figure 6.13: Evolution of Signal over Background variable (S/B) as function of multiplicity cut, starting from tight selection with a total of 1 hit per layer, and ending by a loose cut with 27 hits per layer.

number in all layers, event is accepted. To study different possibilities, we start by a very tight cut of 1 hit per layer for the 3 OD layers, and increase it to 27.

- **Dynamic cuts** require different number of multiplicity between layers with AND between ODs. Again, the event will be accepted in case the imposed condition is fulfilled. Several cuts were checked, starting by very tight cut with multiplicity of 1-2-5 for the different OD layers. No specific order is requested. These numbers will be increased together by 1 until 27.

Figure 6.13 shows the evolution of Signal over Background variable as function of multiplicity cut, starting form tight selection with a total of 2 hits per layer, and ending by a loose cut with 27 hits per layer. Signal and background are defined referring to the iteration algorithm. As expected, tight multiplicity cut improves the S/B ratio. The best ratio comes from the A7L1+ station with $\sim$ 12. With very tight multiplicity cuts we end up with a S/B between 4 and 6.

Looking to the evolution of statistical errors using static cuts (figure 6.14) it's clear that inner stations (A7L1 and A7R1) are more sensitive to the tight multiplicity selection. The combined statistical error for both negative and positive side reach the level of $\sim$8.5 μm for A7R1 and $\sim$5.5 μm for A7L1. For outer station, statistical errors are less then 2 μm for multiplicity cut larger than 3.

To have a complete view, one should look also to the evolution of systematic errors (figure 6.15) and to the distance measurement fluctuations (table 6.3).
Systematic errors (continuous line for static cuts, and dashed line for dynamic cuts) look much

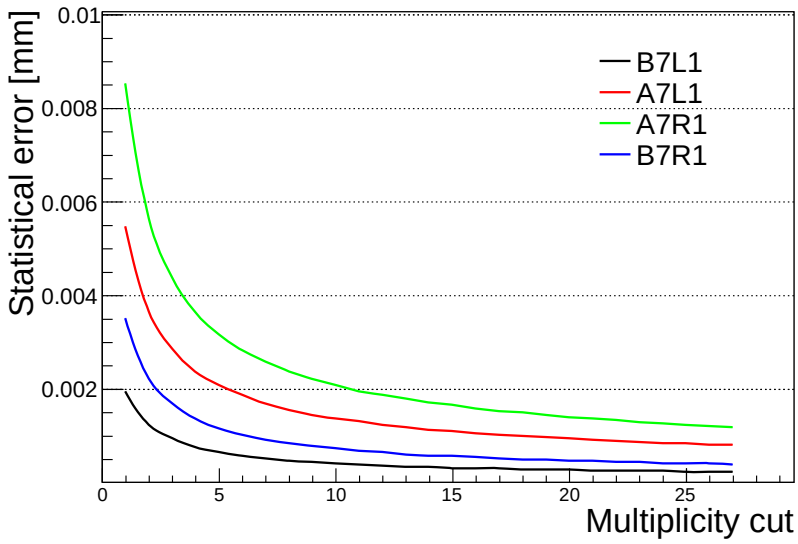

Figure 6.14: Evolution of distance measurement statistical error as function of multiplicity cut, starting from tight selection with a total of 1 hit per layer, and ending by a loose cut with 27 hits per layer.

more sensitive to the multiplicity cuts, especially for the inner station where A7L1 expands $\sim$ 50% between tight and loose cuts. These systematics are estimated using the algorithm described above. They are the reflection of background contamination. For tight cuts where S/B was improved, systematics are at the minimum. They increase with more relaxed cuts.

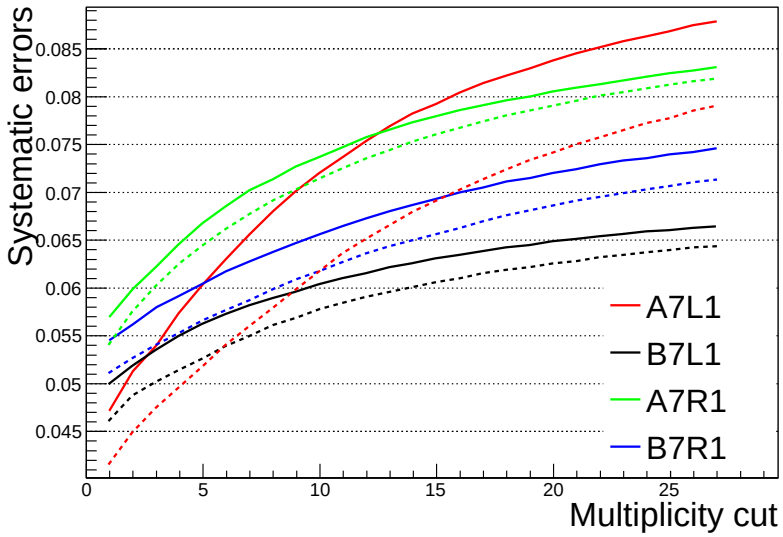

Figure 6.15: Evolution of distance measurement systematical errors as function of multiplicity cut, starting from tight selection with a total of 1 hit per layer, and ending by a loose cut with 27 hits per layer. Station are represented in different colors, continuous lines standing for static cuts, and dashed lines for dynamic cuts.

Table 6.3: Distance measurement fluctuations [μm] over the variation of multiplicity cuts

Station	Static cuts	Dynamic cuts	Combined
B7L1	4	3	4
A7L1	4	5	8
A7R1	3	7	8
B7R1	6	5	6

Figure 6.15 shows also the difference between cuts, where dynamic cuts return lower systematics. We have to mention that statistical errors are at the same level for both cuts. Dynamic multiplicity cuts, with a value of 3, will be chosen for the following analysis and measurement. This means we request at least 3-4-7 hits for different OD layers.

Distance measurement have shown a fluctuation between 3 and 7 μm (see table 6.3). Both cuts strategies were reported in this table with an additional column of maximum fluctuation considering both cuts. These will be consider as selection cuts systematics and be added to the final systematical uncertainty.

6.5.3 Distance of different runs at 6.5 σ_y

Figure 6.16 shows the distance measurement using the iteration algorithm, after the application of the multiplicity selection cut. Different runs are shown, and one combined run merges all. The error bars represent the quadratic sum of the statistical errors, and the preliminary systematic errors described in § 6.5.1. Horizontal black line represent the measured distance of all runs combined, with corresponding errors (blue area).
All measurements match the combine run distance within the errors bars. Merging all events together increase statistics, and reduce the total errors on the measurement. Figure 6.16 also shows the stability of the iteration algorithm, which return consistent distance with different data sets.

6.5.4 Systematics and results

6.5.4.1 Advanced systematics studies

Systematics of the background contamination, estimated before using the iteration algorithm, are totally related to the S/B ratio, which may not reflect the real precision of the measurement, or other hidden biases such as metrology imperfections introduced in 5.1.3.1. For this reason,

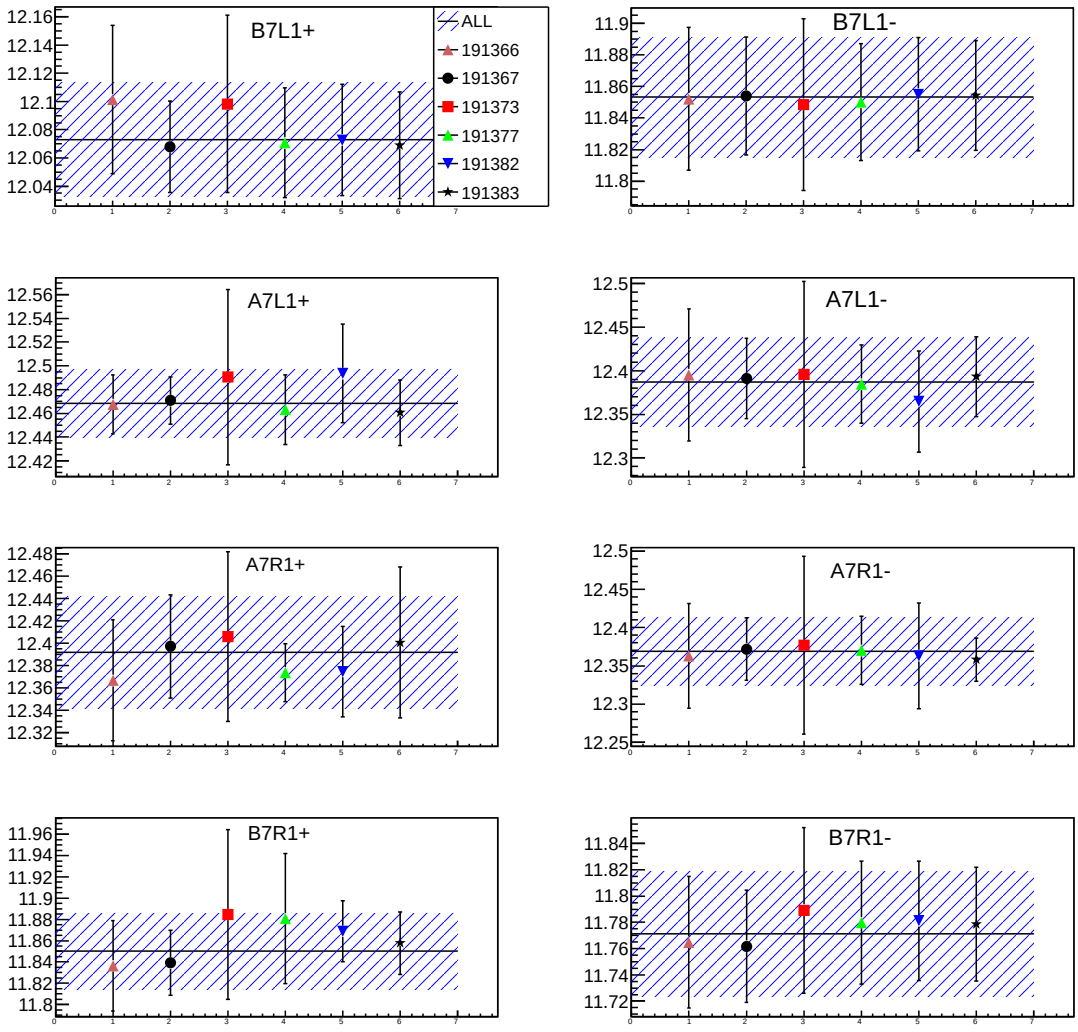

Figure 6.16: Distance measurement using the iteration algorithm for different runs.

an independent study was developed for better estimation of these systematics.
It's based on simulation, where we attend to use the difference between simulated distance (D_{true}) and reconstructed one (D_{rec}), taking into account background and detector metrology effect.
For this advanced systematic study, we proceed as follow:

1. Get a distance measurements, applying iteration algorithm on data distributions
2. Use these measurements (which differ from station to station) as input for the simulation procedure
3. Run the minimization procedure in order to build a simulation model as close as possible to the data, as described in § 7.2
4. Calculate the simulated distance D_{rec}, using the iteration algorithm, and compute $\Delta_d = D_{rec} - D_{true}$ and represents the bias due to background, method in use, and metrology imperfections

5. Repeat step (2), (3), and (4) by scanning around the initial distance calculated in (1). Scan limit[3] will be ± 80 μm, by steps of 10 μm
6. Consider the *maximum* Δ_d in the scanned range, as a conservative systematic errors σ_b of the distance measurement

Figure 6.17 shows the variation of Δ_d in the scanned range (horizontal axis) for all stations. The 0 on the vertical axis represents the origin of the scan, or the data distance measurement (step (1) on the previous list), and the origin of the vertical axis means that $D_{rec} = D_{true}$.

Table 6.4 summarizes the distance measured by each OD side, with corresponding sys-

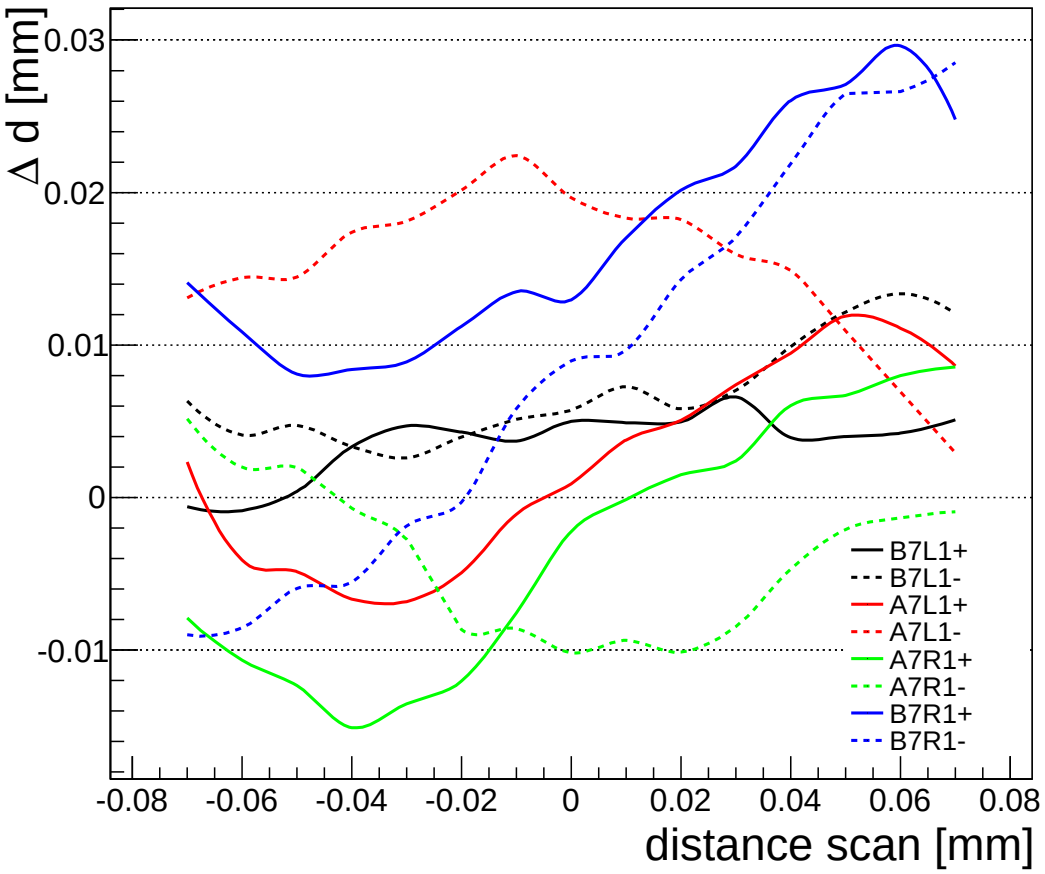

Figure 6.17: Variation of the difference between simulated distance and reconstructed one (Δ_d), in a range of ± 80 μm for different stations.

tematical and statistical errors. Statistical errors estimation takes into account ODs different resolution (see table 5.1 and method description in § 5.2.6).

[3]This limit is inspired from the preliminary systematics results estimated by the application of iteration algorithm on the data.

Table 6.4: Distance measurements, statistical errors, background and detector imperfection systematics σ_b, of all stations (and sides).

Station	**distance [mm]**	stat. [mm]	σ_b [mm]
B7L1+	12.073	0.001	0.006
B7L1-	11.850	0.001	0.013
A7L1+	12.468	0.003	0.012
A7L1-	12.387	0.003	0.022
A7R1+	12.397	0.005	0.015
A7R1-	12.369	0.004	0.010
B7R1+	11.847	0.001	0.029
B7R1-	11.773	0.002	0.028

6.5.4.2 Results

For physics analysis, we have to provide the distance separating central detector edges (MD edges). To do so, we calculate the mean distance of both OD measurements sides (+ and - sides). This distance will be used for the alignment procedure which is the first step in physics analysis. Furthermore, we have to take into account other systematics, such as:

- selection cuts σ_c, reported in § 6.5.2
- detector absolute alignments σ_{det}, estimated during test beam analysis (§ 5.2.6), and including:
  - fibre absolute position alignment with respect to MD
  - MD edge position measurements precision
  - systematics of the test beam analysis methods

Distance between upper and lower MD, with corresponding systematical, statistical errors and combined errors (quadratic sum of all errors contributions), are reported in table 6.5. Combination of all propagated errors show that inner station are more precise than outer ones, even with low statistics condition. We succeed to measure two distances with a precision of 18 and 22 μm ($\approx$ 0.2 %). The outer station B7L1 shows the largest systematic uncertainty due to the fact that it wasn't calibrated during TB. Thus, inner stations will be used later for the alignment procedure as they present better precision than outer one.

Table 6.5: Distance measurements results, with propagated systematical and statistical errors, for different station. σ_b is background systematic, σ_{det} stands for TB calibration systematics and σ_c for selection cuts. Unit of measurement is [mm]

Station	Distance	Stat.	σ_b	σ_{det}	σ_c	Combined
B7L1	11.962	0.001	0.010	0.080	0.004	0.081
A7L1	12.428	0.003	0.018	0.008	0.008	0.022
A7R1	12.383	0.005	0.013	0.009	0.008	0.018
B7R1	11.810	0.002	0.029	0.008	0.006	0.031

6.6 Possibility to improve results using multi tracks algorithm

6.6.0.3 Motivations

Multi tracks algorithm was developed to improve the number of reconstructed tracks, by considering events with 2 (or more) tracks. It aims to improve statistics and measurement precision. The motivation to this study is represented in figure 6.18, where plots shown the distribution of tracks, over the different multi tracks cases. The 16 ODs are shown in this figure, with a red label for outer stations, and blue label for inner stations. Plots can be interpreted also as a comparison between single track algorithm an multi tracks. The number "1" on the *x*-axis, represents single tracks cases, and numbers from "2" to "6" are multi tracks cases.
Considering outer stations, it turns out that number of events with two tracks is higher than the one with one track, which reveals the importance of this study, for the statistical improvements. This observation can be explained by the high level of showers seen in outer stations.
For inner stations the number of single track is the dominant one, then we do not expect significant improvement of the measurement.

6.6.0.4 Analysis strategy

Since the analysis proceeds with upper and lower detectors in an independent way, the first step will be to match different reconstructed tracks with the original paths. Challenge comes from the high background level seen during data taking. To do so, an analysis was developed to check if this algorithm improve distance measurements, by improving the signal over background ratio.

As mentioned in § 5.1.2.2 the maximum number of reconstructed tracks per OD is 6, using multi tracks algorithm. As starting point we consider only 2 tracks per OD. In the ideal case (with no background), 2 tracks return 2 possible combinations, where only one of them is

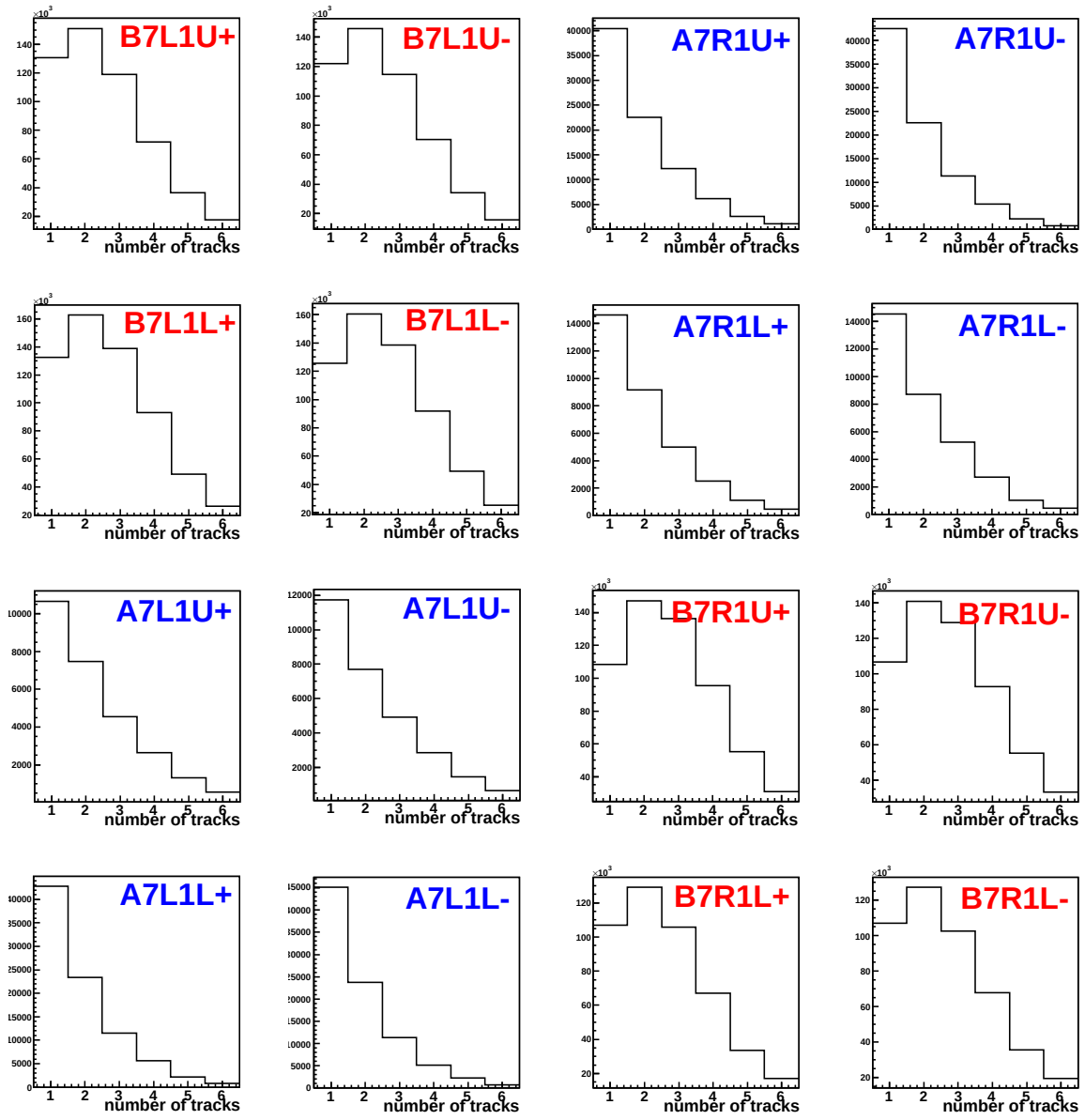

Figure 6.18: Number of reconstructed tracks for the same recorded events. Multi tracks algorithm was limited to max of 6 tracks. The 16 ODs are shown in this figure. Outer stations labeled in red, and blue labels for inner stations.

correct, as detailed in § 5.1.3.

This simple strategy could not be applied with high background contaminations seen in data. In other words, we were not able to use multi tracks algorithm independently to calculate the distance. Based on that we will introduce another strategy, which will call back single track algorithm in order to get a preliminary distance measurement. Afterwards, we used this "known" measurement to constrain all possible tracks combinations (between upper and lower OD) and find the best candidate(s).

We proceed as follow:

1. get a preliminary distance measurement, by selecting events with only 1 tracks in both ODs. Use the iteration algorithm to measure the distance, as explained in §6.5
2. re-scan the run and select multi tracks events (maximum number of allowed tracks can be fixed in advance)
3. make all combinations between tracks of the upper and lower ODs
4. the best track candidate(s) is the one returning the closest distance to preliminary one, calculated in step (1)
5. possible candidate(s) have to pass dynamic multiplicity cuts, with 5-10-15 per layers (for more details about this cut, check §6.5.2)
6. number of accepted candidates do not exceed the half of the maximum allowed tracks per detector. For 4 allowed tracks, maximum of 2 candidates are accepted

6.6.0.5 Results

With this strategy we succeeded to reconstruct again distance distribution based only on multi tracks cases. Since we can decide the number of allowed reconstructed tracks per OD, we made a scan, starting by 2 tracks and ending by 6 (the maximum), to check what case improves the measurement. Figure 6.19 shows the distance measurement results, using different configurations, for run 191367. The points represent different cases with different maximum of accepted tracks for each case, excluding single track one. For example the 3 tracks configuration, take into account events with 2 or 3 reconstructed tracks. Errors on the distance measurement were estimated using the iteration algorithm, in addition of the statistical errors. Inner stations measurements are totally biased by the low statistics condition (expected in the beginning of this analysis). Single track algorithm will stay a good choice to these stations.
Looking for outer ones, we succeeds to reproduce compatible distance measurement in comparison to single track algorithm and measurement method, but we do not succeed to reduce systematical errors of the measurement. Unfortunately, S/B ratio is higher in multi tracks configurations, thus these measurement will no be used for physics analysis later.
At this point, table 6.5 is the final reference.

6.7 Conclusion

In this chapter we described and summarized the overlap detectors performance during data taking phase. They were used for the first time during the $\beta^* = 90$ m data taking of October 2011. Detectors have shown good performances in general at the triggering level, and fibres efficiency studies. Multiplicity studies has reflected the following state: inner stations were dominated by single halo particles while the outer stations were affected by showers initiated

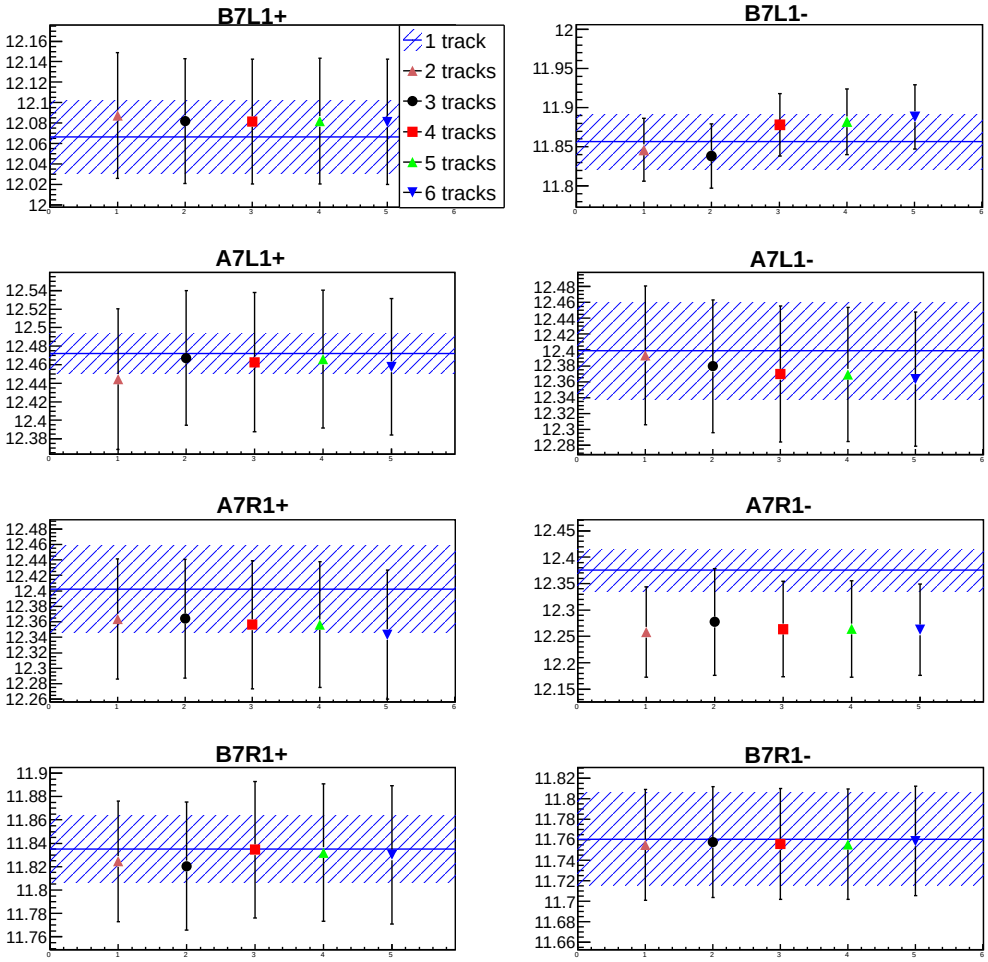

Figure 6.19: Comparison of the distance calculated using different multi tracks options. The blue horizontal line represents the distance measured using only single tracks, with the corresponding errors (blue zone). The maximum number of tracks used for the reconstruction is shown in different colors.

in the inner ones.
Backgrounds could not be predicted and simulated. Data taking was the first opportunity to study background contamination and impact, on the distance measurements. Simulation was developed for this purpose and used to make advanced systematic uncertainties studies.

Data quality during data taking was a real challenge for analysis. The high level of background and the unpredictable state of the beam halo were behind the development of the OD analysis. Final distance measurement results are based on reconstructed tracks using single track algorithm. Multi tracks algorithm presented a coherent results with single track, within the error bars. But since systematical error have shown no improvement, multi track results will not be used in the analysis later on.

As mentioned in the introduction of chapter 5, the distance measurement precision have a direct impact on the total cross-section and luminosity measurements. For the time being, we succeed to measure two distances with a precision of 18 and 22 μm ($\approx$ 0.2 %) which is

enough for actual run conditions (reminding that the 10 μm or $\approx$ 1 % was requested to the high β^* runs with a distance of 1-2 mm).
Later, we have only to choose the most precise measurement of one station, and use it for relative alignment procedure, described in following chapter. Distances measured by other stations, with higher uncertainties, will not be taken into account. These stations will be relatively aligned with respect to the chosen one, using reconstructed elastic tracks in the main detector.

Concerning the 10 μm challenge for future high β^* runs, based on what we have seen until now, two points may let this precision possible:

- first one is to collect more statistics especially for inner detector to reduce impact of the statistical errors
- second one is to improve background investigations, and simulation models development. They may better describe the data. This may lead to develop other methods and tools for the analysis. One can imagine a data background subtraction using simulation, to get rid of the tails around the peak, and reduce its impact on systematic errors

The study presented in this chapter was my first experience with data analysis for physics uses. I have developed most of methods, algorithms, and analysis shown in this chapter. I also developed an automatic procedure and software for the next data taking, to give a fast feedback and preliminary distance measurements for any future runs. Advanced studies came later with simulation, data quality, and selection cuts as described in this chapter. These procedures and tools can be used or developed by any member of the team for next runs.

Chapter 7

Total cross section measurement

The $\beta^* = 90$ m optics described in [60] was developed as an intermediate step on the way to ultimate 2625 m optics. It will allow for the first total cross section (σ_{tot}) and nuclear slope (b) measurements in the very forward region by ALFA and TOTEM. The theoretical motivation was introduced in § 3.5. The main parameters used in the 2625 m β^* optics have been kept in the 90 m optic, in particular, the phase advance between the IP and the RPs is $\approx 90°$ and the dispersion is equal to zero.
This chapter is dedicated to the analysis of the 90 m run. After the introduction of the beam condition, and Monte Carlo (MC) simulation strategy, we will go through the analysis chain in § 7.3. And by the end of this chapter we will present the first ALFA measurement of total cross section and nuclear slope, as a result of this analysis.

7.1 The run conditions

The data were accumulated during October 2011 in a serie of runs with specific beam conditions. The very specific condition was the β^* value; for this set of runs the value was 90 m.
The bunch intensities for the two colliding bunches were 7.10^{10} and 1.10^{10} for the non-colliding bunches (13 in total). The collisions rates were optimized by the use of various luminosity online reference counters; the most sensitive at these low intensities was LUCID_Event_AND. The rate variation could also nicely be observed by any of the ALFA detectors, even though in garage position, as can be seen in figure 7.1.

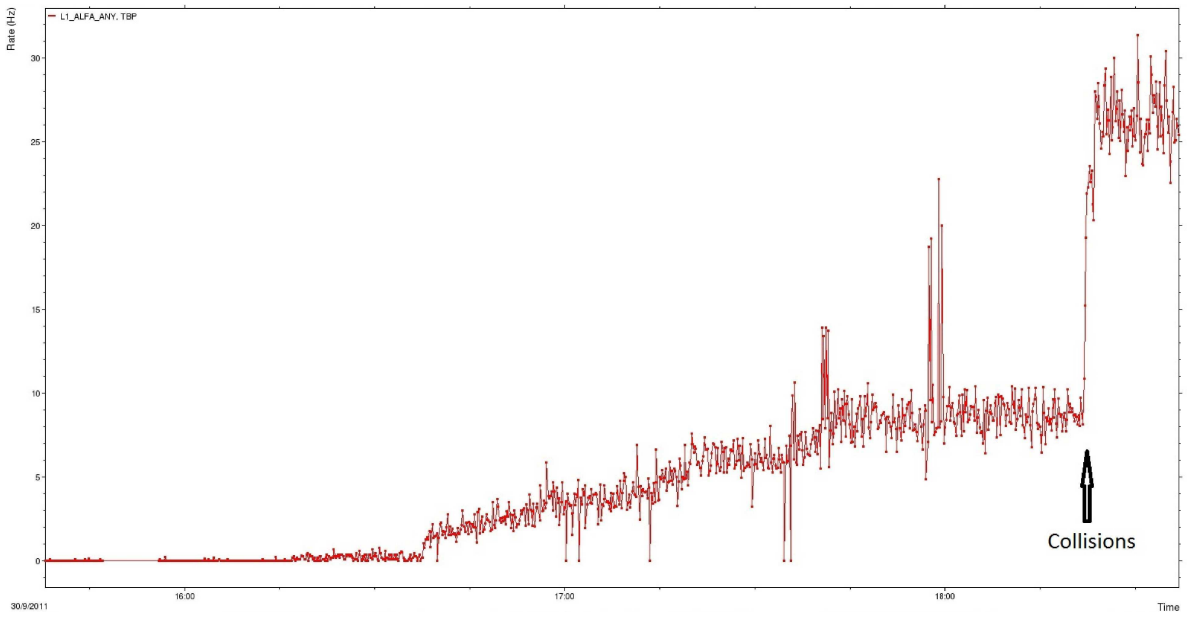

Figure 7.1: Rate evolution during collision optimization, the *x* axis represents the time and *y* axis the rate in Hz [61].

7.1.1 Optics parameters

The 2625 m optics is designed for a beam energy of 7 TeV. It requires a very low emittance of 1 μm and inversion of the polarity of the Q4 magnet. We know now, that such conditions will not be possible to obtain before the year 2014. The ALFA roman pots have been installed in the last short shut down and was available for data taking in the second part of 2011 [60].

The main parameters of the 90 m β^* optics are listed in table 7.1 for a normalized emittance equals to 3.75 μm.rad which was the emittance expected for LHC as indicated in 1.1. The main parameters used in the 2625 m β^* optics have been kept in the 90 m β^* optics. In particular, the vertical phase advance between the IP and the RPs is equal to 90°, dispersion and α at IP are equals to zero. With these values, the vertical and horizontal beam sizes at IP reach 300 μm.
Figure 7.2 shows the evolution of the betatron ($\beta(s)$) and dispersion ($D(s)$) functions, for beam 1 and 2, as function of the longitudinal position (s). The IP is around 550 m, where dispersion is 0 and $\beta^* = 90$ m.

7.2 Simulation

The good knowledge of the optics parameters (table 7.1) and beam conditions are crucial for simulation. Another important parameter is the precise measurement of the detector position

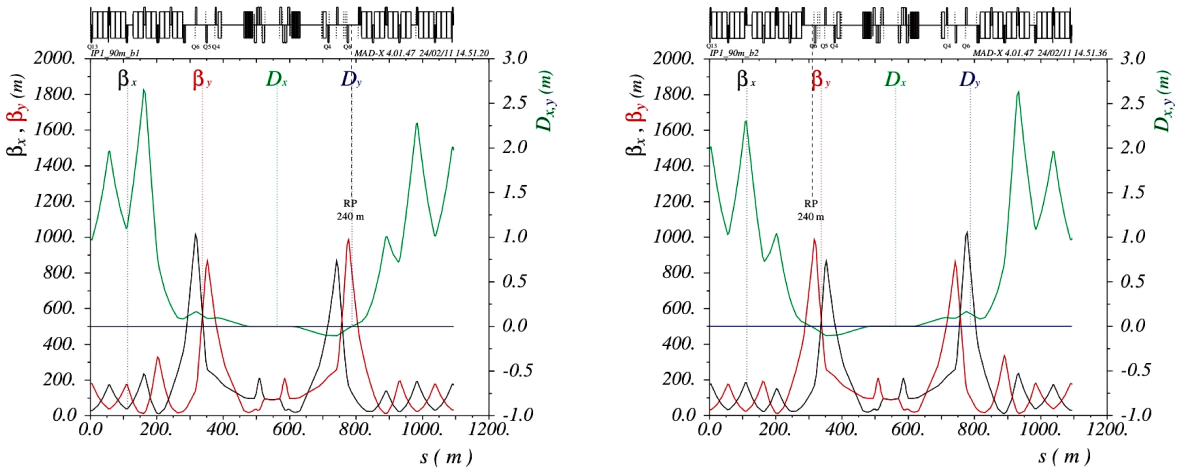

(a) 90m ALFA optics for beam 1

(b) 90m ALFA optics for beam 2

Figure 7.2: $\beta(s)$ betatron and $D(s)$ dispersion functions for beam 1 and 2, as function of s position along the beam axis [49].

Table 7.1: 90 m β^* optics parameters for beam 1 (LHC version V6.503) [60].

IP		**RPs**	
ε_N (μm.rad)	3.75	β_x (m)	193.5 – 124.2
β_x^* (m)	90	β_y (m)	857.5 – 780.4
β_y^* (m)	90	σ_x (μm)	374 – 353
α^*	0.0	σ_y (μm)	926 – 883
D_y^* (m)	0.0	σ_x' (μrad)	2.67 – 2.83
$D_y^{*'}$	0.0	σ_y' (μrad)	1.08 – 1.13
σ^* (mm)	0.3	$\Delta\psi_x$ (2π)	0.515 – 0.519
$\sigma^{*'}$ (μrad)	3.33	$\Delta\psi_y$ (2π)	0.249 – 0.250

with respect to the beam core, or what we will call later “alignment”. In the following a brief description of the simulation procedures is given. More details can be found in [45, 49].

Elastic protons are generated randomly with PYTHIA8 [62]. The simulation takes into account elastic parameters ρ, σ_{tot} and the nuclear slope b, based on different physics models. The size, divergence of the beam, vertex smearing and energy dispersion are also included in the generator.

Knowing the initial position and scattering angle, elastic protons will be transported to the RP position, using the MadX [63] software, which take into account the magnet strength and position, to calculate the transfer matrix parameters (introduced in § 1.2.4).

Once the elastic scattered proton is transported, the knowledge of the detectors position (with respect to the beam center) and geometry, allows to tag the relevant protons that would be used for the measurement of t-spectrum.

Figure 7.3 shows simulated tracks map of elastic events for the β^* 90m optics. It also figure out the beam profile at RPs position. The beam is stretched in the vertical direction, due to the ALFA special optics configuration (mainly to the 90° phase advance in vertical direction).

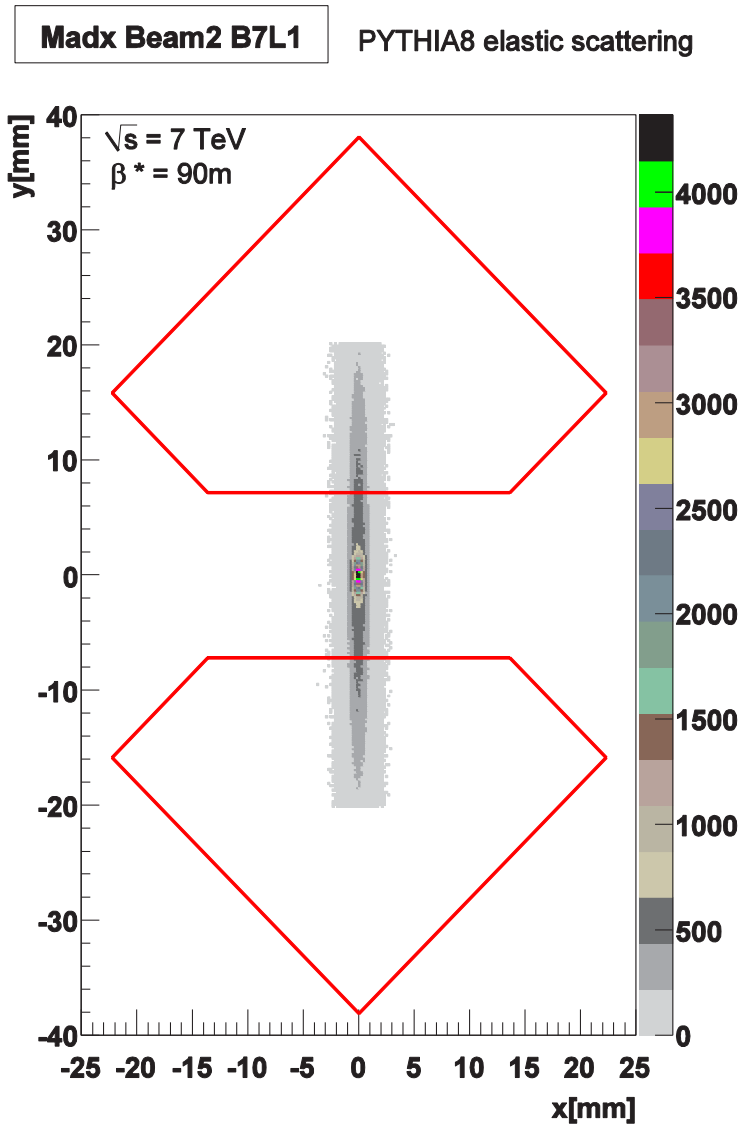

Figure 7.3: Simulated tracks map of elastic events for the β^* 90m optics. Events were generated by PHYTIA8 and the transport from ATLAS to the ALFA stations at 241 m distance to the IP performed by the MADX matrix program. Just the positions of passing protons are shown - no reconstruction algorithm was applied. For illustration also tracks points outside the geometrical acceptance are shown.

7.3 Analysis chain

The analysis chain is summarized in the diagram of the figure 7.4. The collected **raw data** (fibres hits) is transformed to **reconstructed tracks**. This step will be followed by the **alignment** procedure, which gives the absolute position of each detector with respect to the beam center. Then, the **event selection** checks for elastic events and partially reduce background. Afterwards, the reconstruction of the t-spectrum (t-**reco**) will be possible using different reconstruction methods. The **unfolding** is crucial to correct for detector effect, then **acceptance** and **efficiency** correction lead us to the dN/dt distribution. In these last 3 steps, knowledge of the **optics** is important. **Luminosity normalization** transforms the dN/dt to dσ/dt distribution, where one can deduce the σ_{tot} and b-slope parameter.

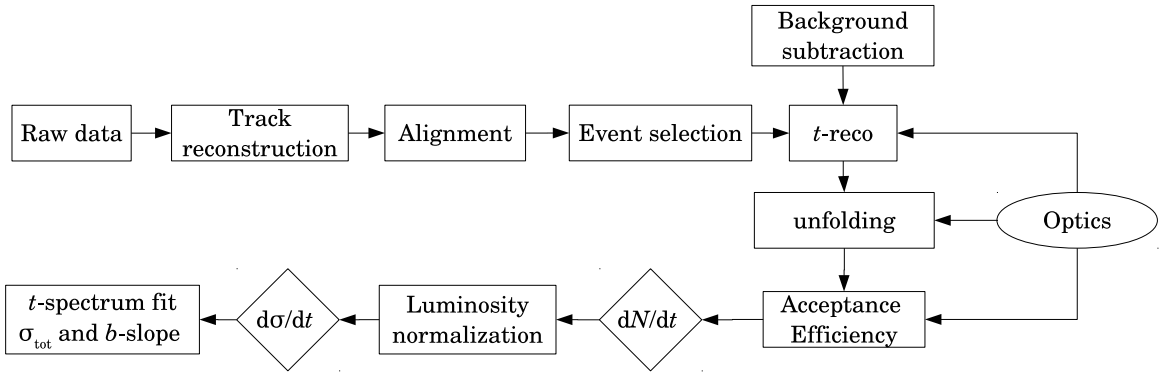

Figure 7.4: The analysis workflow, from raw data to the differential cross section of the elastic scattering.

7.3.1 Detectors alignments

The goal of the alignment of the ALFA detector system is to express the tracks, initially reconstructed in the detector coordinate system (DCS), in the beam coordinate system (BCS).

Beam scrapping test

The first part of the alignment is done prior to the data taking in the so-called scrapping exercise. In this exercise, the beam is collimated such that it is symmetric and that only the core of the beam remains (typically 3 to 6 sigmas). The knowledge of the optical functions between the collimators and the detectors allows to infer the position of the beam with about 150 μ m precision. The detectors are brought to position first by coarse steps then by fine steps as we get close to the expected position. When the outside part of the RP will start to

touch the beam, the scattered protons will be detected by to the Beam Loss Monitors (BLM) sitting behind. The signal increase in the BLM will allow calibrating the detector position. A simple scaling will then allow the user to position the detectors at any given distance from the beam center with an accuracy better than 100 microns.

However this level of precision is not sufficient for the data analysis and must be improved. The distance between the active parts of the upper and lower detectors is measured with the overlap detectors. The measurement comes with a systematic uncertainty which will determine the reference station used for the relative alignment of the ALFA detector system.

The alignment of the ALFA detector system is based on the recorded elastic tracks. The back-to-back topology of the elastic scattering provides an powerful tool to perform this operation. It is divided into two steps. First the horizontal alignment parameters are determined. They consist of one offset and one rotation angle for each detector. Once the tracks are corrected the vertical alignment can start.
A very important matter of the alignment procedure is not to use any information from the optics.

Horizontal alignment

The horizontal alignment uses the fact that the elastic scattering pattern is symmetric with respect to the beam center. The gap between the detector does not entail this symmetry contrarily to the vertical direction. Nevertheless one contribution could brake this symmetry, the background events. In this respect, the sample of events used for the alignment must be cleaned and some fiducial cuts must be applied toward the edge of the detector. In order to do so, several iteration are required. Figure 7.5 shows an example of the horizontal alignment, where a linear fit allows determining the rotation angle along the z-axis and the offset of ALFA detector.

Vertical alignment

The final check of the alignment is done using the so-called global tracks in the vertical plane. The back-to-back topology of the elastics events is used to build out of the two outgoing protons a single track. This track will go through the four detectors constituting an arm, i.e. the two upper detectors on *side-A* (on the left of IP) and the two lower detectors on *side-C* (on the right of IP) constitute *arm1* while *arm2* is built of the two lower detectors on *side-A* and the two upper detectors on *side-C* (see figure 7.7). The lever arm represents the distance at which the proton would be intercepted at the same vertical position in absence of any magnetic

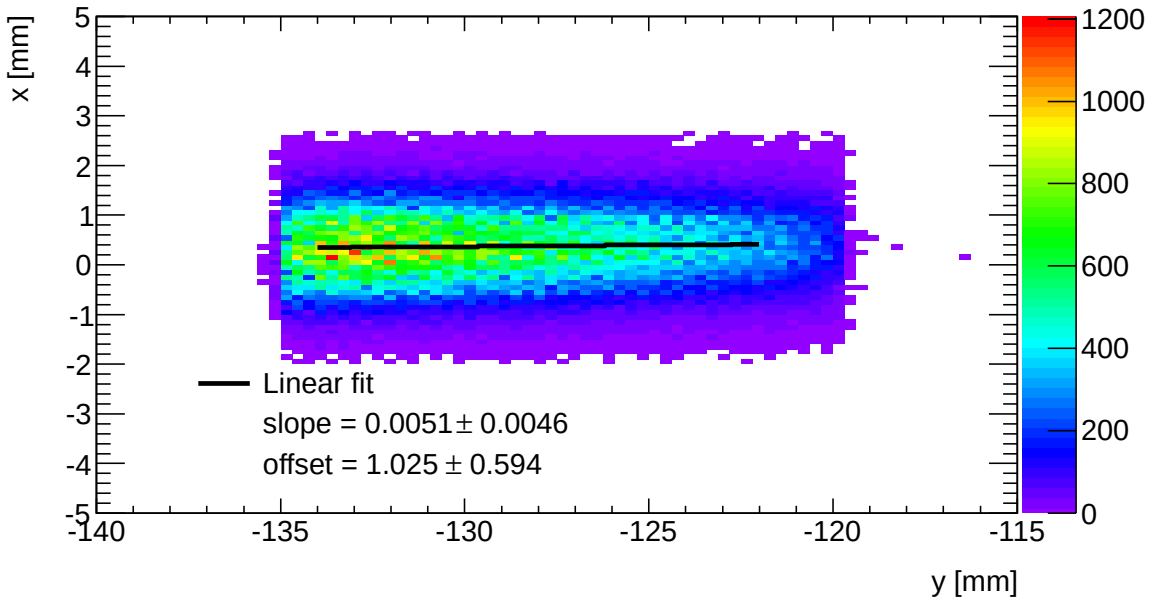

Figure 7.5: Track pattern in DCS. The linear fit allows to determine the rotation angle along the z-axis and the offset of each ALFA detector.

elements. Consequently, the detectors are placed at this distance in order to mimic a straight track. Finally each track is fitted and the residual plots shown in figure 7.6. The mean value of the fitted distributions demonstrate a precision on the relative positioning better than 5 microns. The figure 7.7 displays for the two detection arms the intercept of the fitted global tracks at $s = 0$ (i.e. the ATLAS interaction point). The mean value show an absolute alignment precision in the order of 10 microns. The width of the distribution shows the impact of the angular divergence, i.e. the deviation of the global track from a straight line.

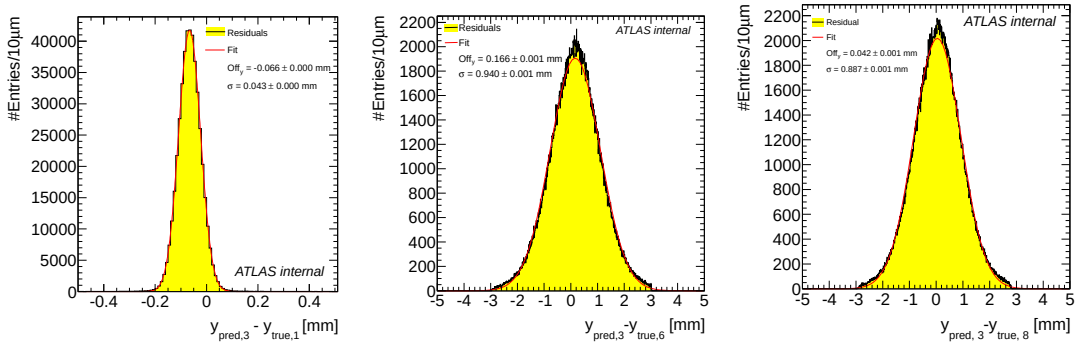

Figure 7.6: Residual distribution using detector 3 (A7L1U) before alignment. The difference in standard deviation between the three distribution is related to the divergence

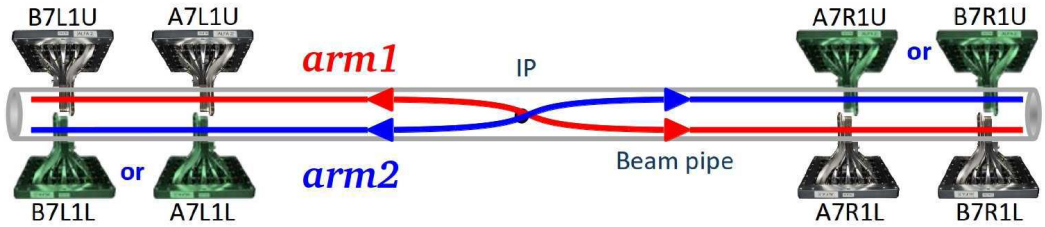

Figure 7.7: Illustration of the two ALFA elastic arms. *Arm1* is defined by the opposite coincidence of the 2 upper detector on the IP left side and 2 lower detector on the right side. *Arm2* is the opposed arm.

7.3.2 Events selection

This section shows the list of selection criteria used to select elastic like events. All the data used in this analysis were recorded in one single run 191373 in October 2011 (see table 6.1). Only one bunch with nominal intensity of about $7 \cdot 10^{10}$ protons is used in the analysis, since the other 13 bunches were all pilot bunches with less intensity but more halo background; Also, the luminosity can be reliably determined only for this bunch. A list of good luminosity blocks was collected requiring an LB duration longer than 60 seconds and a dead-time below 5%. In the list are about 240 LBs and average life fraction is 99.73%. Events in these LBs are then selected at the trigger level requesting the CTP bits L1 ELAST_15 (*arm1* configuration) or L1 ELAST_18 (*arm2*) to be set; ELAST_15 requires the trigger of station (*B7L1U* or *B7L1U*) and (*B7R1L* or *B7R1L*) and ELAST_18 requires the trigger of station (*B7L1L* or *B7L1L*) and (*B7R1U* or *B7R1U*). More information about the ALFA trigger system can be found in § 4.4.2.
At the next stage at least one track is requested to be reconstructed in all four detectors of an arm. To the tracks on the left and right side several cuts are then applied first to ensure that the event is fully contained in the fiducial volume where a high efficiency and good spacial resolution are maintained (figure 7.9(a)), and second on the acollinearity of the events exploiting the back-to-back topology of elastic events.
In detail, the following cuts are applied:

- A cut is put on the vertical coordinate at edge of the detectors close to the beam, the position of the edge was determined by means of metrology and measured in the test beam. The cut is placed at a distance of 60 μm from the edge, where the fibre detection efficiency was measured to be above 99%. The cuts for each detector are summarized in Table 7.2.
- A second vertical cut is put at the other end of vertical range around 20 mm. In this region the contributions from showers generated by particles hitting the beam screen of Q6 increases. Protons hitting the beam screen are outside of the acceptance, but shower fragments might be reconstructed as fake elastic protons. The position of the shadow of the beam screen is visible as an edge in the y-distribution and the center of this edge was

Table 7.2: Vertical acceptance defining cuts for each detector.

Detector	Edge cut [mm]	Beam-screen cut [mm]
1	5.926	20.144
2	-6.074	-18.923
3	6.242	21.155
4	-6.306	-19.934
5	6.167	19.565
6	-6.265	-21.223
7	5.946	18.652
8	-6.114	-20.197

determined. The cut is placed one mm away from this edge sufficiently far to suppress shower contributions. The cut values are also summarized in Table 7.2.

- The acollinearity of elastic events is a good handle against background, on the other side the back-to-back topology is diluted by the beam divergence and detector resolution effects. In practice the cuts are placed on the correlation between left and right measured positions in x and y, as shown in figure 7.8. For the horizontal coordinate some uncorrelated bands appear in the correlation plot which originate from accidental beam halo coincidences. Elastic scattering events are confined in a narrow correlation pattern which can be parametrized by a 2D Gaussian distribution. The widths and angle of rotation are determined simulation and an elliptical cut is placed 3.5 σ (Gaussian σ), preserving more than 99% of the elastic events. For the vertical coordinate simple straight-line cuts are used requiring the events to be at a distance of not more than 3 mm from the diagonal, which is again the case of more than 99% of the elastic events according to simulation.
- A rather discriminant observable against background from halo accidentals and combinations of halo protons and protons from single diffraction is the correlation between the horizontal coordinate and the local horizontal angle reconstructed between two stations. The elastic data appear to be confined to a narrow anti correlation pattern of elliptical shape, while the background populates an correlated vertical band and an ellipse of negative correlation, as shown in figure 7.8. The elastic is again parametrized with a 2D Gaussian function and the elliptical cut is placed at 3.5 σ.

Table 7.3 gives the statistics of run 191373, at different selection cut stages. First row is the total number of recorded events during the runs. Reconstructed elastics row gives the number of elastics event per arm, making sure that L1 trigger has fired and at least one track is reconstructed per detector arm. Back-to-back cuts row shows the total number of events per arm after the selection of (y_A vs. y_C), (x_A vs. x_C) and (θ_x vs. x) cuts. Cuts in y is described by

Table 7.3: Total number of elastic events per arm at different selection levels.

Selection cut	**arm1**	**arm2**
Total recorded events	6620953	
Selected Bunch	1898901	
Good LBs	1822128	
Reconstructed elastics	459229	428213
Back-to-back cuts	434073	410558
Cuts in y	415965	389463
Pile-up	1060	
Total	805428	

figure 7.9(a).
Figure 7.9(b) shows the efficiency of the cuts for different elastic arms as function of t distribution. It was deduced by the application of data selection cuts (elliptical and linear) on the MC generated model. As there is no background in the simulation, we will study the cuts impact on elastics. One can conclude that cuts impact only large t-values.

The data selected after all cuts contain a small fraction of irreducible background at the level of 1%, mostly beam halo accidentals, which are analyzed in § 5.1.3.2. The sample also contains a very small fraction of elastic pile-up events at the level of 0.12%, which are observed in case the two overlapping elastic events are in two different arms and pass individually all cuts. Each of the two elastic events are used for the cross section determination. The same fraction of pile-up events is expected to be present in the same arm, but in this case it is difficult to separate the events. Thus only one event, the more elastic-like, is taken. Therefore a correction is derived for the non-observed pile-up events by scaling the observed elastic pile-up events by a factor of two.
The cut-flow of the number of events in the two arms after each selection or cut is given in table 7.3. At the end of the selection procedure about 800,000 elastic events survived all cuts. A small asymmetry is observed between the two arms, which can be traced back to the detectors not being all at the same distance, asymmetric beam-screen positions and background distributions.

The evolution of the elastic events as function of LB is shown in figure 7.10. The gap in the distribution referred to bad LB and will be removed later. The number of elastics decrease by about 500 events per LB between the begin and the end of the run. Selected events distribution (in red) by the back to back cut, follows the original distribution and show no dependence per LB, or per time (one LB is about 60 seconds). Figure 7.11 shows the horizontal distribution of elastic events at different ALFA detector. Knowing that (x_A vs. x_C) and (θ_x vs. x) affect events with large x value, comparison of the red and black curves shows that events (y_A vs. y_C) is an important complementary cut, which succeeds to reduce bad elastics event at small x value.

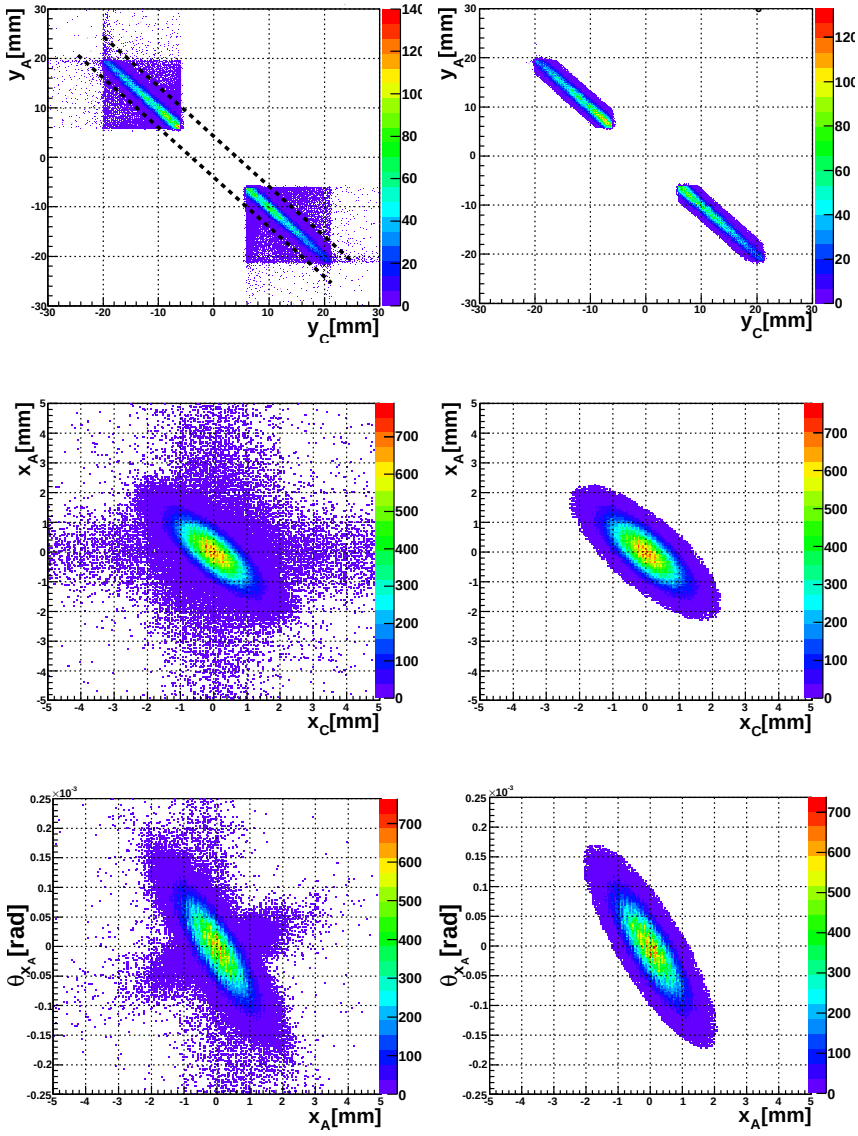

Figure 7.8: Different selection cuts (y_A vs. y_C), (x_A vs. x_C) and (θ_x vs. x) on data distributions. Left plots show distributions before applying cuts. Right plots show clean data distribution.

7.3.3 t-reconstruction methods

This § describes how one can use the detector observables (x and y reconstructed position) to reconstruct the t-variable by two different methods.
One of the methods, called *subtraction* is based on the subtraction of the reconstructed positions on both IP sides ($u_L - u_R$) to cancel the vertex contribution and was introduced in § 4.1.1. The θ^* can be written as:

$$\theta^*_u = \frac{u_L - u_R}{2L_{eff,u}} \equiv \frac{u_A - u_C}{M_{12,A} + M_{12,C}} \tag{7.1}$$

where the left (L) and right (R) notations were replaced by *side-A* and *side-C* notations (introduced in the ATLAS coordinate system § 2.1). Separation of the level arm (or the M_{12} term)

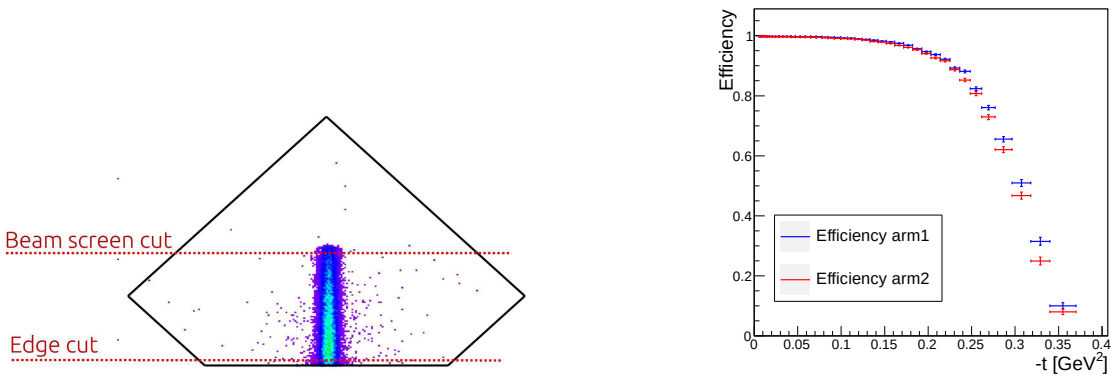

(a) Vertical plane fiducial cuts.

(b) Selection cuts efficiency for different arms. This is the result of a simulation study, where cuts applied on the data were re-applied on simulation.

Figure 7.9: Cuts in y and selection cuts efficiency.

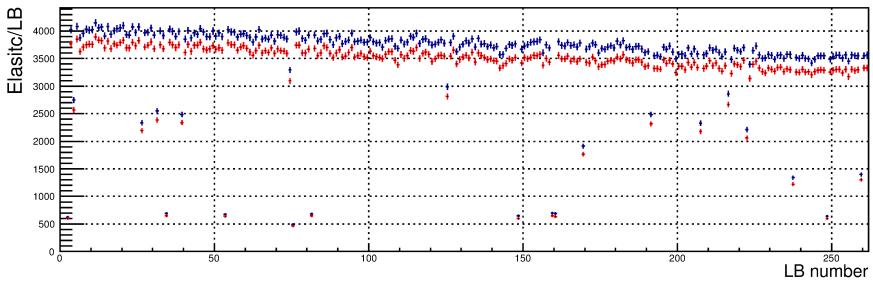

Figure 7.10: Elastic events evolution as function of LumiBlock (LB). Colors refer to elastics before the back-to-back selection cut (blue) and after it (red).

takes into account a slightly larger asymmetry between beam 1 and beam 2.
This method yields already an excellent reconstruction of the vertical scattering angle component with the large level arm $M_{12,y}$. However, in the horizontal plane, the ratio of $M_{11,x}$ to $M_{12,x}$ is less favorable ($\Delta\psi_x = 185°$, see table 7.1), and the $M_{11,x}$ term have to be taken into account. Eq. (7.1) is used for the inner and outer stations separately giving two t-values per event. Finally, one uses:

$$-t_s = \left((\theta^*_{x,s})^2 + (\theta^*_{y,s})^2\right) p^2 \quad , s = 237 \text{ or } 241 \text{ m} \tag{7.2}$$

$$t = (t_{237} + t_{241})/2 \tag{7.3}$$

Another method used for the θ^*_x reconstruction is based on the reconstructed angle (θ_x) at the RP, and called **local angle** method. It uses the $M_{22,x}$ term of the transfer matrix, in order to compute the θ^*_x, which can be written as:

$$\theta^*_x = \frac{\theta_{x,A} - \theta_{x,C}}{M_{22,A} + M_{22,C}} \quad , \tag{7.4}$$

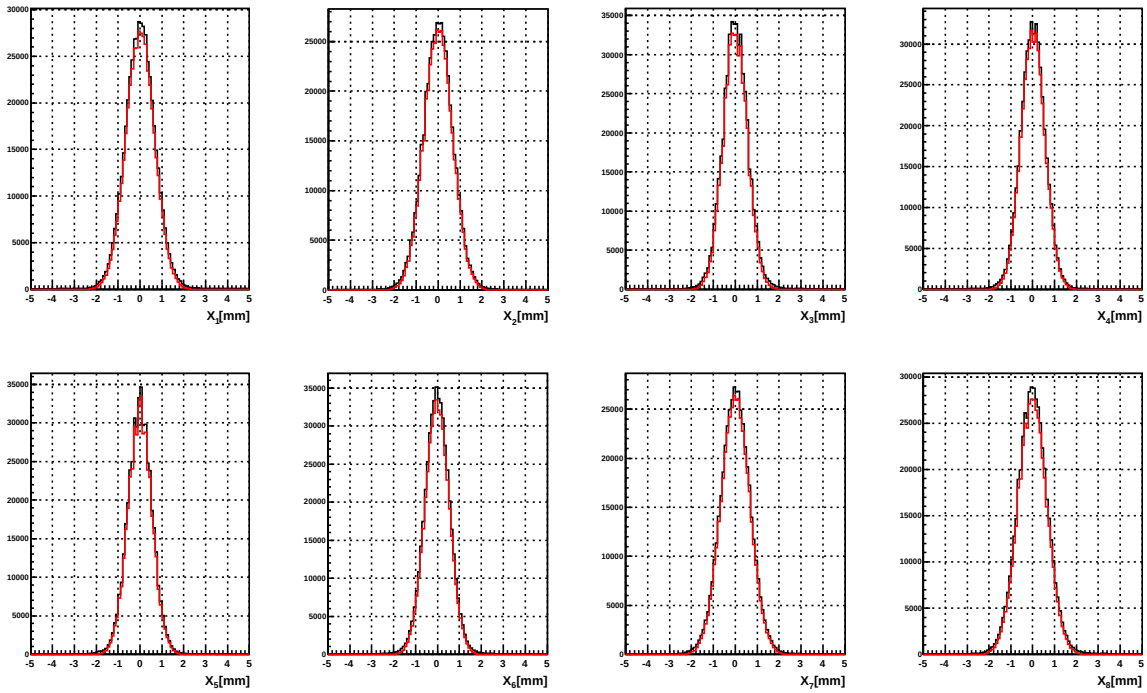

Figure 7.11: Horizontal distribution of the elastic events for different detector. Colors refer to elastics before the back-to-back selection cut (black) and after it (red).

where again the term proportional to the vertex is disregarded. The local angle (θ_x) is calculated using the reconstructed x position in the inner and outer station of the same side (A or C). Only one measurement per event can be done, as there is only one local angle between the two stations, and the matrix elements M_{22} are the same at 237 m and 241 m, no active magnetic element being in between the stations.
The advantage of this method in the horizontal plane lies in the angular lever arm M_{22} being proportional to $\sin(\Delta\psi)$, while the term in $\cos(\Delta\psi)$ is damped by a factor (α) and hence the matrix element is less sensitive to uncertainties in (ψ). On the other hand, the resolution of the local angle is moderate with about 10 μrad, because the distance of the two stations is only about 4 m. As a consequence the t-resolution of the *local angle* method is worse than for the *subtraction* method, but optics-related systematic uncertainties are reduced. This method will suffer of high unfolding correction, as shown in the following. Figure 7.12 shows difference in the t-resolution between both methods. The resolution is defined by the difference between generated-t ($\hat{t}$) and reconstructed one (t_{reco}).

7.3.4 Background

The event selection cuts have been applied on the 3.5 σ level, which keep a very good efficiency. However, there might have been a handful of non-elastic events that have passed the cuts (i.e. background). To estimate the level of contamination by this type of events, we

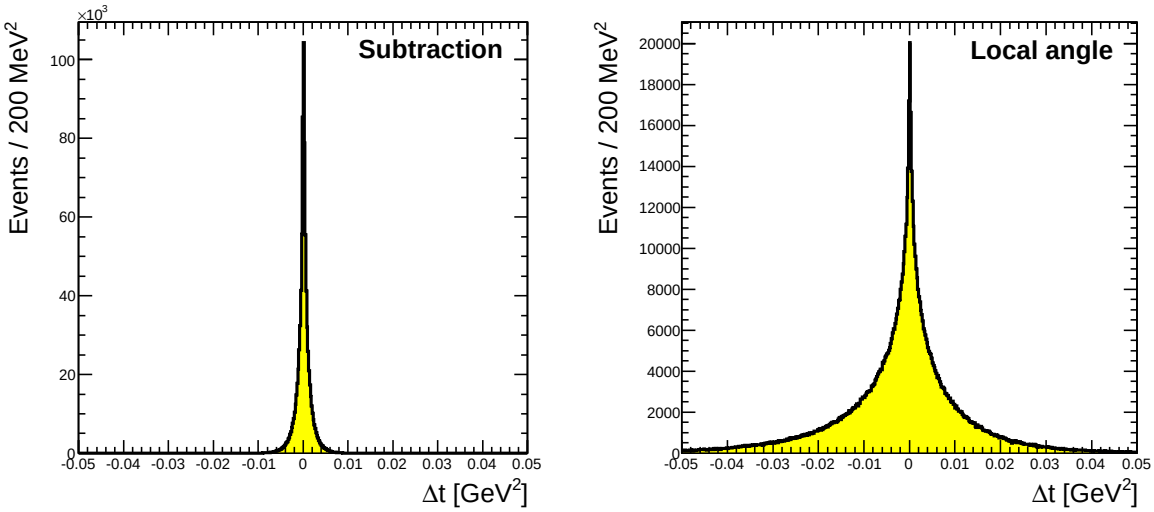

Figure 7.12: t-resolution for different reconstruction method using a MC simulated sample.

studied accidental coincidence of the four upper (resp. lower) detectors. Figure 7.13 shows the background arm configurations. This study requested at least one track per detector of the corresponding arm. The same tracks reconstruction criteria are used, as in the elastic analysis, and a t-spectrum can be reconstructed. This is achieved by inverting the sign of one of the pro-

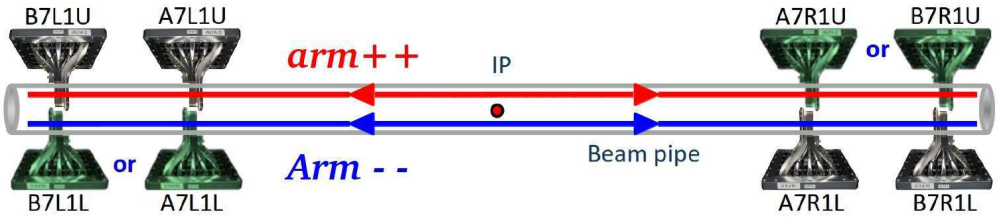

Figure 7.13: Background's arms configuration, $arm{+}{+}$ for upper coincidences and $arm{-}{-}$ for lower ones.

ton track coordinates on either side in order to flip the event artificially from the anti-golden into the golden topology. The limitation of this method is the assumption that the beam halo is the same in the upper and lower detectors and the assignment of the constructed background t-distributions to arms is arbitrary.
Afterwards, events are flipped into the golden configuration by changing the sign at a randomly selected side. After that operation all standard event selection cuts are applied. The resulting number of background events is given in table 7.4 along with statistical and systematic uncertainties. Systematic uncertainties are obtained by changing the side on which the sign is flipped both x and y coordinates and by flipping only the sign in y.

The reconstructed t-spectrum for the elastic sample in arm 1 is compared to the back-

	arm++	arm−−
Nominal	2814	1353
Statistical error	±53	±37
Systematic error	±56	±108

Table 7.4: Number of background events in each arm with systematic uncertainties obtained with the anti-golden method.

ground spectrum in figure 7.14. The shape of the background is clearly different from elastics, much more peaked at small values of t and falling off with a steeper slope. Furthermore the spectrum continues to rise continuously towards small t-values, Accidental protons are in contrast uncorrelated on the right and left side and have an almost flat acceptance up to the detector edge. The background distributions are subtracted on the raw t-spectrum, before the distributions are unfolded to account for resolution effects.

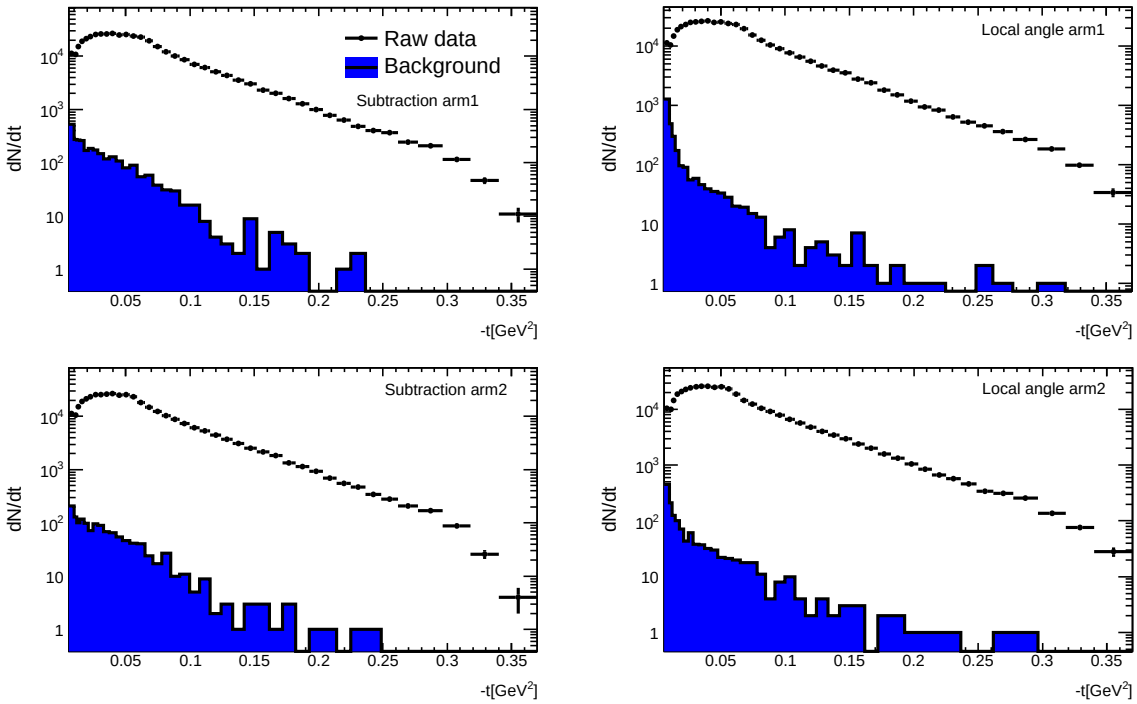

Figure 7.14: Raw data versus background distribution for different arms and t-reconstruction methods.

7.3.5 Unfolding

Experimental distributions of t variable are altered by finite detector resolution and beam smearing effects including divergence of the beam, vertex smearing and energy dispersion.

Accordingly, a transfer of events between different regions of the spectra is expected. The t-reconstruction method itself may increase or reduce this migration effect. Provided that they are well controlled experimentally, all these effects can be included in the Monte Carlo simulation (MC) of the detector response, which can be used to correct the data.

The detector response is encoded in a T-matrix[1] connecting the measured and true variables under study.

In this section a comparison of different unfolding and t-reconstruction methods is represented together with systematic and statistical errors. An Iterative Dynamically Stabilized (IDS) method of data unfolding have been used, of which a full description can be found in [64].

7.3.5.1 Method description

The IDS unfolding uses a regularization function $f(\Delta x, \sigma, \lambda)$ to dynamically reduce the fluctuation which can produce fake event transfers. It is a smooth monotonic function going from 0, when $\Delta x = 0$, to 1, when $\Delta x \gg \sigma$. Δx is the deviation between data and simulation in a given bin with the corresponding error σ, and λ is a scaling factor, used as a regularization parameter.

Performing the comparison between data and reconstructed MC is another important ingredient of the unfolding procedure, keeping in mind that the data may contain structures, which were not (well) simulated in the MC. Operating the regularization function introduced before, it counts the events in data (N_d^{MC}) without including the those corresponding to significant new structures. Data/MC normalization factor is obtained by dividing N_d^{MC} by the number of events in the MC (N_{MC}) in an iterative way.

The T-matrix provided the number of generated events in the bin j and reconstructed in the bin i, A_{ij}. Then, the unfolding probability matrix P_{ij} which corresponds to the probability of an event reconstructed in the bin i to be simulated in the bin j, is written as $P_{ij} = \frac{A_{ij}}{\sum_{k=1}^{n_b} A_{ik}}$. Here n_b is the total number of bins.

Finally, for a bin $j \in [1; n_b]$, the unfolding is given by:

$$u_j = t_j \cdot \frac{N_d^{MC}}{N_{MC}} + \sum_{k=1}^{n_d} f(|\Delta d_k|, \sigma d_k, \lambda)\Delta d_k P_{kj} + (1 - f(|\Delta d_k|, \sigma d_k, \lambda))\Delta d_k \delta_{kj} \qquad (7.5)$$

With $\Delta d_k = d_k - \frac{N_d^{MC}}{N_{MC}} \cdot r_k$, where, for a given bin k, t_k is the number of true MC events, while

[1] Stands for transfer matrix, but to separate it from the optics transfer matrix, we will use the T-matrix notation.

σ is the uncertainty to be used for the comparison of the data (d_k) and the reconstructed MC (r_k).

The first contribution to the unfolded spectrum is given by the normalized true MC term ($t_j \cdot \frac{N_d^{MC}}{N_{MC}}$), which we do not transfer from one bin to another. Then one adds the number of events in the data minus the normalized reconstructed MC, the Δd_k term. A fraction f of these events are unfolded using the estimate of the unfolding probability matrix P, and the rest are left in the original bin.

7.3.5.2 Unfolding correction

Unfolding correction depends on t-reconstruction method in use. The *local angle* method suffers from bad t-resolution, compared to *subtraction* method, as explained in § 7.3.3. Bad resolution causes a large transfer between bins (generation bin and reconstruction one). This can be visualized in figure 7.15, where left (resp. right) plots show the T-matrix distribution for *subtraction* (resp. *local angle*) method. The large spread of the *local angle* T-matrix distribution, is the result of large bin to bin transfer. This T-matrix is produced using the simulation procedure (see § 7.2). Its projection on the x-axis gives the true generated distribution ($t_{true} \equiv \hat{t}_{acc}$), and on the y-axis gives the t-reconstructed distribution, which takes into account the detector resolution[2], and the beam smearing effects.
The unfolding procedures have to be applied independently on each arm, and for different methods. As shown in the general analysis workflow, figure 7.4, the unfolding comes before the application of acceptance and efficiency corrections. It uses the **raw t-reco** as data input, and the simulated T-matrix.
Figure 7.16 shows the unfolding correction needed per arm for both t-reconstruction methods as function of t. The *subtraction* method shows a flat distribution close to 1 (which mean negligible correction need to be applied on the data spectrum), compared to the *local angle* method, which have a large correction factor, up to $\approx 40\%$ at $-t = 0.3$ GeV^2.

This is the results of the IDS unfolding methods. It is instructive to compare the results of different unfolding methods, especially for systematic studies. In the following we will add two different unfolding strategy to our analysis: the baseline bin-by-bin method, and the Singular Value Decomposition (SVD) [65].

[2]Is simulated by randomly spreading each track at the detector using a Gaussian distribution (*sigma* < 30 μm) and characterize the resolution of different detectors.

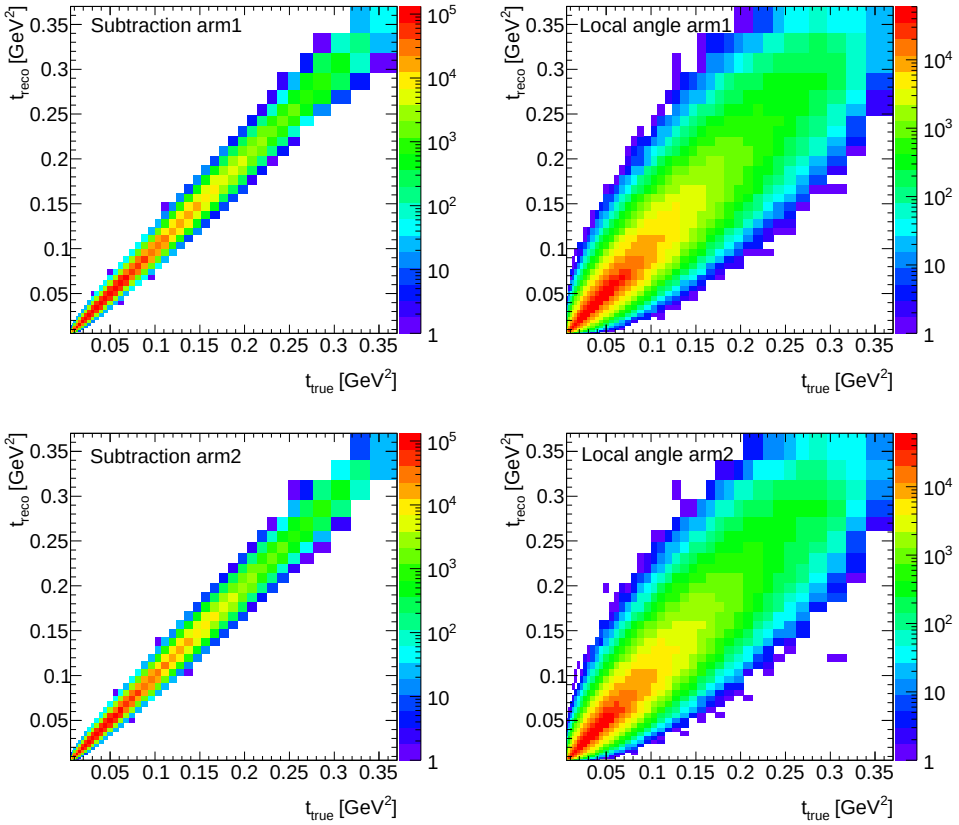

Figure 7.15: T-matrix for different t-reconstruction methods and arms. It's the distribution of the reconstructed t-spectrum (t_{reco}) as function of the true generated one (t_{true})

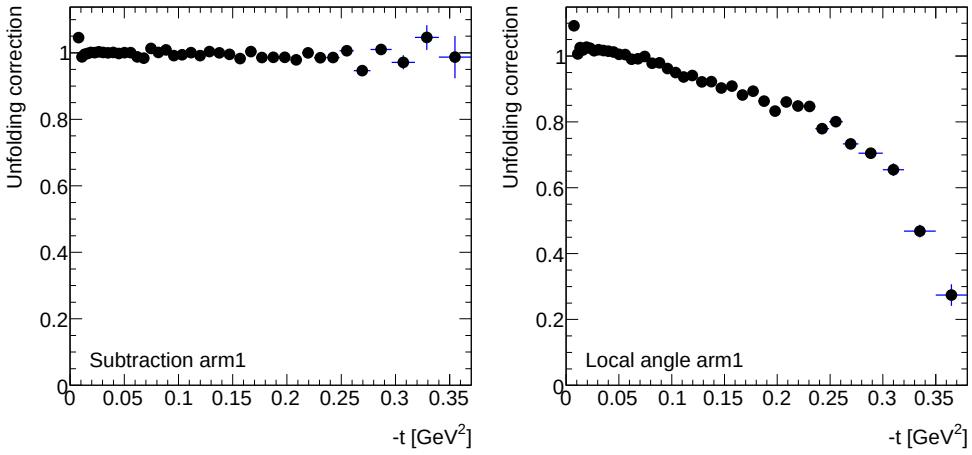

Figure 7.16: Unfolding correction for elastic arm1 and different t-reconstruction methods, as function of t. Elastic arm2 is not shown, but it's similar to arm1. Local angle method requests large unfolding corrections. This is mainly due to the bad t-resolution coming from the use of this method. *Subtraction* shows flat correction over the whole t-range.

7.3.5.3 Statistical uncertainty

Statistical errors are propagated through the unfolding procedure using toy models. *Data toy* models are build, inspired directly by the original data spectrum, by fluctuating spectrum bins

around the statistical errors. In the same way we also generate a *reconstructed MC toys* and a modified T-matrix (*A'*) toys using the reconstructed MC spectrum and the T-matrix (*A*).
The unfolding of the *N data toy* ($N = 1000$) by the (*A'*) results *N toys unfolded spectrum*, therefore one can deduce a mean unfolded spectrum and its corresponding covariance matrix. The covariance matrix is defined as:

$$\mathrm{cov}(X_i, X_j) = \Sigma_{ij} = \frac{1}{N_{toy}} \sum_{toy=1}^{N_{toy}} (X_{toy,i} - \bar{X_i}) \times (X_{toy,j} - \bar{X_j}) \tag{7.6}$$

where, considering an unfolded data toy, $X_{toy,i}$ return the value in a bin i of the toy, $\bar{X_i}$ is the mean toys value of the bin i, and N_{toy} in the total number of generated toys.
This matrix contains all information needed for statistical error propagation, taking into account the bin to bin correlation effect.

Table 7.5: Absolute statistical errors propagated to the different fit parameters, for different unfolding and t-reconstruction methods, using different errors propagation strategies.

Statistical Error	**Subtraction**		**Local-angle**	
Parameters	b-slope [GeV^{-2}]	σ_{tot} [mb]	b-slope [GeV^{-2}]	σ_{tot} [mb]
IDS^{cov}	0.048	0.118	0.043	0.107
IDS^{toy}	0.051	0.133	0.049	0.119
Bin by Bin	0.052	0.130	0.050	0.131

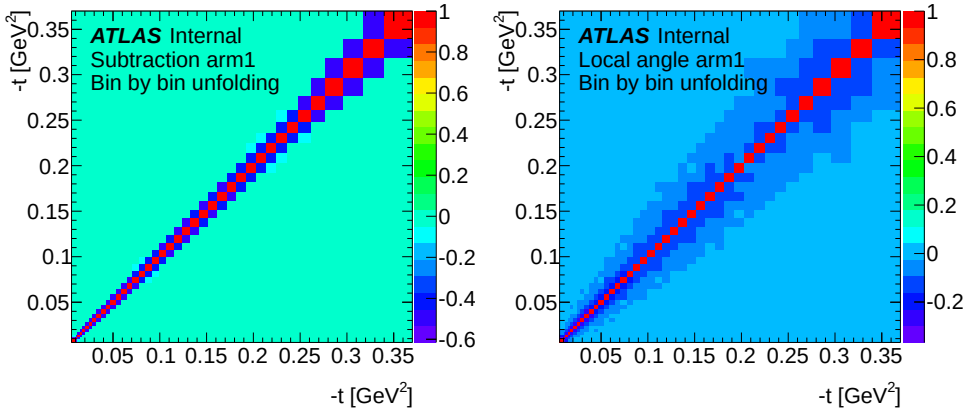

Figure 7.17: Comparison between covariance matrix of *subtraction* (left) and *local angle* (right) strategy for Bin by bin unfolding method.

Unfolded spectrum using *bin by bin* method presents only short range correlation effect between bins, due to the fact that correction is performed by multiplying the reconstructed spectrum by a correction factor. Therefore, considering that non-diagonal term are negligible,

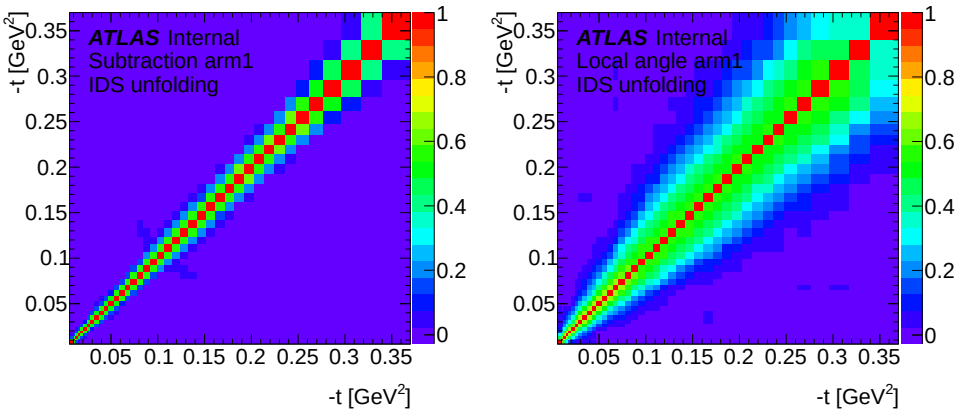

Figure 7.18: Comparison between covariance matrix of *subtraction* (left) and *local angle* (right) strategy for IDS unfolding method.

one can write $\Sigma_{ii} = \sigma_i$ where σ_i represents the statistical error for a given bin (i). In this case, statistical error (σ_i for a given bin i) is the propagated to the fit parameters using the basic χ^2 minimization procedure

$$\chi^2 = \sum_{k=1}^{n_d} \left(\frac{d_k - t_k}{\sigma_k} \right)^2 . \tag{7.7}$$

In the other hand, IDS and SVD methods have shown correlation between bins, due to the bin to bin migration. Correlations are stronger for the *local angle* method than the *subtraction* one (see figure 7.18). Statistical error will be under-estimated (reduced) if propagation do not take correlation terms into account (the non-diagonal matrix term). This error reduction is estimated by $\approx 23\%$ for *subtraction* method, and $\approx 37\%$ for *local angle* method.

As correlation effects are not negligible, data will be fitted using the general χ^2 form, where the covariance matrix is taken into account:

$$\chi^2 = \sum_{i=1}^{n_d} \sum_{j=1}^{n_d} (d_i - t_i) \times (d_j - t_j) \times \Sigma_{ij}^{-1} \tag{7.8}$$

with Σ_{ij}^{-1} represents the inversed covariance matrix of considered bins i and j. Results are summarized in table 7.5, in the IDS^{cov} row.

Another method is also considered. Statistical error is propagated in this case using fit parameters fluctuation of all unfolded data toys. The whole analysis chain (acceptance, reconstruction efficiency, luminosity normalization, ...) is applied for each toy, transforming the $\frac{dN}{dt}$ to $\frac{d\sigma}{dt}$.
Final parameters values are deduced using the mean of all toys fit parameters, and corresponding statistical errors represent the RMS of the toys fit parameters vector. Results are reported in table 7.5, in the IDS^{toy} row.

7.3.5.4 Systematical uncertainty

Systematical errors are estimated by comparing the result of data unfolding with the true MC model, but to have realistic results, one should take into account possible difference between data and MC. Thus, we defined the polynomial function (f) to describe the ratio between *data* and reconstructed MC (*rMC*). This ratio is shown in figure 7.19 for different arms and t-reconstruction methods. In the range of [0.015, 0.130] GeV^2, all ratios are close to 1. It means that the MC model match the data. This was not possible without the fine optic tunning (describes later). The *modified rMC* is the result of the MC bias by the f function.

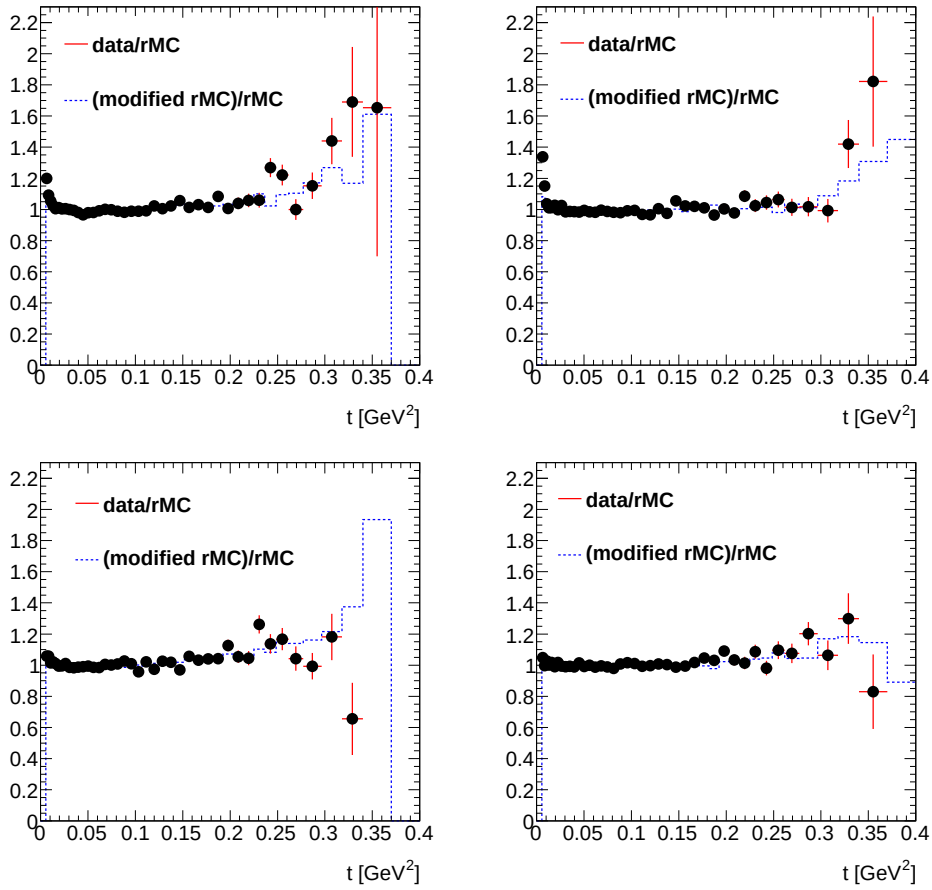

Figure 7.19: Ratio showing the difference between *data* and the reconstructed MC model (*rMC*). It's used then to bias the reconstructed MC (modified *rMC*). Left plots corresponds to arm1 (upper) and arm2 (lower) *subtraction* method, and right ones correspond to the *local angle* t-reconstruction method.

Errors estimation and propagation procedure is summarized in flowchart of the figure 7.20 and detailed in the following:

1. *True MC model* is biased by the difference between *data* and the normalized *rMC*, multiplied by a constant factor, in order to get the *toy data model*;

2. *toy data model* is then folded[3] by the T-matrix A;
3. result of this folding is a *toy reconstructed model*, needed for the unfolding procedure;
4. data is unfolded using the T-matrix A;
5. Systematic uncertainties is then deduced by computing the difference between the unfolding result and the *toy data model*. In other words, it's the difference between the unfolded data and the true MC model, taking into account the data-MC differences, which may be related to other effects (alignments, physics model, ...).

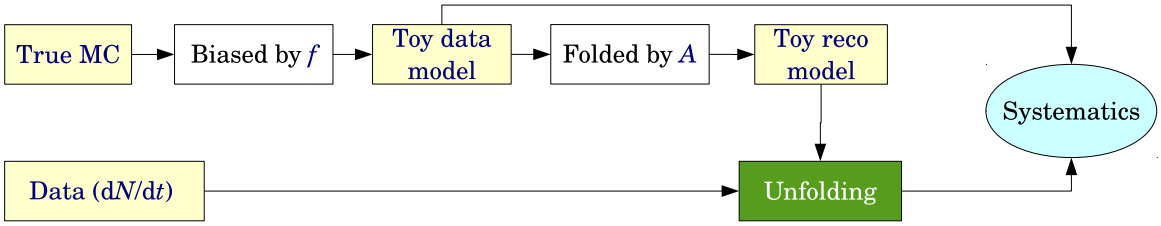

Figure 7.20: Flowchart of the systematic errors estimation.

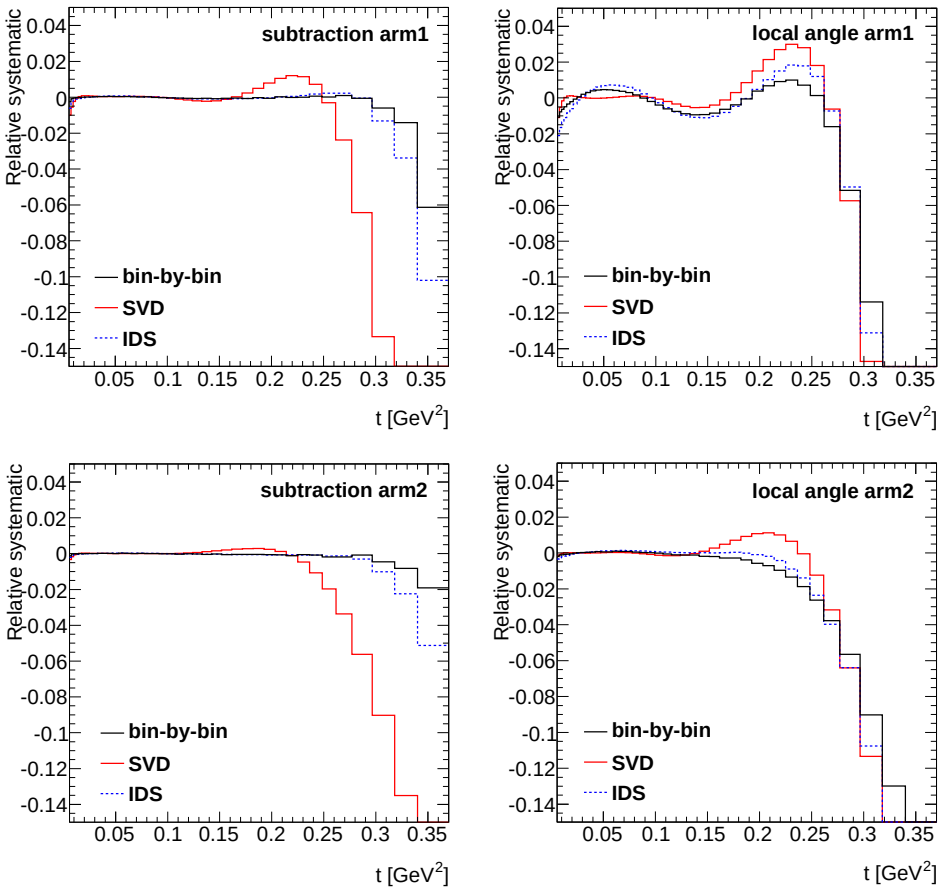

Figure 7.21: The relative systematic errors as function of t-values, for different unfolding and t-reconstruction methods.

[3]Using the folding matrix, which gives the probability for a an event generated in a bin j to be reconstructed in bin i.

Results are shown in figure 7.21 for different unfolding procedure and t-reconstruction methods. The relative errors distribution is mainly related to the "f" function distribution and the unfolding correction. It's negligible (in the order of 1‰) in the range of [0.015, 0.130] GeV^2 (acceptance > 0.3), for both reconstruction methods and arms. Therefore, for large $|t|$-values systematic becomes larger, since the "f" function shows some deviation in this range, and the unfolding correction is higher (in comparison with small t-range).
As for statistical case, errors propagation to the fit parameter is achieved by applying the whole correction procedure on the *data* unfolding result and the *toy data model*, in order to get the $\frac{d\sigma}{dt}$. Then both were fitted, and systematic errors are deduced by comparing the fit result parameters of different cases. Table 7.6 summarizes the systematic error for different unfolding and t-reconstruction methods.
Since the fit is only in the range of [0.015, 0.130] GeV^2, the propagated error is negligible as expected from the relative systematic distributions. The "Method" raw in table 7.6 is the maximum deviation between different unfolding method results, in term of cross section and b-slope. This error is added to systematic to be more conservative.

Method	**Subtraction**		**Local-angle**	
Parameters	b-slope [GeV^{-2}]	σ_{tot} [mb]	b-slope [GeV^{-2}]	σ_{tot} [mb]
IDS	0.005	0.013	0.006	0.051
SVD	0.011	0.039	0.003	0.032
Bin by Bin	0.021	0.062	0.047	0.124
Methods	0.016	0.078	0.052	0.125

Table 7.6: Absolute systematic errors propagated to the different fit parameters, for different unfolding and t-reconstruction methods.

7.3.6 Acceptance correction

The acceptance correction takes into account the elastic proton loses between the IP and the RP, due to beam losses (i.e. proton hits the beam screen) and the detector acceptance geometry. Acceptance is calculated using the simulation, the Monte-Carlo generator PYTHIA8 produces elastic proton collisions at the IP, where one can reconstruct a t-distribution at the true level ($\hat{t}$). Protons will be transported to the RP station using the MadX software. MadX uses the transfer matrix introduced in (1.4) and takes into account the geometrical form of the LHC elements between the IP and RP. At the RP longitudinal position, elastic protons will be accepted within the transversal geometrical acceptance of the detector. Protons outside the lower and upper detector edge, and beam screen will be rejected. These edges position are deduced from the alignment procedure. Using accepted events, one can compute the $\hat{t}_{acc}$ distribution.

The ratio between ($\hat{t}$) and ($\hat{t}_{acc}$) gives the acceptance distribution, will be used later to correct the data t-spectrum and summarized in table 7.2. This correction takes into account only geometrical effects (detector edge and beam screen). Figure 7.22 shows the acceptance correction as function of t. Thus, we distinguish two different behaviors: below ≈ 0.6 GeV^2, an increasing acceptance due to lower edge limits, and beyond this value a decreasing acceptance due to beam screen and upper edge limits.
Correction below 30% will not be considered in the final fit. Therefore, the fit region is limited to [0.015, 0.130] GeV^2.

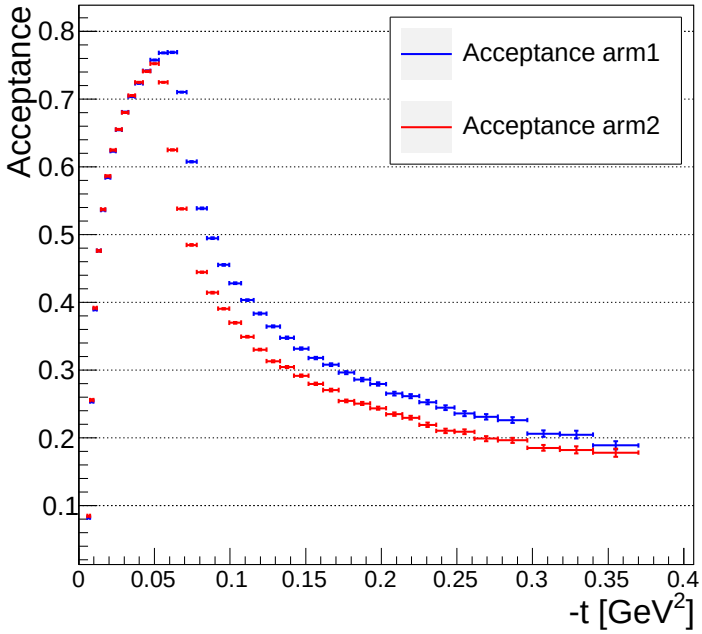

Figure 7.22: Acceptance calculated using PYTHIA 8 for elastic proton generation and MadX to transport them to the RPs. The range between 0 and 0.06 GeV^2 is the detector edge acceptance limits, and the range > 0.6 GeV^2 show the beam screen limits. Asymmetric acceptances are due to different beam screen cuts.

7.3.7 Efficiency estimation

For elastic events with two protons in back-to-back configuration one would expect a reconstructed track in each of the four detectors of the corresponding elastic arm. But due to electromagnetic showers, background or pile-up events it is possible to have more than one track in one or several detectors. To a certain amount these additional tracks are handled and reconstructed by the multiple track algorithm. But in case of large amount of tracks, the reconstruction will fail and no track at all will be reconstructed. This leads to a reconstruction inefficiency of elastic events.

The track reconstruction efficiency for elastic events is in general a function of t and defined as:

$$\varepsilon(t) = \frac{N_{\text{reco}}(t)}{N_{\text{reco}}(t) + N_{\text{fail}}(t)} \tag{7.9}$$

where N_{reco} is the number of fully reconstructed elastic events, in other words, have at least one reconstructed proton track in each of the four detectors of one elastic arm. N_{fail} is the number of partially and not reconstructed elastic events, which have reconstructed tracks in less than four detectors of one elastic arm or no track at all. The determination of reconstruction efficiency in such a way uses only data and is independent of Monte-Carlo simulations.
The 3/4 cases represented in figure 7.23, is the dominant inefficiency case. Eq. (7.9) can then

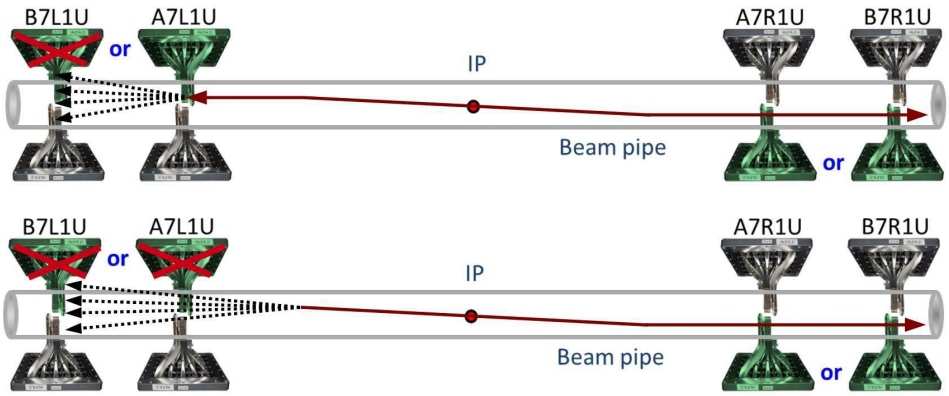

Figure 7.23: Upper figure illustrates the 3/4 inefficiency case, where 3 of 4 detectors reconstruct tracks (in the same arm), and lower figure shows 2/4 case.

be written as:

$$\varepsilon_{3/4}(t) = \frac{N_{4/4}(t)}{N_{4/4}(t) + N_{3/4}(t)}. \tag{7.10}$$

is determined, without considering the other cases, to verify the t-independence of ε. In order to get $N_{3/4}(t)$, elastic events with only three detectors with reconstructed tracks are taken and reconstructed for t with the *subtraction* method. The use of the *local angle* method is not possible here, because a reconstructed track in one detector is missing and therefore the local angle can only be reconstructed on one side of the IP. The number of fully reconstructed events $N_{4/4}(t)$ is also determined by reconstructing the corresponding events for t with the *subtraction* method. Figure 7.24 shows $\varepsilon_{3/4}(t)$ for both elastic arms separately. A linear function is fitted to both efficiency distributions and shows a small residual t-dependence with a slope of $s_{1368} = (-0.01948 \pm 0.00905)$ for arm 1368 and $s_{2457} = (-0.01602 \pm 0.00985)$ for arm 2457. This is consistent with the assumption of t-independence, but a systematic uncertainty will be assigned due to the small residual slope.

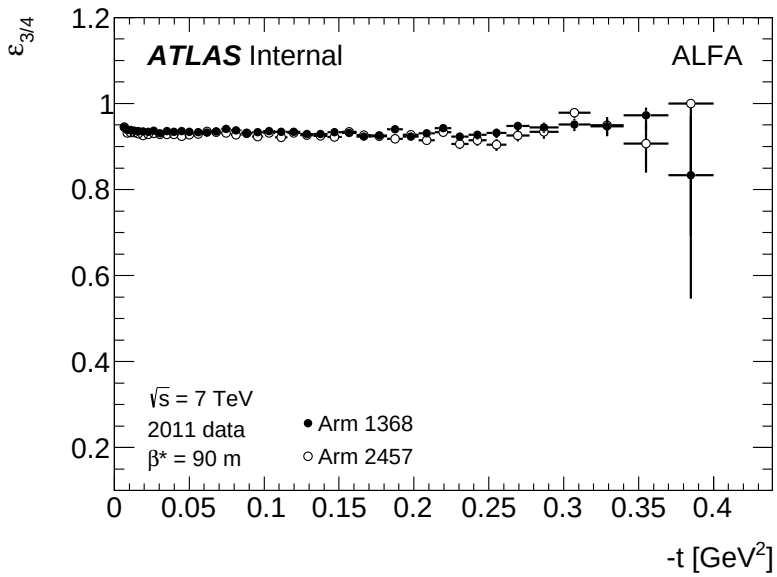

Figure 7.24: Reconstruction efficiency of case 3/4 as a function of t for elastic arm 1368 and 2457 [61].

7.3.8 t-fit and determination of σ_{tot} and b-slope

The long chain of corrections (unfolding, acceptance, efficiency, ...) and background subtraction aims to give the correct number of elastic events per arm, collected during the run period. At this level we assume that we determine the N_{el}, which represents the number of elastic events. The t-elastic distribution is defined as $\mathrm{d}N_{el}/\mathrm{d}t$, which is the deferential number of elastics as function of t.
Thus, the differential elastic cross section can be derived, using eq.(1.1):

$$\frac{\mathrm{d}\sigma_{el}}{\mathrm{d}t} = \frac{1}{L}\frac{\mathrm{d}N_{el}}{\mathrm{d}t} \tag{7.11}$$

where L represents the integrated luminosity. The integrated luminosity value is given by the ATLAS Lumi-group after a deep investigation for this special ALFA run with low luminosity condition. The luminosity value is estimated using the BCMV_OR algorithm, calibrated using vdM scan. The integrated luminosity for the ALFA run is 78413 mb^{-1} and systematical error estimation is summarized in table 7.7.
The theoretical prediction for the differential elastic cross section including the interference term according to equation 3.16 is fit to the corrected t-spectrum with two free parameters, the total cross section σ_{tot} and b, while all other parameters in equation 3.16 are fixed to nominal values, in particular $\rho = 0.14$.

Table 7.7: List of the systematic uncertainties affecting the luminosity determination in the high β^* run (in %) [66].

Measurements	Sys. uncer. [%]
BCM drift	± 0.25
Background subtraction	± 0.20
Time stability	± 1.00
Consistency among measurements	± 1.60
vdM scan	± 1.53
Total uncer.	± 2.45

7.4 Optic problem

The precision of the *t*-reconstruction depends on the knowledge of the elements of the transport matrix. From the design of the 90m optics and with the alignment parameters of the magnets, the magnet currents and the field calibrations all transport matrix elements can be calculated. This initial set of matrix elements is referred to as design optics.
In September/October 2012, once for the first time the analysis chain had been completed for both *subtraction* and *local angle* reconstruction methods, the difference in σ_{tot} measurements between both methods was $\approx 4\%$.
Knowing that the main different between the two methods is the transfer matrix parameters (*subtraction* uses the M_{12} term, and *local angle* method uses the M_{22} term), and after having discarded all other potential explanations, it turns out that important corrections are needed to the design optics, in particular in the horizontal plane where the phase advance is close to 180° and the lever arm M_{12} is rather sensitive to the exact value of $\Delta\psi$, given the term in $\sin(\Delta\psi)$.
It is therefore required to determine the optics parameters from a global fit with constraints obtained from ALFA and machine measurements, using the design optics parameters as start value.

7.4.1 Constraints on optics from data

The recorded elastic tracks can be used to derive directly from the data certain constraints on the beam optics. Two classes are distinguished:

1. From correlations between positions or angles measured either at the *side-A* and *side-C* or at inner and outer stations of ALFA the ratio of matrix elements in the beam transfer matrix are inferred. The resulting constraints are fully independent of any optics input.

2. From correlations in the reconstructed scattering angles using different methods further constraints on matrix elements are derived as rescaling factors. The rescaling factors indicate the amount of rescaling needed to be applied to a given matrix element ratio in order to equalize the measurement of the scattering angle. These constraints depend on the given optics model.

For the first case, several methods have been developed to determine the constraints, and all methods have been validated with simulations including beam transport by MadX. For some constraints a small bias is introduced by the method, resulting from the limited resolution, and a Monte Carlo correction is applied.

The second case of constraints is derived from the assumption that the reconstructed scattering angle must be the same for different methods for a consistent beam optics model. Thus these constraints are obtained for a given reference optics, which is taken to be the design optics.
The most illustrating case is the comparison of the scattering angle in the horizontal plane reconstructed with the *subtraction* method, based on the position and M_{12} , and the *local angle* method, based on the local angle and M_{22} . To derive the constraint a profile histogram is filled with the selected elastic events where the scattering angle from the *subtraction* method is recorded on the *x*-axis and the difference in the scattering angle from the *local angle* and *subtraction* methods $\Delta\theta_x^*$ is recorded on the *y*-axis, as shown in figure 7.25.
If the design optics used in the reconstruction was identical to the real optics, then an es-

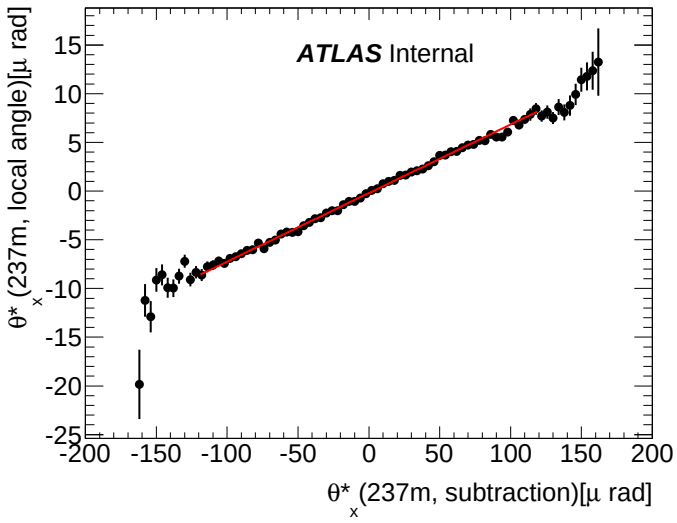

Figure 7.25: The difference in reconstructed scattering angle $\Delta\theta_x^*$ between *subtraction* and *local angle* method as function of the scattering angle from *subtraction* method for the inner detectors. In each bin of the scattering angle the mean value of $\Delta\theta_x^*$ is recorded and the error bar represents the RMS. The line represents the result of a linear fit.

Table 7.8: Summary of the ALFA constraints on beam optics with combined uncertainties [61].

Constraint	Value	stat	syst	total
$M_{12,x}(237\text{m})B_2/B_1$	1.0048	0.0015	0.0026	0.0031
$M_{12,x}(241\text{m})B_2/B_1$	1.0037	0.0010	0.0021	0.0024
$M_{22,x}B_2/B_1$	0.9934	0.0007	0.0046	0.0047
$M_{12,y}(237\text{m})B_2/B_1$	0.9956	0.0001	0.0025	0.0025
$M_{12,y}(241\text{m})B_2/B_1$	0.9975	0.0001	0.0025	0.0025
$M_{12,y}237/241B_2$	1.0488	0.0001	0.0010	0.0010
$M_{12,y}237/241B_1$	1.0480	0.0001	0.0010	0.0010
$M_{22,y}B_2/B_1$	0.9797	0.0002	0.0208	0.0208
$M_{12,x}/M_{22,x}(237\text{m})$	1.0565	0.0003	0.0055	0.0055
$M_{12,x}/M_{22,x}(241\text{m})$	1.0482	0.0002	0.0032	0.0032
$M_{12,y}/M_{22,y}(237\text{m})$	1.0047	0.0001	0.0060	0.0060
$M_{12,y}/M_{22,y}(241\text{m})$	1.0052	0.0001	0.0063	0.0063
$M_{12,y}/M_{12,x}(237\text{m})$	0.9713	0.0052	0.0084	0.0099
$M_{12,y}/M_{12,x}(241\text{m})$	0.9883	0.0057	0.0093	0.0109

sentially flat shape would be observed, with a small slope of about 1% induced by limited resolution of the *local angle* measurement. Figure 7.25 reveals that the scattering angle is measured differently for difference methods, and that difference increases linearly with the absolute value of the scattering angle with a slope of about 6%. This effect can be explained by the difference between the true transport matrix elements and the design transport matrix. The fitted slope is a measure of the true ratio of the matrix elements used in the reconstruction M_{12}/M_{22} to the matrix element ratio in the design optics.
The constraint extracted from the linear fit to the profile histogram is hence defined as:

$$R\left(\frac{M_{12}^x}{M_{22}^x}\right) = \frac{\left(\frac{M_{12}^x}{M_{22}^x}\right)^{\text{true}}}{\left(\frac{M_{12}^x}{M_{22}^x}\right)^{\text{design}}} \quad . \tag{7.12}$$

A summary of the ALFA constraints values obtained from data, is presented in table 7.8, where a list of 14 constraints is shown.

7.4.2 Determination of optics

The set of constraints described in the previous §is used to determine the optics between the IP and the RP on both sides. The free parameters in this determination are the quadrupole strength together with their longitudinal position. This parameters are known with a given

Table 7.9: Fit result for the effective optics, the errors are obtained from the fit and don't include systematic uncertainties.

$\Delta k(Q_1Q_3)$ beam 1	$\Delta k(Q_1Q_3)$ beam 2
2.98 ± 0.15	3.30 ± 0.12

precision defining the phase space of the minimization. From the interaction point to the Roman pots, the magnetic elements of interest are 6 quadrupoles among which the inner triplets. Considering the two beams, it makes a total of 24 free parameters.

Given the large number of free optics parameters (strengths of six quadrupoles in each beam, several alignment constants per quadrupole) and the limited amount of constraints, the phase space of free parameters has to be restricted. The result for the total cross section depends on k-values of the quadrupoles and the main sensitivity is on the inner triplet magnets Q1 and Q3. The choice of Q1 and Q3 is motivated by the maximum sensitivity but is to some extend arbitrary, another choice of magnet strengths to adjust, eventually in combination with mis-alignment offsets, would eventually lead to the same *effective optics* in the sense that the resulting transport matrix is the same. Both Q1 and Q3 were produced at Fermilab, while Q2 was produced at KEK, which could explain a calibration offset below 0.5%.

Therefore, only an inter-calibration offset of Q1 and Q3, called hereafter $\Delta k(Q_1Q_3)$ is fit to the data, independent for beam 1 and beam 2. All other parameters are fixed to design values. The result of this 2-parameter fit is given in table 7.9.

7.5 Results and uncertainties

The raw t-spectrum is reconstructed for the sample of elastic candidates obtained after applying the event selection outlined in Section 7.3.2 using the effective optics described in Section 7.4.1 for the different t-reconstruction methods.
Several corrections are then applied to the raw spectra dN/dt in order to calculate the differential elastic cross section. Most of the corrections are done individually in each arm to get the corrected spectra dN/dt, which are then combined and divided by the integrated luminosity to yield the differential cross section.
In a given t bin, i, the differential cross section is obtained from:

$$\frac{d\sigma}{dt_i} = \frac{1}{\Delta t_i} \cdot \frac{\mathscr{M}^{-1}[N_i - B_i]}{A_i \cdot \varepsilon_i^{\text{cut}} \cdot \varepsilon_i^{\text{reco}} \cdot \varepsilon_i^{\text{trig}} \cdot \varepsilon_i^{\text{DAQ}} \cdot \text{L}} \quad , \tag{7.13}$$

where Δt_i is the bin width in t, $\mathscr{M}^{-1}$ represents the unfolding procedure applied to the background-subtracted number of events $N_i - B_i$, A_i is the geometrical acceptance, $\varepsilon_i^{\text{cut}}$ is the efficiency of

the background rejection cuts to select elastic events inside the geometrical cuts, $\varepsilon_i^{\text{reco}}$ is the reconstruction efficiency, $\varepsilon_i^{\text{trig}}$ is the trigger efficiency, $\varepsilon_i^{\text{DAQ}}$ is the dead-time correction and L is the integrated delivered luminosity for the selected LBs.

The binning of the t-spectrum is selected according to the expected t-resolution at small t to a width of 1.5 times the resolution in σ and at larger t an increased width assuming exponential fall of the distribution.

Figure 7.26 shows the final distribution of the differential elastic cross section after merging both elastic arms. Its parametrization described in § 7.3.8 gives the total cross section and nuclear slope measurements. The fit range is limited to the acceptance correction range, as mentioned before. Both bottom plots show the fit quality over the whole t-range for both reconstruction methods.

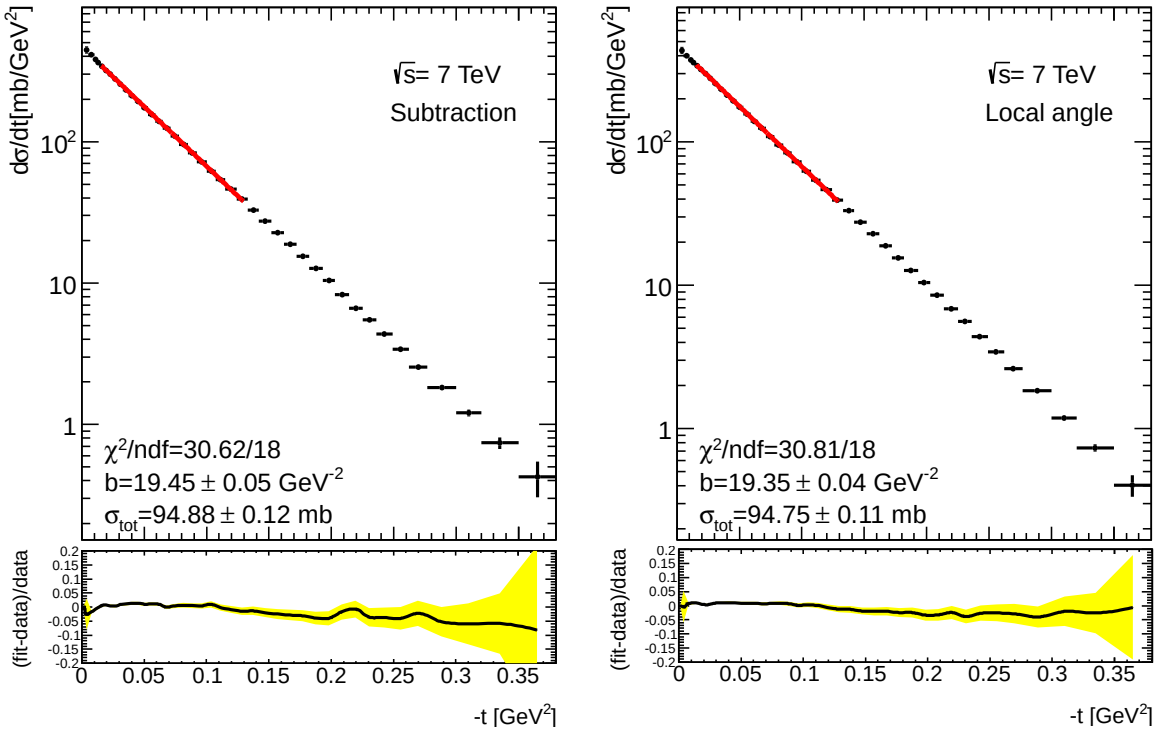

Figure 7.26: The elastic differential cross section distribution fitted using parametrization described in § 7.3.8. Left side corresponds to the *subtraction* method, and right one to the *local angle*. The results for σ_{tot}, b-slope, and the fit χ^2/ndf figure out on the plots.

7.5.0.1 Statistical uncertainties

Here's the list of the statistical uncertainties to be included in the t-fit:

- acceptance correction statistical error, due to the MC simulation limited statistics; 20 M generated elastic where $\approx$ 4 M go through the detectors acceptances
- statistical efficiency cuts error, due to the MC
- error on the track reconstruction efficiency described in § 7.3.7
- error on luminosity measurement due to limited stastics; provided by the ATLAS Lumi group

This list of uncorrelated errors is added (in quadrature) to the diagonal term of the covariance matrix introduced in § 7.3.5.3. It summarized the data stastical error and includes the bin-to-bin correlations due to the unfolding procedure. Afterwards, the fit procedure uses the general χ^2 form presented in eq.(7.8) to correctly propagate the stastical error to the fit parameters.

7.5.0.2 Systematical uncertainties

A long list of systematical uncertainties have to be propagated to the σ_{tot} and b-slope, results of the fit. One can distinguish four different systematic categories:

- **optics:** It is subject to several systematic uncertainties which affects the t-spectrum and the analysis of the total cross section. Variations of the effective optics are obtained for the following systematic effects: constraint systematics, quadrupoles alignment, $\Delta kQ1Q3$ fit errors, and the variation of magnets strength about 0.1%
- **luminosity:** Systematic errors on luminosity were provided by the ATLAS Lumi-group (see table 7.7)
- **experimental uncertainties:** it groups all systematic result of the experimental procedure:
  - reconstruction efficiency: estimated by the variation of event selection cuts between 2.5 σ and 4 σ for elliptical cuts, and in the range of [2.5, 3.5] mm for the linear cuts
  - unfolding: detailed in § 7.3.5.4 and takes into account differences between the MC model and data
  - alignment: is the combination of the distance measurement systematics and the alignments method. Vertical and Horizontal alignments have different systematic errors; $\pm$60 μm in y and $\pm$10 μm in x
  - detector resolution: is varied by its systematic uncertainty in the simulation, replacing the tuned resolution describing the data by the values from the full simulation (underestimating the space resolution by 3-4 μm), by the measured test beam resolutions (overestimating the measured residuals by 4-5 μm) and by using a y-dependent resolution function instead of a flat resolution per detector

  - emittance: used to calculate the angular divergence in the simulation was varied by $\pm 10\%$
  - beam energy: referring to a recent study in [67], the LHC beam energy uncertainty is estimated to 0.65% at 7 TeV
  - t-reconstruction method: to take into account the measurement differences between *subtraction* and *local angle* method
  - the impact of a residual non-vanishing crossing angle in the horizontal plane of $\pm 10\mu$rad corresponding to the precision of measurement using the beam position monitors is evaluated by repeating the simulation with that crossing angle

- **theoretical uncertainties:** it groups systematic result of the theoretical model in use and the difference between models:
  - physics model: since the t-fit aims to determine the b-slope parameter too, we have to set a theoretical value for b-slope for generated model in the simulation procedure. Different theoretical models give a difference between ± 2 GeV^{-2} for the nuclear slope value. It will be modified in the generator PYTHIA8 [62]
  - fit function: additional studies to the fit function in order to take into account the parametrization systematics. For this reason we will add a quadrature term to the exponential fit with become $\exp(-b|t| + ct^2)$, and also we will variate the the ρ value by (± 0.02)
  - fit range: as explained before the fit range is defined by the acceptance distribution. We have only considered t-range above 0.3 acceptance correction. This range will be variated between 0.2 and 0.5 for fit stability systematic studies
  - CNI term: the fit is repeated with only the pure nuclear amplitude included, whereas in the nominal analysis also the CNI terms are included. The impact of the Coulomb term is very small in the selected t-range, but the interference yields a negative contribution of up to 1 %

Different systematic errors are propagated to the fit parameter using the maximum and minimum deviation technique. For example, we take the upper and lower error alignment limits, then we rerun our analysis chain for both cases, and we compute the difference in fit parameters between the maximum and minimum case. Measurements results and propagated uncertainties are detailed in the table 7.10 for different t-reconstruction methods.

The fit result using the subtraction method yields $\sigma_{tot} = 94.88 \pm 0.12$ mb and $b = 19.45 \pm 0.05$ GeV^{-2} while the local angle method results are $\sigma_{tot} = 94.75 \pm 0.11$ mb and $b = 19.34 \pm 0.04$ GeV^{-2}. The quality of fits is relatively poor with a χ^2/N_{dof} of 1.7 for both methods, which may indicate imperfections in effective optics, as is also probed by the difference in total cross section and slope between the different methods, which is larger than the statistical uncertainty. As nominal method the subtraction method is retained because of its much better

Table 7.10: Total cross section and nuclear slope measurement results for different t-reconstruction method. Corresponding systematical and statistical uncertainties are also presented. Details about systematical errors label can be found in § 7.5.0.2

	Subtraction		Local angle	
	σ_{tot} [mb]	b [GeV^{-2}]	σ_{tot} [mb]	b [GeV^{-2}]
Fit result	94.88	19.45	94.75	19.35
Stat. err.	0.12	0.05	0.11	0.04
Optics	0.67	0.27	0.28	0.13
Luminosity	1.15	-	1.15	-
Background	0.18	0.03	0.14	0.03
Reco Eff.	0.41	-	0.41	-
Detector resolution	0.03	0.01	0.37	0.14
Unfolding	0.07	0.02	0.12	0.04
total align.	0.24	0.04	0.14	0.01
Emittance	0.14	0.02	0.14	0.03
Beam energy	0.10	0.03	0.05	0.01
Crossing angle x	0.06	0.02	0.02	0.05
t-rec. method	0.13	0.10	0.13	0.10
Phys. mod.	0.01	0.01	0.17	0.10
ρ value	0.18	0.02	0.18	0.02
Fit func.	0.19	-	0.52	-
Fit Range	0.03	0.00	0.00	0.01
No CNI	0.50	0.09	0.50	0.09
Total sys.	1.56	0.31	1.54	0.27

t-resolution and weaker dependence on the detector modeling details as opposed to all other methods depending on the local angle, despite the fact that subtraction method depends more on optics details.

7.6 Discussion

TOTEM has used the same data to perform a luminosity-independent measurement of the total cross section by a simultaneous determination of elastic and inelastic event yields, and a ρ-independent measurement without using the optical theorem by summing directly elastic and inelastic [68] cross sections. Using the luminosity-dependent method also applied for our measurement TOTEM quotes a result of $\sigma_{tot} = 98.6 \pm 2.2$ mb, which is about 3.7 mb higher than our result. Assuming that the uncertainties are fully uncorrelated the difference between ATLAS and TOTEM corresponds to 1.33 σ. The uncertainty of the TOTEM result is dominated by the luminosity provided by CMS with an error of $\pm$4%, while our new measurement benefits from a smaller luminosity uncertainty of only 2.45% [61].

The TOTEM measurements using the luminosity-dependent and independent methods differ by only 0.5 mb, indicating that potential offsets between the ATLAS and CMS luminosity scales can't be the only explanation for the total cross section discrepancy. A recently discovered beam-beam effect lowers the luminosity scale by 1.41% in ATLAS. It was not yet known at the time of the TOTEM publication [68]. While TOTEM claims that the contribution of the CNI term is beyond their experimental sensitivity and thus not included in their fits, the present analysis reveals in contrast that omitting this term lowers the total cross section by as much as 0.5 mb. Another source for the discrepancy could be the beam optics. TOTEM uses only the local angle method for t-reconstruction and in our case using the local angle method without further tuning gives a total cross section about 2 mb higher than the effective optics [61].
The present analysis has carefully compared different t-reconstruction methods and the consistency at the level of 0.2 mb supports the correctness of the effective optics. The value of the nuclear slope determined by TOTEM is with $b = 19.89 \pm 0.27$ GeV^{-2} about 0.44 GeV^{-2} larger than our measurement, however given the larger uncertainties the discrepancy is lower than 2 σ.

7.7 Conclusion

In this chapter we describe the measurement of the total pp cross section from elastic scattering using the optical theorem with the ALFA sub-detector from data recorded in 2011 during

a special run with high β^* optics. The analysis is using data-driven methods to determine relevant beam optics parameters, reconstruction efficiency and to tune the simulation. A key element for this analysis is the determination of the effective beam optics, which takes into account measurements from ALFA sensitive to ratios of transport matrix elements and calibration uncertainties of the quadrupoles. A careful evaluation of the associated systematic uncertainties includes in particular the comparison of different t-reconstruction methods being sensitive to different transport matrix elements. A dedicated effort was made by the luminosity task force group to determine the absolute luminosity for this run taking into account the very special conditions at low μ. From a fit to the differential elastic cross section we determine the total cross section at the LHC at $\sqrt{s} = 7$ TeV to be:

$$\sigma_{\text{tot}}(pp \to X) = \left(94.88 \pm 0.12_{\text{stat.}} \pm 1.56_{\text{syst.}}\right) \text{ mbarn},$$

where the systematic uncertainty is dominated by the uncertainty on the luminosity, followed by the error on the effective optics and uncertainties related to the extrapolation to $t \to 0$.

This measurement is about 3.7 mbarn lower than the previous result from the TOTEM collaboration [68], taking the quoted uncertainties as uncorrelated this deviation corresponds to a discrepancy of 1.33 σ. Future analyses of the already recorded data at 8 TeV both with the same optics at $\beta^* = 90$ m and at yet higher $\beta^* = 1$ km will yield more insight in this discrepancy.

The analysis chain was presented and detailed in § 7.3. Since ALFA was taking data for the first time, the present analysis was fully developed during the last two years. In the following I resume my main contribution in this analysis:

- event selection cut where I have studied several cuts and options before we come to the final one presented in § 7.3.2
- t-reconstruction section with the additional *local angle* method; this method allowed us later to discover the optic problem
- background studies and *subtraction* technique
- the unfolding study. It was one of the main task which I have developed with the helps of an ATLAS expert (M. Bogdan), who's give me an important feedback. An unfolding package was then provided to the ALFA analysis group, and will be used for future data taking analysis
- statistical and systematical propagation to the final results

Moreover, I have my independent analysis chain software, developed and updated since the beginning of 2012. It was an independent tool used mainly to cross check with the main ALFA analysis chain. This helps to fix several bugs in both chains and prove to be useful. Moreover, this gives me a good and useful experience at different analysis stages, starting by the simulation, passing by the reconstruction and the application of different correction factor, and ending by the fit parametrization, measurement, and errors propagation.

Conclusion

This thesis presents my work on the ATLAS/ALFA roman pot system. It starts by the description of the experimental framework, LHC and ATLAS. Some beam dynamics notions are introduced in the first chapter, to be used in this thesis, since the LHC optics take an important role in the understanding of the analysis results. A summary of different luminosity measurement techniques for the ATLAS experiment are presented in chapter 3. Moreover, the ALFA theoretical motivations are introduced and followed by a description of the ALFA system and beam optics requirements.

Since my thesis starts during the last ALFA test beam at CERN in October 2010, I took a part of the test beam operational and analysis team. At the time, my main task was to study the performance of the 14 ALFA Overlap Detectors (ODs), calibrated them, and studied how far we can rely on the precision of these detectors. Their role is the measurement of the distance separating lower and upper main detector, with a precision in the order of 10 μm, using coincidence of halo beam protons. The importance of the distance measurement is the direct impact of the precision on the luminosity and total cross section measurements.
Chapter 5 describes the dedicated procedures to calibrate the OD system. This calibration was not possible without a precise alignment between the ALFA and the telescope system (telescope setups are used as independent reference). Furthermore, the detector resolution was studied to be used in the distance measurement statistical errors estimation. At the end of the chapter I present a list of different systematic uncertainty studies with a table explaining the expected precision of different detectors.
Results show a precision better than 10 μm (comparing OD measurements to an independent telescope measurement) with a sufficient statics, which make the detectors ready for the data taking round in the LHC tunnel.

Once installed in the tunnel, the first ATLAS/ALFA data taking took place in September 2011. My participation covered 2 areas:

1. operational: detectors commissioning, electronics and triggers validation. I have also participated to the data taking
2. analysis: distance measurement analysis using ODs, physics data analysis, and development of an independent full analysis chain in order to cross check results with the main ALFA chain.

Chapter 6 is about the distance measurement analysis, using the calibrated ODs. The high level of background and the unpredictable state of the beam halo have pushed the analysis challenge to the limits, and are behind the development of the OD analysis. For the time being, we succeed to measure two distances with a precision of 18 and 22 μm (≈ 0.2 %) which is enough for actual run conditions, where one can see the negligible effect of the vertical alignment on the σ_{tot} measurement in table 7.10.
Systematic investigations are behind the development of the distance analysis chain, where I had try to give the most realistic estimation of systematic errors due to the background contaminations. The simulations have been developed to adapt the data taking conditions, and with a dedicated fine tuning it solved the systematic issue.

The physics analysis of this run, including the measurement of the σ_{tot} and b-slope at 7 TeV are detailed in the last chapter, starting by reconstructed raw data till the fit of the final $\mathrm{d}\sigma_{el}/\mathrm{d}t$ distribution. Elastic events are biased by a small fraction of irreducible background, which have been subtracted from the raw data spectrum. Afterwards, an unfolding study is presented using an Iterative Dynamically Stabilized (IDS) method to correct for detector and beam smearing effect. In addition results of this method are compared to a bin by bin and single value decomposition unfolding methods, with an advanced systematic and statistical uncertainty studies.
Simulations have been developed for unfolding, also it is used to calculate the acceptance and selection efficiency correction. Finally, the differential elastic cross section distribution is deduced after the normalization of the differential elastic events distribution by the integrated luminosity. The parametrization of this distribution ($\mathrm{d}\sigma_{el}/\mathrm{d}t$) allows the measurement of the total proton-proton cross section (σ_{tot}) and the nuclear slope (b-slope).
The results have shown that:

$$\sigma_{\mathrm{tot}}(pp \to X) = \left(94.88 \pm 0.12_{\mathrm{stat.}} \pm 1.56_{\mathrm{syst.}}\right) \text{ mbarn}$$

and

$$b = \left(19.45 \pm 0.05_{\mathrm{stat.}} \pm 0.31_{\mathrm{syst.}}\right) \text{ GeV}^{-2}$$

This thesis gave me the chance to work on different experimental physics areas, starting by instrumentation and calibration of the detector, going through physics analysis and some advanced uncertainty studies, and ending by physics results and new measurements. All these steps cover an important part of an experimental physicist work. Moreover, it allowed me to discover and develop many skills such as the data analysis, programing, hardware (detec-

tors, electronics, triggers, ...) and communication (weekly presentations, poster, international conferences, ...).

In the near future the LHC will deliver collisions at $\sqrt{s} = 14$ TeV, which will allow for new measurements and studies at this new energy scale. In the other hand, the optics and the machine will be developed to produce the high β^* conditions, which allow an independent measurement of the luminosity using the ALFA detectors. The work presented in this thesis will be the baseline for the future analysis and developments.

Remerciements

Je remercie Monsieur Achille Stocchi davoir accepté être président du jury et surtout pour son support à la fin de mon contrat. Je remercie vivement Madame Corinne Augier et Monsieur Christophe Royon davoir acceptés dêtre rapporteurs et de donner de leur temps pour juger ce travail. Je remercie Monsieur Vit Vorobel davoir accepté de faire partie du jury de ma thèse.

Patrick je te remercie pour ta confiance en moi, ta sympathie et ton support. Tu étais toujours là pour me motiver et m'aider à réordonner mes priorités. Tu as toujours réussi à me diriger de ta faon intelligente avec des interventions courtes mais efficaces. J'ai eu la chance de travailler avec toi qui donne une importance équivalente à la formation scientifique et personnelle. Un grand merci aussi pour ton support de tous les jours, pour tous les bons moments qu'on a passé ensemble durant les voyages ou pendant les nos nombreux dners (fondue, BBQ, tartiflette, etc...)

Matthieu tu es ami, un grand frère, et un collègue avec lequel j'ai adoré travailler et discuter. Je me rappellerai toujours tes petits exercices ROOT à mon arrivée, la première semaine au CERN, nos meetings Overlap sur ton tableau et toutes les grandes discussions stratégiques sur les analyses ;). Je me rappellerai également tous les moments à Prague, à Lisbonne, à Cracovie, à Giessen, à Genève et enfin à Saint-Genis. Tu étais un acteur nécessaire à l'avancement de ma thèse... Pour tout cela, merci!

Nicolas et Laurent merci pour les dernières répétitions de ma thèse et pour votre support, Daniel merci pour toutes nos discussions et pour tes passages requérant régulièrement des nouvelles de ALFA. Sophie merci pour ton support. Grâce à toi jai bien avance sur le sujet de loptique. Merci à toute léquipe ATLAS au LAL pour votre accueil et tous les moments quon a partagés ensemble.

ATLAS/ALFA group thank you for all the support and your confidence in my working tasks, I appreciated that you supported me in some very dedicated analysis. Thank you also for all the good time during travels, Bowling and BBQ. I was lucky to work with Per, Karlheinz, Patrick, Sune, Hasko, Kris, Kristof, Tom, ...

Merci pour Lan, Driss, Ali, et tous les amis avec qui jai passé les pauses café, les déjeunés et les weekends. Vous êtes super!!!

Et pour la famille au Liban :
أمي وأبي، أهديكم هذا العمل المتواضع الذي أعتبره ثمرة دعمكم وتضحياتكم الجبارة. ستبقون دوماً مثلاً صالح لنا ولأبنائنا.

أخي وصديقي رباح، هذه الاطروحة لا تستحق أن نمضي أياماً بعيدين قسراً، لكن طريق العلم والمعرفة غالباً ما يتطلب بعض التضحيات. يوماً بعد يوم تؤكد لي أكثر وأكثر أنك دائماً على قدر التطلعات والامال وأن غدك مشرق بإذن الله.

إيهاب، وعد وشادي، من كان يتخيل أن نجتمع في نفس المدينة في هذه السنة الأخيرة من اطروحتي. شكراً على كل الدعم والحب الذي منحتموني إياه، خاصةً في الضروف الصعبة. اتمنى أن نجتمع في مدن أخرى وإنشاءالله دائماً في لبنان.

List of Tables

List of Figures

Bibliography

[1] L. R. Evans and P. Bryant, *LHC Machine*, J. Instrum. **3** (2008) S08001. 164 p. This report is an abridged version of the LHC Design Report (CERN-2004-003).

[2] The ALICE Collaboration, *The ALICE experiment at the CERN LHC. A Large Ion Collider Experiment*, J. Instrum. **3** (2008) S08002. 259 p. Also published by CERN Geneva in 2010.

[3] The CMS Collaboration, *The CMS experiment at the CERN LHC. The Compact Muon Solenoid experiment*, J. Instrum. **3** (2008) S08004. 361 p. Also published by CERN Geneva in 2010.

[4] The LHCb Collaboration, *The LHCb Detector at the LHC*, J. Instrum. **3** no. LHCb-DP-2008-001. CERN-LHCb-DP-2008-001, (2008) S08005. Also published by CERN Geneva in 2010.

[5] The LHCf Collaboration, *The LHCf detector at the CERN Large Hadron Collider*, J. Instrum. **3** (2008) S08006.

[6] The TOTEM Collaboration, *The TOTEM Experiment at the CERN Large Hadron Collider*, J. Instrum. **3** (2008) S08007.

[7] CERN, *LHC Lumi Days: LHC Workshop on LHC Luminosity Calibration*. CERN, Geneva, 2011. Organisers: Burkhardt, Helmut; Ferro-Luzzi, Massimiliano; Mangano, Michelangelo.

[8] K. Wille, *The physics of particle accelerators: an introduction*. Oxford Univ. Press, Oxford, 2000.

[9] S. M. White, H. Burkhardt, and P. Puzo, *Determination of the Absolute Luminosity at the LHC*. PhD thesis, Orsay, Université Paris-Sud 11, Orsay, 2010. Presented on 11 Oct 2010.

[10] The ATLAS Collaboration, *The ATLAS Experiment at the CERN Large Hadron Collider*, J. Instrum. **3** (2008) S08003. 437 p. Also published by CERN Geneva in 2010.

[11] C. W. Fabjan and T. W. Ludlam, *Calorimetry in high-energy physics*, Annu. Rev. Nucl. Part. Sci. **32** no. CERN-EP-82-37, (1982) 335–389. 31 p.

[12] The ATLAS Collaboration, *Readiness of the ATLAS Liquid Argon Calorimeter for LHC Collisions*, Eur. Phys. J. C **70** no. arXiv:0912.2642. CERN-PH-EP-2010-041, (2010) 723–753. 31 p.

[13] *Measurements of the properties of the Higgs-like boson in the two photon decay channel with the ATLAS detector using 25* fb^{-1} *of proton-proton collision data*, Tech. Rep. ATLAS-CONF-2013-012, CERN, Geneva, Mar, 2013.

[14] *Measurements of the properties of the Higgs-like boson in the four lepton decay channel with the ATLAS detector using 25 fb1 of proton-proton collision data*, Tech. Rep. ATLAS-CONF-2013-013, CERN, Geneva, Mar, 2013.

[15] The ATLAS Collaboration, *ATLAS Forward Detectors for Measurement of Elastic Scattering and Luminosity*. Technical Design Report. CERN, Geneva, 2008.

[16] The ATLAS Collaboration, *Zero Degree Calorimeters for ATLAS*, Tech. Rep. LHCC-I-016. CERN-LHCC-2007-001, CERN, Geneva, Jan, 2007.

[17] P. Jenni, M. Nordberg, M. Nessi, and K. Jon-And, *ATLAS Forward Detectors for Measurement of Elastic Scattering and Luminosity*. Technical Design Report. CERN, Geneva, 2008.

[18] V. Barone and E. Predazzi, *High-Energy Particle Diffraction*. Texts and monographs in physics. Springer, Berlin, 2002.

[19] *Anneaux de stockage ISR*. Cahier Technique. CERN, Geneva, 1969.

[20] R. Battiston and al., *The Roman pot spectrometer and the vertex detector of experiment UA4 at the CERN SPS collider*, Nucl. Instrum. Methods Phys. Res., A **238** no. CERN-EP-84-156, (1984) 35–44. 29 p.

[21] J. G. Rushbrooke, *The UA5 streamer chamber experiment at the SPS* $p\overline{p}$ *collider*, Phys. Scr. **23** no. CERN-EP-80-104, (1980) 642–648. 26 p.

[22] M. Bertani and al., *Small t physics at the Tevatron collider*,.

[23] F. Abe and al., *Measurement of small angle antiproton-proton elastic scattering at* $\sqrt{s}$ *=546 and 1800 GeV.*, Tech. Rep. 50(ANL-HEP-PR-95-13), Phys. Rev. D, Nov, 1994.

[24] N. Amos and al., *Measurement of ρ, the ratio of the real to imaginary part of the $\overline{p}p$ forward elastic scattering amplitude, at $\sqrt{s} = 1.8$ TeV*, Phys. Rev. Lett. **68** no. FERMILAB-PUB-91-267, (1991).

[25] F. Abe and al., *Precision measurement of the prompt photon cross section in $p\overline{p}$ collisions at $\sqrt{s} = 1.8$ TeV*, Phys. Rev. Lett. **20** no. ANL-HEP-PR-95-016, (1994) 2662–2666. 5 p.

[26] R. Baltrusaitis and al. Phys. Rev. Lett. no. 52, (1984) 1380.

[27] M. Honda and al. Phys. Rev. Lett. no. 70, (1993) 525.

[28] P. Lipari and M. Lusignoli, *Interpretation of the measurements of total, elastic and diffractive cross sections at LHC*, Tech. Rep. arXiv:1305.7216, May, 2013. Comments: 24 pages, 11 figures.

[29] J. Kaspar, *Elastic scattering at the LHC.* PhD thesis, Charles U., 2011. Presented 10 Apr 2012.

[30] J. Beringer and al., *Review of Particle Physics, 2012-2013. Review of Particle Properties*, Phys. Rev. D **86** no. 1, (2012) 010001.

[31] TOTEM collaboration, *First measurement of the total proton-proton cross section at the LHC energy of $\sqrt{s} = 7$ TeV*, EPL **96** no. arXiv:1110.1395. CERN-PH-EP-2011-158. TOTEM-2011-02, (2011).

[32] The ATLAS Collaboration, *Improved luminosity determination in pp collisions at $\sqrt{s}$ = 7 TeV using the ATLAS detector at the LHC*, Tech. Rep. arXiv:1302.4393. CERN-PH-EP-2013-026, CERN, Geneva, 2013.

[33] S. Maettig, *Luminosity Measurements with the ATLAS Detector*. PhD thesis, Hamburg U., Jun, 2012. Presented 06 Aug 2012.

[34] W. Bonivento, *Online luminosity monitoring with liquid Argon calorimeters at ATLAS and D0*, Tech. Rep. ATL-LARG-2001-001, CERN, Geneva, Nov, 2000. revised version number 1 submitted on 2000-12-22 10:49:45.

[35] HiLum ATLAS Endcap Collaboration, *Relative luminosity measurement of the LHC with the ATLAS forward calorimeter*, J. Instrum. **5** no. arXiv:1005.1784, (2010) P05005. 16 p. Comments: 16 pages.

[36] S. Arfaoui, *The ATLAS liquid argon calorimeter high-voltage system: commissioning, optimisation, and LHC relative luminosity measurement.* PhD thesis, Marseille U., Luminy I U., Geneva, 2011. Presented 14 Oct 2011.

[37] The ATLAS Collaboration, *Luminosity Determination in pp Collisions at $\sqrt{s}$ = 7 TeV using the ATLAS Detector at the LHC.* No. arXiv:1101.2185. CERN-PH-EP-2010-069. 2011.

[38] S. van der Meer, *Calibration of the effective beam height in the ISR*, Tech. Rep. CERN-ISR-PO-68-31. ISR-PO-68-31, CERN, Geneva, 1968.

[39] V. Papadimitriou, *Luminosity determination at the Tevatron,*. Comments: 5 pages, 8 figures, LHC Lumi days Workshop at CERN in January of 2011.

[40] V. Khoze, *Indirect luminosity measurements: theoretical assessment. Selected topics on the precision of luminometry at the LHC (as seen through the theorists eyes),*.

[41] C. Gabaldon, *Measurement of the Luminosity by the ATLAS Experiment*, Tech. Rep. ATL-LUM-PROC-2011-004, CERN, Geneva, Oct, 2011.

[42] R. C. Fernow, *Introduction to experimental particle physics*. Cambridge Univ. Press, Cambridge, 1986.

[43] R. G. Newton, *Optical theorem and beyond*, American Journal of Physics **44** no. 7, (1976) 639–642.

[44] G. Giacomelli, *Hadron-hadron elastic scattering and total cross sections at high energies*, Tech. Rep. DFUB-94-9, Bologna Univ. Ist. Fs., Bologna, May, 1994.

[45] M. Heller, *Mesure de la luminosité absolue et de la section efficace totale proton-proton dans l'expérience ATLAS au LHC*. PhD thesis, Orsay, Université Paris-Sud 11, Orsay, 2010. Presented on 05 Mar 2010.

[46] Amsterdam-CERN-Genoa-Naples-Palaiseau-Pisa Collaboration, *The real part of the proton-antiproton elastic scattering amplitude at the centre of mass energy of 546 GeV*, Phys. Lett. B **198** no. CERN-EP-87-147, (1987) 583–589. 15 p.

[47] V. Berardi and al, *Total cross-section, elastic scattering and diffraction dissociation at the Large Hadron Collider at CERN: Addendum to the TOTEM Technical Design Report*. Technical Design Report TOTEM. CERN, Geneva, 2004. Submitted on 18 Jun 2004.

[48] R. Castaldi and G. Sanguinetti, *Elastic scattering and total cross-section at very high energies*, Annu. Rev. Nucl. Part. Sci. **35** no. CERN-EP-85-36, (1985) 351–395. 61 p.

[49] S. Cavalier, *Détermination des paramètres optiques nécessaires pour la mesure de la luminosité absolue et de la section efficace totale dans ATLAS*. PhD thesis, Orsay, Université Paris Sud, Orsay, 2013.

[50] V. M. Abazov and al., *The Upgraded D0 Detector*, Tech. Rep. physics/0507191. FERMILAB-Pub-2005-341-E, FERMILAB, Batavia, IL, Jul, 2005.

[51] Mokhov, private communications.

[52] C. Augier, *Mesure de la partie réelle de l'amplitude de diffusion élastique proton-antiproton vers l'avant, à l'énergie dans le référentiel du centre de masse de 541 GeV*. PhD thesis, Paris Sud, Orsay, 1993. Presented on 15 Mar 1993.

[53] S. Jakobsen, *Performance evaluation and optimization of the luminosity detector ALFA*. PhD thesis, Bohr Inst., Copenhagen, Denmark, 2010. Presented on 16 Jul 2010.

[54] S. Jakobsen, *Measurement of elastic scattering with ALFA*, Internal note (2012).

[55] S. Ask and al., *Luminosity measurement at ATLAS: Development, construction and test of scintillating fibre prototype detectors*, tech. rep., 2006. `arXiv:physics/0605127 [physics]`.

[56] P. Barrillon and al., *64-channel Front-End readout chip - MAROC datasheet*, tech. rep., LAL, Orsay, 2008.

[57] C. Joram, H. Stenzel, and A. Braem, *Basic Considerations on the Overlap Detectors of the ATLAS ALFA system*, Tech. Rep. ATL-LUM-PUB-2007-002. ATL-COM-LUM-2006-009. CERN-ATL-LUM-PUB-2007-002, CERN, Geneva, Jun, 2006.

[58] Http://www.eudet.org.

[59] *Test Beam 2010 note*, in preparation.

[60] S. Cavalier, P. Puzo, H. Burkhardt, and P. Grafstrom, *90 m β^* Optics for ATLAS/ALFA*, 2nd International Particle Accelerator Conference, San Sebastian, Spain no. CERN-ATS-2011-134, (2011) 3 p.

[61] ATLAS/ALFA team, *Measurement of the total cross section in pp collisons at $\sqrt{s} = 7$ TeV from elastic scattering with the ATLAS detector*, Not yet published (2013) .

[62] Http://http://home.thep.lu.se/torbjorn/pythia.html.

[63] Http://mad.web.cern.ch.

[64] B. Malaescu, *An Iterative, Dynamically Stabilized (IDS) Method of Data Unfolding,*. Contribution to the proceedings of PHYSTAT2011. To be published in a CERN yellow report.

[65] A. Höcker and V. G. Kartvelishvili, *SVD approach to data unfolding*, Tech. Rep. hep-ph/9509307. LAL-95-55. MC-TH-95-15, Paris 11. Lab. Accél. Linéaire, Orsay, Sep, 1995.

[66] ATLAS Collaboration, *Improved luminosity determination in pp collisions at $\sqrt{s} = 7$ TeV using the ATLAS detector at the LHC*, EPJC no. NN, (2013) NN.

[67] J. Wenninger, *Energy Calibration of the LHC Beams at 4 TeV*, Tech. Rep. CERN-ATS-2013-040, CERN, Geneva, May, 2013.

[68] TOTEM Collaboration, *Measurement of proton-proton elastic scattering and total cross-section at* $\sqrt{s} = 7$ *TeV*, EPL no. 101, (2013) 21002.